Development of Novel Photocatalytic Overall Water Splitting Systems at Elevated Temperatures for Efficient Hydrogen Evolution

Yiyang Li

Inorganic Chemistry Laboratory

Department of Chemistry

St Peter's College

University of Oxford

A thesis submitted for the degree of Doctor of Philosophy

Michaelmas Term 2021

Table of Contents

Dedication

To my family
and my country,
with my deepest love

Declaration

I confirm that all the research described in this thesis is my own work unless otherwise stated. All the materials used in this thesis from other sources have been properly cited and fully acknowledged.

Yiyang Li

Acknowledgments

During the more than four years' life as a DPhil student at Oxford, there are a lot of people I would like to acknowledge, without whom I would never be able to accomplish my DPhil project and write up this thesis.

Firstly, I would like to thank my supervisor, Prof. Edman Tsang, for giving me the opportunity of working in his research group, for all his help, advice and guidance, and for his enthusiasm and kindness that inspired me throughout my DPhil study. There is no need to say that there have been quite a few hard times during this journey, and it is Edman who has supported me to overcome the difficulties and has led me to the right directions. Having known Edman for about five years, I feel that he is more than a supervisor to me now, but a mentor of life, and a friend.

Secondly, my research could not be possible without the professional assistance that I obtained throughout the DPhil project. Especially, I would like to thank:

Prof. Robert A. Taylor, Dr. Timothy Putchler, Dr. Mo Li and Vitaly Osokin (Oxford Physics) for the help on time-resolved photoluminescence spectroscopy;

Dr. Dharmalingam Prabhakaran (Oxford Physics) for kindly providing the light concentrated furnace for my experiments;

Dr. William Myers (Oxford Chemistry) for the help and trainings on the electron paramagnetic resonance spectroscopy;

Prof. Chen Wu, Zihan Wang (School of Materials Science and Engineering, Zhejiang University) for the magnetic measurements of my materials;

Prof. Yunhao Lu (Department of Physics) and Yiqi Wang (School of Materials Science and Engineering) in Zhejiang University for the DFT calculations in Chapter 5;

Prof. Xin-Ping Wu and Hui Zhou (School of Chemistry and Molecular Engineering, East China University of Science and Technology) for the DFT calculations in Chapter 6;

Prof. Georg Held and Dr. Alex Large (Diamond Light Source) for the help and training on the AP-XPS technique;

Prof. Rafal E. Dunin-Borkowski and Dr. András Kovács (Ernst Ruska-Centre for Microscopy and Spectroscopy with Electrons and Peter Grünberg Institute) for the microscopic studies in Chapter 5.

Dr. Songhua Cai (Department of Applied Physics, The Hong Kong Polytechnic University) for the microscopic studies presented in Chapter 6.

Dr. Guangchao Li (Wuhan Institute of Physics and Mathematics, Chinese Academy of Sciences) for the solid-state NMR studies.

Having obtained their assistance and support, have I been able to better conduct my own research and help the other group members. Also, I would like to thank all the reviewers who have peer-reviewed my papers during my DPhil study.

Thirdly, I want to thank the examiners of my *viva voce*, namely, Prof. Andrew Mills and Prof. Ludmilla Steier, for an enjoyable and unforgettable DPhil *viva* with inspiring questions and discussions.

Moreover, many thanks are given to the members of the Tsang group. Especially, I would like to thank Dr. Jianwei Zheng, Dr. Yung-Kang Peng and Dr. Liangsheng Hu for the guidance and assistance at the very beginning of my DPhil project. Also, I would like to thank Dr. Tuğçe Ayvalı and Dr. Pu Zhao for the help and support on the lab work and discussions of all kinds of problems. Many thanks are given to Christopher Foo who has collaborated with me on the photocatalytic water splitting project and explored the photocatalysts using the synchrotron techniques. I would also like to thank Dr. Tianyi Chen for the help on electron microscopy. Great thanks are given to Eloise Wootton for proofreading this thesis.

Furthermore, I want to express my gratitude to Dr. Jiaao Wei, Dr. Yao Meng, Dr. Jiaying Mo, Dr. Simson Wu, and Dr. Linus Wei-Che Lin for the unforgettable experience and joyful times, which will always be a precious part of my memory.

Last, but definitely not least, I would never reach where I am today without my family and friends. Many thanks are given to my lifelong friends, Chengxiao Liu and Fan Wu, who have always been supporting me at all my hard and perplexing times. Great gratitude must be given to my beloved parents and all my family members, thank you for all your unconditional and selfless love, and powerful support in all kinds throughout my life, especially at those most difficult times I have been through. Most importantly, I would like to thank my one and only love, Yu He, the love of my life, for the precious, incredible and irreplaceable love, who has made me complete, and my life colourful and meaningful.

Abstract

Environmental and energy issues have become one of the most important issues that human beings are facing, and carbon neutrality is a communal target worldwide nowadays. With the strong international incentives to decarbonise our fuels and chemicals, the solar-light-driven photocatalytic overall water splitting (POWS) reaction provides a promising and renewable way to store and utilise the abundant solar energy in the form of hydrogen which is the cleanest chemical fuel for mankind. Numerous materials and catalytic systems have been developed for more effective solar energy conversion, however, the performance achieved so far is still unsatisfactory.

In this context, this thesis has particularly focused on the design and development of novel POWS systems at elevated temperatures. Different semiconductor materials such as TiO_2 and MoS_2 were systematically studied in this thesis. In-depth catalytic activity studies illustrated the temperature effect on the POWS performance. Comprehensive surface characterisations combined with a series of spectroscopic, imaging and computational techniques were conducted to unravel the relationship between the activity and the structures of the catalysts.

Subsequently, various strategies have been proposed for improving the POWS activity at elevated temperatures, including the use of local electric field and local magnetic field. Remarkable charge polarisation effects have been identified in each case. Finally, it is demonstrated that the POWS system studied in this thesis could split seawater into H_2 and O_2 with extraordinarily high solar-to-hydrogen conversion efficiency of 20.3 % at 270 ^oC, exhibiting high potential for future practical applications.

List of Abbreviations

2D	Two Dimensional
AFM	Atomic Force Microscopy
AP-XPS	Ambient Pressure - X-Ray Photoelectron Spectroscopy
BE	Binding Energy
CTAB	Cetyltrimethylammonium Bromide
DFT	Density Functional Calculations
DMSO	Dimethyl Sulfoxide
E_{ads}	Adsorption Energy
EDS/EDX	Energy Dispersive X-Ray Spectrometry
EXAFS	Extended X-Ray Absorption Fine Structure
fcc	Face Centred Cubic
FTIR	Fourier-Transform Infrared Spectroscopy
FWHM	Full Width at Half Maximum
GC	Gas Chromatography
HAADF	High Angle Annular Dark Field
HEP	Hydrogen Evolution Photocatalyst
HER	Hydrogen Evolution Reaction
HRTEM	High-Resolution Transmission Electron Microscopy
IEF	Internal Electric Field
LA	Lewis Acid
LDH	Layered Double Hydroxide
LEF	Local Electric Field
MFE	Magnetic Field Effect
M_s	Saturation Magnetisation

NMR	Nuclear Magnetic Resonance
OEP	Oxygen Evolution Photocatalyst
OER	Oxygen Evolution Reaction
PEC	Photoelectrochemical
POWS	Photocatalytic Overall Water Splitting
PV-E	Photovoltaic-electrolysis
QE	Quantum Efficiency
SEM	Scanning Electron Microscope
SQUID	Superconducting Quantum Interference Device
STEM	Scanning Transmission Electron Microscopy
STH	Solar To Hydrogen
TCD	Thermal Conductivity Detector
TEM	Transmission Electron Microscopy
TEOS	Tetraethyl Orthosilicate
TMP	TriMethylPhosphine
TMPO	TriMethylPhosphine Oxide
TRPL	Time-Resolved Photoluminescence
TTIP	Titanium Tetra-Iso-Propoxide
UV-Vis DRS	Ultraviolet-Visible Diffuse Reflectance Spectroscopy
V_O	Oxygen Vacancy
XANES	X-Ray Absorption Near Edge Structure
XAS	X-Ray Absorption Spectroscopy
XPS	X-Ray Photoelectron Spectroscopy
XRD	X-Ray Diffraction Spectroscopy

List of publications

Journal articles

1. **Y. Li,** H. Zhou, S. Cai, D. Prabhakaran, W. Niu, A. Large, G. Held, R. A. Taylor, X.-P. Wu*, S. C. E. Tsang*, Photocatalytic Splitting of Seawater with Remarkable Solar-To-Hydrogen Efficiency. **2022,** *In Review.*
2. Z. Wang[#], **Y. Li[#],** C. Wu*, S. C. E. Tsang*, Electric-/magnetic-field-assisted photocatalysis: Mechanisms and design strategies. *Joule,* **2022,** *In Press.*
3. **Y. Li,** Z. Wang, Y. Wang, A. Kovács, C. Foo, R. E. Dunin-Borkowski, Y. Lu, R. A. Taylor, C. Wu* and S. C. E. Tsang*, Local Magnetic Spin Mismatch Promoting Photocatalytic Overall Water Splitting with Exceptional Solar-to-Hydrogen Efficiency. *Energy Environ. Sci.* **2022,** *15,* 265–277.
4. **Y. Li,** S. C. E. Tsang*, Unusual Catalytic Properties of High-Energetic-Facet Polar Metal Oxides. *Acc. Chem. Res.* **2021,** *54(2),* 366–378.
5. **Y. Li,** S. Wu, J. Zheng, Y.-K. Peng, D. Prabhakaran, R. A. Taylor, S. C. E. Tsang*, 2D photocatalysts with tuneable supports for enhanced photocatalytic water splitting. *Materials Today* **2020,** *41,* 34−43. **(Inner Cover)**
6. **Y. Li,** S. C. E. Tsang*, Recent Progress and Strategies for Enhancing Photocatalytic Water Splitting, *Materials Today Sustainability* **2020,** *9,* 100032.
7. **Y. Li,** Y.-K. Peng, L. Hu, J. Zheng, D. Prabhakaran, S. Wu, T. J. Puchtler, M. Li, K.-Y. Wong, R. A. Taylor, S. C. E. Tsang*, Photocatalytic Water Splitting by N-TiO_2 on Polar Oxides with Exceptional Quantum Efficiencies at Elevated Temperatures. *Nat. Commun.* **2019,** *10,* 4421. **(Editor's Highlight)**
8. J. Zheng, K. Lebedev, S. Wu, C. Huang, T. Ayvalı, T.-S. Wu, **Y. Li,** P.-L. Ho, Y.-L. Soo, A. Kirkland, S. C. E. Tsang*, High Loading of Transition Metal Single Atoms on Chalcogenide Catalysts, *J. Am. Chem. Soc.* **2021,** *143 (21),* 7979–7990.
9. J. Mo, E. C. M. Barbosa, S. Wu, **Y. Li,** Y. Sun, W. Xiang, T. Li, S. Pu, A. Robertson, T.-S. Wu, Y.-L. Soo, T. V. Alves, P. H. C. Camargo, W. Kuo, S. C. E. Tsang, Atomic-Precision Tailoring of Au–Ag Core–Shell Composite Nanoparticles for Direct Electrochemical-Plasmonic Hydrogen Evolution in Water Splitting, *Adv. Funct. Mater.* **2021,** *31,* 2102517.
10. C. Foo, **Y. Li,** K. Lebedev, T. Chen, S. Day, C. Tang, S. C. E. Tsang*, Characterisation of oxygen defects and nitrogen impurities in TiO_2

photocatalysts using variable-temperature X-ray powder diffraction. *Nat. Commun.* **2021,** *12,* 661.

11. T. Yoskamtorn, P. Zhao, X.-P. Wu*, K. Purchase, F. Orlandi, P. Manuel, J. Taylor, **Y. Li,** S. Day, L. Ye, C. C. Tang, Y. Zhao, S. C. E. Tsang*, Responses of Defect-Rich Zr-Based Metal-Organic Frameworks toward NH_3 Adsorption. *J. Am. Chem. Soc.* **2021,** *143,* 3205−3218.
12. J. Zheng, L. Lu, K. Lebedev, S. Wu, P. Zhao, I. J. McPherson, T.-S. Wu, R. Kato, **Y. Li,** P.-L. Ho, G. Li, L. Bai, J. Sun, D. Prabhakaran, R. A. Taylor, Y.-L. Soo, K. Suenaga, S. C. E. Tsang*, Fe on molecular-layer MoS_2 as inorganic Fe-S_2-Mo motifs for light-driven nitrogen fixation to ammonia at elevated temperatures. *Chem Catalysis,* **2021**, *1 (1),* 162-182.
13. Z. Tan, G. Li, H.-L. Chou, **Y. Li,** X. Yi, A. H. Mahadi, A. Zheng*, S. C. E. Tsang, Y.-K. Peng*, Differentiating Surface Ce Species Among CeO_2 Facets by Solid-State NMR for Catalytic Correlation. *ACS Catal.* **2020,** *10,* 4003−4011.
14. Y.-K. Peng*, B. Keeling, **Y. Li,** J. Zheng, T. Chen, H.-L. Chou, T. J. Puchtler, R. A. Taylor, S. C. E. Tsang*, Unravelling the key role of surface features behind facet-dependent photocatalysis of anatase TiO_2. *Chem. Commun.,* **2019,** *55,* 4415−4418.

Patent

1. S. C. E. Tsang (2021), Photocatalyst and use thereof. International Patent Publication No. WO/2019/239129; European Patent Publication No. EP3807220. (*Contributor*)

Conference

1. **Y. Li,** J. Zheng, S. Wu, C. Foo, S. C. E. Tsang*, Local Polarization Promoted Visible-Light-Driven Overall Water Splitting at Elevated Temperatures. Oral Presentation Abstract for the *17th International Congress on Catalysis (ICC)* **2020.** (Cancelled due to Covid-19)

Chapter 1 Introduction

1.1 Background

1.1.1 Photocatalysis

Catalysis is defined as the process of increasing the rate of a chemical reaction by adding an appropriate material known as a catalyst which can lower the activation energy of the chemical reaction. Catalysts are not consumed in the reaction and therefore can be recycled and reused in principle.[1] Photocatalysis, compared to conventional catalysis, normally requires light irradiation with the appropriate wavelength. Photons are absorbed and electrons in the photocatalysts are excited to higher energy levels, leaving a photo-generated hole in the lower energy levels. The photo-generated electrons and holes subsequently participate in the chemical redox reactions.[2]

Photocatalysis using semiconductor catalysts is a relatively new and fast-growing research area, and many self-cleaning architectural materials (such as glass, paint, fabric, etc.) based on photocatalytic principles have been commercialised and widely used.[3] In addition, photocatalysis has also been considered as a convenient and environmentally friendly approach for converting solar energy into chemical energy in the form of chemical fuels.[2] Many early reports are focused on the TiO_2-based semiconductor photocatalysts for photocatalytic water splitting.[4–7] In recent years, photocatalysis has been of great importance in many fields such as energy regeneration (*e.g.*, H_2 production from splitting water), green chemical synthesis, environmental protection (*e.g.*, degradation of organic dyes, air and water purification, etc.) and CO_2 reduction to fuels, and a wide range of materials have emerged as promising photocatalysts.[8–15]

1.1.2 Conversion and storage of solar energy

Energy and environmental issues have been of increasing importance in recent decades, due to the dramatic global climate issues arising from the use of fossil fuels. Thus, renewable and carbon-emission-free energy sources are in great demand. Solar energy is an abundant and clean energy resource, making it an ideal choice to meet future demands, and it has become one of the most promising renewable replacements for fossil fuels because it is cheap, widely distributed and almost inexhaustible.[8,16–19] However, an obvious disadvantage is that natural solar light is diffuse, intermittent, and fluctuating, which hinders the direct use of solar energy.[14–17] Instead, for practical application, the solar energy must be efficiently converted into other energy forms such as electrical energy, chemical energy and thermal energy, etc., which are storable and transportable, and can be easily used on demand.[20–24] Such requirement has motivated various research fields including solar cells, photocatalysis, photothermal effect, etc. Photovoltaic (PV) panels, or solar panels, which convert solar energy to electrical energy by the photovoltaic effect, have been widely used all around the world. The current PV market is nearly dominated by crystalline silicon single-junction PV cells which outperform other counterparts with lower capital costs. Other potential materials for PV cells have been developed as well, such as halide perovskite materials, which have received increasing attention in recent years.[19] PV panels can either be used to provide power directly, or in many cases, can be connected to an electrolyser for the subsequent production of chemical products. Such an integrated system is commonly known as a photovoltaic-electrolysis (PV-E) system. Moreover, photoelectrochemical (PEC) cells are also widely studied for the conversion of solar energy. A PEC cell normally consists of a photoanode/photocathode, a

counter electrode, electrolyte, and external circuit. To further simplify the system, particulate photocatalytic systems have been developed and extensively studied. Unlike PV-E and PEC systems, a particulate photocatalytic system only requires a very simple set-up. Photocatalyst particles are directly dispersed in the appropriate solvent to form a suspension which contains the reactant. Photons from solar light are absorbed by the photocatalyst particles to trigger subsequent physical and chemical processes, including the generation of excited electrons and holes, surface redox reactions, etc., and solar energy is finally stored in chemical products. Chemical products such as H_2, H_2O_2, NH_3, etc. made from common substances like H_2O and CO_2 using the energy of sunlight are known as solar fuels.[25] Generation of solar fuels has become one of the main targets of photocatalysis in the recent decades.

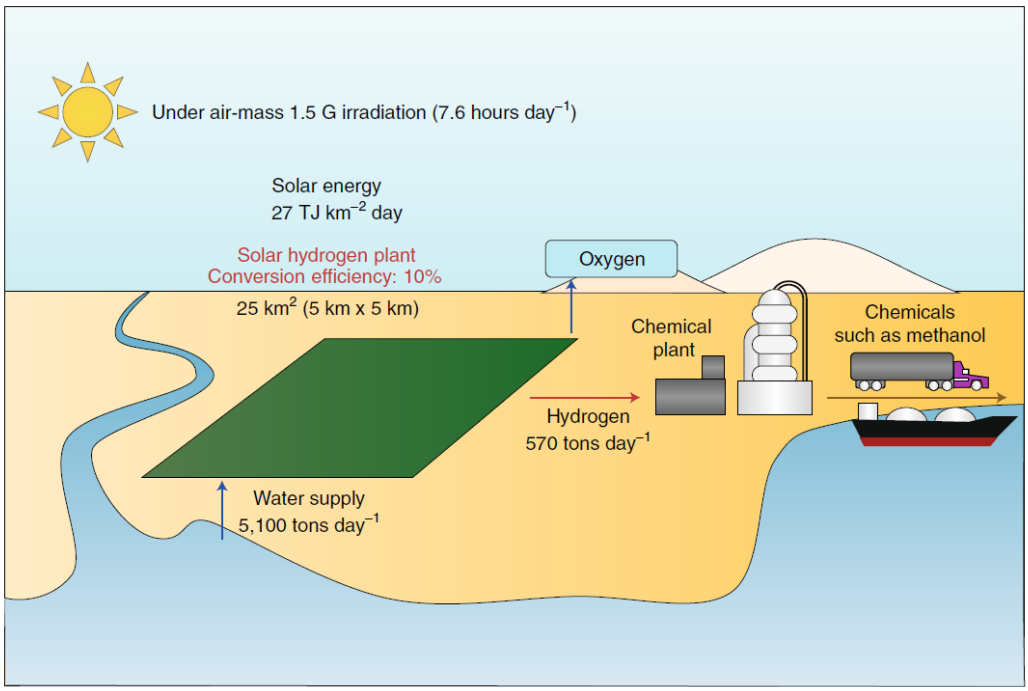

Figure 1.1 Schematic illustration of large-scale hydrogen production via solar energy and subsequent utilisation. Reproduced from ref. 26. Copyright 2010 American Chemical Society.

1.1.3 Hydrogen as a clean solar fuel

Solar-to-chemical energy conversion provides a highly promising means of storing solar energy efficiently as sustainable chemical fuels with minimal environmental impact or carbon emission. Among the potential chemical fuels produced from solar energy conversion, H_2 is one of the most attractive candidates as it offers the highest power density (143 MJ kg^{-1}) and the only product of its combustion is water.[27–30] Therefore, the solar-light-driven photocatalytic overall water splitting (POWS) reaction is considered to provide a platform for H_2 production. Water is decomposed to produce H_2 and O_2 in the presence of an appropriate photocatalyst under sunlight irradiation in such POWS system and subsequently, the produced H_2 can be used to generate power in a fuel cell or combined with CO_2 for the syntheses of other chemicals such as methanol.[30] An illustration of H_2 production from solar means and the subsequent utilisation is given in Figure 1.1. Clearly, using H_2 as a renewable chemical fuel offers the opportunity for human beings to mitigate the severe climate and environmental issues that we are facing, and also contributes to the sustainable developments of human societies.

1.2 POWS on semiconductor photocatalysts

1.2.1 Fundamental principles

Fujishima and Honda demonstrated a photoelectrochemical water splitting system in 1972,[5] which has been frequently referred to as the first demonstration of the photocatalytic water splitting reaction. In fact, the photo-induced oxygen evolution on TiO_2 can date back to 1968.[4] the POWS reaction catalysed by semiconductor materials has been extensively studied for decades, and significant progress has been achieved since then.[5] A wide range of semiconductors, such as TiO_2, $SrTiO_3$,

GaN, CdS, MoS_2 and some organic conjugated semiconductors, have been developed and extensively studied as photocatalysts.[17,22,23,31–36] Generally, the POWS reaction over semiconductor materials involves the following fundamental processes (Figure 1.2a):[37–39] (1) generation of the excited charge carriers: the semiconductor absorbs the photons of appropriate energy range to excite the electrons from the valence band (VB) to the conduction band (CB), leaving a hole in the VB; (2) separation and migration of the charge carriers: the photo-generated electrons and holes separate from each other and travel to the corresponding surface trapping sites of the catalyst particles. Some of the electrons and holes recombine with each other, accompanied by heat loss or fluorescence irradiation; (3) occurrence of surface chemical reactions for H_2 and O_2 evolution: protons in water are reduced by the excited electrons in the CB to produce H_2, and simultaneously, water is oxidised by the photo-generated holes in the VB for O_2 evolution. Therefore, to achieve the stoichiometric H_2 and O_2 evolution, the valence band maximum (VBM) should be more positive than = +1.23 V (vs. NHE) and the conduction band minimum (CBM) should be more negative than = 0.00 V (vs. NHE) to allow the O_2 and H_2 evolution reactions to happen readily to sustain the photocatalysis (Figure 1.2b). These reactions are summarised below:

Hydrogen evolution reaction (HER):

$$\textit{In an acidic aqueous solution: } 2H^+ + 2e^- \rightarrow H_2$$

$$\textit{In an alkaline aqueous solution: } 2H_2O + 2e^- \rightarrow H_2 + 2OH^-$$

Oxygen evolution reaction (OER):

$$\textit{In an acidic aqueous solution: } 2H_2O \rightarrow O_2 + 4e^- + 4H^+$$

$$\textit{In an alkaline aqueous solution: } 4OH^- \rightarrow O_2 + 4e^- + 2H_2O$$

Obviously, the minimum band gap of the semiconductor POWS photocatalyst is 1.23 eV, corresponding to a wavelength of around 1000 nm. It should be noted that despite the wide range of solar spectrum, most solar radiation lies in the visible light regime, which contributes 43% of total solar energy.[37] Thus, an ideal photocatalyst for the water splitting reaction should possess a band gap of lower than 3.1 eV (corresponding to a wavelength of 400 nm) so as to efficiently utilise the visible light, bearing in mind that the band gap should be at least 1.23 eV to provide sufficient thermodynamic driving force for the water splitting reaction.

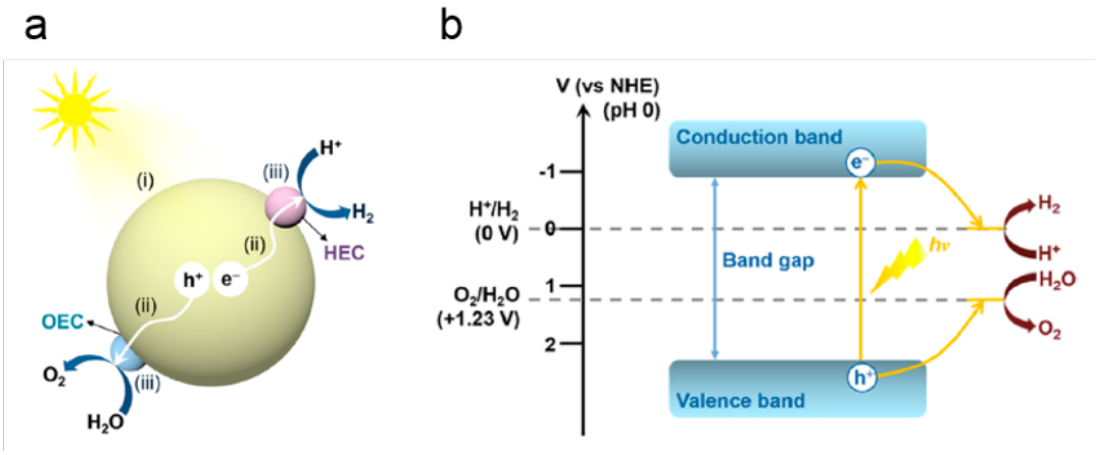

Figure 1.2 (a) Fundamental steps during photocatalytic water splitting on a semiconductor photocatalyst: **(i)** photo-excitation, **(ii)** charge separation and transport, and **(iii)** surface chemical reactions; **(b)** Schematic band structure and energy levels for photocatalytic water splitting based on one-step excitation. Reproduced from ref. [37]. Copyright 2020 American Chemical Society.

The POWS performance is usually evaluated by H_2 evolution rate, quantum efficiency (QE) and solar-to-hydrogen (STH) conversion efficiency. H_2 evolution rate directly indicates how fast H_2 is produced in a photocatalytic system. QE is the ratio of the number of H_2 molecules evolved to the number of photons of a given energy that shines on the photocatalyst. It is normally measured at a specific wavelength or a small wavelength range rather than a wide spectrum, so as to understand the behaviour of a photocatalytic system at different wavelengths. QE

is defined by the following equation:

$$\text{QE (\%)} = \frac{\text{Number of } H_2 \text{ molecules} \times 2}{\text{Number of incident photons}} \times 100\ \% \qquad \textbf{Equation 1.1}$$

The STH conversion efficiency is a standardised index focusing on the overall energy conversion efficiency from solar energy to chemical energy, which is defined as follows:

$$\text{STH (\%)} = \frac{\text{Evolved } H_2 \text{ amount} \times \Delta G}{P \times S \times t} \times 100\ \% \qquad \textbf{Equation 1.2}$$

where P is the power of solar irradiation (0.1 W cm^{-2}), S is the illuminating area in square centimetres; t is the time of reaction in seconds; ΔG is the Gibbs free energy for the POWS reaction under the reaction conditions; the evolved H_2 amount is typically given in moles.

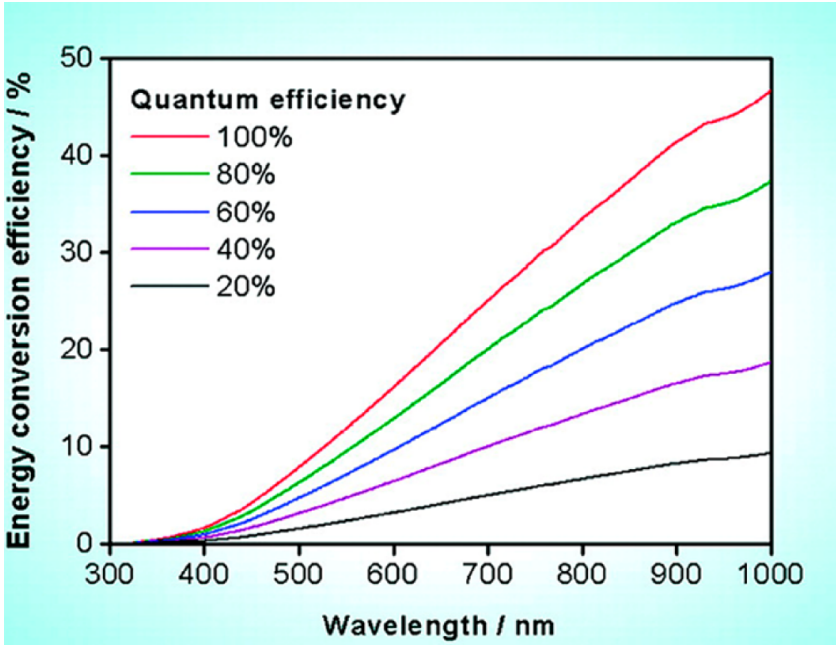

Figure 1.3 Calculated STH conversion efficiency values as functions of the maximum absorption wavelength for a one-step POWS using semiconductor photocatalysts with various QEs. The calculations are based on standard AM 1.5G solar irradiation. Reproduced from ref. [26]. Copyright 2010 American Chemical Society.

The STH is closely related to the absorption property of the photocatalysts. Assuming that only UV light up to 400 nm can be absorbed by the semiconductor

photocatalyst with a QE of 100%, the STH would be limited to 2% (if heat loss is neglected),[26] as illustrated in Figure 1.3. If the absorption range is extended into the visible light region up to 700 and 1000 nm, the maximum STH efficiency would be increased to 25% and 47%, respectively (Figure 1.3). The United States Department of Energy has proposed a goal of producing H_2 at a cost of 2.00-4.00 USD kg^{-1} so as to obtain an economically viable alternative to fossil fuels.[40] To achieve this goal, a recent study suggested that a photocatalytic reaction system should have a STH efficiency of 10% and a lifetime of 10 years.[41] Likewise, assuming a QE of approximately 100%, a photocatalyst requires an absorption edge of 520 nm to attain the target STH of 10%. In contrast, a semiconductor capable of harvesting light up to 650 nm could have a QE of less than 60% to achieve the target STH. Obviously, in order to obtain a satisfactory POWS system, studies should focus on the semiconductor materials that have good visible light absorption properties.

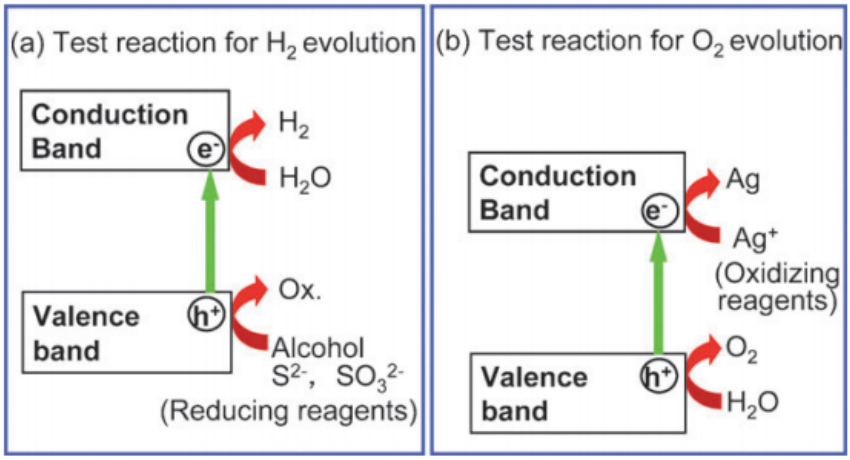

Figure 1.4 Illustration of the sacrificial HER and OER systems in the presence of different sacrificial reagents (half reactions of water splitting reaction). Reproduced from ref. [8]. Copyright 2009 Royal Society of Chemistry.

As mentioned before, the POWS reaction involves two half reactions: H_2 evolution reaction (HER) and O_2 evolution reaction (OER), which have been extensively

explored separately, with the help of various sacrificial reagents.[31,32,42–44] As mentioned before, excited electrons and holes are generated upon absorption of photons, and then H^+ are reduced by the electrons, while H_2O or OH^- are oxidised by the holes at appropriate band positions. However, for some semiconductor materials, the band positions only partly fulfil the thermodynamic requirements for POWS reaction, for example, the CB (or VB) is not negative (or positive) enough to drive the HER (or OER), while the other band is at the appropriate position, thus sacrificial reagents are required to assist the redox cycles. The sacrificial reagents act as hole (or electron) scavengers so as to keep the charge balance of the photocatalysts. For example, organic chemicals such as methanol and ethanol are most widely used as the hole-scavengers to facilitate the photocatalytic HER, because they are readily oxidised by the photo-generated holes in the VB;[45–47] while $FeCl_3$, $AgNO_3$, KIO_3, etc. are frequently used as electron-scavengers in photocatalytic OER systems, since these oxidative species can consume the photo-generated electrons in the CB.[48–50] Such sacrificial systems are illustrated in Figure 1.4, which should be differentiated from overall water splitting system, since H_2 and O_2 are not generated stoichiometrically in these sacrificial systems. Han and Hu have recently reported enhanced H_2 production using methanol as a hole-scavenger at elevated temperatures and found that the methanol decomposition also contributed to the overall H_2 production.[32] However, the use of sacrificial reagents exhibits several disadvantages, such as adding up to the total capital cost and leading to unwanted by-products (hydrocarbons and alcohols, etc.). For example, when carrying out OER using $AgNO_3$ as the electron-scavenger (Figure 1.4b), Ag nanoparticles could form after reacting with the photo-generated electrons and cover the active sites on the surface of photocatalysts,

therefore reduce the stability and lifetime of the photocatalytic system. All these above-mentioned disadvantages would largely hinder the further practical applications of such systems.

1.2.2 Developments of the POWS system

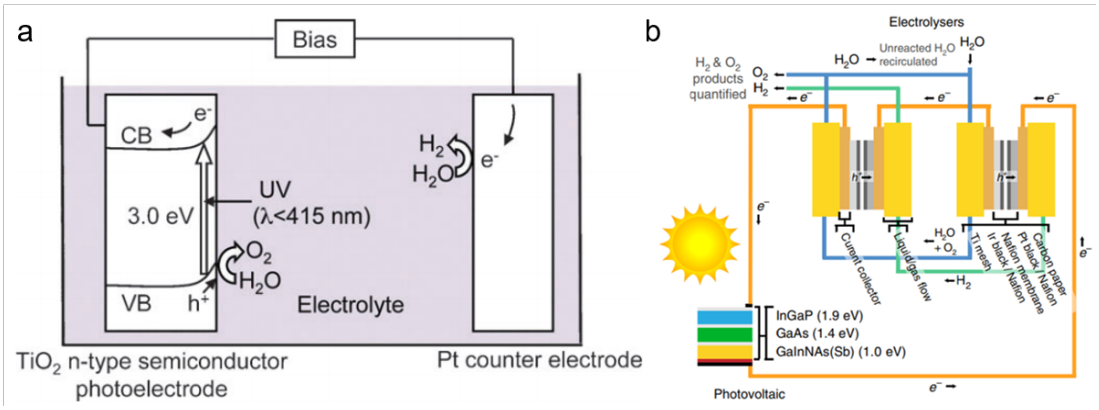

Figure 1.5 (a) Honda–Fujishima effect-water splitting using a n-type TiO_2 photoelectrode.[8] **(b)** A recently reported PV-E device which consists of a triple-junction solar cell and two PEM electrolysers connected in series, showing a STH efficiency over 30%. Reproduced from ref. [51]. CC BY 4.0.

As mentioned in Section 1.1.2, several systems have been developed to convert solar energy to other energy forms. The pioneering study of POWS was demonstrated using a PEC cell, where n-type semiconductor, TiO_2, was engaged as the photoanode. UV-Vis irradiation of wavelengths shorter than 415 nm was applied to the TiO_2 photoanode and a platinum black electrode was used as the counter electrode (Figure 1.5a). Photocurrents of a few mA and a quantum efficiency of 0.1% were observed in this pioneering study, which then encouraged extensive studies of POWS systems.[5] PV-E cells have been used for H_2 evolution from water splitting as well. Photons from solar light are absorbed and converted to electricity by the PV panels, and then the photocurrent can be transferred to an electrolyser where water is electrolysed to produce H_2 and O_2 stoichiometrically.[51] Such a PV-E POWS system combines the advantages of PV panels and

electrolysers: high solar-to-electricity efficiency and high Faraday efficiency of electrolysers, resulting in high overall STH conversion efficiencies (Figure 1.5b). However, the main drawback of the PV-E system is the complicated equipment and high cost.

Particulate POWS systems have been attracting increasing interest in recent years and have been considered as a low-cost technology with the potential to enable large-scale solar H_2 production, because of the ready synthesis of the associated photocatalysts as well as the simple reactor and facility designs.[52–54] Unlike the PEC and PV-E cells, a particulate POWS system only involves the use of photocatalyst particles without further sophisticated fabrications (Figure 1.6). Thus, through my DPhil project, I mainly work on the particulate POWS system and this will be the focus of this thesis.

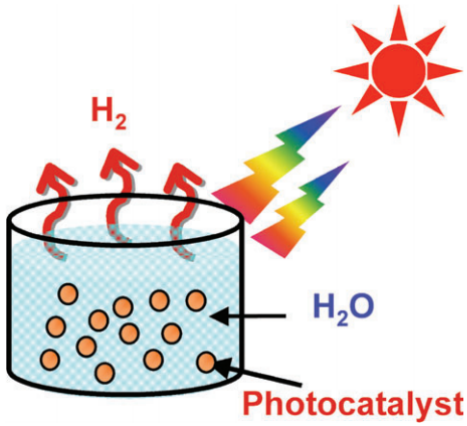

Figure 1.6 Solar H_2 production from POWS reaction using particulate photocatalysts dispersed in water under solar light irradiation. Reproduced from ref. [8]. Copyright 2009 Royal Society of Chemistry.

As mentioned before, a POWS system needs to drive both HER and OER simultaneously, which means in a conventional POWS system, the CB and VB positions are required to be at the appropriate energy levels, and additionally, the band gap should be relatively narrow to efficiently take up the visible light. In reality,

it is very difficult for only one material to fulfil all these requirements at the same time. Apart from the previously mentioned sacrificial systems, the Z-scheme POWS system has been developed to overcome such difficulties, in which two or more different semiconductor materials are included. A Z-scheme POWS reaction normally involves the two-step photo-excitation of a H_2 evolution photocatalyst (HEP) and an O_2 evolution photocatalyst (OEP), both of which have narrow band gaps. Therefore, the required potential difference is divided into several contributions, and thus the band gap of the photocatalytic material does not have to straddle both the H_2 and O_2 evolution potentials. Hence, narrow band gap semiconductors that are active only for proton reduction or water oxidation can be employed to split water using solar energy, and the aforementioned sacrificial systems of the half reactions can be integrated to form a Z-scheme POWS system. Similar to the conventional one-step POWS system, in a Z-scheme system, photons trigger the generation of electron-hole pairs in both the HEP and OEP, and then H^+ ions are reduced on the CB of the HEP, while O_2 is produced on the VB of the OEP (Figure 1.7).

To complete the whole POWS cycle, the electrons in the CB of the OEP must pass through a redox shuttle to combine with holes in the VB of the HEP.[55] Redox couples, such as Fe^{3+}/Fe^{2+},[56–58] IO_3^-/I^-,[59–61] etc. have been widely used as the redox shuttles in order to mediate the electron transfer between the HEP and OEP. However, the presence of redox shuttles could also bring undesired side reactions, and sometimes the by-products could result in shading of the photocatalysts from incident light. Thus, some groups have reported the successful fabrication of redox shuttle-free Z-scheme systems in which case the inter-particle electron transfer is achieved by forming attractive electrostatic force between the OEP and HEP

particles,[62,63] allowing the electrons to migrate between particles when they are in contact with each other. Based on such ideas, more and more redox-shuttle-free Z-scheme systems are emerging, and new constructions have been developed to realise efficient electron transfer from the OEP to the HEP.[64–66]

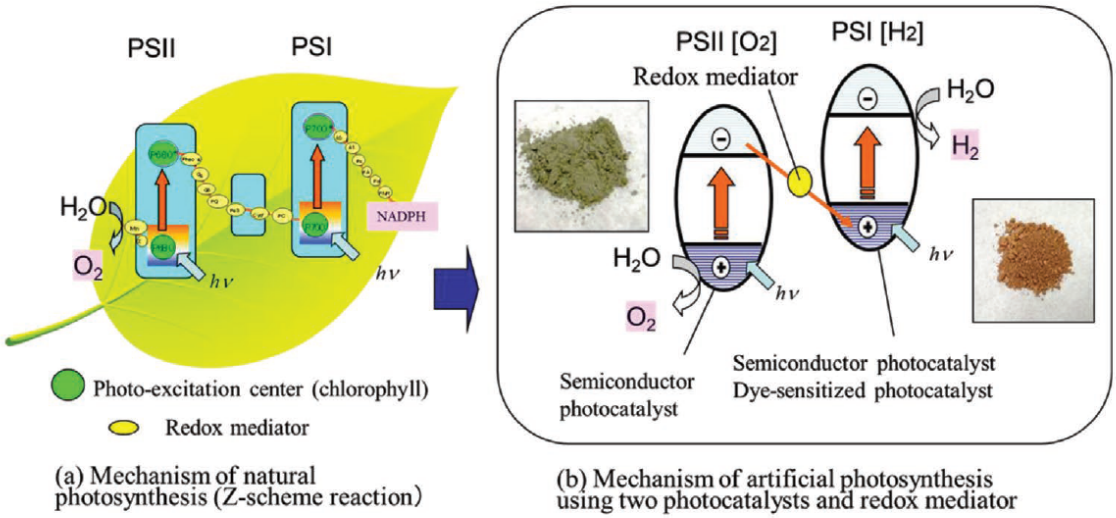

Figure 1.7 Z-scheme POWS system mimicking the natural photosynthesis mechanism for artificial photosynthesis. **(a)** Natural photosynthesis system in plants; **(b)** Z-scheme POWS system involving HEP and OEP. (PS: photosystem) Reproduced from ref. [67]. Copyright 2018 Wiley-VCH.

1.2.3 Factors affecting the POWS performance

As previously mentioned, the overall POWS performance depends on the efficiency of each fundamental step, and each step, if not efficient, could hamper the overall photocatalytic activity. Therefore, the overall solar energy conversion efficiency, η_{total}, should take into account the efficiencies associated with these three fundamental processes and thus is determined as follows:[37]

$$\eta_{total} = \eta_{absorption} \times \eta_{separation} \times \eta_{reaction} \qquad \textbf{Equation 1.3}$$

The photon absorption efficiency, $\eta_{absorption}$, is defined as the fraction of electron−hole pairs generated by the photon irradiation. The separation efficiency, $\eta_{separation}$, is the fraction of photo-generated charge carriers that separate and

migrate to the surface of photocatalyst particles. The reaction efficiency, $\eta_{reaction}$, is the efficiency of the surface chemical reactions. All these three efficiencies should be high enough to obtain an ideal η_{total} for POWS reaction, so, different methodologies have been developed to improve the efficiency of each step, which are discussed in detail in the following section.

1.3 Strategies for enhancing the POWS performance

1.3.1 Enhancing light absorption

As discussed in the previous section, the POWS performance is determined by the efficiency of each fundamental step, therefore, much effort has been made to gain a deeper understanding, leading to different strategies to promoting each step. First of all, an efficient photocatalyst for POWS reaction must have a broad absorption range to take up the photons from solar irradiation, which means the band gap of the semiconductor material is relatively narrow. Thus, band structure engineering has been developed as a useful technique to narrow the wide band gap of materials to the visible light regime to maximise the solar energy capturing[7,68–72]. One of the most widely used methods is doping with anions or cations, which inserts new band levels between the original band gap of the semiconductors or facilitates a band shift to narrow the band gap, thus enhancing the light absorption properties[71,72]. One of the milestone studies is the anion-doped TiO_2, which was first reported by Asahi *et al.* First-principle calculations were carried out on C, N, F, S and P doped TiO_2 (Figure 1.8a), showing that N-doped TiO_2 should possess the best visible light absorption compared with other anion-doping[7]. Subsequently, numerous works were carried out on N-doped TiO_2. UV-Vis spectroscopy shows that the absorption of N-doped TiO_2 is extended to *ca.* 500nm compared with the absorption edge of 380 nm for pristine TiO_2. N species

are observed by X-ray photoelectron spectroscopy (XPS), showing peaks at 396eV and 400eV attributed to substitutional and interstitial N species, respectively[7,73,74]. It is also noted that such cation or anion doping is always accompanied by the formation of surface/bulk defects, such as oxygen vacancies (V_Os) in the case of N-doped TiO_2, which are also believed to provide intermediate band levels or extra energy states that can trap electrons, and contribute to enhanced visible light absorption[75–82].

In actual fact, surface defects are ubiquitous in most semiconductor materials, and tailoring the defects is recognised as an effective strategy to manipulate the physical and chemical properties, including electronic structure, surface adsorption properties, charge density, charge separation, etc.[83–86]. The surface defect engineering techniques have also been widely studied, especially the V_Os in metal oxides such as TiO_2. V_Os exist naturally in most metal oxides at very low density levels, but higher V_O density can be easily achieved by some simple chemical treatments, such as ion doping[73,78], H_2 reduction[68], $NaBH_4$ chemical reduction[87,88], plasma treatment[89], and exfoliation to form two-dimensional (2D) materials[90], etc. Much attention has been given to deeply reduced TiO_2, also known as ‘black titania’, since the pioneering work of Mao *et al.* in 2011, in which pure TiO_2 was treated in a high-pressure H_2 atmosphere at 200 ^oC and 20 bar for five days[68]. The obtained material was black in colour and exhibited greatly enhanced light absorption up to 900 nm, and the photocatalytic H_2 evolution performance was improved as well (Figure 1.8b). Raman spectroscopy was used to examine the black titania, and indicated that the deep hydrogenation introduces defects that can activate the zone-edge and otherwise Raman-forbidden modes by breaking the Raman selection rule[68]. VB XPS suggests that the VB of TiO_2

shifts largely by about 2.18eV, resulting in the greatly enhanced visible light absorption and photocatalytic performance.[68] Subsequently, TiO_2 in different colours have been developed. Liu *et al.* synthesised a series of coloured TiO_2 materials by changing the hydrogenation temperatures, which in turn, modified the visible light absorption range.[91] Defects in such materials are normally characterised by electron paramagnetic resonance (EPR) spectroscopy. The signals of Ti^{3+} arising from its 3d electrons normally appear in the range of g=1.95-1.98. Meanwhile, O_2 molecules can be trapped at the V_O site to form O_2^- species, resulting in signals of g=2.00-2.02[92,93]. Both Ti^{3+} and V_O species are considered to contribute to the enhanced visible light absorption and photocatalytic performance. Other than V_O in TiO_2 based materials, V_O in other semiconductor materials like CeO_2, perovskite, Fe_2O_3, WO_3 and $BiVO_4$, also promote visible light absorption.[84,88,94–96] Much progress has indeed been achieved in enhancing the visible light absorption by defect engineering techniques, which has greatly increased the use of solar energy. Other techniques, such as sensitisation with organic dyes, where the dye acts as a photosensitiser and injects electrons into the CB, have also been reported to enhance the visible light absorption of the semiconductor photocatalysts[70]. However, it is also found that the surface defects are not always stable enough throughout the whole catalytic process and can be readily replenished by contact with oxygen or water. Although bulk defects still take up the visible light, surface defects are no longer present, and the lack of surface catalytic activation sites can be harmful to the photocatalytic performance. I also obtained similar observation in my DPhil project and this will be further discussed in the following chapters. This observation may also explain the fact that enhanced visible light absorption does not necessarily lead to better POWS performance.

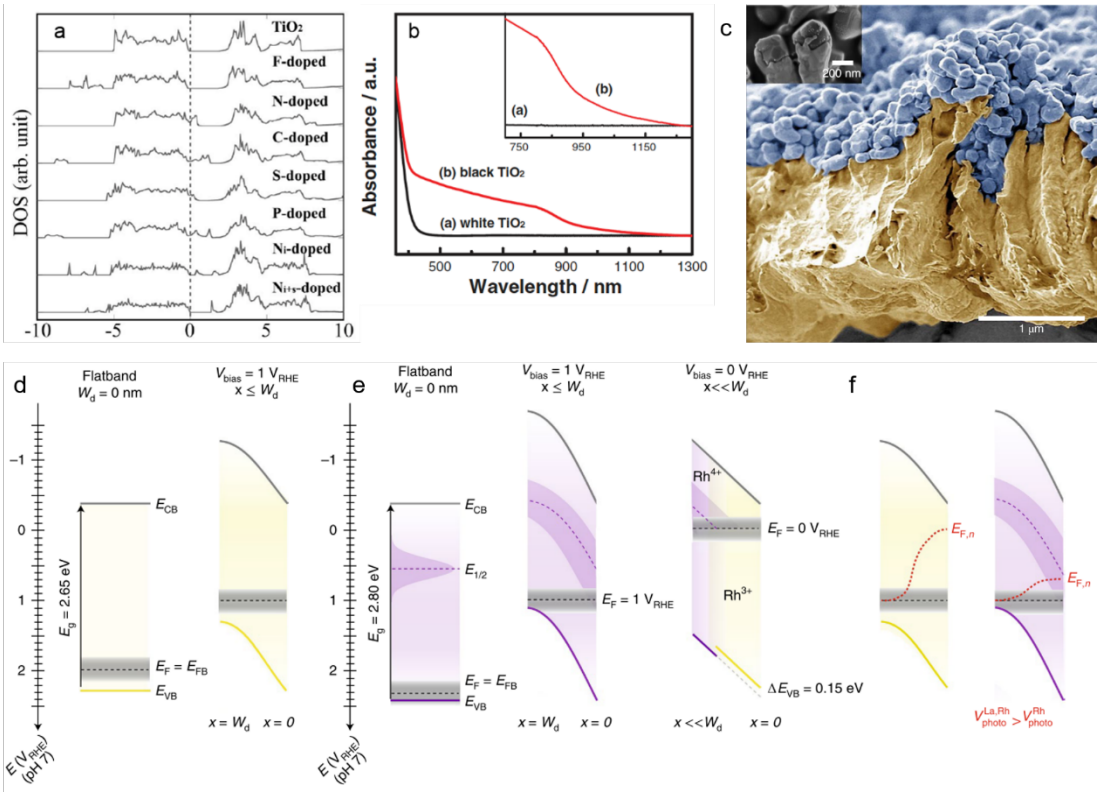

Figure 1.8 (a) Total DOSs of the doped TiO_2; Reproduced from ref. [7]. Copyright 2001 AAAS. **(b)** Spectral absorbance of the white and black TiO_2 nanocrystals. The inset enlarges the absorption spectrum in the range from approximately 750-1200 nm. Reproduced from ref. [68]. Copyright 2011 AAAS. **(c)** A cross-sectional SEM image of the photocatalyst sheets, showing a monolayer of partially sintered (La),Rh:$SrTiO_3$ particles (blue) embedded (inset) in a 2 μm thick gold back contact (yellow). **(d, e)** Model of surface depletion in La,Rh:$SrTiO_3$ **(d)** and Rh:$SrTiO_3$ **(e)** at different applied potentials in the dark. **(f)** Photovoltage build up in La,Rh:$SrTiO_3$ (left) and Rh:$SrTiO_3$ (right) under illumination at positive device operation potentials. Reproduced from ref. [97] with permission.

On the other hand, cation doping has also been widely reported as a promising strategy for tailoring the band gap and other photochemical properties.[98,99] Very recently, Domen *et al.* has developed a band gap-engineered oxide, La and Rh co-doped $SrTiO_3$ (La,Rh:$SrTiO_3$), which exhibited an enhanced QE of 33% in the visible regime and an overall STH efficiency of more than 1% using a 'photocatalyst sheet' device (Figure 1.8c).[64,100–102] With the help of the time-resolved spectroscopic techniques and DFT calculations, it has been shown that the Rh-doping induces a strong downward shift in the flat band potential and narrows the effective optical gap of $SrTiO_3$, thus creating a p-type visible light

absorber. Meanwhile, co-doping with La is demonstrated to be an elegant approach for facilitating the separation of the charge carriers, since the positive flat band potential and the absence of a mid-gap energy state enable strong downward band bending for La,Rh:$SrTiO_3$ (Figures 1.8d-1.8f). Such features subsequently result in efficient bipolar charge accumulation and remarkable photocatalytic performance.[97]

1.3.2 Facilitating separation of charge carriers

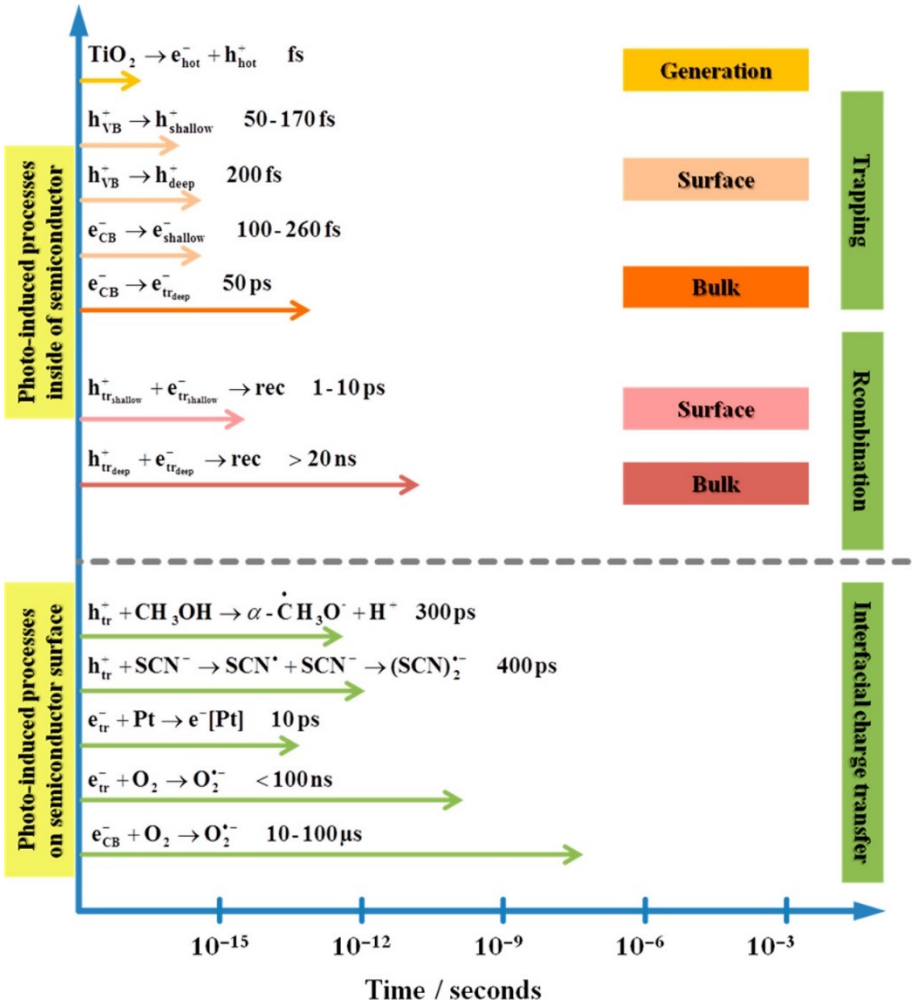

Figure 1.9 Photoinduced reactions in TiO_2 photocatalysis and the corresponding time scales. Reproduced from ref. [103] with permission.

Apart from capturing photons from solar light with corresponding band gap, the separation of the photo-generated charge carriers is also of extremely great

importance. As mentioned in the previous section, extensive efforts have been invested to extend the visible light absorption, however, poor POWS performance under visible light irradiation and ambient conditions still hinder their further applications. This is mainly due to the rapid recombination of charge carriers to dissipate the captured solar energy to heat or photoluminescence. In terms of the time scales of each process, the photo-excited electron-hole pairs are generated in femtoseconds after the light irradiation, while the separation and migration of the charge carriers normally take hundreds of femtoseconds or even picoseconds to take place (Figure 1.9). Instead of migrating to the surface and reacting with chemical species, the electrons and holes will recombine to give out the energy in the form of heat, and this process generally take place in several picoseconds. However, the interfacial charge transfer to the chemical species is relatively slow compared with the above steps, which takes place from hundreds of picoseconds to even microseconds, leading to the fact that most photo-excited electrons and holes favour recombination with each other instead of migration to the surface.[38,104] Therefore, although the visible light absorption is largely enhanced for many semiconductor photocatalysts, only a small amount of the photo-generated electrons and holes can travel through the photocatalyst particles and reach the surface, leading to the poor QEs. The photo-generated charge carriers must possess a sufficient lifetime to capture the H^+ and OH^- species derived from water dissociation to allow efficient photocatalysis to take place.[23] Recent reports show that polarisation plays an important role in the separation of these photo-generated electrons and holes, which prolongs the charge carrier lifetime, effectively leading to enhanced photocatalytic performance.[105–107] Various methodologies have been developed to promote the separation of the photo-

generated electrons and holes on the catalyst surface and suppress the recombination process, including shape and facet engineering, heterojunction formation, and introduction of internal electric fields, etc.[105–110]

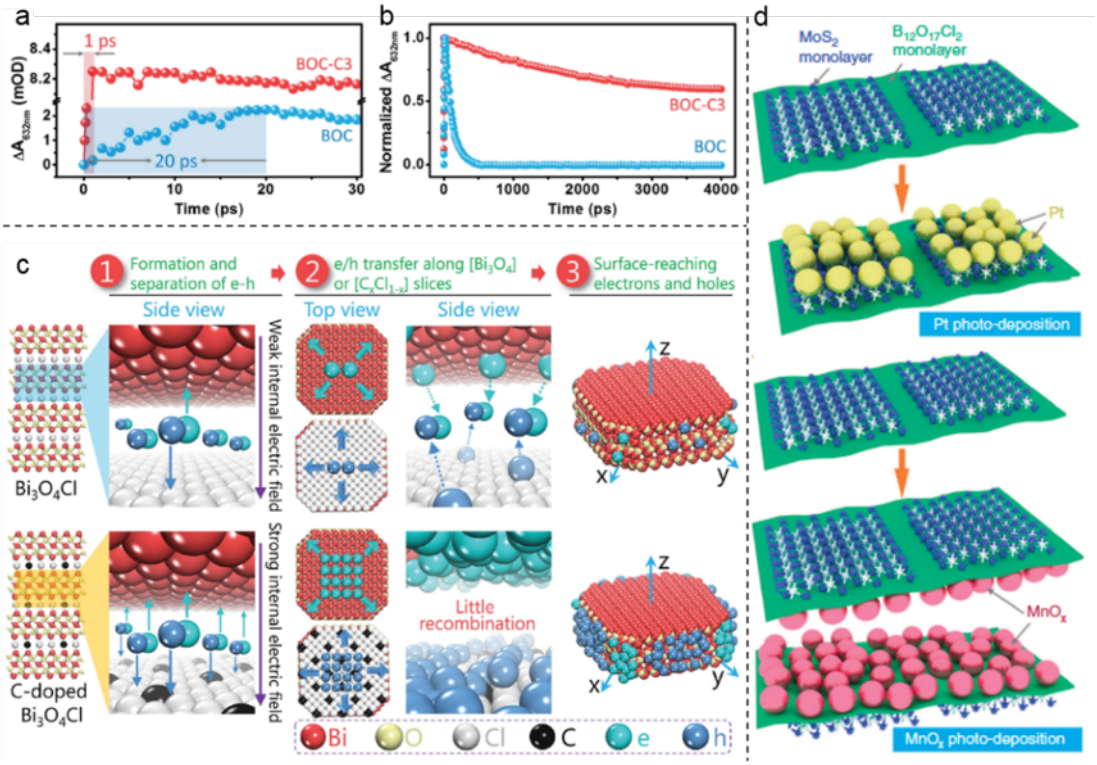

Figure 1.10 (a) Kinetic traces (probed at 632 nm) as a function of probe delay time and **(b)** their corresponding normalised traces. All these data were recorded with a 400 nm laser pulse (120 fs); Reproduced with permission from ref. [106]. **(c)** Schematic illustration of the separation and migration of electrons and holes in the bulk of the pure and C-doped Bi3O4Cl; Reproduced with permission from ref. [106]. **(d)** Schematic illustration of Pt and MnOx photo-depositions on BOC-MS. Reproduced with permission from ref. [107].

The design of an internal electric field (IEF) to enhance the polarisation within the photocatalyst particles has recently been demonstrated to be an effective approach for improving the charge separation both in bulk and on the surface of the photocatalysts[105–107]. It is noteworthy that Zhang's group reported a new strategy to introduce an IEF to Bi_3O_4Cl by carbon atom incorporation[106]. The resulting C-doped Bi_3O_4Cl achieved a bulk-charge separation efficiency of 80%, therefore the charge carrier lifetime was prolonged from less than 500 ps to around

4000 ps (Figures 1.10a and b), which is attributed to the strong IEF due to the potential difference between the doped and undoped layers (Figure 1.10c). The catalyst enabled the photocatalytic water oxidation half reaction under visible light irradiation in the absence of sacrificial reagents; however, H_2 was scarcely detected because the CB is more positive than the H_2-evolving potential. It was claimed that the photo-generated electrons either reduced O_2 to give H_2O_2 or came into the solution to form solvated electrons, but no direct evidence was given[106]. Subsequently, the same research group also reported a Janus Cl_2-$Bi_{12}O_{17}$-MoS_2 bilayer junction photocatalyst with an even stronger IEF for H_2 evolution (Figures 1.10d and e), in which the carrier lifetime was claimed to be 3446 ns and a H_2 evolution rate of 33mmol $g^{-1}h^{-1}$ was obtained in the presence of ascorbic acid as the hole scavenger[59].

A facile and versatile method to tune the local electric field (LEF) with the help of polar-faceted materials has recently been developed in our group, in which a strong LEF is obtained by engaging polar-faceted metal oxides as a support. Firstly, we need to understand how polarisation occurs in a solid-state material. Taking a simple ionic model of MgO as an example, Figure 1.11 shows the energy levels of filled O 2p and unfilled Mg 3s orbitals. For these isolated hard ionic species, the ionic charge distribution Mg^{2+}-O^{2-} is clearly not stable in the gas phase (the O^{2-} ion does not even exist because the second electron affinity of O is highly endothermic). However, these ions can be stabilised in a solid ionic lattice, so they experience a summation of long-range Coulomb potentials from the ions in the lattice positions (the so-called Madelung potential) of appropriate sign. At oxide sites the Madelung potential is positive and thus stabilises electrons; at cation sites it is negative and correspondingly destabilising, as shown in Figure 1.11. Thus, the

most stable crystal structure is composed of ions interspersed with nearby counter ions and so on in the lattice. If some charges are dislocated from the lattice, polarisation occurs.

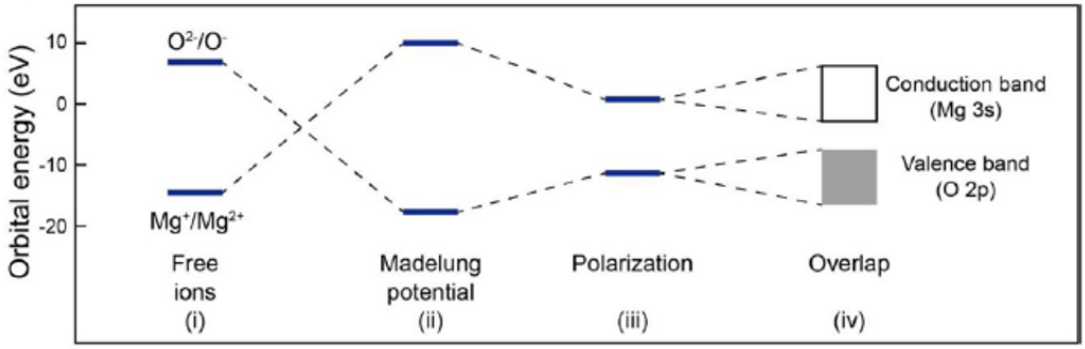

Figure 1.11 Orbital energies of filled oxygen 2p and empty magnesium 3s levels in different states. Reproduced from ref. [83]. Copyright 2020 American Chemical Society.

The polarisation has been shown to lower the energy of empty (metal) levels and raise that of filled (oxygen) levels; hence, the binding energies of electrons in filled levels is reduced. Finally, the broadening of electronic levels due to overlap between ions gives bands rather than discrete energy levels. In the crystal facets, similar ion distributions exist in the energy-minimised packing (Figure 1.12). The most stable surfaces of MgO in this case are (100) or ($\bar{1}$10), where cations and anions are evenly interspersed, obtaining the Madelung stabilisation. Although exposure of high-energetic facets such as O- or Mg-terminated (111) is thermodynamically unfavourable, it can be kinetically controlled during crystal growth. It is noteworthy that these thermodynamically unstable high-energetic facets tend to reduce the surface energy through relaxation processes, which can exert unusual effects such as band gap reduction, charge carrier stabilisation, enhanced adsorption of counter ions, and induced surface reconstruction. Polarity effects have long been studied in catalysis since the late 20th century, and the studies covered semiconductor surfaces, oxide surfaces, ultra-thin oxide films and

oxide interfaces.[111–113]

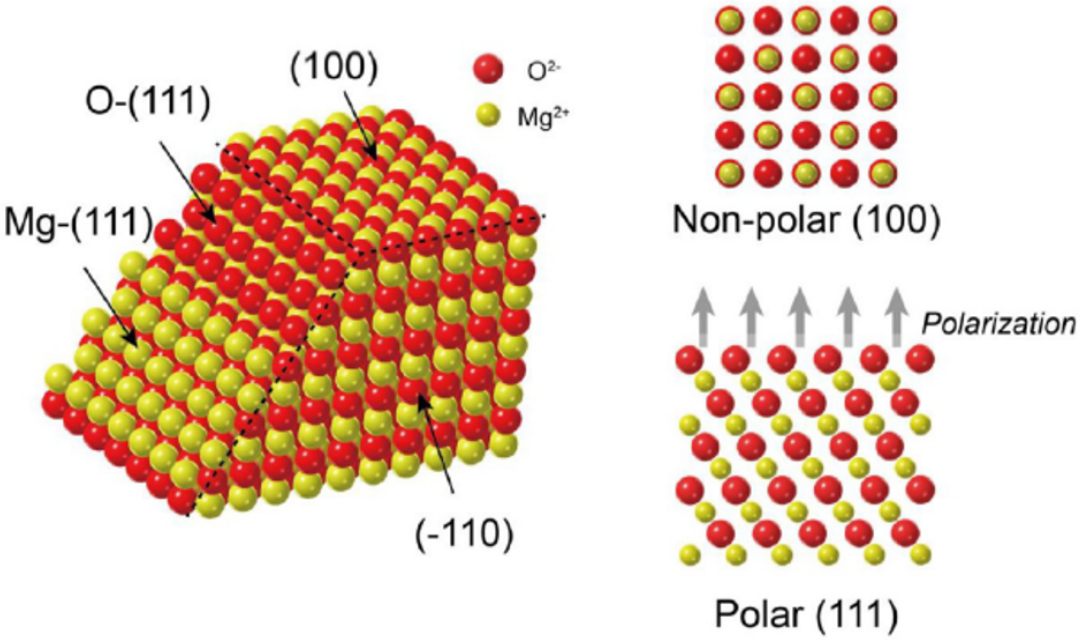

Figure 1.12 Structural model of different exposed facets of MgO crystals: Crystal packing of polar and nonpolar faceted MgO. Arrows indicate the polarisation near the polar surface. Reproduced from ref. [83]. Copyright 2020 American Chemical Society.

For polar surfaces, the orientation is such that each repeat unit grows in the direction perpendicular to the surface, resulting in a non-zero dipole moment on the surfaces (as indicated in Figure 1.12). Thus, electric fields and electrostatic forces are generated on polar surfaces.[111] Due to the presence of a macroscopic dipole, their surface properties and local environment strongly differ from those in the bulk or their non-polar counterparts. High surface energy means that the polar surfaces have a large tendency to cancel out the polarity, by charge transfer or introduction of compensating charges in the outer plane.[112] However, the rigidity of some oxides hampers such processes and leaves considerable polarity and electrostatic forces on the polar surfaces, which could be good candidates for our local polarisation effect study. Solid state NMR and TEM were used to confirm that the surface polarity of crystalline MgO(111) facets induced significant chemical

shifts.[73] In my DPhil project, I discovered that the polar-faceted MgO(111) could greatly prolong the lifetime of the photo-generated charge carriers in the N-doped TiO_2 materials, while non-polar MgO(100) and MgO(110) showed no apparent influence. Accordingly, the MgO(111) promoted Au/N-doped TiO_2 photocatalyst gave a much enhanced and stable H_2 evolution rate of 11092 μmol $g^{-1}h^{-1}$ at 270°C. The QEs of 81.8% at 437 nm and 3.2% at 1000 nm were also achieved with the inclusion of MgO(111). We believe that the use of polar-faceted MgO(111) can introduce an LEF, which prolongs the charge carrier lifetime and therefore enhances the photocatalytic water splitting activities. The effect of different sizes and morphologies of the MgO supports were also studied, which will be discussed in detail in the following chapters.

More systematic studies were carried out on a two-dimensional (2D) material, single layer MoS_2 (SL-MoS_2), whilst other polar-faceted oxides such as CeO_2(100) nanocubes (NCs) and ZnO(0001) nanoplates (NPs) were also used to study the LEF effect. The SL-MoS_2 was combined with different polar-faceted metal oxide supports as mentioned before. As expected, the photocatalytic activities are greatly improved by the polar-faceted oxides. TRPL spectroscopy confirmed the changes of the charge carrier lifetime of the photocatalysts, which showed nearly the same trend as the POWS activities. Therefore, the remarkable enhancement of photocatalytic activities is attributed to the prolonged the charge carrier lifetime. A strong LEF is exerted on the catalyst by the surface of the polar-faceted oxide supports, and such polarisation facilitates the separation of photo-excited electron-hole pairs on the catalyst surface at the interface and therefore suppresses the recombination process. Also noteworthy is that the POWS activity and the charge carrier lifetime both show a linear relationship with the total polarity of the polar

material support, which further confirms that the local polarisation effect contributes to the separation of the photo-excited electron-hole pairs, leading to the prolonged charge carrier lifetime and the enhanced photocatalytic activities and QEs. This simple and versatile approach may contribute to the rational design of photocatalysts with suppressed recombination, for not only the water splitting system, but also other valuable photocatalytic processes. This part of study will be demonstrated more deeply in Chapter 4.

1.3.3 Promoting surface reactions

To achieve more efficient surface HER and OER, various cocatalysts are commonly engaged for different purposes, including lowering the activation energy, lowering the overpotentials of H_2 and O_2 evolution, facilitating the surface chemical reactions, and suppressing the backward water-formation reaction, etc., thus, they are of great interest in the field of POWS reaction, and have been extensively explored[114–120]. Generally, metals such as Pt, Pd, Au, Ru, Ni and Rh are considered as good H_2 evolution cocatalysts, while the metal oxides of Ir, Mn, Co and Ru function as the O_2 evolution cocatalysts[121]. Cocatalysts are capable of extracting the photo-generated electrons or holes from the semiconductor, depending on the nature of the cocatalyst used, therefore, they could act as surface trapping sites, where the electrons/holes accumulate and surface reactions take place.[23]

H_2 evolution cocatalysts such as Pt are widely used and much progress has been made in developing novel cocatalysts. Recently, our laboratory has found that Au nanoparticles introduced by the photoreduction method show a strong promoting effect in an N-doped TiO_2 photocatalytic water splitting system, leading to a 90% increase in the H_2 evolution rate.[73] It should be noted that some metal

nanoparticles such as Au and Ag can introduce the localised surface plasmon resonance (LSPR) effect which may offer a potentially useful approach to enhancing the visible light absorption of wide band gap semiconductors. LSPR is an optical phenomenon in which the electron cloud on a metal NP oscillates in resonance with the electric field induced by the incident light (which is actually an electromagnetic field). This effect can trigger intense electric fields at the NP surfaces, giving rise to sharp spectral absorption and scattering peaks (as illustrated in Figure 1.13). The frequency of this resonance can be tuned by controlling the NP size and shape, as well as constructing a core-shell structure, resulting in a potentially wide absorption range within the visible light regime.[122–124]

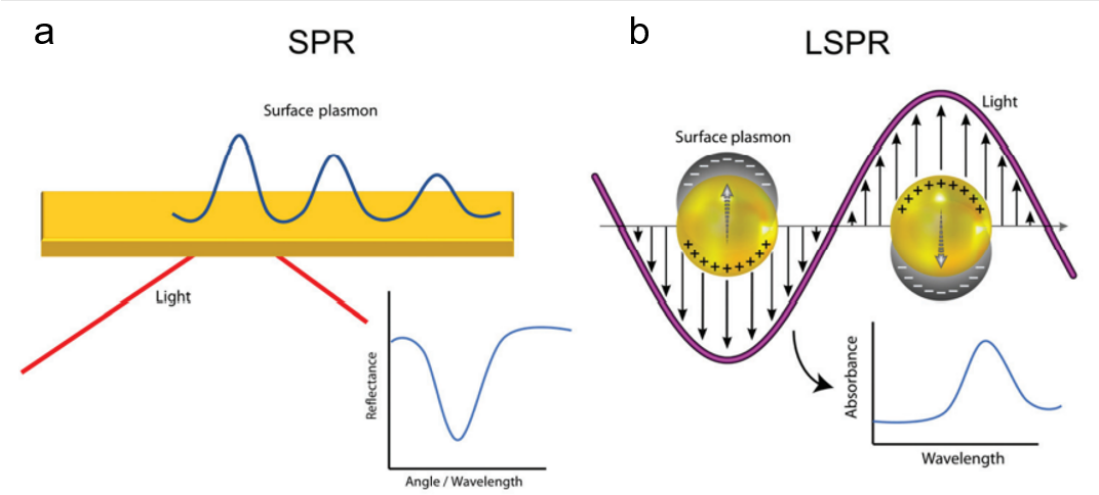

Figure 1.13 (a) Prism coupling configuration of SPR, where a light beam impinges on a thin metallic film deposited on a prism. P-polarised light absorbed by the surface plasmon is seen from a minimum in the reflection spectra. **(b)** Representation of the localised surface plasmon on nanoparticles and absorbance spectra obtained for binding events on nanoparticles. Reproduced with permission from ref. [125].

However, it is noteworthy that H_2 evolution cocatalysts also accelerate the thermodynamically favourable reverse reaction: the water formation reaction, which is not desirable in a highly efficient POWS system. Therefore, efforts have

been made to suppress the backward reaction, whilst also promoting the forward reaction[23]. A bimetallic cocatalyst system was reported by the Domen group, where a Rh@Cr_2O_3 core-shell structure was synthesised by selective photo-reduction: the protective Cr_2O_3 shell in the catalyst prevented the evolved O_2 from reaching the Rh core, therefore limiting the possibility of the evolved O_2 to be reduced again (Figure 1.14).[114,126] Microscopic evidence showed that the core-shell structure was successfully achieved by the photo-deposition method; Spectroscopic studies also confirmed the compositions and chemical states of the Rh core and the Cr_2O_3 shell. Building upon such observation, it was shown that a solid-solution photocatalyst, GaN:ZnO, exhibited greatly enhanced POWS activity after loading with a Rh@Cr_2O_3 core-shell structure due to the backward reaction being suppressed.[127] Using other noble metals, such as Pt and Ir, as the metal core can also lead to similar performance.[114] A similar modification method was also developed to promote the POWS reaction effectively: amorphous oxyhydroxides of group IV and V transition metals (Ti, Nb, Ta) were introduced to a semiconductor photocatalyst, in which the amorphous oxyhydroxides covered the whole photocatalyst particles, creating a core-shell structure[126]. The POWS performance was successfully enhanced after this surface modification, resulting from the prevention of the reverse reaction. The amorphous oxyhydroxide layers were believed to function as molecular sieves which selectively filter the reactant and product molecules. The core-shell structures were confirmed by microscopic studies, and the permeation behaviour on the core-shell structures was also studied in detail[126]. It was demonstrated that this structure was effective for POWS reaction even when the active sites were covered by the coating, because of a permeation-controlled behaviour: small H^+ ions were allowed to permeate into the

shell, and the evolved H_2 molecules were allowed to diffuse out. However, as shown in Figure 1.14b, O_2 molecules struggle to permeate into the shell due to their relatively large molecule sizes. In addition, H_2 molecules could hardly come back in the shell due to the concentration gradient, thus, H_2 molecules would favourably diffuse out. As a result, this permeation-controlled core-shell structure enabled the prevention of the reverse reaction without suppressing the forward reaction, leading to a more efficient POWS reaction.

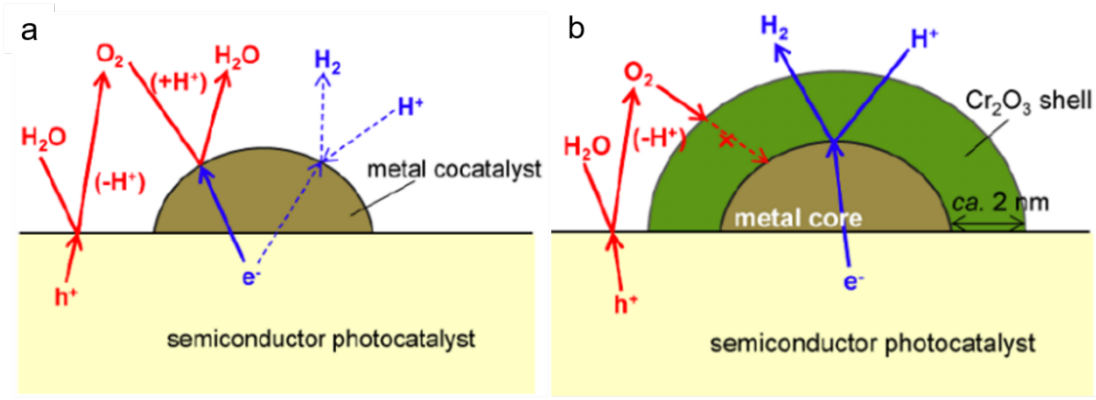

Figure 1.14 Schematic of the differences of the chemical processes before **(a)** and after **(b)** the construction of the core-shell structured cocatalysts. Reproduced with permission from ref. [114].

1.3.4 Photocatalysis at elevated temperatures

It should be noted that POWS has been extensively studied mainly at room temperature for several decades, however, it is well known that elevated temperatures can lead to enhanced performance of endothermic reactions both thermodynamically and kinetically, and possibly could lead to new understandings of this system. Thermolysis of water requires extremely high temperature of more than 1000 ^{o}C which is not practical[128], but photocatalysis promoted by elevated temperatures is presumably able to provide a novel alternative for the solar energy utilisation especially as the thermal energy could also be provided by solar means. Moreover, infrared (IR) light contributes almost 50% of the whole solar spectrum

and can provide the required heat by thermal radiation instead of using additional electric heating devices[37]. A pioneering work has demonstrated a sacrificial photocatalytic H_2 evolution system at elevated temperatures, of which the QE reached 65.7% on a Pt/black TiO_2 catalyst in the visible light range at 280 °C in the presence of methanol as a sacrificial reagent (Figure 1.15).[32] It is claimed that elevated temperatures add to the thermal energy of the reactants and subsequently increase the kinetic driving force, leading to the enhanced H_2 evolution rate and QE. However, the thermal decomposition of methanol also contributed to the overall H_2 production (Figure 1.15a), and inevitably resulted in unwanted production of organic chemicals or carbon emission, hindering its further practical application.

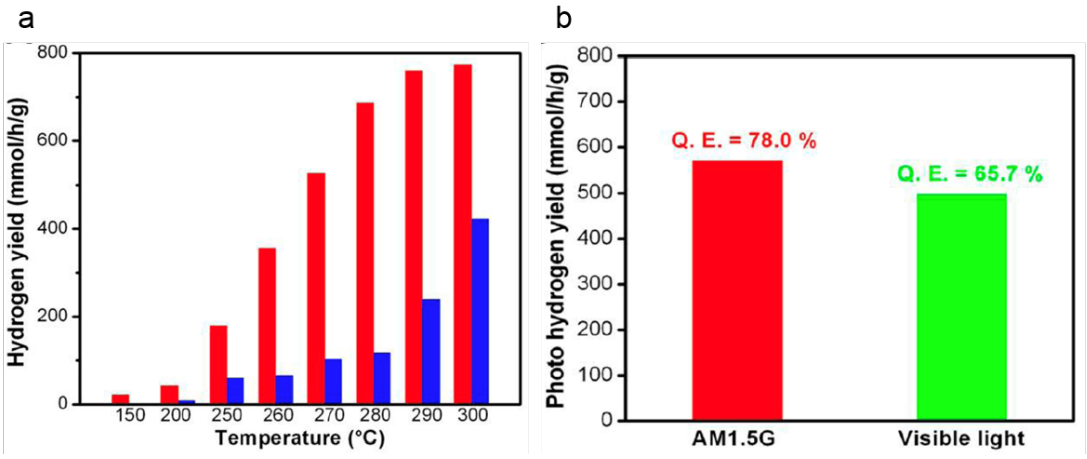

Figure 1.15 (a) Temperature-enhanced photocatalytic H_2 production from H_2O with a sacrificial agent (30% methanol) without light illumination (blue bar) and with AM 1.5 global sunlight illumination (red bar) and **(b)** apparent quantum efficiencies of visible light and AM 1.5 global sunlight over the Pt/black TiO_2 catalyst at 280 °C. Reproduced with permission from ref. [32].

Obviously, a POWS system without the use of any sacrificial reagents will be more favourable and the idea of using elevated temperatures in photocatalytic systems is worth further exploration. A recent attempt on this was reported by Tian *et al.*, where black phosphorous nanosheets were used for a photocatalytic HER system

at elevated temperature as well.[129] It was shown that amorphous cobalt phosphide supported black phosphorous exhibited around nine times enhancement of H_2 evolution activity at 353 K compared with that at room temperature, showing a QE of 42.55 % at 430 nm without addition of any sacrificial reagent in this photocatalytic system. Although this catalyst showed good stability at room temperature, it did not give a stoichiometric amount of O_2 at 353 K, indicating there was photo-corrosion of the catalyst at this elevated temperature. Therefore, special attention should be given to the photocatalyst stability for the photocatalytic systems operated at elevated temperatures. Also noteworthy is that the water dissociation equilibrium to H^+ and OH^- is greatly dependent on temperature: it can be promoted to about 25 times that at room temperature (about 1×10^{-14}) and peaks at around 270 ^oC before rapidly declining[130]. Obviously, enhanced concentrations of H^+ and OH^- are also beneficial to the photocatalytic water splitting performance kinetically. As mentioned before, in-depth investigation of the POWS systems at elevated temperatures above 200 ^oC is still absent in literature right now. Hence, through my DPhil study, I focused on the exploration of POWS systems at elevated temperatures using semiconductor materials as the photocatalysts, and the reactions were conducted in a closed batch reactor (Figure 1.16). At the beginning of my DPhil project, with the help of electron paramagnetic resonance (EPR) spectroscopy, I found that the surface modifications of the semiconductor photocatalysts could be eliminated easily when in contact with water and air, and the surface defects, such as V_Os could be regenerated at elevated temperatures, whether in N_2, liquid water or water vapour. Experimental (*e.g.*, in-situ structural characterisations) and computational studies suggested that the oxygen mobility could be greatly enhanced at elevated temperatures for TiO_2-based materials,

which led to substantially enhanced POWS performance. Such enhanced oxygen mobility in oxide materials at elevated temperatures has also been widely studied and used in the solid oxide fuel cells.[131] Time-resolved photoluminescence (TRPL) spectroscopy was then used to probe the recombination rate of photo-excited electron-hole pairs. Although no obvious change was observed when the TRPL experiments were conducted in air without water at different elevated temperatures, it was interesting to find that the charge carrier lifetime varies with the pH change.[73] As previously mentioned, the water dissociation constant increases with the temperature and peaks at 270 ^{o}C, thus, the obvious response of the charge carrier lifetime to the pH change indicated that the increased concentration of H^+ and OH^- ions in water at elevated temperatures could also influence the separation of the photo-generated charge carriers. More details will be discussed in the following chapters of this thesis. Clearly, all these above-mentioned results indicate that performing high-temperature photocatalysis exhibit major advantages of facilitating the POWS reaction.

1.4 Aims and objectives

As demonstrated before, the POWS at elevated temperatures is a promising approach to converting solar energy to chemical fuel in the form of H_2, but it still lacks in-depth investigation. Therefore, in this thesis, I aim to explore the POWS at elevated temperatures as a novel technique to produce solar fuel. The POWS reaction was carried out at different temperatures to study the temperature effect on this system first. Starting from the most widely studied photocatalyst, TiO_2, I managed to enhance its visible light absorption by N-doping, and synthesised a range of other semiconductor materials as the photocatalysts.

As previously discussed, to make the solar-light-driven POWS system competitive

for H_2 production, the quantum efficiency needs to undergo a substantial increase, and facilitating the separation of the photo-generated charge carriers by increasing the local polarisation has become the key. Consequently, different strategies have been explored through my DPhil study, which are demonstrated in this thesis. Systematic investigations have been conducted to investigate the effect of the local electric field introduced by polar-faceted support materials, such as polar-faceted oxides and layered double hydroxides (LDHs), which are strongly polarised on the surface. Moreover, magnetic field effects are also explored by placing semiconductor photocatalysts near the superparamagnetic nanoparticles. Extensive catalytic studies have been carried out. Deeper understanding of the novel POWS system cannot be obtained without thorough characterisations of the materials. Thus, a wide range of spectroscopic and microscopic characterisation techniques were involved to investigate the relationships between structure and performance. In combination with the computational studies, possible mechanisms of the novel POWS system at elevated temperatures have been derived.

Particulate photocatalytic water splitting systems have the advantage of simplicity and low cost over other solar energy conversion techniques, such as photovoltaic-electrolysis systems and photoelectrochemical devices, however, the highest solar-to-hydrogen conversion efficiency reported so far is only around 1%.[102] There is no doubt that future work should be focusing on improving this efficiency to approximately 10% to meet the practical application requirement.[37,121] Therefore, new strategies to harness the visible or even infrared light are still desirable. Novel approaches to suppress the charge carrier recombination and the backward reactions are also required. The following inter-related processes such as

separation, purification, transportation, and utilisation of the H_2 fuel remain challenging as well. All these aspects are tremendously essential to realise the efficient and sustainable production of H_2 via solar-light-driven water splitting.

1.5 Thesis overview

This thesis contains seven chapters, with Chapters 3 to 6 describing and discussing the experimental and computational work performed throughout my DPhil project.

Chapter 1 (the current chapter) introduces the background of solar energy conversion and the photocatalytic overall water splitting system, and provides the fundamental principles of photocatalysis and definitions of the relevant terms. Some conventional and effective strategies to improving the POWS performance are then summarised and discussed, including defect engineering, deposition of cocatalysts, etc. The main challenge in this research field, the suppression of charge recombination, is then clarified. Building upon such background, a novel POWS system at elevated temperatures is then proposed and discussed, which serves as the focus of my DPhil project and this thesis. The overall aim of the thesis is outlined as a conclusion of this chapter.

Chapter 2 starts with the experimental protocols of the synthesis methods and outlines various methods of catalytic performance testing. It is then followed by the detailed description of the background and theory of the main characterisation techniques used in this thesis.

Chapter 3 demonstrates the feasibility of the POWS reaction using elevated temperatures on TiO_2-based materials. The background with particular emphasis on the temperature effects on POWS reaction and the modifications of TiO_2 is

covered. The band gap structure of the commercial P25 TiO_2 is engineered by N-doping to improve the visible light absorption. Extensive characterisations are included to investigate the structure and the physical chemical properties, especially the surface properties. Comprehensive photocatalytic tests are performed, including the temperature effect, surface metal nanoparticle deposition, stability tests, etc. Time-resolved photoluminescence spectroscopy is used to investigate the charge separation process. A potential mechanism is derived based on the above observations.

Chapter 4 focuses on the fabrication of local electric fields (LEFs) to promote the POWS performance. Different polar-faceted metal oxides including CeO_2, MgO, ZnO, and LDHs are synthesised and assembled with semiconductor materials. Non-polar CeO_2, MgO, and ZnO are also included for comparison. Apart from the N-doped TiO_2 demonstrated in Chapter 3, a 2-dimensional (2D) transition metal dichalcogenide (TMD) material, monolayer MoS_2, is also covered in this chapter. Extensive efforts are made to investigate the properties of the polar facets and the monolayers with the help of microscopic techniques. Systematic photocatalytic tests are performed and relationships between the POWS performance, the charge carrier lifetime, and the strength of LEFs are also demonstrated in this chapter.

Chapter 5 investigates the magnetic field effects (MFEs) on the POWS performance. To enhance the local magnetic flux near the photocatalyst particles, I managed to combine the N-doped TiO_2 with superparamagnetic Fe_3O_4 nanoparticles (NPs) via a sol-gel method. An external magnetic field is provided by two permanent magnets placed in parallel. Photocatalytic tests are carried out to scrutinise the effect of the external magnetic field strength and the concentration

of Fe_3O_4 NPs in the photocatalysts. Careful analysis of the catalytic results and computational studies is covered, which suggests that both the charge and spin properties of the electrons play important roles in the POWS system in the presence of a local magnetic field.

Chapter 6 starts to investigate a more practical case - the photocatalytic splitting of seawater. The effects of different electrolytes on the POWS performance will be discussed in this chapter. It is shown that the neutral electrolyte solutions could greatly enhance the POWS performance by facilitating the charge carriers' separation. Different characterisation techniques including time-resolved photoluminescence, *in situ* X-ray photoelectron spectroscopy, etc. are used to understand the charge separation processes. Artificial seawater samples are prepared in lab and natural seawater was collected from Bournemouth, UK, all of which are shown to enhance the POWS activity at elevated temperatures.

Chapter 7 summarises the findings in the previous chapters and provides perspectives to the future research in the related research fields.

1.6 References

1. Bowker, M. *Heterogeneous catalysis: Fundamentals and applications*. *Catalysis Letters* vol. 142 (Kluwer Academic Publishers, 2012).
2. Qiu, J., Zhang, X., Feng, Y., Zhang, X., Wang, H. & Yao, J. Modified metal-organic frameworks as photocatalysts. *Applied Catalysis B: Environmental* vol. 231 317–342 (2018).
3. Mills, A., Johnston, J. & O'Rourke, C. Photocatalyst Activity Indicator Inks, paii s, for Assessing Self-Cleaning Films. *Accounts Mater. Res.* **3**, 67–77 (2022).
4. Boddy, P. J. Oxygen Evolution on Semiconducting TiO2. *J. Electrochem. Soc.* **115**, 199 (1968).
5. Fujishima, A. & Honda, K. Electrochemical Photolysis of Water at a Semiconductor Electrode. *Nature* **238**, 37–38 (1972).
6. Fujishima, A., Rao, T. N. & Tryk, D. A. Titanium dioxide photocatalysis. *J. Photochem. Photobiol. C Photochem. Rev.* **1**, 1–21 (2000).
7. Asahi, R., Morikawa, T., Ohwaki, T., Aoki, K. & Taga, Y. Visible-light photocatalysis in nitrogen-doped titanium oxides. *Science* **293**, 269–271 (2001).

8. Kudo, A. & Miseki, Y. Heterogeneous photocatalyst materials for water splitting. *Chem. Soc. Rev.* **38**, 253–278 (2009).

9. Li, P., Zhou, Y., Zhao, Z., Xu, Q., Wang, X., Xiao, M. & Zou, Z. Hexahedron prism-anchored octahedronal CeO2: Crystal facet-based homojunction promoting efficient solar fuel synthesis. *J. Am. Chem. Soc.* **137**, 9547–9550 (2015).

10. Tu, W., Zhou, Y. & Zou, Z. Photocatalytic conversion of CO2 into renewable hydrocarbon fuels: State-of-the-art accomplishment, challenges, and prospects. *Advanced Materials* vol. 26 4607–4626 (2014).

11. Zou, Z., Ye, J., Sayama, K. & Arakawa, H. Direct splitting of water under visible light irradiation with an oxide semiconductor photocatalyst. *Nature* **414**, 625–627 (2001).

12. Chen, H., Nanayakkara, C. E. & Grassian, V. H. Titanium dioxide photocatalysis in atmospheric chemistry. *Chem. Rev.* **112**, 5919–5948 (2012).

13. Chen, C., Ma, W. & Zhao, J. Semiconductor-mediated photodegradation of pollutants under visible-light irradiation. *Chem. Soc. Rev.* **39**, 4206–4219 (2010).

14. Yan, S. C., Li, Z. S. & Zou, Z. G. Photodegradation performance of g-C3N4 fabricated by directly heating melamine. *Langmuir* **25**, 10397–10401 (2009).

15. Han, R., Andrews, R., O'Rourke, C., Hodgen, S. & Mills, A. Photocatalytic air purification: Effect of HNO3 accumulation on NOx and VOC removal. *Catal. Today* **380**, 105–113 (2021).

16. Moniz, S. J. A., Shevlin, S. A., Martin, D. J., Guo, Z. X. & Tang, J. Visible-light driven heterojunction photocatalysts for water splitting-a critical review. *Energy Environ. Sci.* **8**, 731–759 (2015).

17. Wang, Y., Vogel, A., Sachs, M., Sprick, R. S., Wilbraham, L., Moniz, S. J. A., Godin, R., Zwijnenburg, M. A., Durrant, J. R., Cooper, A. I. & Tang, J. Current understanding and challenges of solar-driven hydrogen generation using polymeric photocatalysts. *Nat. Energy* **4**, 746–760 (2019).

18. Ran, J., Zhang, J., Yu, J., Jaroniec, M. & Qiao, S. Z. Earth-abundant cocatalysts for semiconductor-based photocatalytic water splitting. *Chem. Soc. Rev.* **43**, 7787–7812 (2014).

19. Zhu, S. & Wang, D. Photocatalysis: Basic principles, diverse forms of implementations and emerging scientific opportunities. *Adv. Energy Mater.* **7**, 1700841 (2017).

20. Green, M. A. & Bremner, S. P. Energy conversion approaches and materials for high-efficiency photovoltaics. *Nat. Mater.* **16**, 23–34 (2016).

21. Tachibana, Y., Vayssieres, L. & Durrant, J. R. Artificial photosynthesis for solar water-splitting. *Nat. Photonics* **6**, 511–518 (2012).

22. Zhang, L., Ran, J., Qiao, S. Z. & Jaroniec, M. Characterization of semiconductor photocatalysts. *Chem. Soc. Rev.* **48**, 5184–5206 (2019).

23. Wolff, C. M., Frischmann, P. D., Schulze, M., Bohn, B. J., Wein, R., Livadas, P., Carlson, M. T., Jäckel, F., Feldmann, J., Würthner, F. & Stolarczyk, J. K. All-in-one visible-light-driven water splitting by combining nanoparticulate and molecular co-catalysts on CdS nanorods. *Nat. Energy* **3**, 862–869 (2018).

24. Landman, A., Dotan, H., Shter, G. E., Wullenkord, M., Houaijia, A., Maljusch, A., Grader, G. S. & Rothschild, A. Photoelectrochemical water splitting in separate oxygen and hydrogen cells. *Nat. Mater.* **16**, 646–651 (2017).

25. Jafari, T., Moharreri, E., Amin, A. S., Miao, R., Song, W. & Suib, S. L. Photocatalytic

water splitting - The untamed dream: A review of recent advances. *Molecules* **21**, 900 (2016).

26. Maeda, K. & Domen, K. Photocatalytic water splitting: Recent progress and future challenges. *J. Phys. Chem. Lett.* **1**, 2655–2661 (2010).

27. Zhou, G., Shan, Y., Wang, L., Hu, Y., Guo, J., Hu, F., Shen, J., Gu, Y., Cui, J., Liu, L. & Wu, X. Photoinduced semiconductor-metal transition in ultrathin troilite FeS nanosheets to trigger efficient hydrogen evolution. *Nat. Commun.* **10**, 399 (2019).

28. Chen, X., Shen, S., Guo, L. & Mao, S. S. Semiconductor-based photocatalytic hydrogen generation. *Chem. Rev.* **110**, 6503–6570 (2010).

29. Li, Q., Guo, B., Yu, J., Ran, J., Zhang, B., Yan, H. & Gong, J. R. Highly efficient visible-light-driven photocatalytic hydrogen production of CdS-cluster-decorated graphene nanosheets. *J. Am. Chem. Soc.* **133**, 10878–10884 (2011).

30. Mazloomi, K. & Gomes, C. Hydrogen as an energy carrier: Prospects and challenges. *Renew. Sustain. Energy Rev.* **16**, 3024–3033 (2012).

31. Tang, J., Durrant, J. R. & Klug, D. R. Mechanism of photocatalytic water splitting in TiO2. Reaction of water with photoholes, importance of charge carrier dynamics, and evidence for four-hole chemistry. *J. Am. Chem. Soc.* **130**, 13885–13891 (2008).

32. Han, B. & Hu, Y. H. Highly Efficient Temperature-Induced Visible Light Photocatalytic Hydrogen Production from Water. *J. Phys. Chem. C* **119**, 18927–18934 (2015).

33. Duonghong, D., Borgarello, E. & Grätzel, M. Dynamics of Light-Induced Water Cleavage in Colloidal Systems. *J. Am. Chem. Soc.* **103**, 4685–4690 (1981).

34. Yin, X. L., Li, L. L., Jiang, W. J., Zhang, Y., Zhang, X., Wan, L. J. & Hu, J. S. MoS2/CdS Nanosheets-on-Nanorod Heterostructure for Highly Efficient Photocatalytic H2 Generation under Visible Light Irradiation. *ACS Appl. Mater. Interfaces* **8**, 15258–15266 (2016).

35. Zhang, Z., Qian, Q., Li, B. & Chen, K. J. Interface Engineering of Monolayer MoS2/GaN Hybrid Heterostructure: Modified Band Alignment for Photocatalytic Water Splitting Application by Nitridation Treatment. *ACS Appl. Mater. Interfaces* **10**, 17419–17426 (2018).

36. Lu, Q., Yu, Y., Ma, Q., Chen, B. & Zhang, H. 2D Transition-Metal-Dichalcogenide-Nanosheet-Based Composites for Photocatalytic and Electrocatalytic Hydrogen Evolution Reactions. *Adv. Mater.* **28**, 1917–1933 (2016).

37. Wang, Q. & Domen, K. Particulate Photocatalysts for Light-Driven Water Splitting: Mechanisms, Challenges, and Design Strategies. *Chem. Rev.* **120**, 919–985 (2020).

38. Peng, Y. K. & Tsang, S. C. E. Facet-dependent photocatalysis of nanosize semiconductive metal oxides and progress of their characterization. *Nano Today* **18**, 15–34 (2018).

39. Li, Y. & Tsang, S. C. E. Recent Progress and Strategies for Enhancing Photocatalytic Water Splitting. *Mater. Today Sustain.* **9**, 100032 (2020).

40. Shaner, M. R., Atwater, H. A., Lewis, N. S. & McFarland, E. W. A comparative technoeconomic analysis of renewable hydrogen production using solar energy. *Energy Environ. Sci.* **9**, 2354–2371 (2016).

41. Hisatomi, T. & Domen, K. Reaction systems for solar hydrogen production via water splitting with particulate semiconductor photocatalysts. *Nat. Catal.* **2**, 387–399 (2019).

42. Liu, N., Schneider, C., Freitag, D., Venkatesan, U., Marthala, V. R. R., Hartmann, M., Winter, B., Spiecker, E., Osvet, A., Zolnhofer, E. M., Meyer, K., Nakajima, T., Zhou, X. & Schmuki, P. Hydrogenated anatase: Strong photocatalytic dihydrogen evolution without the use of a co-catalyst. *Angew. Chem. Int. Ed.* **53**, 14201–14205 (2014).

43. Park, K. H., An, Y., Jung, S., Park, H. & Yang, C. The use of an n-type macromolecular additive as a simple yet effective tool for improving and stabilizing the performance of organic solar cells. *Energy Environ. Sci.* **9**, 3464–3471 (2016).

44. Liu, G., Pan, J., Yin, L., Irvine, J. T., Li, F., Tan, J., Wormald, P. & Cheng, H. M. Heteroatom-modulated switching of photocatalytic hydrogen and oxygen evolution preferences of anatase TiO 2 microspheres. *Adv. Funct. Mater.* **22**, 3233–3238 (2012).

45. Zalas, M. & Laniecki, M. Photocatalytic hydrogen generation over lanthanides-doped titania. *Sol. Energy Mater. Sol. Cells* **89**, 287–296 (2005).

46. Sasikala, R., Sudarsan, V., Sudakar, C., Naik, R., Sakuntala, T. & Bharadwaj, S. R. Enhanced photocatalytic hydrogen evolution over nanometer sized Sn and Eu doped titanium oxide. *Int. J. Hydrogen Energy* **33**, 4966–4973 (2008).

47. Jing, D., Zhang, Y. & Guo, L. Study on the synthesis of Ni doped mesoporous TiO2 and its photocatalytic activity for hydrogen evolution in aqueous methanol solution. *Chem. Phys. Lett.* **415**, 74–78 (2005).

48. Yan, H., Zhang, X., Zhou, S., Xie, X., Luo, Y. & Yu, Y. Synthesis of WO3 nanoparticles for photocatalytic O2 evolution by thermal decomposition of ammonium tungstate loading on g-C 3N4. *J. Alloys Compd.* **509**, L232–L235 (2011).

49. Ogawa, K., Tomita, O., Takagi, K., Nakada, A., Higashi, M. & Abe, R. Improved activity of hydrothermally-prepared WO3 photocatalysts by sodium salt additives. *Chem. Lett.* **47**, 985–988 (2018).

50. Townsend, T. K., Sabio, E. M., Browning, N. D. & Osterloh, F. E. Photocatalytic water oxidation with suspended alpha-Fe 2O 3 particles-effects of nanoscaling. *Energy Environ. Sci.* **4**, 4270–4275 (2011).

51. Jia, J., Seitz, L. C., Benck, J. D., Huo, Y., Chen, Y., Ng, J. W. D., Bilir, T., Harris, J. S. & Jaramillo, T. F. Solar water splitting by photovoltaic-electrolysis with a solar-to-hydrogen efficiency over 30%. *Nat. Commun.* **7**, 13237 (2016).

52. Pinaud, B. A., Benck, J. D., Seitz, L. C., Forman, A. J., Chen, Z., Deutsch, T. G., James, B. D., Baum, K. N., Baum, G. N., Ardo, S., Wang, H., Miller, E. & Jaramillo, T. F. Technical and economic feasibility of centralized facilities for solar hydrogen production via photocatalysis and photoelectrochemistry. *Energy Environ. Sci.* **6**, 1983–2002 (2013).

53. Goto, Y., Hisatomi, T., Wang, Q., Higashi, T., Ishikiriyama, K., Maeda, T. Sakata, Y., Okunaka, S., Tokudome, H., Katayama, M., Akiyama, S., Nishiyama, H., Inoue, Y., Takewaki, T., Setoyama, T., Minegishi, T., Takata, T., Yamada, T. & Domen, K. A Particulate Photocatalyst Water-Splitting Panel for Large-Scale Solar Hydrogen Generation. *Joule* **2**, 509–520 (2018).

54. Fabian, D. M., Hu, S., Singh, N., Houle, F. A., Hisatomi, T., Domen, K., Osterloh, F. E. & Ardo, S. Particle suspension reactors and materials for solar-driven water splitting. *Energy Environ. Sci.* **8**, 2825–2850 (2015).

55. Wang, Y., Suzuki, H., Xie, J., Tomita, O., Martin, D. J., Higashi, M., Kong, D., Abe, R. & Tang, J. Mimicking Natural Photosynthesis: Solar to Renewable H2 Fuel Synthesis by Z-Scheme Water Splitting Systems. *Chem. Rev.* **118**, 5201–5241

(2018).

56. Suzuki, H., Tomita, O., Higashi, M. & Abe, R. Tungstic acids H2WO4 and H4WO5 as stable photocatalysts for water oxidation under visible light. *J. Mater. Chem. A* **5**, 10280–10288 (2017).

57. Sasaki, Y., Iwase, A., Kato, H. & Kudo, A. The effect of co-catalyst for Z-scheme photocatalysis systems with an Fe3+/Fe2+ electron mediator on overall water splitting under visible light irradiation. *J. Catal.* **259**, 133–137 (2008).

58. Kato, H., Hori, M., Konta, R., Shimodaira, Y. & Kudo, A. Construction of Z-scheme type heterogeneous photocatalysis systems for water splitting into H 2 and O 2 under visible light irradiation. *Chem. Lett.* **33**, 1348–1349 (2004).

59. Tabata, M., Maeda, K., Higashi, M., Lu, D., Takata, T., Abe, R. & Domen, K. Modified Ta3N5 powder as a photocatalyst for O 2 evolution in a two-step water splitting system with an iodate/iodide shuttle redox mediator under visible light. *Langmuir* **26**, 9161–9165 (2010).

60. Higashi, M., Abe, R., Ishikawa, A., Takata, T., Ohtani, B. & Domen, K. Z-scheme overall water splitting on modified-TaOn photocatalysts under visible light (λ < 500 nm). *Chem. Lett.* **37**, 138–139 (2008).

61. Abe, R., Takata, T., Sugihara, H. & Domen, K. Photocatalytic overall water splitting under visible light by TaON and WO3 with an IO3-/I- shuttle redox mediator. *Chem. Commun.* 3829–3831 (2005).

62. Jia, Q., Iwase, A. & Kudo, A. BiVO4-Ru/SrTiO3:Rh composite Z-scheme photocatalyst for solar water splitting. *Chem. Sci.* **5**, 1513–1519 (2014).

63. Sasaki, Y., Nemoto, H., Saito, K. & Kudo, A. Solar water splitting using powdered photocatalysts driven by Z-schematic interparticle electron transfer without an electron mediator. *J. Phys. Chem. C* **113**, 17536–17542 (2009).

64. Wang, Q., Hisatomi, T., Suzuki, Y., Pan, Z., Seo, J., Katayama, M., Minegishi, T., Nishiyama, H., Takata, T., Seki, K., Kudo, A., Yamada, T. & Domen, K. Particulate Photocatalyst Sheets Based on Carbon Conductor Layer for Efficient Z‐Scheme Pure-Water Splitting at Ambient Pressure. *J. Am. Chem. Soc.* **139**, 1675–1683 (2017).

65. Iwase, A., Ng, Y. H., Ishiguro, Y., Kudo, A. & Amal, R. Reduced graphene oxide as a solid-state electron mediator in Z-scheme photocatalytic water splitting under visible light. *J. Am. Chem. Soc.* **133**, 11054–11057 (2011).

66. Pan, Z., Zhang, G. & Wang, X. Polymeric Carbon Nitride/Reduced Graphene Oxide/Fe2O3: All-Solid-State Z-Scheme System for Photocatalytic Overall Water Splitting. *Angew. Chem. Int. Ed.* **58**, 7102–7106 (2019).

67. Miseki, Y. & Sayama, K. Photocatalytic Water Splitting for Solar Hydrogen Production Using the Carbonate Effect and the Z-Scheme Reaction. *Adv. Energy Mater.* **9**, 1–15 (2019).

68. Chen, X., Liu, L., Yu, P. Y. & Mao, S. S. Increasing solar absorption for photocatalysis with black hydrogenated titanium dioxide nanocrystals. *Science* **331**, 746–750 (2011).

69. Liu, N., Häublein, V., Zhou, X., Venkatesan, U., Hartmann, M., MačKović, M., Nakajima, T., Spiecker, E., Osvet, A., Frey, L. & Schmuki, P. 'Black' TiO2 Nanotubes Formed by High-Energy Proton Implantation Show Noble-Metal-co-Catalyst Free Photocatalytic H2-Evolution. *Nano Lett.* **15**, 6815–6820 (2015).

70. Etacheri, V., Di Valentin, C., Schneider, J., Bahnemann, D. & Pillai, S. C. Visible-light activation of TiO2 photocatalysts: Advances in theory and experiments. *J.*

Photochem. Photobiol. C Photochem. Rev. **25**, 1–29 (2015).

71. Choi, W., Termin, A. & Hoffmann, M. R. The role of metal ion dopants in quantum-sized TiO2: Correlation between photoreactivity and charge carrier recombination dynamics. *J. Phys. Chem.* **98**, 13669–13679 (1994).

72. Asahi, R., Morikawa, T., Irie, H. & Ohwaki, T. Nitrogen-doped titanium dioxide as visible-light-sensitive photocatalyst: Designs, developments, and prospects. *Chem. Rev.* **114**, 9824–9852 (2014).

73. Li, Y., Peng, Y.-K., Hu, L., Zheng, J., Prabhakaran, D., Wu, S., Puchtler, T. J., Li, M., Wong, K.-Y., Taylor, R. A. & Tsang, S. C. E. Photocatalytic water splitting by N-TiO2 on MgO (111) with exceptional quantum efficiencies at elevated temperatures. *Nat. Commun.* **10**, 4421 (2019).

74. Wang, J., Tafen, D. N., Lewis, J. P., Hong, Z., Manivannan, A., Zhi, M., Li, M. & Wu, N. Origin of photocatalytic activity of Nitrogen-doped TiO2 nanobelts. *J. Am. Chem. Soc.* **131**, 12290–12297 (2009).

75. Ansari, S. A., Khan, M. M., Ansari, M. O. & Cho, M. H. Nitrogen-doped titanium dioxide (N-doped TiO2) for visible light photocatalysis. *New J. Chem.* **40**, 3000–3009 (2016).

76. Sato, S. Photocatalytic activity of NOx-doped TiO2 in the visible light region. *Chem. Phys. Lett.* **123**, 126–128 (1986).

77. Livraghi, S., Paganini, M. C., Giamello, E., Selloni, A., Di Valentin, C. & Pacchioni, G. Origin of photoactivity of nitrogen-doped titanium dioxide under visible light. *J. Am. Chem. Soc.* **128**, 15666–15671 (2006).

78. Di Valentin, C., Pacchioni, G., Selloni, A., Livraghi, S. & Giamello, E. Characterization of paramagnetic species in N-doped TiO 2 powders by EPR spectroscopy and DFT calculations. *J. Phys. Chem. B* **109**, 11414–11419 (2005).

79. Wang, G., Wang, H., Ling, Y., Tang, Y., Yang, X., Fitzmorris, R. C., Wang, C., Zhang, J. Z. & Li, Y. Hydrogen-treated TiO2 nanowire arrays for photoelectrochemical water splitting. *Nano Lett.* **11**, 3026–3033 (2011).

80. Cowan, A. J., Tang, J., Leng, W., Durrant, J. R. & Klug, D. R. Water splitting by nanocrystalline TiO 2 in a complete photoelectrochemical cell exhibits efficiencies limited by charge recombination. *J. Phys. Chem. C* **114**, 4208–4214 (2010).

81. Imanishi, A., Okamura, T., Ohashi, N., Nakamura, R. & Nakato, Y. Mechanism of water photooxidation reaction at atomically flat TiO 2 (rutile) (110) and (100) surfaces: Dependence on solution pH. *J. Am. Chem. Soc.* **129**, 11569–11578 (2007).

82. Padilha, A. C. M., Raebiger, H., Rocha, A. R. & Dalpian, G. M. Charge storage in oxygen deficient phases of TiO2: Defect Physics without defects. *Sci. Rep.* **6**, 2–8 (2016).

83. Li, Y. & Tsang, S. C. E. Unusual Catalytic Properties of High-Energetic-Facet Polar Metal Oxides. *Acc. Chem. Res.* **54**, 366–378 (2021).

84. Zhang, Y. C., Li, Z., Zhang, L., Pan, L., Zhang, X., Wang, L., Fazal-e-Aleem & Zou, J. J. Role of oxygen vacancies in photocatalytic water oxidation on ceria oxide: Experiment and DFT studies. *Appl. Catal. B Environ.* **224**, 101–108 (2018).

85. Long, M. & Zheng, L. Engineering vacancies for solar photocatalytic applications. *Cuihua Xuebao/Chinese J. Catal.* **38**, 617–624 (2017).

86. Esch, F., Fabris, S., Zhou, L., Montini, T., Africh, C., Fornasiero, P., Comelli, G. & Rosei, R. Chemistry: Electron localization determines defect formation on ceria

substrates. *Science* **309**, 752–755 (2005).

87. Tan, H., Zhao, Z., Niu, M., Mao, C., Cao, D., Cheng, D., Feng, P. & Sun, Z. A facile and versatile method for preparation of colored TiO2 with enhanced solar-driven photocatalytic activity. *Nanoscale* **6**, 10216–10223 (2014).

88. Tan, H., Zhao, Z., Zhu, W. Bin, Coker, E. N., Li, B., Zheng, M., Yu, W., Fan, H. & Sun, Z. Oxygen vacancy enhanced photocatalytic activity of pervoskite SrTiO3. *ACS Appl. Mater. Interfaces* **6**, 19184–19190 (2014).

89. Nakamura, I., Negishi, N., Kutsuna, S., Ihara, T., Sugihara, S. & Takeuchi, K. Role of oxygen vacancy in the plasma-treated TiO2 photocatalyst with visible light activity for NO removal. *J. Mol. Catal. A Chem.* **161**, 205–212 (2000).

90. Guan, M., Xiao, C., Zhang, J., Fan, S., An, R., Cheng, Q., Xie, J., Zhou, M., Ye, B. & Xie, Y. Vacancy associates promoting solar-driven photocatalytic activity of ultrathin bismuth oxychloride nanosheets. *J. Am. Chem. Soc.* **135**, 10411–10417 (2013).

91. Zhou, X., Liu, N. & Schmuki, P. Photocatalysis with TiO2 Nanotubes: 'Colorful' Reactivity and Designing Site-Specific Photocatalytic Centers into TiO2 Nanotubes. *ACS Catal.* **7**, 3210–3235 (2017).

92. D'Arienzo, M., Carbajo, J., Bahamonde, A., Crippa, M., Polizzi, S., Scotti, R., Wahba, L. & Morazzoni, F. Photogenerated defects in shape-controlled TiO 2 anatase nanocrystals: A probe to evaluate the role of crystal facets in photocatalytic processes. *J. Am. Chem. Soc.* **133**, 17652–17661 (2011).

93. Carter, E., Carley, A. F. & Murphy, D. M. Evidence for O2- radical stabilization at surface oxygen vacancies on polycrystalline TiO2. *J. Phys. Chem. C* **111**, 10630–10638 (2007).

94. Singh, A. P., Kodan, N., Dey, A., Krishnamurthy, S. & Mehta, B. R. Improvement in the structural, optical, electronic and photoelectrochemical properties of hydrogen treated bismuth vanadate thin films. *Int. J. Hydrogen Energy* **40**, 4311–4319 (2015).

95. Wang, G., Ling, Y., Wang, H., Yang, X., Wang, C., Zhang, J. Z. & Li, Y. Hydrogen-treated WO 3 nanoflakes show enhanced photostability. *Energy Environ. Sci.* **5**, 6180–6187 (2012).

96. Wang, L., Wang, Y., Cheng, Y., Liu, Z., Guo, Q., Ha, M. N. & Zhao, Z. Hydrogen-treated mesoporous WO3 as a reducing agent of CO2 to fuels (CH4 and CH3OH) with enhanced photothermal catalytic performance. *J. Mater. Chem. A* **4**, 5314–5322 (2016).

97. Moss, B., Wang, Q., Butler, K. T., Grau-Crespo, R., Selim, S., Regoutz, A., Hisatomi, T., Godin, R., Payne, D. J., Kafizas, A., Domen, K., Steier, L. & Durrant, J. R. Linking in situ charge accumulation to electronic structure in doped SrTiO3 reveals design principles for hydrogen-evolving photocatalysts. *Nat. Mater.* **20**, 511–517 (2021).

98. Konta, R., Ishii, T., Kato, H. & Kudo, A. Photocatalytic Activities of Noble Metal Ion Doped SrTiO3 under Visible Light Irradiation. *J. Phys. Chem. B* **108**, 8992–8995 (2004).

99. Herrmann, J. M., Disdier, J. & Pichat, P. Effect of chromium doping on the electrical and catalytic properties of powder titania under UV and visible illumination. *Chem. Phys. Lett.* **108**, 618–622 (1984).

100. Wang, Q., Hisatomi, T., Ma, S. S. K., Li, Y. & Domen, K. Core/shell structured La- and Rh-Codoped SrTiO3 as a hydrogen evolution photocatalyst in Z-scheme overall water splitting under visible light irradiation. *Chem. Mater.* **26**, 4144–4150

(2014).

101. Wang, Q., Li, Y., Hisatomi, T., Nakabayashi, M., Shibata, N., Kubota, J. & Domen, K. Z-scheme water splitting using particulate semiconductors immobilized onto metal layers for efficient electron relay. *J. Catal.* **328**, 308–315 (2015).

102. Wang, Q., Hisatomi, T., Jia, Q., Tokudome, H., Zhong, M., Wang, C., Pan, Z., Takata, T., Nakabayashi, M., Shibata, N., Li, Y., Sharp, I. D., Kudo, A., Yamada, T. & Domen, K. Scalable water splitting on particulate photocatalyst sheets with a solar-to-hydrogen energy conversion efficiency exceeding 1%. *Nat. Mater.* **15**, 611–615 (2016).

103. Schneider, J., Matsuoka, M., Takeuchi, M., Zhang, J., Horiuchi, Y., Anpo, M. & Bahnemann, D. W. Understanding TiO2 Photocatalysis: Mechanisms and Materials. *Chem. Rev.* **114**, 9919–9986 (2014).

104. Hussain, H., Tocci, G., Woolcot, T., Torrelles, X., Pang, C. L., Humphrey, D. S., Yim, C. M., Grinter, D. C., Cabailh, G., Bikondoa, O., Lindsay, R., Zegenhagen, J., Michaelides, A. & Thornton, G. Structure of a model TiO2 photocatalytic interface. *Nat. Mater.* **16**, 461–467 (2017).

105. Chen, F., Huang, H., Guo, L., Zhang, Y. & Ma, T. The Role of Polarization in Photocatalysis. *Angew. Chem. Int. Ed.* **58**, 10061–10073 (2019).

106. Li, J., Cai, L., Shang, J., Yu, Y. & Zhang, L. Giant Enhancement of Internal Electric Field Boosting Bulk Charge Separation for Photocatalysis. *Adv. Mater.* **28**, 4059–4064 (2016).

107. Li, J., Zhan, G., Yu, Y. & Zhang, L. Superior visible light hydrogen evolution of Janus bilayer junctions via atomic-level charge flow steering. *Nat. Commun.* **7**, 11480 (2016).

108. Li, R., Zhang, F., Wang, D., Yang, J., Li, M., Zhu, J., Zhou, X., Han, H. & Li, C. Spatial separation of photogenerated electrons and holes among {010} and {110} crystal facets of BiVO 4. *Nat. Commun.* **4**, 1432–1437 (2013).

109. Li, L., Yan, J., Wang, T., Zhao, Z. J., Zhang, J., Gong, J. & Guan, N. Sub-10 nm rutile titanium dioxide nanoparticles for efficient visible-light-driven photocatalytic hydrogen production. *Nat. Commun.* **6**, 5881 (2015).

110. Liu, G., Yang, H. G., Pan, J., Yang, Y. Q., Lu, G. Q. M. & Cheng, H. M. Titanium dioxide crystals with tailored facets. *Chem. Rev.* **114**, 9559–9612 (2014).

111. Noguera, C. Polar oxide surfaces. *J. Phys. Condens. Matter* **12**, R367–R410 (2000).

112. Goniakowski, J., Finocchi, F. & Noguera, C. Polarity of oxide surfaces and nanostructures. *Reports Prog. Phys.* **71**, 1 (2008).

113. Noguera, C. & Goniakowski, J. Polarity in oxide nano-objects. *Chem. Rev.* **113**, 4073–4105 (2013).

114. Takata, T., Pan, C., Nakabayashi, M., Shibata, N. & Domen, K. Fabrication of a core-shell-type photocatalyst via photodeposition of group IV and v transition metal oxyhydroxides: An effective surface modification method for overall water splitting. *J. Am. Chem. Soc.* **137**, 9627–9634 (2015).

115. Sun, S., Hisatomi, T., Wang, Q., Chen, S., Ma, G., Liu, J., Nandy, S., Minegishi, T., Kayayama, M. & Domen, K. Efficient Redox-Mediator-Free Z‐Scheme Water Splitting Employing Oxysulfide Photocatalysts under Visible Light.pdf. *ACS Catal.* **8**, 1690–1696 (2018).

116. Chen, S., Takata, T. & Domen, K. Particulate photocatalysts for overall water splitting. *Nat. Rev. Mater.* **2**, 17050 (2017).

117. Li, Z., Zhang, F., Han, J., Zhu, J., Li, M., Zhang, B., Fan, W., Lu, J. & Li, C. Using Pd as a Cocatalyst on GaN–ZnO Solid Solution for Visible-Light-Driven Overall Water Splitting. *Catal. Letters* **148**, 933–939 (2018).

118. Inoue, Y. Photocatalytic water splitting by RuO2-loaded metal oxides and nitrides with d0- and d10 -related electronic configurations. *Energy Environ. Sci.* **2**, 364–386 (2009).

119. Jo, W. J., Kang, H. J., Kong, K. J., Lee, Y. S., Park, H., Lee, Y., Buonassisi, T., Gleason, K. K. & Lee, J. S. Phase transition-induced band edge engineering of BiVO4 to split pure water under visible light. *Proc. Natl. Acad. Sci. U. S. A.* **112**, 13774–13778 (2015).

120. Asai, R., Nemoto, H., Jia, Q., Saito, K., Iwase, A. & Kudo, A. A visible light responsive rhodium and antimony-codoped SrTiO3 powdered photocatalyst loaded with an IrO2 cocatalyst for solar water splitting. *Chem. Commun.* **50**, 2543–2546 (2014).

121. Wang, Z., Li, C. & Domen, K. Recent developments in heterogeneous photocatalysts for solar-driven overall water splitting. *Chem. Soc. Rev.* **48**, 2109–2125 (2019).

122. Hou, W. & Cronin, S. B. A review of surface plasmon resonance-enhanced photocatalysis. *Adv. Funct. Mater.* **23**, 1612–1619 (2013).

123. Wang, Z., Yang, C., Lin, T., Yin, H., Chen, P., Wan, D., Xu, F., Huang, F., Lin, J., Xie, X. & Jiang, M. H-doped black titania with very high solar absorption and excellent photocatalysis enhanced by localized surface plasmon resonance. *Adv. Funct. Mater.* **23**, 5444–5450 (2013).

124. Ingram, D. B. & Linic, S. Water splitting on composite plasmonic-metal/semiconductor photoelectrodes: Evidence for selective plasmon-induced formation of charge carriers near the semiconductor surface. *J. Am. Chem. Soc.* **133**, 5202–5205 (2011).

125. Masson, J. F. Portable and field-deployed surface plasmon resonance and plasmonic sensors. *Analyst* **145**, 3776–3800 (2020).

126. Maeda, K., Teramura, K., Lu, D., Saito, N., Inoue, Y. & Domen, K. Noble-Metal/Cr2O3 Core/Shell Nanoparticles as a Cocatalyst for Photocatalytic Overall Water Splitting. *Angew. Chemie* **118**, 7970–7973 (2006).

127. Maeda, K., Teramura, K., Lu, D., Saito, N., Inoue, Y. & Domen, K. Roles of Rh/Cr2O3 (Core/Shell) Nanoparticles Photodeposited on Visible-Light-Responsive (Ga1-xZnx)(N1-xOx) Solid Solutions in Photocatalytic Overall Water Splitting. *J. Phys. Chem. C* **111**, 7554–7560 (2007).

128. Rao, C. N. R. & Dey, S. Solar thermochemical splitting of water to generate hydrogen. *Proc. Natl. Acad. Sci. U. S. A.* **114**, 13385–13393 (2017).

129. Tian, B., Tian, B., Smith, B., Scott, M. C., Hua, R., Lei, Q. & Tian, Y. Supported black phosphorus nanosheets as hydrogen-evolving photocatalyst achieving 5.4% energy conversion efficiency at 353 K. *Nat. Commun.* **9**, 1397 (2018).

130. Bandura, A. V. & Lvov, S. N. The ionization constant of water over wide ranges of temperature and density. *J. Phys. Chem. Ref. Data* **35**, 15–30 (2006).

131. Foo, C., Li, Y., Lebedev, K., Chen, T. T., Day, S., Tang, C. & Tsang, S. C. E. Characterisation of oxygen defects and nitrogen impurities in TiO2 photocatalysts using variable-temperature X-ray powder diffraction. *Nat. Commun.* **12**, 661 (2021).

Chapter 2 Experimental and Characterisation Methods

2.1 Material synthesis

2.1.1 Preparation of titanium oxide (TiO_2)

Pristine TiO_2 samples were obtained from different sources. Phase-pure anatase TiO_2 is commercially available (ST-01 TiO_2 powder, Ishihara Sangyo, Japan, mean particle size *ca.* 5 nm). Phase-pure rutile TiO_2 powder was purchased from Sigma-Aldrich (mean particle size < 100 nm). Commercial Degussa P25 was also engaged in this research project, which is a widely used photocatalyst containing about 80% of anatase and 20% of rutile phase. TiO_2 nanoparticles was also prepared via sol-gel method (mean particle size *ca.* 25.4 nm). Typically, solution A was prepared by adding 5 mL of titanium tetraisopropoxide (TTIP) in 15 mL ethanol and solution B was obtained by mixing 10 mL of deionised water, 10 mL of ethanol and 1 mL of acetic acid. Then solution A was slowly added to solution B dropwise under vigorous magnetic stirring. After a transparent gel forms, it was left still for aging at room temperature overnight (without stirring), following by drying in vacuum oven at 70 ^oC. Then the obtained dry gel was calcined in an air flow at 400 ^oC for 2 h to obtain the TiO_2 nanoparticles (white powder), which were then collected for further use.

2.1.2 Synthesis of N-doped TiO_2 (N-TiO_2) using NH_3 treatment

The N-TiO_2 was prepared by treating the pristine TiO_2 with pure NH_3 gas. In a typical experiment, 250 mg of TiO_2 sample powder (Degussa P25, sol-gel TiO_2, anatase or rutile) was put into a quartz boat which was then loaded in a tubular furnace. The temperature was subsequently elevated to the required temperature in the range of 550-750 ^oC in a step of 5 ^oC min^{-1} in a pure NH_3 gas flow. The

treatment was maintained for 8 h before cooling down to room temperature naturally. The samples were denoted as N-P25-T, N-sgTiO_2-T, N-TiO_2(A)-T or N-TiO_2(R)-T depending on the precursor that was used, where T represents the treatment temperature in NH_3. Colour of the obtained N-TiO_2 powders varies with the NH_3 treatment temperature, with N-P25-550 showing a yellow colour, while N-P25-620 showing a dark blue colour (Figure 2.1). The as-prepared materials were collected and used without further treatment unless specified.

Figure 2.1 A photographic image of N-doped P25 TiO_2 materials. From left to right: pristine P25, N-P25-550, N-P25-600, N-P25-620, and N-P25-660.

2.1.3 Synthesis of the facet-engineered N-TiO_2

The synthesis of the facet-engineered TiO_2 nanocrystals was adopted from our previous work:[1] 5.0 mL of titanium butoxide, $Ti(OC_4H_9)_4$, was mixed with 0.6 mL of hydrofluoric acid (48 wt.%) in a 50-mL Teflon-lined autoclave and subsequently heated to 180 °C at a rate of 5 °C min^{-1}. The temperature was kept at 180 °C for 24 h. After the hydrothermal process, the as-obtained white precipitate was washed with ethanol and deionised water for three times, respectively, and then dried in an oven at 80 °C overnight. For N-doping, typically, 200 mg as-prepared

facet-controlled TiO_2 was put in a quartz boat which was then transferred to a tubular furnace. The sample was then heated to 600 ^oC at a rate of 5 °C min^{-1} and kept for 2 h under NH_3 flow, after which it was allowed to cool down naturally and the dark blue powder, N-doped TiO_2 (N-TiO_2), was collected. The N-TiO_2 photocatalyst, unless stated, was loaded with 1 wt.% Pt nanoparticles as the H_2 evolution cocatalyst via a photo-deposition method before the photocatalytic tests. The photo-deposition process is described in the following sub-section.

2.1.4 Synthesis of N-TiO_2 using controlled oxidation method

N-TiO_2 was also prepared by oxidising titanium nitride powders, which was adopted from literature.[2] Typically, 500 mg of commercial titanium nitride powder (Sigma-Aldrich, mean particle size < 300 nm) was put into a quartz boat which was then loaded in a tubular furnace. Then the sample was calcined in O_2 flow at 400 ^oC, 500 ^oC, 600 ^oC and 700 ^oC, respectively, with a temperature ramping of 5 ^oC min^{-1}. The oxidation process took 2 h before cooling down to room temperature naturally.

2.1.5 Metal loading of N-TiO_2

Supported N-TiO_2 catalysts were prepared via a photo-deposition method: 100 mg of the N-TiO_2 was suspended in 60 mL methanol aqueous solution (50 vol. %) under vigorous stirring, and then the aqueous solution containing the required amount of the corresponding metal precursor was added into the above suspension. This suspension was then irradiated under a 300W UV lamp (Helios Italquartz S.R.L.) for 2 h before being filtered and washed with water and ethanol for 3 times, respectively. The final product was collected after being dried in a 70 ^oC oven overnight. In a photo-deposition process, the photo-generated electrons

in the conduction band (CB) reduce the metal ions in the solution, forming metal nanoparticles. Methanol acts as a sacrificial reagent, also known as the electron-scavenger, which is oxidised by the photo-generated holes in the valence band (VB), producing CO_2, CO, or other organic products. Clearly, not all kinds of metal nanoparticles can be deposited using this method: the CB minimum must have a more negative potential than the reduction potential of the metal ions, enabling the electrons in the CB to reduce the metal ions.[3] Size and morphology of the deposited metal NPs were studied by TEM in this thesis. The photocatalytic reactions of the photo-deposition are shown below.

$$M^{n+} + n\, e^- \rightarrow M$$

$$MeOH + n\, h^+ \rightarrow H_2O + CO_2 + Organic\ products \text{ (Not balanced)}$$

2.1.6 Synthesis of single-layer molybdenum disulphide (SL-MoS_2)

Single layer MoS_2 was prepared using the method adopted from our previous report:[4] Typically, 2 g of commercial bulk MoS_2 powder was soaked in 16 mL of 1.6 M n-butyl lithium/hexane solution for 72 h under a N_2 atmosphere. After the lithium intercalation process, the above suspension was diluted with 50 mL of hexane and centrifuged to collect the intercalated MoS_2. The collected MoS_2 was then dried under N_2. Subsequently, the powder was immersed in 500 mL of water and the resulting suspension was sonicated for 12 h to assist the exfoliation process. The dispersion was centrifuged at 4000 rpm for 15 min to remove unexfoliated precursors and only the supernatant was collected. Eventually, the exfoliated MoS_2 monolayers remained totally suspended in aqueous solution. To collect the SL-MoS_2 in a powder form, HCl solution was added dropwise into the above SL-MoS_2 colloid until the pH value reaching around 7. The precipitate was

then washed and collected by centrifugation several times and the final product was dried at 60 ^{o}C under vacuum overnight.

2.1.7 Synthesis of metal decorated SL-MoS_2

Metal decorated SL-MoS_2 materials (denoted as M:SL-MoS_2, where M represents the metal doping) were prepared using a hydrothermal method. Typically, the required amount of corresponding metal precursors (calculated loading amount of 2 wt.%) and 150 mg of thiourea were added to 10 mL of water and left overnight to form the complex. Subsequently this solution was then mixed with a 50 mL colloid containing 180 mg SL-MoS_2 (30 v/v% isopropanol/water with 50 mg of polyvinylpyrrolidone). A mixed homogeneous solution was then transferred to an autoclave with a 120-mL Teflon lining, followed by hydrothermal treatment at 160 °C for 24 h. After the reaction, the precipitate was washed three times using deionised water and then dried under vacuum for 12 h and finally treated with H_2 at 300 °C for 1 h prior to storage.

2.1.8 Synthesis of magnesium oxide (MgO) with different dominating facets

MgO(111) was prepared by a hydrothermal method. Typically, 2.0 g of $MgCl_2$•$6H_2O$ and 0.12 g of benzoic acid was dissolved in 60 mL of deionised water at room temperature under sonication for 1 h. The mixture was then stirred for 10 minutes before 20 mL of 2 mol L^{-1} NaOH (aq.) solution was added dropwise. The resulted slurry was collected and subsequently transferred to a 100 mL-autoclave with Teflon lining and gradually heated to 180 ^{o}C in an oven and maintained at this temperature for 24 h. The resulted solid was separated by filtration followed by washing with water and drying at 80 ^{o}C under vacuum overnight, and then the $Mg(OH)_2$ precursor was collected. MgO(111) nanosheets were obtained after

calcining the above $Mg(OH)_2$ precursor in an air flow at 500 °C for 6 h.[5,6]

MgO(110) was prepared by reconstruction of the commercial MgO powders. Typically, 500 mg of commercial MgO was reacting with 100 mL of deionised water at 120 °C for 5 h (in a closed hydrothermal autoclave) to form magnesium hydroxide. The resulted magnesium hydroxide powders were then collected by filtration and was subsequently dried at 60 °C in air overnight. Then they were heated under dynamic vacuum at 500 °C for 6 h to form the MgO(110) white powders.[7,8]

MgO(100) was prepared by calcining the commercial magnesium nitrate ($Mg(NO_3)_2$). In a typical synthesis, 500 mg of $Mg(NO_3)_2$ was placed in a quartz boat and loaded in a tubular furnace, and then the temperature was increased to 500 °C in a step of 5 °C min^{-1}. The sample was then calcined in an air flow for 6 h.[9,10]

2.1.9 Synthesis of cerium oxide (CeO_2) of different morphologies

CeO_2(100) nanocubes were synthesised via a hydrothermal process based on previous reports.[11,12] 1.0 g of $Ce(NO_3)_3 \cdot 6H_2O$ was added to a 60 mL of 15 mol L^{-1} NaOH aqueous solution under vigorous stirring and kept stirring for 15 min. Afterwards, the solution was transferred to a Teflon lined 120mL-autoclave inside an oven of 180 °C, which was then left for 12 h. Following hydrothermal synthesis, the autoclave was allowed to cool down to room temperature naturally. The obtained powder was collected by centrifugation, and then washed 3 times with deionised water and dried at 70 °C under vacuum overnight.

For the synthesis of CeO_2 nanospheres, 1 mmol of $Ce(NO_3)_3 \cdot 6H_2O$ was dissolved in 32 mL of 0.078 mol L^{-1} NaOH (aq.) solution in a 100-mL round bottom reaction

flask.[13] The mixture was vigorously stirred at room temperature for 24 h in air, and the colour changed to pale yellow. The CeO_2 nanospheres were then collected by centrifugation at 5000 rpm for 10 min, and washed with ethanol and deionised water, each for three times, then dried at 70 ^oC under vacuum overnight.

2.1.10 Synthesis of zinc oxide (ZnO) nanoplates and nanorods

ZnO(0001) nanoplates were prepared according to our previous reports:[14,15] 6.0 g of zinc acetate dihydrate ($Zn(Ac)_2 \cdot 2H_2O$) and 3.84 g of hexamethylenetetramine (HMT, $C_6H_{12}N_4$) were dissolved in 48 mL of deionised water. The solution was transferred into a 100-mL Teflon-lined autoclave after a 10-min stirring. The autoclave was then put into an oven and maintained at 100 °C for 24 h and then allowed to cool down to room temperature naturally. The white precipitate was collected by centrifugation at 5000 rpm for 10 min, after which the supernatant was discarded. The solid was washed repeatedly with ethanol and water to remove excess precursor, and then was dried at 70 ^oC overnight. The resulted powder was calcined in air at 450 °C for 2 h with a heating rate of 10 °C min^{-1}.

The synthesis of ZnO nanorods is also based on our previous reports:[14,15] 1.487 g of zinc nitrate hexahydrate ($Zn(NO_3)_2 \cdot 6H_2O$) and 6 g of NaOH were dissolved in 10 mL of deionised water. Then 100 mL of ethanol was added to the above solution, afterwards 5 mL of 1,2-ethanediamine (EDA) was added into the mixture. Then the mixture was transferred to a covered plastic container with a volume of 250 mL. The reaction container was kept at room temperature under constant stirring for 3 days. After the synthesis a white precipitate was centrifuged and washed with deionised water and ethanol repeatedly. The resulted powder was calcined in air at 450 °C for 2 h with a heating rate of 10 °C min^{-1} after being dried at 70 ^oC under vacuum overnight.

2.1.11 Synthesis of layered double hydroxides (LDHs)

All LDHs were synthesised by similar co-precipitation method: magnesium chloride ($MgCl_2$) and the corresponding trivalent metal precursor ($CrCl_3 \cdot 6H_2O$, $Fe(NO_3)_3 \cdot 9H_2O$, $Co(NO_3)_2 \cdot 6H_2O$ and $Al(NO_3)_3 \cdot 9H_2O$ for MgCr-LDH, MgFe-LDH, MgCo-LDH and MgAl-LDH, respectively) were dissolved in 100 mL of deionised water firstly. And the molar ratio of Mg and the trivalent metal was controlled as 3:1. Then this solution and 1 mol L^{-1} NaOH (aq.) were added simultaneously into 25 mL water in a 250-mL three-neck round bottom flask. pH was controlled at different values by adding 1 mol L^{-1} NaOH (aq.) solution, because the required pH for different LDHs varies with the solubility product (MgCr-LDH: pH=7; MgFe-LDH: pH=10; MgCo-LDH: pH=10; MgAl-LDH: pH=10). Afterwards the slurry was kept under vigorous stirring for 2 h before centrifugation and washing with water. The obtained solid product was dispersed in water for further use.

2.1.12 Assembly of the photocatalysts with metal oxides or LDHs

Photocatalysts were mixed and ground with different polar or non-polar metal oxides thoroughly at the required ratio (typically 1:1 mass ratio) and allowed to disperse in water and sonicated for 2 h, filtered, dried and calcined in N_2 flow at 400 ^oC for 2 h prior to use.

The assembly of photocatalysts with LDHs was modified from a reported method in literature:[16] photocatalysts were mixed with different LDHs thoroughly at a 1:1 mass ratio and dispersed in 50 mL water, followed by refluxing at 60 ^oC for 1 h.[16] Subsequently the flask was cooled down to room temperature naturally and then the solid was separated by centrifugation at 5000 rpm for 10 min and washed with deionised water for 3 times. The product was dried under vacuum for further use.

2.1.13 Synthesis of iron oxide (Fe_3O_4) and Fe_3O_4@SiO_2 nanoparticles

The synthesis method was modified from our previous study.[17] The iron-oleate complex was first prepared by reacting metal chlorides and sodium oleate. Typically, 1.08 g of $FeCl_3 \cdot 6H_2O$ and 3.65 g of sodium oleate were firstly dissolved in a mixture of 8 mL of ethanol, 6 mL of distilled water, and 14 mL of hexane. The solution was then heated to 70 ^oC and maintained for 2 h, after which the upper organic layer containing the iron-oleate complex was washed for three times with distilled water. Hexane was evaporated after washing, and iron-oleate complex was obtained in solid form. For the preparation of 8 nm Fe_3O_4 NPs, 20 mg of the iron-oleate complex and 300 μL of oleic acid were dissolved in 20 mL of 1-octadecene at room temperature. Then the mixture was heated to 310 °C with a constant heating rate of 5 °C min^{-1}, and kept for 30 min before cooled to room temperature. Ethanol was then added to the mixture, resulting in a black precipitate, which was separated via centrifugation. The product was then washed with isopropanol/hexane several times and dried in an oven. The Fe_3O_4 NPs with different mean particle sizes were also prepared by the same procedure by controlling the amount of oleic acid (450 μL for 10.1 nm; 600 μL for 17.5 nm).

Fe_3O_4@SiO_2 was prepared from reverse micelles using a previously reported procedure. Briefly, 2 mg of Fe_3O_4 nanoparticles and 100 μL of tetraethyl orthosilicate (TEOS) were added to a heterogeneous solution containing cyclohexane (24 mL), hexanol (4.8 mL), Triton X-100 (6 mL, surfactant for the controlled growth of SiO_2), and deionised water (1 mL). After 6 h of stirring, $NH_3 \cdot H_2O$ (30 wt.%) (100 mL) was added to initiate the hydrolysis of TEOS. The reaction was allowed to continue for another 24 h with stirring at room temperature. The product was well dispersed in ethanol and further purified by centrifugation

(14500 rpm, 10 min).

2.1.14 Synthesis of the N-TiO_2, Fe_3O_4/N-TiO_2 and Fe_3O_4@SiO_2/N-TiO_2

TiO_2 nanoparticles was synthesised via a sol-gel process: solution A was prepared by adding 5 mL of TTIP in 15 mL ethanol, and solution B was obtained by mixing 10 mL of deionised water, 10 mL of ethanol and 1 mL of acetic acid. Then solution A was added to solution B dropwise under vigorous stirring. After a transparent gel forms, it was then aged overnight, following by drying in vacuum oven at 70 ^oC. Then obtained dry gel was then calcined in N_2 atmosphere at 400 ^oC for 2 h to obtain the TiO_2 nanoparticles, followed by NH_3 treatment at 600 °C for 10 h for N-doping.

Fe_3O_4/N-TiO_2 and Fe_3O_4@SiO_2/N-TiO_2 photocatalysts were synthesised following the similar procedure, but adding the Fe_3O_4 or Fe_3O_4@SiO_2 nanoparticles which were dispersed in ethanol in advance to the solution A. Photocatalysts containing different amount of Fe_3O_4 were also synthesised by this method by changing the amount of Fe_3O_4 NPs added to the solution A. The Fe_3O_4 NPs content were calculated to be 10%, 20%, 30% and 40% by weight, and the as-obtained samples were denoted as Fe_3O_4/N-TiO_2-0, Fe_3O_4/N-TiO_2-1, Fe_3O_4/N-TiO_2-2 and Fe_3O_4/N-TiO_2-3, respectively.

2.2 Characterisation techniques

2.2.1 X-ray diffraction (XRD)

XRD is one of the most widely used techniques to investigate the crystallographic structure of solid-state materials.[18] The interatomic distances in crystalline materials are comparable with the wavelengths of X-ray (both in the Angstrom range), which enables the incident X-ray to diffract through the crystallographic

planes which act as gratings. Structural information of crystalline materials including phase identification, lattice constant calculation, particle size estimation and unit cell parameters, *etc.* can be derived from the diffractograms[19,20]. The high energy X-ray photons are able to penetrate deeply into the material and thus XRD is typically regarded as a macroscopic characterisation technique for well-crystalline bulk structure[21].

For lab-sourced X-ray diffractometers, high speed electrons are generated from a heated filament of the cathode and targeted towards a metal target typically made up of copper and tungsten. Such collision will cause the ejection of core electrons from the metal target and then the electrons from higher energy levels will transfer to the lower energy levels to occupy the vacancy. This electron transfer between different energy levels results in the X-ray emission with a wavelength specific to the metal target. Then the X-ray beam will be monochromated and allowed to illuminate onto the sample material at different incident angles. If the sample is well crystalline, the X-ray beams diffract through the interlayer spacing grating of the material and undergo constructive or destructive interference to produce a unique diffraction pattern: the constructive interference appear as peaks in XRD diffractograms, while the beams undergone destructive interference cancel out each other and will not be observed. The interlayer spacing, d, can then be derived from Bragg's Law (Equation 2.1):[22]

$$n\lambda = 2\,d\sin\theta \qquad \textbf{Equation 2.1}$$

where λ is the wavelength of the X-ray beam, d is the interlayer spacing, and θ is the angle between the incident X-ray and scattering planes.

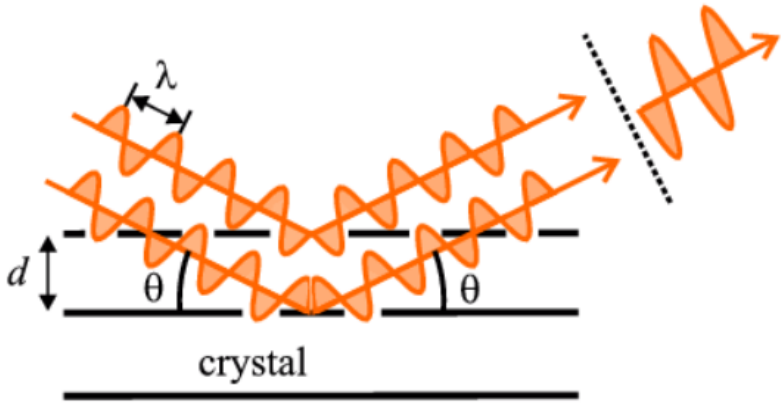

Figure 2.2 Bragg's Law depicting the relationship between interlayer spacing, diffraction angle, and wavelength of X-ray. Reproduced from ref. [22].

Lattice parameters can be further derived from Miller Indices for different crystallographic systems. For example, for non-cubic hexagonal crystal structure, the relationship between lattice parameter and interlayer spacing can be depicted by (Equation 2.2):

$$\frac{1}{d} = \frac{4}{3}\left(\frac{h^2 + hk + k^2}{a^2}\right) + \frac{l^2}{c^2} \qquad \textbf{Equation 2.2}$$

where d is the interlayer spacing; h, k, l is the Miller indices and a, c are the lattice parameters.

The sharp and well-defined peaks in the diffractograms arise from the destructive interference that took place at all incident angles other than the diffraction angles. However, when the size of the material decreases, defects like edges and steps would readily form, which lead to a wider distribution of interlayer spacing and result in peak broadening. Thus, building upon this phenomenon, it is possible to estimate particle size from the peak broadening measured with the full width at half maximum (FWHM) of the peak. The Scherrer equation is frequently used for determination of crystallite sizes from XRD diffractograms (Equation 2.3).

$$\tau = \frac{K\lambda}{\beta \cos\theta} \qquad \textbf{Equation 2.3}$$

where τ is the size of the crystallite; K is a dimensionless shape factor (typical value is about 0.9); λ is the wavelength of X-ray photon, β is the line broadening at FWHM after subtracting the instrumental line broadening (in radians); and θ is the diffraction angle.

In this thesis, XRD diffractograms were collected on a Bruker D8 Advance diffractometer with LynxEye detector and Cu Kα1 radiation (λ= 1.5406 Å), operating at 40 kV and 25 mA (step size at 0.019°, time per step at 0.10 s, total number of steps at 4368), unless specified. Samples in powder form were pressed onto a glass preparative slide which was then attached to a sample holder. All measurements were scanned at 2θ of 5-90^{o}.

2.2.2 Electron paramagnetic resonance (EPR) spectroscopy

EPR, also known as electron spin resonance (ESR) spectroscopy, is a powerful technique for studying materials with unpaired electrons. EPR spectroscopy is particularly useful for studying metal complexes, organic radicals and defects of solid-state materials. In quantum mechanics, every electron has a magnetic moment and a spin quantum number of $m_s = \frac{1}{2}$ or $-\frac{1}{2}$, which have the same energy in the absence of any external magnetic fields. While in the presence of an external magnetic field with a strength of B_0, the electron's magnetic moment aligns itself either antiparallel or parallel to the field, which means the original energy state splits to two different energy states, known as the Zeeman effect (Figure 2.3A). The energy of each state can be defined by Equation 2.4:

$$E_{Zeeman} = m_s g_e \mu_B B_0 \qquad \textbf{Equation 2.4}$$

$$\Delta E = g_e \mu_B B_0 \qquad \textbf{Equation 2.5}$$

where E_{Zeeman} is the Zeeman energy; m_s is the spin quantum number; g_e is the electron's ***g***-factor ($g_e = 2.0023$ for the free electron) and μ_B is the Bohr magneton.

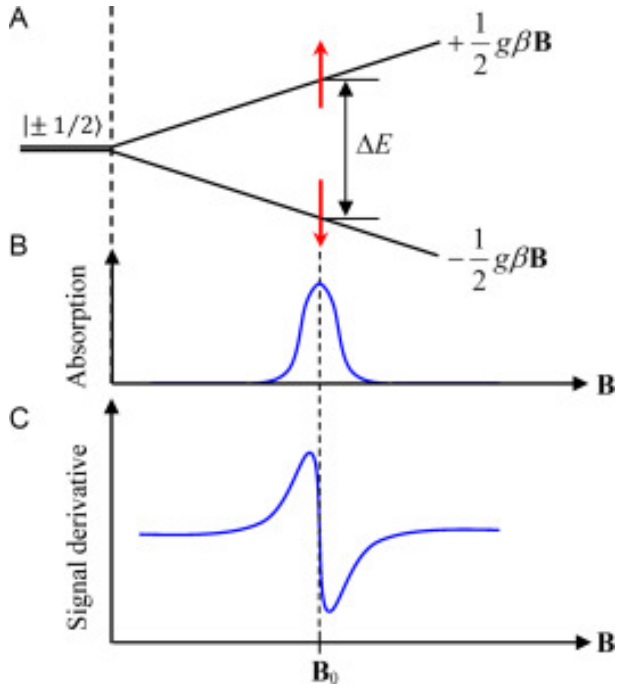

Figure 2.3 (A) Zeeman splitting of the degenerate electronic spin states for an S = 1/2 system. **(B)** An electron can absorb energy to make a transition to the excited state resulting in an EPR absorption line. **(C)** Typical experimental EPR resonance line. The point where the line crosses the baseline determines the resonance magnetic field, , which allows the determination of the ***g***-factor of the system.[23]

Therefore, the energy difference between the lower and the upper state ΔE can be defined as in Equation 2.5 for unpaired free electrons. Clearly, this equation indicates that the energy splitting is directly proportional to the strength of the applied magnetic field. Besides, electrons can change the spin states by either absorbing or emitting a photon of energy, $h\nu$, such that the resonance condition, $h\nu = \Delta E$, is obeyed. This leads to the fundamental equation of EPR spectroscopy:

$$h\nu = g_e \mu_B B_0 \qquad \textbf{Equation 2.6}$$

In actual experiments, the majority of EPR measurements are performed with microwaves in the 9-10 GHz region, with magnetic fields corresponding to around

3500 Gauss (0.35 Tesla). Furthermore, frequency of the microwave is usually kept fixed, and by increasing the strength of the external magnetic field, the energy gap is widened until it matches the energy of the microwaves, as shown in Figure 2.3A. This is when the unpaired electrons can readily transfer between the two spin states. Since there typically are more electrons in the lower state, due to the Maxwell–Boltzmann distribution, there is a net absorption of the microwave, thus the absorption is monitored and recorded into a spectrum (Figure 2.3B). Most commonly, the continuous wave EPR (cw-EPR) spectra are recorded and published as the first derivative of the absorption spectra (Figure 2.3C).

In this thesis, cw-EPR is involved to study the unpaired electron species in the solid-state semiconductor photocatalysts and supports, such as the electrons trapped in surface defects (colour centres) and the *d*-electrons of transition metals. The spectra were collected by an X-band (9.4 GHz) Bruker EMX spectrometer at 293 K. 50 mg powder of each sample was weighed and put into a glass EPR tube (0.60 i.d. and 0.84 o.d.). All X-Band spectra were collected over a field range of 1000 Gauss and 15 scans were taken and averaged for each measurement. Signal intensity vs. electron spin numbers were calculated from the double integration of a defined peak range of the spectra. All measurements were taken in the Centre for Advanced Electron Spin Resonance (CAESR), Department of Chemistry, University of Oxford.

2.2.3 Nuclear magnetic resonance (NMR)

NMR is concerned with the interaction between isolated spin pairs of a target nuclei. NMR is used mainly to investigate the unique features of polar surfaces in this thesis, with the help of organic chemicals as surface probes. Recent studies from our group have shown that the surface features on the exposed polar facets

can be investigated by probe-assisted solid-state NMR (ssNMR) technique.[1,15,24] Among NMR-active basic probes (*e.g.*, ^{13}C, ^{15}N, ^{31}P, *etc.*), ^{31}P nucleus with 100% natural abundance and a wide chemical shift (δ ^{31}P) range over 430 ppm has been proved a sensitive and reliable technique capable of providing both qualitative information (the type, *i.e.*, Brønsted or Lewis acid, and strength of acid sites) and quantitative information (concentration of each site). We have engaged trimethyl phosphine (TMP) and trimethyl phosphine oxide (TMPO) as surface probes in our studies. This is based on the fact that the nucleophilic probe TMP or TMPO molecule can form stable adducts with the exposed Lewis acid (LA) sites (*i.e.*, cations or protons) on the surface. It should be noted that the LA strength is sensitive to its chemical micro-environment and can be influenced by the local electron density, resulting in different binding energies between the surface and the probes. Also, the different binding energies would then lead to different δ ^{31}P of the corresponding surface LA-probe complexes. For example, we recently reported that in the case of TiO_2 nanostructures, stronger interaction between TMP and surface Ti pushes δ ^{31}P toward downfield (*i.e.*, zero ppm), Ti cations on different facets promoted with various surface groups can thus be distinguished by corresponding chemical shifts and analysed quantitatively.[1]

For a nucleus with a spin of one half (*e.g.*, ^{1}H, ^{13}C, ^{15}N, ^{31}P, *etc.*), it has two linearly independent spin states, with $m = \frac{1}{2}$ or $-\frac{1}{2}$, which is also referred to as spin-up and spin-down, respectively. In the absence of a magnetic field, these states have the same energy. Hence the number of nuclei in these two states will be almost equal at thermal equilibrium. If a nucleus is placed in a magnetic field, however, the two spin states no longer have the same energy as a result of the interaction between the nuclear magnetic dipole moment and the external magnetic field:

obviously, the direction of nuclear magnetic dipole moment can be either aligning with the magnetic field or opposing it, resulting in an energy difference (ΔE) between the two spin states that is proportional to the magnetic field strength (Equation 2.7).[25] The effective magnetic moment is affected by the chemical environment of the target nuclei in which electron shielding effect in different extent could result in a variation of chemical shift.

$$\Delta E = \gamma \hbar B_0 \qquad \textbf{Equation 2.7}$$

where γ is the gyromagnetic ratio, $\hbar$ is the reduced Planck constant and B_0 is the strength of the external magnetic field.

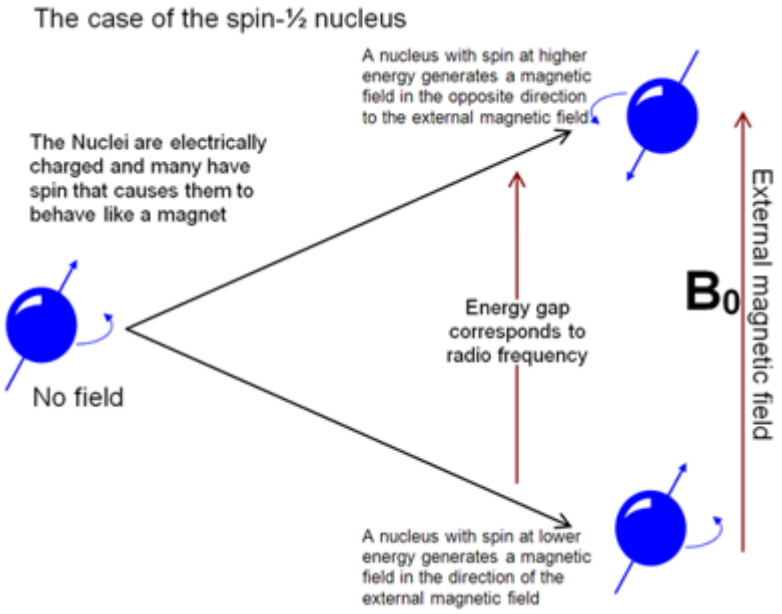

Figure 2.4 Image showing the energy gap between the spin states in which the magnitude has a direct relationship with the chemical shift in NMR. Figure reproduced from ref.[26].

In this thesis, this probe-assisted solid-state NMR was used to characterise the polar-faceted and non-polar metal oxide supports, illustrating the unique physical and chemical properties of the polar surfaces. The ssNMR experiments were carried out using a Bruker Avance III 400WB spectrometer at room temperature for both ^{1}H and ^{31}P nucleus. Particularly, the high-power decoupling (HPDEC) was

thus used for the quantitative ^{31}P analysis. The radiofrequency for decoupling was 59 kHz. The spectral width was 400 ppm, from +200 to −200 ppm. All the ssNMR results in this thesis were obtained by Dr. Guangchao Li and the samples were synthesised by myself.

2.2.4 X-ray photoelectron spectroscopy (XPS)

X-ray photoelectron spectroscopy is a powerful characterisation technique for surface sciences study that can identify the chemical state of a material, providing useful information such as chemical composition, chemical states of elements, state of hybridisation, as well as the bonding environment.[27] In contrast to that in XRD, the beam used for XPS is usually regarded as soft X-ray where the source element is aluminium instead of copper resulting in a much lower photon energy (Al Kα: 1486.7 eV vs Cu Kα: 8047.8 eV). As a result, XPS has high sensitivity for the surface detection, especially for the first few atomic layers given its much lower penetration ability. Theoretically, XPS is based on photoelectric effect where electrons of the target element absorb X-ray photons to be excited and eventually be ejected as photoelectrons where its kinetic energy is measured (Figure 2.5). This relationship is described by Rutherford:

$$E_{binding} = hv - E_{kinetic} - \varphi \qquad \textbf{Equation 2.8}$$

where $E_{binding}$ is the binding energy of the excited electron to the nucleus, h is the Planck constant, v is the frequency of the X-ray radiation, $E_{kinetic}$ is the kinetic energy of the photoelectron, φ is the work function of the spectrometer.

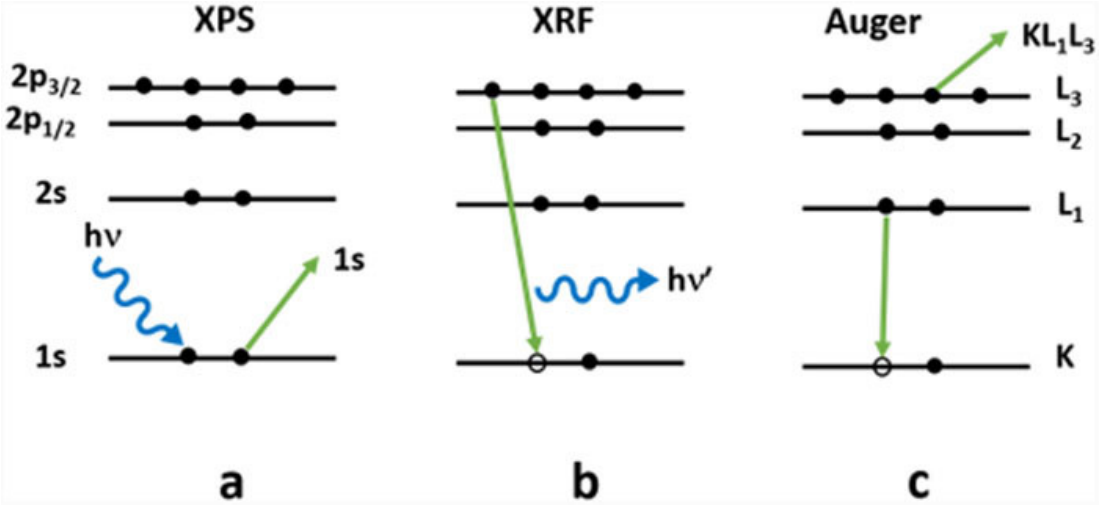

Figure 2.5 Processes that result from x-ray bombardment of a surface include **(a)** emission of a photoelectron, **(b)** x-ray fluorescence, and **(c)** emission of an Auger electron. Reproduced with permission from ref. [27].

Typical lab-sourced X-ray photoelectron spectrometers perform the measurement in an air-tight sample chamber under ultra-high vacuum. This could not only avoid photoelectrons, which have a limited mean free path, from colliding with any gaseous molecules, but also protecting the sensitive microchannel plates in the detectors from moisture.[28] A survey scan for the analysis of elemental composition can be obtained by scanning the binding energy (BE) from 0 eV to 1400 eV. Each of the peak corresponds to the core energy levels of a specific element in which the number of detected electrons is directly related to the elemental composition that could be accurately determined by further incorporating the relative sensitivity factor (RSF).[28] To obtain information of oxidation states, a high-resolution scan can be performed for a specific binding energy range. By comparing the measured BE with the standard BE in the database, information of the change of chemical states can be obtained.

In this thesis, XPS was used mainly to study the chemical states of nitrogen element in the N-doped TiO_2 materials to determine its chemical environment. X-ray photoelectron spectroscopy measurements were performed on a PHI

Quantum-2000 photoelectron spectrometer (Al Kα with 1486.7 eV operating at 15 kV, 35 W and 200 μm spot size) and an Omicron Sphera II hemispherical electron energy analyser. XPS measurements were carried out on the Thermo Scientific model Nexsa. The aluminium anode tube for the X-ray emission was operated at a voltage of 12 kV and kept constant during all measurements. Survey scans were obtained at a pass energy of 200 eV, 5 scans with step size 1 eV, whereas for those detailed spectra 50 eV pass energy, 10 scans with 0.1 eV step size were used. In-situ XPS was carried out in the Diamond Light Source, with the professional assistance from Dr. Alexander Large and Prof. Georg Held.

2.2.5 Ultraviolet-visible diffuse reflectance spectroscopy (UV-Vis DRS)

UV-Vis DRS is complementary to UV-Vis absorption spectroscopy, which is more frequently used when studying the light absorption properties of solid-state semiconductor materials. Unlike the conventional UV-Vis absorption spectroscopy, where the transmission of light is measured, UV-Vis DRS records the remission (includes both specular reflection and diffusely back-scattered light) by a material. Experimentally, appropriate light sources are used to provide the ultraviolet light, visible light or near infrared light irradiation, and the reflectance of the light is recorded against the wavelength of the light irradiation. This technique is very useful when determining the band gap of semiconductor materials. To achieve this, the reflectance spectra are firstly converted by Kubelka-Munk equation:

$$F(R_\infty) = \frac{(1 - R_\infty)^2}{2R_\infty} = \frac{K}{S} \qquad \textbf{Equation 2.9}$$

where R_∞ is the remission fraction of an infinitely thick layer; *K* and *S* are the absorption and back-scattering coefficients, respectively.

Moreover, Tauc proposed a method of estimating the band gap energy of

semiconductors using optical absorption spectra, which was further developed by Davis and Mott.[29] The Tauc method is based on the assumption that the energy-dependent absorption coefficient can be expressed by the following equation:

$$(\alpha h\nu)^{\frac{1}{\gamma}} = B(h\nu - E_g) \qquad \textbf{Equation 2.10}$$

Where α is the absorption coefficient, h is the Planck constant, ν is the photon's frequency, E_g is the band gap energy, and B is a constant. The γ factor depends on the nature of the electron transition and is equal to $\frac{1}{2}$ or 2 for the direct and indirect transition band gaps, respectively.[29]

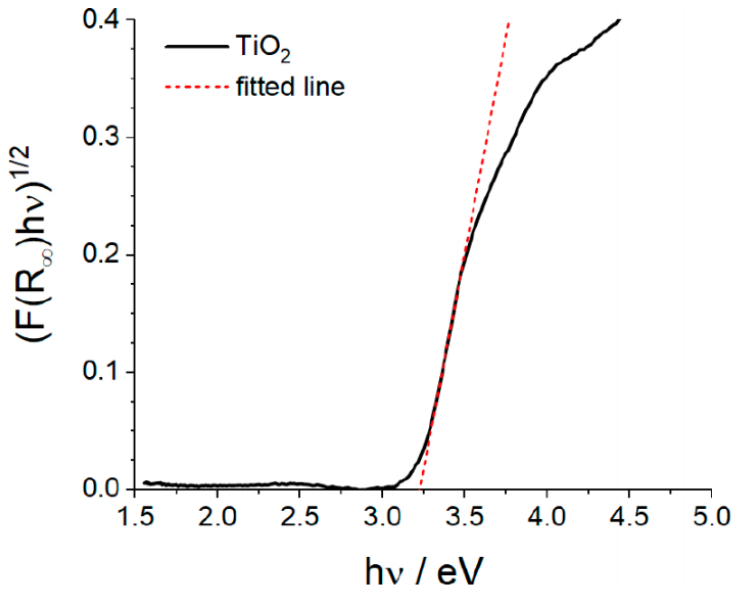

Figure 2.6 Method of band gap energy (E_g) determination from the Tauc plot. The linear part of the plot is extrapolated to the x-axis.[29]

In the case of solid-state semiconductors, where UV-Vis DR spectra are collected rather than absorption spectra, as mentioned above, the measured reflectance spectra can be transformed to the corresponding absorption spectra by Equation 2.9, and $F(R_\infty)$ is put into the Equation 2.10 instead of α. Then $(F(R_\infty)h\nu)^{\frac{1}{\gamma}}$ is plotted against $h\nu$, as shown in Figure 2.6. The region showing a steep, linear

increase of light absorption with increasing energy is characteristic of semiconductor materials. The x-axis intersection point of the linear fit of the Tauc plot gives an estimated band gap energy.

UV-Vis DR spectra were obtained from a Perkin Elmer Lambda 750S UV-visible spectrometer at room temperature (equipment provided by the Chemistry Teaching Laboratory, University of Oxford). 50±5 mg of each sample was loaded and pressed onto a sample holder and UV-Vis spectra were recorded within the wavelength range of 200-1500 nm.

2.2.6 Raman spectroscopy

Raman spectroscopy is a widely used characterisation technique typically used to determine vibrational modes of molecules and solid-state materials, which can provide a structural fingerprint by which the chemical species can be identified. Raman spectroscopy depends on inelastic scattering of photons, which is known as Raman scattering, where a photon excites the sample. The name of *Raman Spectroscopy* typically refers to vibrational Raman using laser wavelengths which are not absorbed by the sample. A source of monochromatic laser in the visible, near infrared, or near ultraviolet regime is normally used. It should be noted that the magnitude of the Raman scattering correlates with polarizability of the electrons in a system. The Raman Effect is based on the interaction between the electron cloud of a sample and the external electric field of the monochromatic light, which can create an induced dipole moment within the molecule based on its polarizability. The photon excitation puts the system into a virtual energy state for a short time before the photon is emitted. After the Raman scattering event, the sample is in a different rotational or vibrational state, which means the energy of the emitted photon is of either lower or higher energy than the original incident

photon in order to keep the total energy the same. This energy difference is equal to that between the initial and final rovibronic states of the studied sample. If the final state is higher in energy than the initial state, the scattered photon will be shifted to a lower frequency (lower energy). This shift in frequency is called a Stokes shift, or downshift. If the final state is lower in energy, the scattered photon will be shifted to a higher frequency, which is called an anti-Stokes shift, or upshift. The shifts in photon energy offer information about the vibrational modes in the system. Raman shifts are typically recorded in wavenumbers ($\tilde{\nu}$), which have units of inverse length (cm^{-1}), as this value is directly related to energy. In order to convert between spectral wavelength and wavenumbers of shift in the Raman spectrum, the following formula can be used:

$$\Delta\tilde{\nu} = \frac{1}{\lambda_0} - \frac{1}{\lambda_1} \qquad \textbf{Equation 2.11}$$

For a molecular system to exhibit the Raman effect, there must be a change in its polarizability with respect to the vibrational coordinate corresponding to the rovibronic state. Thus, Raman spectroscopy is considered as a complementary technique to infrared spectroscopy. In this thesis, Raman spectra were recorded on a Perkin Elmer Raman Station 400 F spectroscopy system with a laser excitation of 532 nm (equipment provided by the Chemistry Teaching Laboratory, University of Oxford). Samples were exposed for 10 seconds for each scan and 8 scans were adopted for each measurement.

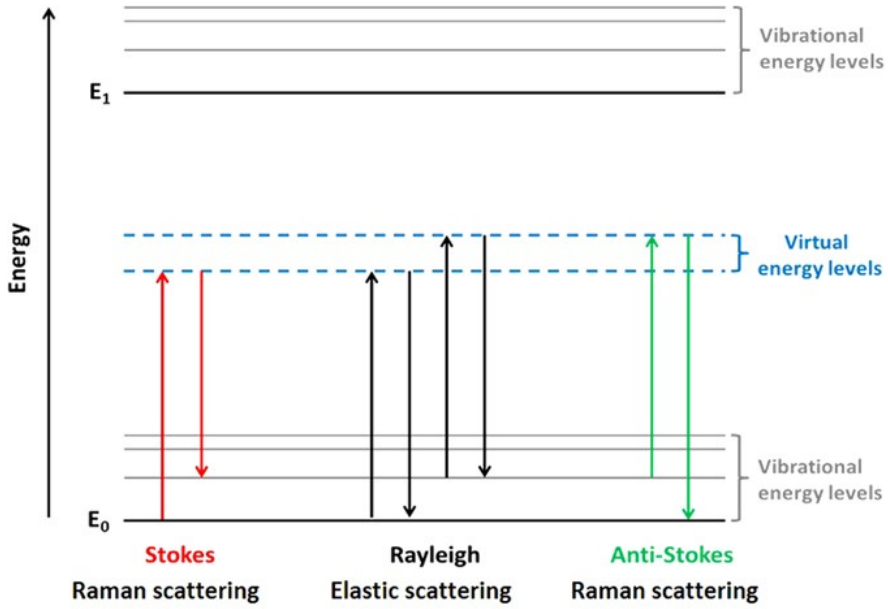

Figure 2.7 "Jablonski" style diagram of energetic transitions involved in Raman scattering. Rayleigh scattering is elastic: the incident photon is of the same energy as the scattered photon. Raman scattering is inelastic; in Stokes scattering, the incident photon is of greater energy than the scattered photon, while in anti-Stokes scattering, the incident photon is of lower energy.[30]

2.2.7 Time-resolved photoluminescence (TRPL) spectroscopy

PL is a light emission phenomenon from any form of matter after the absorption of photons (electromagnetic radiation). Upon absorption of photons, photoexcitation takes place: electrons are excited to a higher energy level from a lower level in an atom by the absorbed photons. The excited electrons will subsequently go through relaxation processes and recombination. Radiative recombination will then give photoluminescence where photons are emitted. Thus, PL spectroscopy is of great importance to studying the electron transition behaviours in semiconductor materials.

In this thesis, all the PL measurements were performed under a non-resonant excitation condition, where the samples are excited with some excess energy. This is also the typical situation used in most PL experiments in literature, because the excitation beam can be easily discriminated using an optical filter. After excitation,

the laser photons induce a coherent polarisation in the sample (*i.e.*, the transitions between electron and hole states oscillate with the laser frequency and a fixed phase). Such polarisation de-phases typically within 100 fs in case of non-resonant excitation due to ultra-fast Coulomb- and phonon-scattering.[31] Subsequently, the dephasing leads to creation of populations of electrons and holes in the conduction band (CB) and the valence band (VB), respectively. During this lifetime a fraction of electrons and holes may form excitons, depending on the intrinsic properties of the material, and also the experimental conditions, such as lattice temperature, excitation density, as well as on the intrinsic material parameters. In the first a few hundreds of femtoseconds after excitation, the charge carriers are scattered by phonons, or at elevated carrier densities via Coulomb-interaction. The carrier system successively relaxes to the Fermi–Dirac distribution typically within the first picosecond. Finally, the carrier system cools down under the emission of phonons (optical phonons and/or acoustic phonons). This can take up to several nanoseconds, depending on the material system, the lattice temperature, and the excitation conditions such as the surplus energy. Obviously, the charge carriers lose some energy during the relaxation processes, resulting in the electrons appearing near the conduction band minima (CBM) and holes near the valence band maxima (VBM). Then the electrons and holes may undergo the radiative recombination to give PL or non-radiative recombination pathways, such as Auger recombination. Time periods between absorption and PL emission vary with the fundamental processes that the charge carriers undergo, ranging from short femtosecond-regime to milliseconds for phosphorescence processes. In special circumstances, delay of emission may even span to minutes. Therefore, measuring the decay in PL may give information about the electron transition

processes in a sample material. TRPL is such a method where the sample is excited with a laser pulse and then the decay in PL with respect to time is measured. This technique is useful for measuring the minority carrier lifetime of semiconductors.

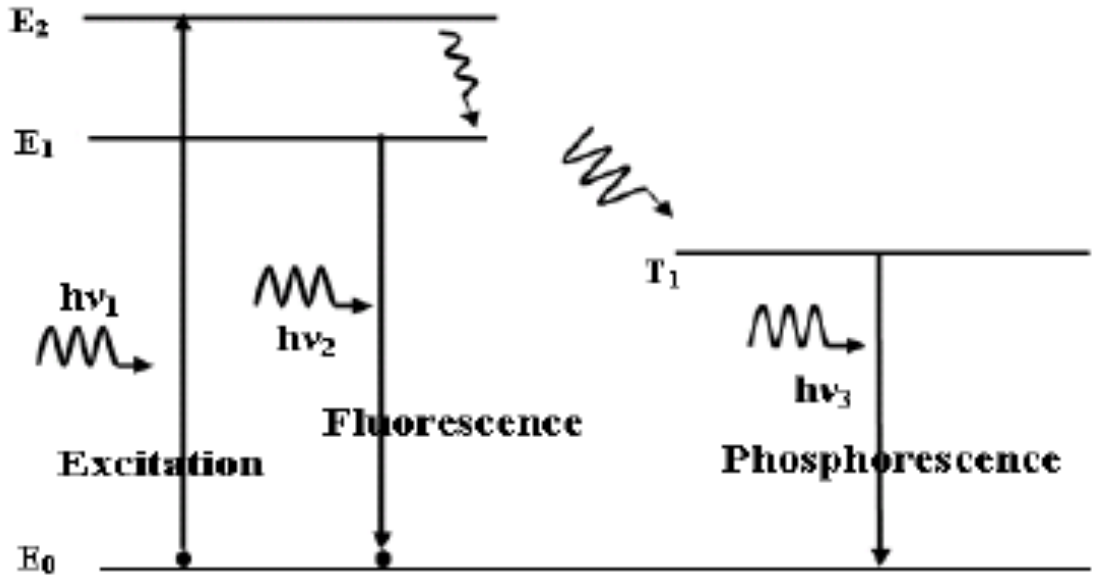

Figure 2.8 Energy diagram showing light absorption and the processes involved in the photoluminescence.[32]

In this thesis, TRPL was involved to study the change of charge carrier lifetime of the photocatalysts, which indicated the effect of local fields on the charge separation processes of the semiconductor materials. Typically, the PL spectra and the corresponding lifetime of the photo-generated charge carriers were obtained from a bespoke micro-photoluminescence setup, in which a Ti-Sapphire laser (λ = 266 nm, pulse duration = 150 fs, repetition rate = 76 MHz) is directed onto the sample. The diameter of the laser spot on the sample was *ca.* 200 micron, and the laser output power was tuned at 2 mW. It should be clarified that this results in a power density of 5000 mW cm^{-2}, which is 50 times of the power density of solar light. Time-resolved measurements are performed using the spectrometer as a monochromator before passing the selected signal to a photomultiplier tube

(PMT) detector with an instrument response function width of ~150 ps connected to a time-correlated single-photon counting module. The TRPL measurements were carried out under a pulse-picking mode: the recorded signals were selected using a pulse picker to ensure that the consecutive recorded signals had a long-enough delay (*ca.* 100 ns) to allow the excited charge carriers to decay to the ground states, therefore avoiding the accumulation of charge carriers. The charge carrier lifetime is obtained by fitting the corresponding background-corrected PL spectrum with a mono- or bi-exponential decay function (mono- or bi-exponential decay means there is/are one or two kinds of recombination rate(s) of the charge carriers), as shown in Equation 2.12.:

Mono- $$y = A_1 e^{-t/\tau_1} + y_0$$

Bi- $$y = A_1 e^{-t/\tau_1} + A_2 e^{-t/\tau_2} + y_0$$ **Equation 2.12**

where A_1, A_2, τ_1 and τ_2 are the fitting parameters and y_0 is a constant.

The TRPL measurements were performed in the Department of Physics, University of Oxford, where I have been working as a visiting student, supervised by Prof. Robert A. Taylor. Professional assistance was kindly offered by Dr. Timothy Putchler, Dr. Mo Li and Vitaly Osokin.

2.2.8 Transmission electron microscopy (TEM)

It is widely accepted that the catalytic performance is closely related to the shape and morphology of the catalyst and the catalytic support[14,33,34]. Therefore, researchers have been making great efforts in visualising and imaging the materials with high resolution in order to rationally design functional catalysts. In contrast to the standard light microscopy which is limited by the Abbe resolution of 1 μm set by the wavelength of visible light (Equation 2.13), transmission electron

microscopes (TEM) use transmission electron beam of which the de Broglie wavelength is significantly smaller than that of visible light[35]. The operation energy of TEM ranges from 100 to 200 keV, which is corresponding to an electron beam with wavelength from 2.5 to 3.7 pm, offering a resolution of 0.3 nm. Moreover, the wavelength of the electrons can be tuned even smaller in order to obtain a higher resolution (at the risk of damaging the samples due to higher applied voltage).[36] On the other hand, additional detectors could be equipped to the TEM, which would offer simultaneous acquisition of information on elemental composition (Energy Dispersion X-ray spectroscopy, EDX or EDS) and electronic structure (Auger electrons) in addition to the microscopic imaging.

$$d = \frac{\lambda}{2n\,sin\theta} \qquad \textbf{Equation 2.13}$$

where d is the feature size, λ is the wavelength of light, n is the refraction index of the medium, and θ is the half-angle subtended by the objective lens.

Typically, the measurements take place in an ultra-high vacuum (10^{-6} mbar) chamber to avoid inelastic collision of electrons with any surrounding gaseous molecules that would lead to the deviation of pathway of the electron beam. The transmitted electrons will then interact with the sample in an extent according to the electron density of different atomic species, which are then refocused, magnified and projected onto a fluorescent screen. Following this, a charge coupled device is used to convert the beam into digital signals for imaging.

Transmission electron microscopes can be operated in 2 modes, *i.e.*, bright field and dark field. For the bright field measurements, the transmitted electron beam is captured by the aperture and the scattered electrons are blocked. As a result, materials with high mass (or high electron density) with appear darker whereas

the background appears bright. On the other hand, in dark field mode, scattered electrons are selected with the aperture instead, which means the background, where electrons can directly transmitted through, will be black out while the material of interest will appear bright depending on the electron density.[37] The dark field mode is important when the contrast between the background and sample is low, especially when the nanoparticles are small in size and drowned by the background.

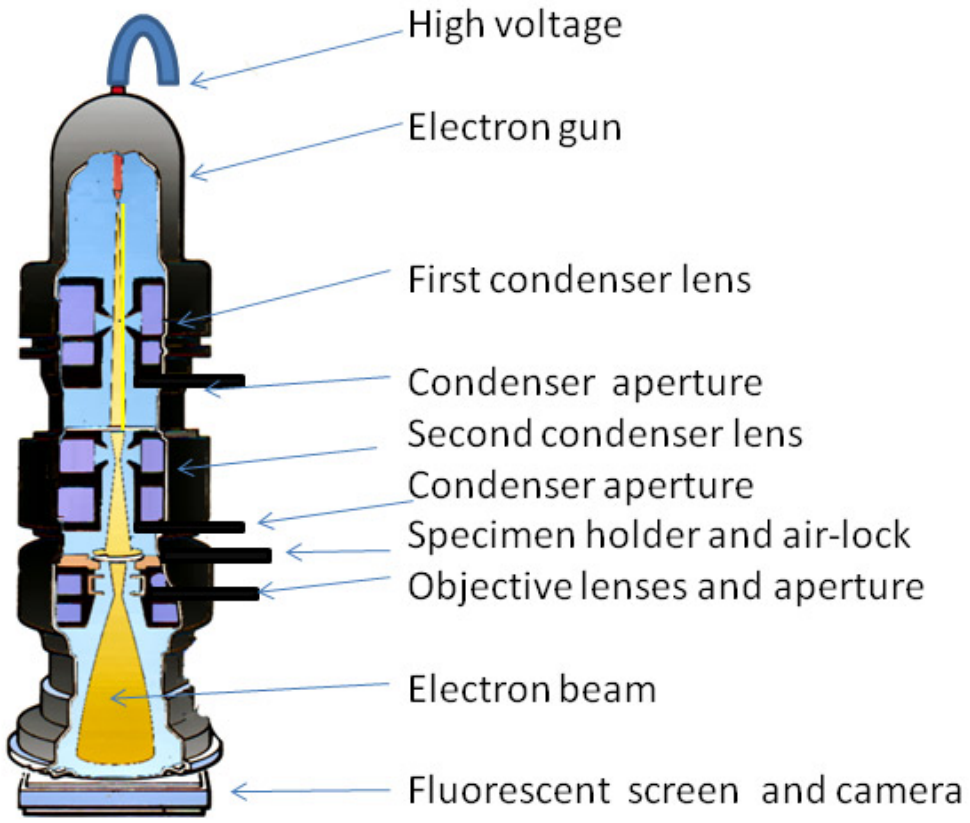

Figure 2.9 Image showing the principal components of a transmission electron microscope (TEM). Figure reproduced from ref. [37].

In this thesis, TEM was used to image the morphology of the photocatalysts and catalyst supports. More discussions will be given in the following chapters. In this thesis, the morphologies and microstructures of the photocatalysts were examined by high-resolution TEM (HRTEM) using a JEOL 3000F microscope operated at

300 kV. TEM specimens were prepared by pipetting 5 μL of the sample dispersion in ethanol onto holey carbon-coated copper mesh grids (400 meshes). TEM images in this thesis were obtained by Dr. Tianyi Chen in the Department of Materials, University of Oxford.

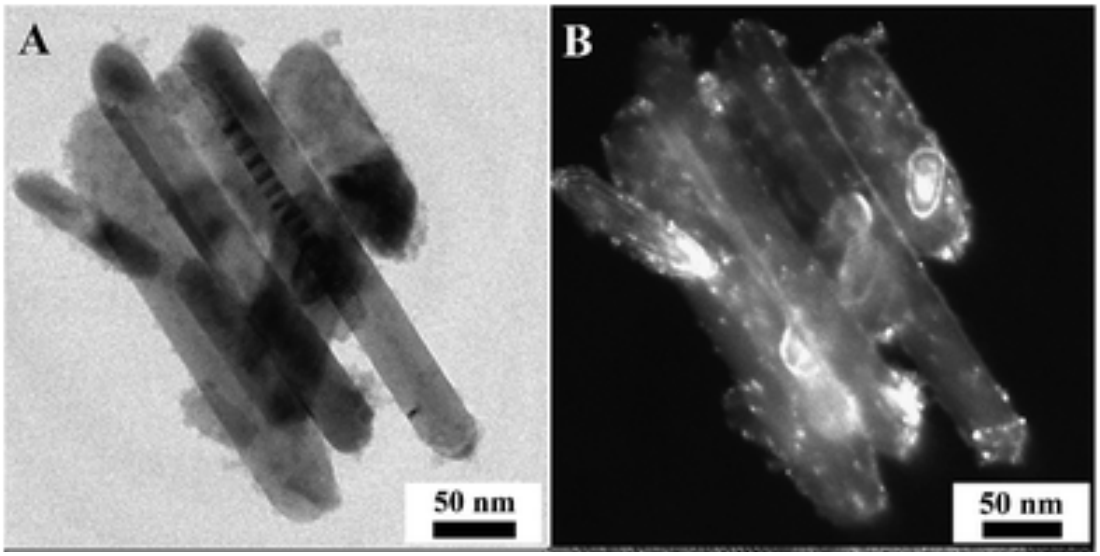

Figure 2.10 Images demonstrating the difference in image when operated in **(A)** bright field mode and **(B)** dark field mode. Figure reproduced from ref. [38].

2.2.9 Scanning transmission electron microscopy (STEM)

Like TEM, high angle annular dark field-scanning transmission electron microscopy (HAADF-STEM) operates via transmission of an electron beam through the sample material. Instead of using an aperture to select the electron beam, STEM is equipped with a condenser lens to converge electron beam to an ultra-fine spot of 0.05 – 0.2 nm, which is then rastered across the sample by a scanning coil.[39] An annular dark field (ADF) detector is then used to capture the scattered electrons and exclude the unscattered electrons at a high angle (> 5^{o}) via the dark field imaging mode. As described above, the scattered electrons (sample material of interest) appear bright while the transmitted ones (background with no scattering occurred) appear black under this mode.

HAADF-STEM is especially significant in imaging materials with high electron density, for instance metal nanoparticles. In conventional catalysis, catalyst materials are usually composed of transition metal (TM) active centre supported on inorganic oxides where HAADF-STEM serves as an ideal technique to image the TM as very bright spots with the lightly-coloured support in the background. However, in the case that the active centre and the catalyst support both contain TMs, the contrast between them could be negligible, thus, they can hardly be differentiated from each other. In such cases, electron energy loss spectroscopy (EELS) is usually simultaneously acquired to give the unique absorption edge of a particular metal, thus, the chemical species of different TMs can be confirmed.[39]

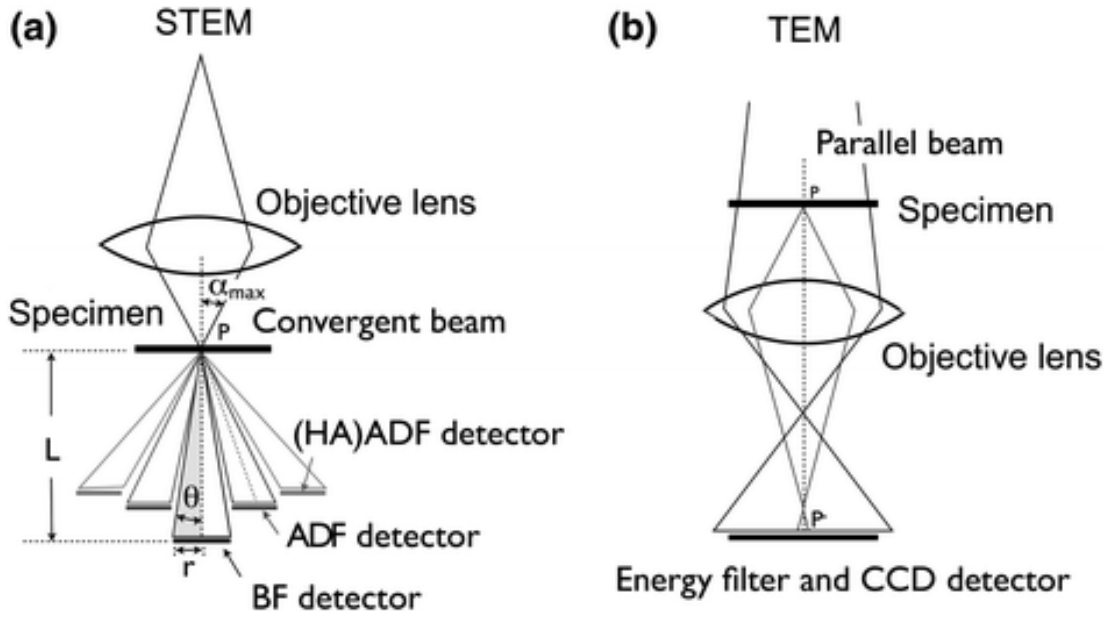

Figure 2.11 Schematic illustration of the differences in configuration and detectors between **(a)** STEM and **(b)** TEM. Reproduced with permission from ref. [40].

In this thesis, HAADF-STEM and EELS were performed respectively to showcase the atomic dispersion of Ru species supported on the 2D MoS_2 monolayers. The sharp contrast of Ru appearing as a very bright spot compared to the MoS_2 background indicated the clear observation of the atomic positions of Ru. HAADF-STEM samples were ground and coated onto a holey carbon coated Cu TEM grid.

The analysis was performed on the JEOL-JEM2100 Aberration-Corrected Transmission Electron Microscope using the following instrumental conditions: Voltage 200 kV; Dark-field (Z-contrast) imaging in scanning mode using an off-axis annular detector and capable of atomic-resolution imaging. Professional assistance was kindly offered by Zihan Wang, Dr. Songhua Cai, Prof. Rafal E. Dunin-Borkowski and Dr. András Kovács.

2.2.10 Gas chromatography (GC)

In this thesis, the gaseous products of the photocatalytic water splitting reaction were separated and analysed in GC equipped with thermal conductivity detectors (TCD) using He and N_2 as carrier gases. In a typical GC analysis, a known volume of gaseous or liquid analyte is injected through a rubber disk and into a hot, temperature-controlled port attached to the column. As the carrier gas transports the analyte molecules through the column, there is adsorption of the analyte molecules either onto the column walls or onto packing materials (stationary phase) in the column to give separation. Since each type of molecule has a different rate of progression, the various components of the analyte mixture are separated as they progress along the stationary phase and reach the end of the column at different times (retention time). A detector is used to monitor the time at which each component reaches the outlet and ultimately the amount of that component can be determined. Generally, substances are identified (qualitatively) by the order in which they elute from the column and by the retention time of the analyte in the column. Other parameters that can be used to alter the order or time of retention are the carrier gas flow rate, column length and the temperature.

2.2.11 Superconducting quantum interference device (SQUID)

In my DPhil project, the magnetic field effects on the photocatalytic performance were investigated, therefore, static magnetic properties of the solid-state semiconductor photocatalysts were studied by SQUID magnetometer. Taking ferromagnetic materials such as iron as an example, the atomic dipoles align themselves when an external magnetic field is applied. However, when the external field is removed, some of the alignment will be retained: the material has become magnetised. To demagnetise the material, it requires heat or a magnetic field in the opposite direction. Such phenomenon is known as magnetic hysteresis. Due to the magnetic hysteresis, the field strength ***H*** is not in a linear relationship with magnetisation ***M*** in such materials. If the relationship between ***H*** and ***M*** is plotted for increasing levels of field strength, ***M*** follows the initial magnetisation curve, which increases rapidly at first and then approaches an asymptote called magnetic saturation. If the magnetic field is now reduced monotonically, M follows a different curve. At zero field strength, the magnetisation is offset from the origin by an amount called the remanence. If the ***M***-***H*** curve is plotted for all strengths of applied magnetic field, we will obtain a hysteresis loop called the main loop, as shown in Figure 2.12. The width of the middle section along the ***H*** axis is twice the coercivity of the material (Coercivity is a measure of the ability of a ferromagnetic material to withstand an external magnetic field without becoming demagnetised).[41] Magnetic hysteresis loops are not exclusive to materials with ferromagnetic ordering. Other materials also exhibit this phenomenon, such as paramagnetic and superparamagnetic materials, which show different characteristic hysteresis loops (Figure 2.12).[42] The phenomenon of hysteresis is considered as the result of two effects: rotation of magnetisation and changes in

size or number of magnetic domains. In a single-domain magnet, the magnetisation responds to a magnetic field by rotating. Larger material can be divided into lots of magnetic domains. Within each domain, the magnetisation does not vary in direction or magnitude; but in the thin domain walls between domains, the direction of magnetisation rotates from the direction of one domain to another. If the magnetic field changes, the walls move, changing the relative sizes of the domains.

In this thesis, the materials used can be mainly classified as paramagnetic, superparamagnetic, ferromagnetic, and diamagnetic materials. Diamagnetism appears in all materials and is the tendency of a material to oppose an applied magnetic field. Paramagnetic materials contain unpaired electrons. An unpaired electron can align its magnetic moment in any direction. When an external magnetic field is applied, these magnetic moments will tend to align themselves in the same direction as the applied field, thus reinforcing it. Ferromagnetic materials also have unpaired electrons. However, in addition to the electrons' tendency to align their magnetic moments parallelly to an applied field, there is also a tendency for these magnetic moments to align parallelly to each other to maintain a low-energy state. Thus, even in the absence of an applied field, the magnetic moments of the electrons in the material spontaneously line up parallel to one another. When a ferromagnetic material is sufficiently small, it acts like a single magnetic spin that is subject to Brownian motion. Therefore, its response to a magnetic field is qualitatively similar to the response of a paramagnetic material, but much larger. These materials are known as superparamagnetic materials.

When measuring the magnetisation properties, in general, the sample material is placed in a varying external ***H*** field, as induced by an electromagnet, and the

resulting magnetic flux density (***B*** field) is measured, generally by the inductive electromotive force introduced on a pickup coil nearby the sample. This produces the characteristic ***B*-*H*** curve; because the hysteresis indicates a memory effect of the magnetic material, the shape of the ***B*-*H*** curve depends on the history of changes in ***H***. Alternatively, the hysteresis can be plotted as magnetisation ***M*** in place of ***B***, giving an ***M*-*H*** curve. These two curves are directly related, which can be converted by Equation 2.14:

$$\boldsymbol{B} = \mu_0(\boldsymbol{H} + \boldsymbol{M}) \qquad \textbf{Equation 2.14}$$

where μ_0 is magnetic permeability.

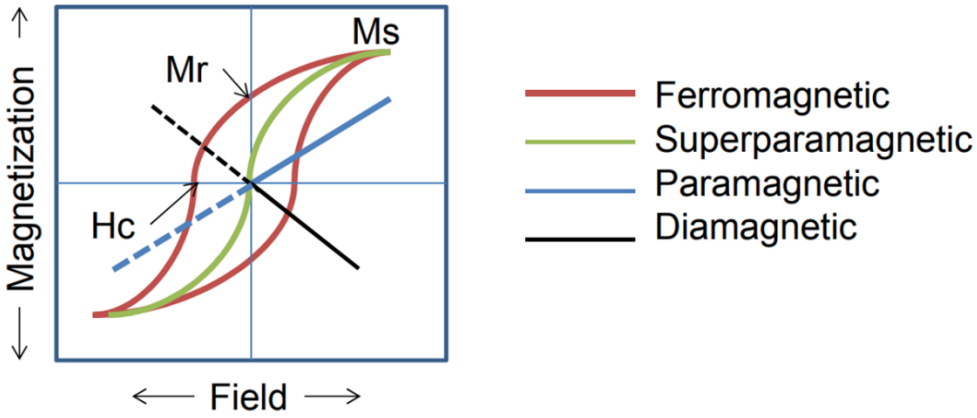

Figure 2.12 Characteristic hysteresis loops of different magnetic orderings.[43]

In this thesis, the magnetisation curves were obtained on a superconducting quantum interference device (SQUID, Quantum Design MPMS-XL-5), which is a very sensitive magnetometer used to measure extremely subtle magnetic fields, based on superconducting loops containing Josephson junctions (The Josephson effect occurs when two superconductors are placed in proximity, with some barrier or restriction between them. It produces a supercurrent that flows continuously without any voltage applied, across a device known as a Josephson junction).[44] More details are discussed in the following chapters. SQUID measurements

shown in Chapter 5 were kindly carried out by Zihan Wang and Prof. Chen Wu in Zhejiang University, P. R. China.

2.3 Catalytic testing

2.3.1 Photocatalytic overall water splitting (POWS) activity tests

Figure 2.13 Photocatalytic batch reactor for the POWS reaction at elevated temperatures used in this thesis.

The POWS reaction was carried out in a 25-mL stainless steel batch reactor equipped with two quartz windows with an illuminated area of 0.785 cm^2 (10 mm in diameter and 18 mm in thickness each, images shown in Figure 2.13). In a typical experiment, 5 mg of catalyst was added to 5 mL of aqueous solution (pure water, artificial seawater or natural seawater) in a glass lining (20 mm i.d. × 24 mm o.d. × 52 mm height) under magnetic stirring (750 rpm) as a particulate suspension, then the batch reactor was purged with continuous Ar gas flow for 5 min after well-sealed to remove the dissolved O_2 in water. Then the batch reactor was pressurised with 6 bar of inert Ar gas. The reactor would then be allowed to heat up to the required elevated temperature with its saturated water vapour pressure (*e.g.*, *ca.* 60 bar at 270 ^oC).

The use of water vapour at low pressure was also studied instead of the liquid

water at its saturated pressure. The photocatalytic activity was determined by measuring the amounts of H_2 and O_2 evolved. Reactions were carried out in the same windowed batch reactor, but the photocatalyst was first deposited onto a glass slide and put into the batch reactor, facing towards the light irradiation path through the silica window. A fixed amount of water was added into the batch reactor at room temperature. This amount of water was calculated to generate the required pressure when totally vaporised at 270 ^oC. As a result, variable pressures of water vapour were established below the saturated pressure of water at 270 ^oC. After the addition of water, the reactor was allowed to reach the designated temperature.

Tungsten light (70 W, Glamox Professional 2000) or VeraSol solar simulator (AM 1.5G, 100 mW cm^{-2}) was then used to provide the irradiation through the silica windows when the reactor reached the required temperature. After a 2-hour reaction, the batch reactor was cooled down naturally to room temperature.

The amounts of O_2 and H_2 were measured by a gas chromatograph (GC) equipped with two thermoconductivity detectors (TCDs) with He and N_2 as carrier gas, respectively, for better sensitivity of each gas. The gaseous product was sampled by a 0.25-mL Ni sampling loop, and the separation of gaseous components were completed in Agilent J&W CP-Molsieve 5Å columns. The gaseous sample was brought into the GC by the inner pressure of the batch reactor, and the sampling loop is connected to the atmosphere so the pressure inside the sampling loop was considered as 1 atm. GC analysis was also carried out before reactions to make sure the air and dissolved O_2 were completed removed. The GC signals were calibrated by external standard quantitation, so that the concentrations (in percentage) of H_2 and O_2 could be calculated from the corresponding peak area. The pressurised gas in the reactor was released to a balloon, of which the volume

was measured using a water drainage method, thus, the total volume of gas at 1 bar and room temperature could be obtained. Finally, amounts of the generated H_2 and O_2 were calculated using the ideal gas law.

2.3.2 Photocatalytic activity tests with light furnace

The photocatalytic water splitting reaction was also investigated in a light furnace, in which light was the only energy source, and no electrical heating device was engaged. Conditions were the same as those for the typical photocatalytic water splitting activity test previously mentioned. However, the light source was generated by a four-mirror floating-zone light furnace (Operated at 66.7 V, 15.58 A and 1039 W) from Crystal Systems Inc. equipped with four halogen lamps to mimic a solar concentrator: the concentrated light was applied through the quartz windows to heat the batch reactor to 270^{o}C at saturated equilibrium pressure of water and at the same time irradiated photocatalyst. After 2 h, the reactor was cooled down naturally and the amounts of H_2 and O_2 were measured by GC equipped with TCDs.

2.3.3 Quantum efficiency (QE) measurements and calculation

Apparent quantum efficiency was measured in the same batch reactor and conditions were kept the same as those for a typical POWS test, while the batch reactor was then irradiated by a 300 W Xenon lamp (Newport) using different bandpass filters (UV-Vis spectra of the filters are given in Figure 2.14). The power of light was measured using a standard photodiode power sensor (Thorlabs S121C), which had been calibrated by Thorlabs before it was delivered, thus it was used without further calibration. Then the number of photons was calculated from the measured power at each wavelength. The apparent QE can be calculated

using Equation 2.15.

$$QE\ (\%) = \frac{Number\ of\ H_2\ molecules \times 2}{Number\ of\ incident\ photons} \times 100\% \qquad \textbf{Equation 2.15}$$

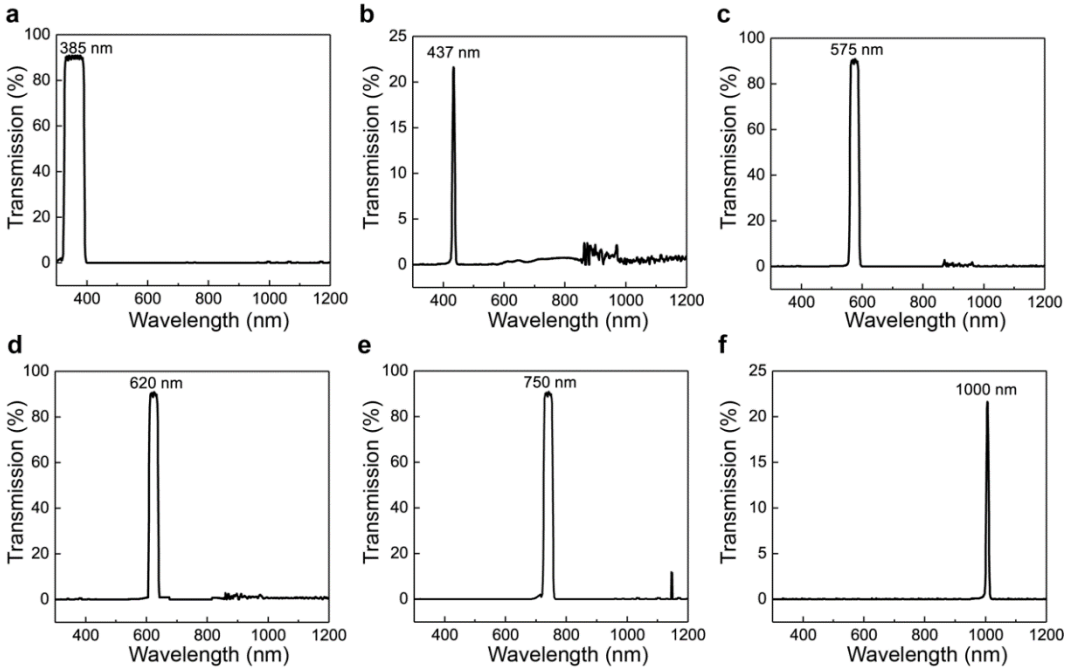

Figure 2.14 UV-Vis transmission spectra of the bandpass filters which were used in QE measurements.

An example is given below, taking Fe_3O_4/N-TiO_2-4 as an example (demonstrated in Chapter 5, and more details are given in Appendix Note 1):

For the measurement of the QE of the Fe_3O_4/N-TiO_2-4 photocatalyst at 437 nm, the H_2 amount analysed by GC is 5.25 μmol in the 2-hour experiment, corresponding to 3.159×10^{18} H_2 molecules ($N = n \times N_A$). During the period of 2 hours, the energy of the light irradiation: $W=P\times t$. With the bandpass filter of 437 nm, the light irradiation power was measured to be P = 0.45 mW at the centre of the batch reactor (the power of light was measured using a Thorlabs S121C standard photodiode power sensor, which had been calibrated by Thorlabs before it was delivered, and was used without further calibration), therefore, the energy W = 0.00045 × 7200 = 3.24 J, which contains the photon (437 nm) numbers of

7.123×10^{18} ($\varepsilon = h\nu$). Then, the QE can be calculated using Equation 2.15.

$$\text{QE (\%)} = (2\times3.159\times10^{18})/ (7.123\times10^{18}) \times100\% = 88.7\ \%$$

All the QE values in this thesis are calculated likewise. The irradiation power measured in the centre of the batch reactor at each wavelength is summarised in Table 2.1.

Table 2.1 Irradiation power measured in the centre of the batch reactor using the bandpass filters at different wavelengths. A 300-W Xe arc lamp was used as the light source, and the power was measured using a Thorlabs S121C standard photodiode power sensor

Wavelength (nm)	**Power (mW)**
385	1.03
437	0.45
575	1.21
620	5.07
750	3.11
1000	1.07

2.3.4 Solar-to-hydrogen (STH) efficiency measurements and calculation

The η_{STH} was measured with a similar procedure: the POWS performance was evaluated by adding a certain amount (typically 20 mg of the TiO_2-based photocatalyst unless specified otherwise) of photocatalyst which contained 20 mg of N-TiO_2 to 5 mL of Milli-Q H_2O under vigorous magnetic stirring (600 rpm), then the suspension was irradiated by a VeraSol solar simulator (AM 1.5G, 100 mW cm^{-2}, 1 sun). The amounts of H_2 and O_2 were measured by a GC equipped with TCDs. The η_{STH} can then be calculated by the following equation:

$$STH\ (\%) = \frac{Evolved\ H_2\ amount \times \Delta G}{P \times S \times t} \times 100\% \qquad \textbf{Equation 2.16}$$

where P is the power of solar irradiation (0.1 W cm^{-2}), S is the illuminating area in square centimetres; t is the time of reaction in seconds; ΔG is the Gibbs free

energy for the POWS reaction under the reaction conditions; the evolved H_2 amount is typically given in moles.

2.4 Density functional theory (DFT) calculations

In Chapter 6, all spin-polarised DFT calculations were carried out using the Vienna *ab-initio* Simulation Package (VASP).[45] Electronic exchange and correlation were treated within the generalised gradient approximation (GGA) by using the Perdew-Burke-Ernzerhof (PBE) functional.[46] The projector-augmented wave (PAW) method [47] with an energy cut-off of 400 eV was employed to describe the interactions between the core and valence electrons with the Ti (3*s*, 3*p*, 3*d*, 4*s*), O (2*s*, 2*p*), N (2*s*, 2*p*), Na (3*s*), Mg (3*s*), Al (3*s*, 3*p*), K (3*s*, 3*p*, 4*s*), Ca (3*s*, 3*p*, 4*s*), P (3*s*, 3*p*), S (3*s*, 3*p*) and Cl (3*s*, 3*p*) shells being treated as valence electrons. For all the calculations, we applied the on-site Coulomb interaction correction with an effective *U* value of 4.2 eV on the Ti 3*d* orbitals to describe the localised electronic states accurately.[48,49]

The N-doped anatase TiO_2(101) and the N-doped reconstructed anatase TiO_2(001)-(1×4) surfaces were constructed.[50] The former surface was extended at a (2×2) cell, and the slab contains four TiO_2 layers; a 2 × 3 × 1 *k*-point mesh was used for the calculations. The latter surface was extended at a (2×1) cell, and the slab contains eight TiO_2 layers; a 3 × 2 × 1 *k*-point mesh was used for the calculations. We set a vacuum layer of ~15 Å to avoid interactions between neighbouring slabs. Geometry optimisations were converged when the Hellman-Feynman forces of relaxed atoms are less than 0.02 eV $Å^{-1}$. The relative energies of the different N-doped TiO_2(101) and N-doped TiO_2(001)-(1×4) surfaces were calculated to locate the corresponding most favourable doping site of N.

In order to consider ion adsorption and to simulate photo-electron/hole in the system, the correct number of electrons of such system was controlled by the NELECT parameter, which is a common practice reported in the literature.[51,52]

The adsorption energy (E_{ads}) was calculated according to:

$$E_{\mathrm{ads}} = (E_{\mathrm{anion/001}} - E_{\mathrm{anion/water}}) + (E_{\mathrm{cation/101}} - E_{\mathrm{cation/water}})$$

Equation 2.17

where $E_{\mathrm{anion/001}}$, $E_{\mathrm{anion/water}}$, $E_{\mathrm{cation/101}}$, and $E_{\mathrm{cation/water}}$ are the calculated total energies of the N-doped reconstructed anatase TiO_2(001)-(1×4) surface slab with the anion (*e.g.*, Cl^-) being adsorbed on the surface, the N-doped reconstructed anatase TiO_2(001)-(1×4) surface slab with the anion being placed in the middle of the "water" region of the model, the N-doped anatase TiO_2(101) surface slab with the cation (*e.g.*, Na^+) being adsorbed on the surface, and the N-doped anatase TiO_2(101) surface slab with the anion being placed in the middle of the "water" region of the model, respectively. Note that the water environment was treated implicitly using the VASPsol code with a dielectric constant of 78.4.[53] The first part on the right hand side (*i.e.*, $E_{\mathrm{anion/001}} - E_{\mathrm{anion/water}}$) is the adsorption energy of an anion on the N-doped reconstructed anatase TiO_2(001)-(1×4) surface, and the second part on the right hand side (*i.e.*, $E_{\mathrm{cation/101}} - E_{\mathrm{cation/water}}$) is the adsorption energy of a cation on the N-doped anatase TiO_2(101) surface. If the two surfaces are charge-neutral/charged, the E_{ads} of electrolytes before/after excitation (*i.e.*, $E_{\mathrm{ads}}(\mathrm{BE})$/$E_{\mathrm{ads}}(\mathrm{AE})$) can be obtained.

The electrolyte-induced charge polarisation energies (E_{ecp}) can be calculated as follows:

$$E_{\mathrm{ecp}} = E_{\mathrm{ads}}(\mathrm{AE}) - E_{\mathrm{ads}}(\mathrm{BE})$$

Equation 2.18

A negative E_{ecp} indicates that the charge polarisation effect is enhanced by electrolyte.

2.5 References

1. Peng, Y.-K., Hu, Y., Chou, H. L., Fu, Y., Teixeira, I. F., Zhang, L., He, H. & Tsang, S. C. E. Mapping surface-modified titania nanoparticles with implications for activity and facet control. *Nat. Commun.* **8**, 675 (2017).
2. Li, C., Yang, W. & Li, Q. TiO2-based photocatalysts prepared by oxidation of TiN nanoparticles and their photocatalytic activities under visible light illumination. *J. Mater. Sci. Technol.* **34**, 969–975 (2018).
3. Litter, M. I. Heterogeneous photocatalysis: Transition metal ions in photocatalytic systems. *Appl. Catal. B Environ.* **23**, 89–114 (1999).
4. Liu, G., Robertson, A. W., Li, M. M. J., Kuo, W. C. H., Darby, M. T., Muhieddine, M. H., Lin, Y. C., Suenaga, K., Stamatakis, M., Warner, J. H. & Tsang, S. C. E. MoS2 monolayer catalyst doped with isolated Co atoms for the hydrodeoxygenation reaction. *Nat. Chem.* **9**, 810–816 (2017).
5. Zhu, K., Hu, J., Kübel, C. & Richards, R. Efficient preparation and catalytic activity of MgO(111) nanosheets. *Angew. Chem. Int. Ed.* **45**, 7277–7281 (2006).
6. Hu, J., Zhu, K., Chen, L., Kübel, C. & Richards, R. MgO(111) Nanosheets with unusual surface activity. *J. Phys. Chem. C* **111**, 12038–12044 (2007).
7. Richards, R., Li, W., Decker, S., Davidson, C., Koper, O., Zaikovski, V., Volodin, A., Rieker, T. & Klabunde, K. J. Consolidation of metal oxide nanocrystals. Reactive pellets with controllable pore structure that represent a new family of porous, inorganic materials. *J. Am. Chem. Soc.* **122**, 4921–4925 (2000).
8. Verziu, M., Cojocaru, B., Hu, J., Richards, R., Ciuculescu, C., Filip, P. & Parvulescu, V. I. Sunflower and rapeseed oil transesterification to biodiesel over different nanocrystalline MgO catalysts. *Green Chem.* **10**, 373–38 (2008).
9. Hu, J., Song, Z., Chen, L., Yang, H., Li, J. & Richards, R. Adsorption properties of MgO(111) nanoplates for the dye pollutants from wastewater. *J. Chem. Eng. Data* **55**, 3742–3748 (2010).
10. Chen, J., Tian, S., Lu, J. & Xiong, Y. Catalytic performance of MgO with different exposed crystal facets towards the ozonation of 4-chlorophenol. *Appl. Catal. A Gen.* **506**, 118–125 (2015).
11. Torrente-Murciano, L., Gilbank, A., Puertolas, B., Garcia, T., Solsona, B. & Chadwick, D. Shape-dependency activity of nanostructured CeO2 in the total oxidation of polycyclic aromatic hydrocarbons. *Appl. Catal. B Environ.* **132**–**133**, 116–122 (2013).
12. Mai, H. X., Sun, L. D., Zhang, Y. W., Si, R., Feng, W., Zhang, H. P., Liu, H. C. & Yan, C. H. Shape-selective synthesis and oxygen storage behavior of ceria nanopolyhedra, nanorods, and nanocubes. *J. Phys. Chem. B* **109**, 24380–24385 (2005).
13. Manto, M. J., Xie, P. & Wang, C. Catalytic Dephosphorylation Using Ceria Nanocrystals. *ACS Catal.* **7**, 1931–1938 (2017).
14. Liao, F., Huang, Y., Ge, J., Zheng, W., Tedsree, K., Collier, P., Hong, X. & Tsang, S. C. Morphology-dependent interactions of ZnO with Cu nanoparticles at the

materials' interface in selective hydrogenation of CO2 to CH 3OH. *Angew. Chem. Int. Ed.* **50**, 2162–2165 (2011).

15. Peng, Y. K., Ye, L., Qu, J., Zhang, L., Fu, Y., Teixeira, I. F., McPherson, I. J., He, H. & Tsang, S. C. E. Trimethylphosphine-Assisted Surface Fingerprinting of Metal Oxide Nanoparticle by 31P Solid-State NMR: A Zinc Oxide Case Study. *J. Am. Chem. Soc.* **138**, 2225–2234 (2016).
16. Li, J., Zhan, G., Yu, Y. & Zhang, L. Superior visible light hydrogen evolution of Janus bilayer junctions via atomic-level charge flow steering. *Nat. Commun.* **7**, 11480 (2016).
17. Peng, Y. K., Lui, C. N. P., Chen, Y. W., Chou, S. W., Raine, E., Chou, P. T., Yung, K. K. L. & Tsang, S. C. E. Engineering of Single Magnetic Particle Carrier for Living Brain Cell Imaging: A Tunable T1-/T2-/Dual-Modal Contrast Agent for Magnetic Resonance Imaging Application. *Chem. Mater.* **29**, 4411–4417 (2017).
18. Rohrbaugh, W. J. & Wu, E. L. Factors Affecting X-ray Diffraction Characteristics of Catalyst Materials. *ACS Symp. Ser.* **411**, 279–302 (1989).
19. Thamaphat, K., Limsuwan, P. & Ngotawornchai, B. Phase characterization of TiO2 powder by XRD and TEM. *Kasetsart J.(Nat. Sci.)* **42**, 357–361 (2008).
20. Monshi, A., Foroughi, M. R. & Monshi, M. R. Modified Scherrer Equation to Estimate More Accurately Nano-Crystallite Size Using XRD. *World J. Nano Sci. Eng.* **02**, 154–160 (2012).
21. Miller, M. P. & Dawson, P. R. Understanding local deformation in metallic polycrystals using high energy X-rays and finite elements. *Curr. Opin. Solid State Mater. Sci.* **18**, 286–299 (2014).
22. Bragg, W. H. & Bragg, W. L. The reflection of X-rays by crystals. *Proc. R. Soc. A* **88**, 428–438 (1913).
23. Petasis, D. T. & Hendrich, M. P. Quantitative interpretation of multifrequency multimode EPR spectra of metal containing proteins, enzymes, and biomimetic complexes. *Methods Enzymol.* **563**, 171–208 (2015).
24. Peng, Y. K. & Tsang, S. C. E. Facet-dependent photocatalysis of nanosize semiconductive metal oxides and progress of their characterization. *Nano Today* **18**, 15–34 (2018).
25. Keeler, J. Understanding NMR spectroscopy. *Wiley* **43**, 43–5896 (2006).
26. Rabi, I. I., Zacharias, J. R., Millman, S. & Kusch, P. A New Method of Measuring Nuclear Magnetic Moment. *Phys. Rev.* **53**, 318 (1938).
27. Stevie, F. A. & Donley, C. L. Introduction to x-ray photoelectron spectroscopy. *J. Vac. Sci. Technol. A* **38**, 063204 (2020).
28. Held, G., Venturini, F., Grinter, D. C., Ferrer, P., Arrigo, R., Deacon, L., Garzon, W. Q., Roy, K., Large, A., Stephens, C., Watts, A., Larkin, P., Hand, Matthew H., Wang, H., Pratt L., Mudd, J. J., Richardson, T., Patel, S., Hillmana, M. & Scott, S. Ambient-pressure endstation of the Versatile Soft X-ray (VerSoX) beamline at Diamond Light Source. *J. Synchrotron Radiat.* **27**, 1153–1166 (2020).
29. Makuła, P., Pacia, M. & Macyk, W. How To Correctly Determine the Band Gap Energy of Modified Semiconductor Photocatalysts Based on UV-Vis Spectra. *J. Phys. Chem. Lett.* **9**, 6814–6817 (2018).
30. Ember, K. J. I., Hoeve, M. A., McAughtrie, S. L., Bergholt, M. S., Dwyer, B. J., Stevens, M. M., Faulds, K., Forbes, S. J. & Campbell, C. J. Raman spectroscopy and regenerative medicine: a review. *npj Regen. Med.* **2**, 1–10 (2017).

31. Arlt, S., Siegner, U., Kunde, J., Morier-Genoud, F. & Keller, U. Ultrafast dephasing of continuum transitions in bulk semiconductors. *Phys. Rev. B - Condens. Matter Mater. Phys.* **59**, 14860–14863 (1999).

32. Alaoui, I. M. Applications of Luminescence to Fingerprints and Trace Explosives Detection. *NATO Sci. Peace Secur. Ser. B Phys. Biophys.* 189–196 (2009).

33. Duan, X., Qian, G., Zhou, X., Sui, Z., Chen, D. & Yuan, W. Tuning the size and shape of Fe nanoparticles on carbon nanofibers for catalytic ammonia decomposition. *Appl. Catal. B Environ.* **101**, 189–196 (2011).

34. Ma, Z., Zhao, S., Pei, X., Xiong, X. & Hu, B. New insights into the support morphology-dependent ammonia synthesis activity of Ru/CeO $_2$ catalysts. *Catal. Sci. Technol.* **7**, 191–199 (2017).

35. Williams, D. B. & Carter, C. B. The Transmission Electron Microscope. *Transm. Electron Microsc.* 3–17 (1996).

36. Ke, X., Bittencourt, C. & van Tendeloo, G. Possibilities and limitations of advanced transmission electron microscopy for carbon-based nanomaterials. *Beilstein J. Nanotechnol.* **6**, 1541–1557 (2015).

37. Klein, N. D., Hurley, K. R., Feng, Z. V. & Haynes, C. L. Dark Field Transmission Electron Microscopy as a Tool for Identifying Inorganic Nanoparticles in Biological Matrices. *Anal. Chem.* **87**, 4356–4362 (2015).

38. Kundu, P., Deshpande, P. A., Madras, G. & Ravishankar, N. Nanoscale ZnO/CdS heterostructures with engineered interfaces for high photocatalytic activity under solar radiation. *J. Mater. Chem.* **21**, 4209–4216 (2011).

39. Gázquez, J., Sánchez-Santolino, G., Biškup, N., Roldán, M. A., Cabero, M., Pennycook, S. J. & Varela, M. Applications of STEM-EELS to complex oxides. *Mater. Sci. Semicond. Process.* **65**, 49–63 (2017).

40. Wolf, S. G., Shimoni, E., Elbaum, M. & Houben, L. STEM Tomography in Biology. *Cell. Imaging* 33–60 (2018).

41. Akhter, M. A., Mapps, D. J., Ma Tan, Y. Q., Petford-Long, A. & Doole, R. Thickness and grain-size dependence of the coercivity in permalloy thin films. *J. Appl. Phys.* **81**, 4122 (1997).

42. Monod, P., Préjean, J. J. & Tissier, B. Magnetic hysteresis of CuMn in the spin glass state. *J. Appl. Phys.* **50**, 7324–7329 (1979).

43. Kolhatkar, A. G., Jamison, A. C., Litvinov, D., Willson, R. C. & Lee, T. R. Tuning the magnetic properties of nanoparticles. *Int. J. Mol. Sci.* **14**, 15977–16009 (2013).

44. Josephson, B. D. Possible new effects in superconductive tunnelling. *Phys. Lett.* **1**, 251–253 (1962).

45. Kresse, G. & Hafner, J. *Ab initio* molecular-dynamics simulation of the liquid-metal–amorphous-semiconductor transition in germanium. *Phys. Rev. B* **49**, 14251 (1994).

46. Perdew, J. P., Burke, K. & Ernzerhof, M. Generalized Gradient Approximation Made Simple. *Phys. Rev. Lett.* **77**, 1396 (1996).

47. Blöchl, P. E. Projector augmented-wave method. *Phys. Rev. B* **50**, 17953 (1994).

48. Deskins, N. A., Rousseau, R. & Dupuis, M. Distribution of Ti3+ surface sites in reduced TiO2. *J. Phys. Chem. C* **115**, 7562–7572 (2011).

49. Yoon, Y., Du, Y., Garcia, J. C., Zhu, Z., Wang, Z.-T., Petrik, N. G., Kimmel, G. A., Dohnalek, Z., Henderson, M. A., Rousseau, R., Deskins,] N Aaron & Lyubinetsky, I. Anticorrelation between Surface and Subsurface Point Defects and the Impact

on the Redox Chemistry of TiO2(110). *ChemPhysChem* **16**, 313–321 (2015).

50. Lazzeri, M. & Selloni, A. Stress-Driven Reconstruction of an Oxide Surface: The Anatase TiO2(001)−(1×4) Surface. *Phys. Rev. Lett.* **87**, 266105 (2001).

51. Li, F., Wang, D. & Gong, X. Q. Subtle structure matters: boosting surface-directed photoelectron transfer via the introduction of specific monovalent oxygen vacancies in TiO2. *Phys. Chem. Chem. Phys.* **23**, 19854–19861 (2021).

52. Yan, L. & Chen, H. Migration of holstein polarons in anatase TiO2. *J. Chem. Theory Comput.* **10**, 4995–5001 (2014).

53. Mathew, K., Sundararaman, R., Letchworth-Weaver, K., Arias, T. A. & Hennig, R. G. Implicit solvation model for density-functional study of nanocrystal surfaces and reaction pathways. *J. Chem. Phys.* **140**, 084106 (2014).

Chapter 3 Photocatalytic Overall Water Splitting Reaction at Elevated Temperatures on TiO_2 Based Materials

This chapter is adapted from the work by Yiyang Li, Yung-Kang Peng, Liangsheng Hu, Jianwei Zheng, Dharmalingam Prabhakaran, Simson Wu, Timothy J. Puchtler, Mo Li, Kwok-Yin Wong, Robert A. Taylor and Shik Chi Edman Tsang, published in Nature Communications in 2019. The figures are reproduced with permission. Copyright 2019 CC BY 4.0.[1]

3.1 Introduction

Storage and conversion of solar energy has been catching increasing attention for several decades as a clean energy source since severe environmental issues were caused by the combustion of fossil fuels. And photocatalysis is considered as a promising technique to convert the fluctuated solar energy into stable chemical substances which are easier to store and transfer.[2,3] Among various photocatalytic reactions, the photocatalytic overall water splitting (POWS) reaction is of great importance. Water is decomposed to H_2 and O_2 stoichiometrically under light irradiation in the presence of appropriate photocatalysts in a POWS reaction. The evolved hydrogen is an alternative energy source which has high energy-capacity of 143 MJ kg^{-1} and lots of advantages such as carbon-emission-free, producing only water after its combustion.[4–6] Moreover, except for being used as a chemical fuel, it is also an important raw material for many industrial synthesis processes, such as ammonia synthesis and petrochemical industry.[7]

Although the photo-induced oxygen evolution reaction was reported as early as 1968,[8] the POWS reaction has been extensively explored only since the demonstration over TiO_2 in 1972 by Honda and Fujishima.[9] Even though various

materials have been synthesised and studied since then, TiO_2-based materials are still the most widely studied photocatalysts. Studies of the POWS reaction over TiO_2-based materials mainly focused on using UV irradiation due to the wide band gap of 3.2 eV (corresponding to the wavelength of *ca.* 385 nm),[10,11] however, UV light contributes only about 4% to the solar energy, and nearly 43% of the solar energy lies in the visible light regime, despite of the wide range of solar spectrum.[12] Actually, in terms of an efficient photocatalyst for POWS reaction using solar light, several prerequisites must be fulfilled:[13] (1) the band gap energy is less than 3.0 eV to be able to harness the visible light; (2) valance band maximum is more positive than = +1.23 eV and conduction band minimum is more negative than = 0 eV to make O_2 and H_2 evolution happen; (3) the recombination of excited electrons and holes is greatly suppressed so that they have enough lifetime to travel to the surface active sites and react with the chemical species on the surface of the photocatalysts. Although the photo-reduction of protons for H_2 evolution is generally believed as a kinetically facile process, O_2 evolution from OH^- is a slow fundamental step[1] which is generally a four-electron process.

Therefore, efforts have been made to overcome the drawback of wide band gap and improve the POWS performances of the TiO_2-based materials. It is then found that the absorption of the TiO_2 can be broadened and extended to visible light regime after ion-doping. A breakthrough relying on the anion-doped TiO_2 was reported by Asahi *et al.* in 2001[14] and then one decade later, Chen *et al.* published the work on a deeply hydrogenated black TiO_2,[15] both of which exhibited impressive visible light absorption and enhanced photocatalytic activity. Therefore, coloured TiO_2 were considered as a panacea for the photocatalytic water splitting reaction for some time. Defects such as the oxygen vacancies (V_Os) and the doped

N are believed to provide intermediate band levels/extra states, and contribute to enhanced visible light absorption.[16–18]

In addition to focusing on the visible light absorption properties of the materials, strategies have also been developed to optimise the photocatalytic water splitting systems by promoting the charge transfer or surface reactions. The approaches include cocatalyst decoration, dye-sensitisation and Z-scheme photocatalytic systems, etc. Metals and metal oxides are often engaged as H_2 and O_2 cocatalysts, respectively, to promote the surface evolution reaction by lowering the activation energy.[19] It has also been reported that $Rh@Cr_2O_3$ core-shell structure as cocatalyst can also kinetically prevent the O_2 from reaching the metal surface, therefore limited the possibility of the backward reaction.[20] Dye-sensitisation is also one of the widely used techniques to improve the efficiency of visible light absorption, where the organic dyes are engaged and act as photosensitisers and inject electrons into the conduction band of the semiconductors.[21,22] Besides, Z-scheme photocatalytic system has also obtained attention recently, where normally two photocatalysts are engaged, namely H_2 evolution photocatalyst (HEP) and O_2 evolution photocatalyst (OEP), and sometimes redox shuttles are also required. It has been reported that a Z-scheme POWS system shows a high QE of 30% at 419 nm and STH efficiency of 1.1% with the help of cocatalysts.[23] TiO_2-based materials are also reported to show enhanced performances toward the photocatalytic H_2 evolution reaction (HER) under visible light irradiation in the presence of sacrificial reagents.[24]

3.2 Objectives

As discussed above, much progress has been achieved and different approaches have been developed in recent decades, however, unfortunately the POWS

performances are still far behind the requirement of the practical application. In addition, many POWS systems require the addition of other chemicals except for water, such as the organic dyes, redox shuttles or sacrificial reagents, which add up to the capital costs and more importantly, lead to unwanted side-reactions and by-products. Materials like sulphides and phosphides, although sometimes are reported to show good photocatalytic performances, suffer from the photo-corrosion problems.[2,25,26] While there is scarcely any report of high-rate water splitting system for simultaneous O_2 and H_2 evolution over TiO_2-based materials under visible light irradiation without sacrificial reagents.

It has been mentioned in previous chapters that visible light absorption of TiO_2 has been considerably enhanced, however, high absorption does not necessarily result in high QE or photocatalytic activity: for example, the QE decreased sharply from 90% to less than 5% once ultraviolet irradiation was switched to visible light[27,28] but the reason behind this sudden drop was rarely discussed. It must be noted that the overall photocatalytic performance is not determined only by photons absorption, the efficiencies of the photo-generated charge separation and surface chemical reactions are also important. Therefore, novel systems are urgently needed to improve the POWS performances instead of simply screening different materials. In this chapter, the main objective is to demonstrate a state-of-the-art POWS system at elevated temperatures, where the photo-generated charge carriers' separation is greatly facilitated and the POWS performance is extraordinarily improved. By using the most widely studied photocatalyst, TiO_2, the temperature effect on the POWS system is clearly demonstrated. Moreover, the feasibility and potential of further practical application are also discussed.

3.3 Results and discussion

3.3.1 Characterisations of the N-TiO_2 materials

3.3.1.1 XRD of N-P25 materials

TiO_2 (P25) powder was treated by temperature ramping in an NH_3 flow to a specific temperature T (ranging from 550-660 ^oC, as specified in the sample name) to obtain the N-TiO_2 materials with different concentrations of N-doping, denoted as N-P25-T. At such high temperatures, N element can get into TiO_2 lattice, taking up either the interstitial sites or the substitutional sites that are originally occupied by O atoms. In the case of substitution, each two substitutional N^{3-} ions will kick out three O^{2-} ions to reach charge neutrality, leaving an oxygen vacancy in the material. The above processes will clearly compromise the crystallinity of TiO_2 in the surface and sub-surface regions, rendering the outmost surface amorphous, as later shown by TEM images.

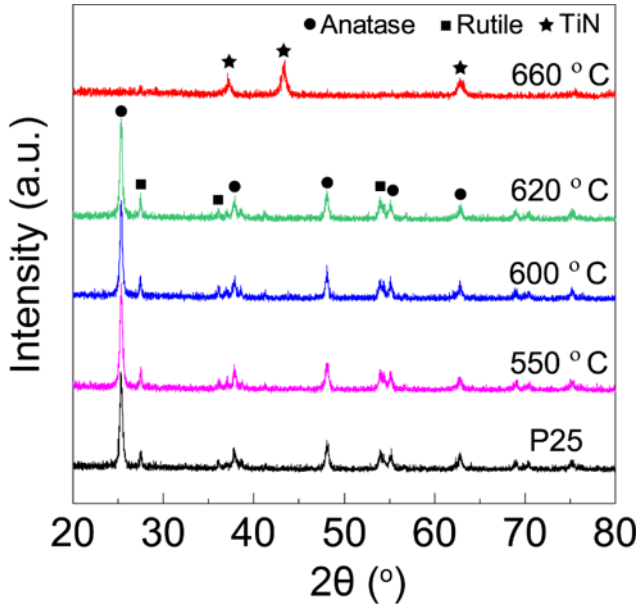

Figure 3.1 XRD patterns of N-P25 obtained at different NH_3 treatment temperatures.

The obtained products were then characterised by XRD, as shown in Figure 3.1.

XRD indicates that N-P25-550, N-P25-600 and N-P25-620 share almost the same patterns with pristine P25, but with a tiny additional peak at 2θ of 36.9° which might be attributed to TiN phase. The major characteristic peaks can be observed at 2θ of 25.3°, 37.9°, 48.1°, 55.2° and 62.9°, which can be attributed to the anatase crystalline structure; and the peaks observed at 2θ of 27.5°, 36.1°, 48.0° and 53.9° can be attributed to the rutile phase. The ratio between the peaks of anatase and rutile maintain unchanged within experimental errors, which means no phase transformation from anatase to rutile has taken place during the NH_3 treatment. However, further increasing the NH_3 treatment temperature to 660 °C leads to a dramatic transformation to a clear titanium nitride structure, and the diffraction peaks of either anatase or rutile have totally disappeared. Therefore, further study will not be carried out on the N-P25-660, but focus on the other N-P25 samples. It should be mentioned that the surface area decreased to 42 $m^2\ g^{-1}$ of N-P25-620 from 57 $m^2\ g^{-1}$ of pristine P25, indicating aggregations during the high temperature treatment. In addition, one of my fellow DPhil students, Christopher Foo, has demonstrated in a separate research that the local TiN phase and a new oxynitride phase (TiO_xN_y) could be observed in the N-P25 samples. Systematic structural study was carried out in his work, with the help of the variable-temperature synchrotron XRD technique (see more details in ref. 29).

3.3.1.2 XPS of N-P25 materials

XPS was also engaged to investigate the chemical status of each element of the N-P25 on the surface and sub-surface region and the Ti 2p, O1s, and N1s spectra are shown in Figure 3.2, respectively. For each sample, two peaks corresponding to Ti $2p_{3/2}$ and Ti $2p_{1/2}$ were observed in the Ti 2p XPS spectra, at the binding energies of 458.5 eV and 464.2 eV, respectively, which can be attributed to the

main characteristic peaks of Ti^{4+} on the surface of N-doped TiO_2 materials. A single peak at 529.6 eV was observed in O1s spectra which is the characteristic peak of lattice oxygen in TiO_2 and N-doped TiO_2. N 1s XPS spectra shows clearly two characteristic peaks, located at 396.4 eV and 400.7 eV, which can be assigned to N substituted at lattice oxygen sites (N_s), and interstitial N atoms (N_i), respectively.[30,31]

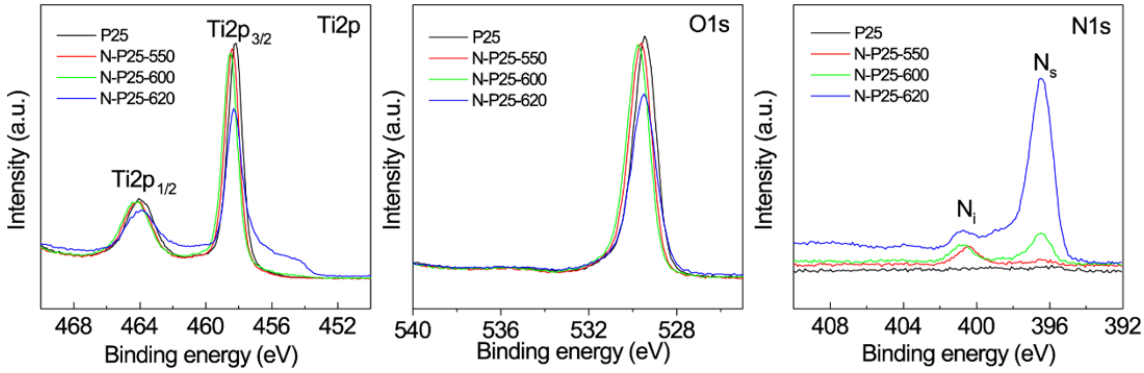

Figure 3.2 XPS spectra of N-P25 treated at different NH_3 treatment temperatures.

It is also noteworthy that only interstitial N is detected in N-P25-550, while with increasing the N-doping level, substitutional N begins to emerge, and the interstitial N levels off at further higher N concentration. Therefore, it is clear that under our N-doping conditions, N atoms preferably occupy the interstitial sites at low doping level, and only start to substitute the O sites when the interstitial sites are saturated. As mentioned previously, the substitutional N atoms occupy the original O positions, and this process is accompanied by the generation of surface oxygen vacancies.[30] Unfortunately, we have not resolved the exact positions of the N_s and N_i in the TiO_2 lattice, due to the lack of expertise of appropriate structural characterisation techniques.

3.3.1.3 UV-Vis absorption of N-P25 materials

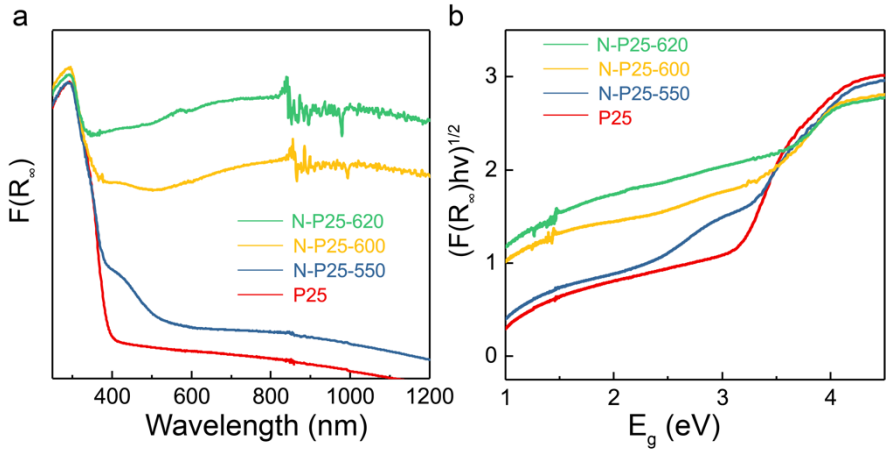

Figure 3.3 (a) UV-Vis absorption spectra of N-P25 treated in NH_3 at different temperatures; **(b)** The corresponding Tauc plots.

UV-Vis spectroscopy was used to characterise the absorption properties of the N-P25 samples, and the UV-Vis spectra are shown in Figure 3.3a. It is obvious that with the inclusion of N, an additional broadened edge at a longer wavelength of 500 nm (visible light) is observed for N-P25-550, apart from the absorption edge at 395 nm (UV light) of pristine P25. Higher N-doping concentrations lead to a significant enhancement of the light absorption property, and result in high absorption in visible and infrared regimes: N-P25-600 and N-P25-620 show quite strong absorption even at 800-1000 nm. Tauc plots are frequently used to evaluate the band gap energy of semiconductor materials, as shown in Figure 3.3b. However, it has been demonstrated that the Tauc plot method for band gap energy evaluation is not suitable for defected materials, such as the N-P25 samples in this chapter, or semiconductor mixtures, since it will give falsely small band gap energies.[32] Although the band gap energy of these samples cannot be obtained from the Tauc plots at this stage, it can be clearly seen from Figure 3.3b that the intrinsic band gap energy of TiO_2 has not been changed after the NH_3 treatment, which is *ca.* 3.2 eV. It has been reported that the introduction of N-doping in TiO_2

can create V_Os and Ti^{3+} and the photo-excitation of these colour centres and defects as extra intraband levels to the conduction band can therefore contribute to the visible light absorption of the N-TiO_2.[31,33]

3.3.1.4 Raman spectra of N-P25 materials

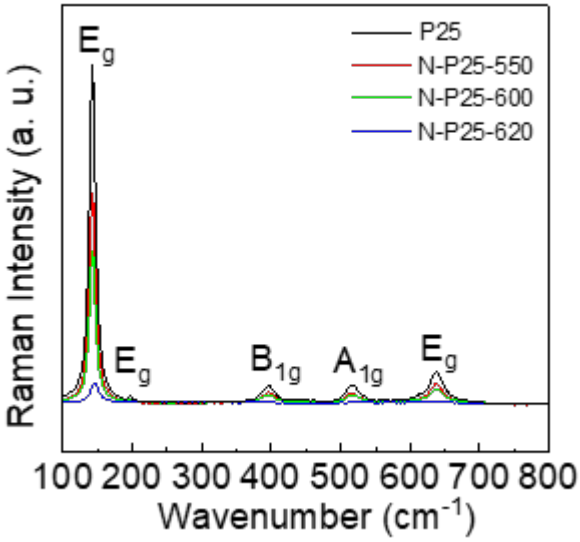

Figure 3.4 Raman spectroscopy of N-doped TiO_2 treated in NH_3 flow at different temperatures.

Raman spectroscopy was then utilised to obtain more structural understanding of the N-P25 samples. As can be seen from Figure 3.4, There are five major peaks located at 144, 196, 396, 544, and 636 cm^{-1}, respectively, which represent E_g, E_g, B_{1g}, A_{1g} and E_g Raman active vibrational modes, indicating the predominant phase of the N-doped TiO_2 is anatase,[34,35] which is consistent with the XRD results. Moreover, the Raman peaks of these samples exhibit different degrees of weakening with inclusion of N doping, implying the disruption of the TiO_2 lattice by interstitial N, substitutional N and V_O which are introduced by the NH_3 treatment.[36,37]

3.3.1.5 HAADF-STEM of N-P25 materials

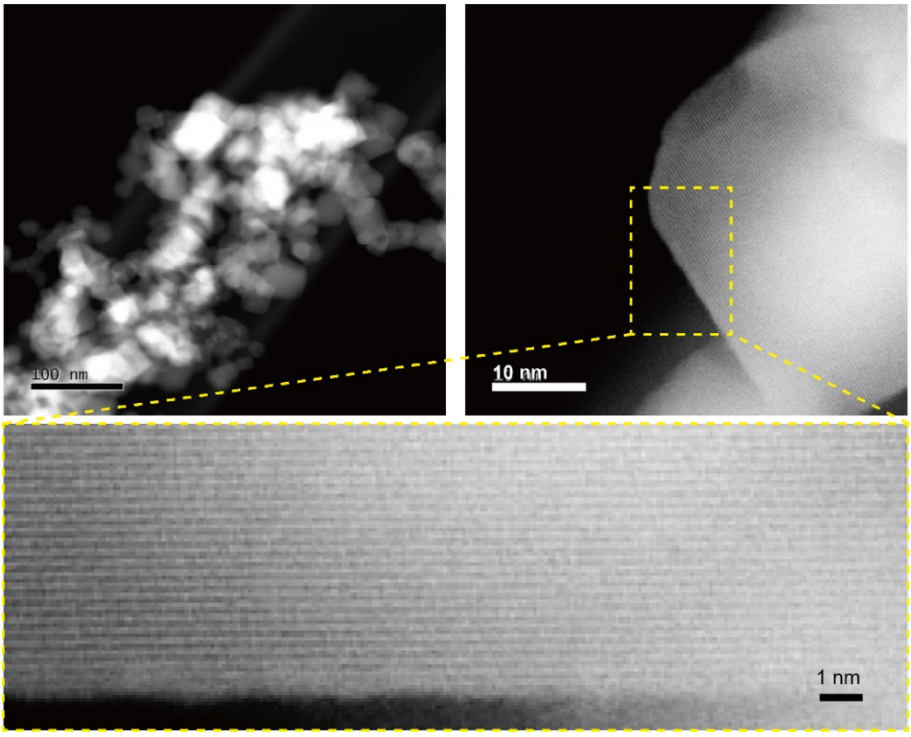

Figure 3.5 HAADF-STEM images of N-P25-620 show the typical lattice spacing of <101> of anatase TiO_2 (0.35±0.02 nm) in the bulk structure. However, the top few atomic layers appear to show an amorphous-like sub-surface with a distorted lattice. Scale bars are indicated in the images. STEM images were acquired by Dr. Tianyi Chen of Prof. Edman Tsang's group.

HAADF-STEM images show the typical lattice spacing of <101> of anatase TiO_2 (0.35±0.02 nm) in the bulk structure. However, the top few atomic layers appear to show an amorphous-like sub-surface with a distorted lattice. Scale bars are given in the images (Figure 3.5).

Now according to all the above characterisations, it is quite clear that after the high-temperature NH_3 treatment, N is doped into the TiO_2 lattice significantly (Figure 3.1), occupying the interstitial sites at low doping levels, and substituting the O atoms at high doping levels (Figure 3.2). Such a heavy N-doping then results in the appearance of a local TiN phase and a TiO_xN_y oxynitride phase, which was observed using the high-resolution synchrotron XRD, but could not be seen clearly

on the XRD patterns in this thesis (Figure 3.1). The formation of these new phases, especially the TiN phase, are responsible to the greatly enhanced absorption in visible and infrared regimes, which actually shows the feature of metallic materials (Figure 3.3). It is noteworthy that these N-doping, O substitution, and new phase generation are mainly happening within the sub-surface region. Therefore, HAADF-STEM images show an amorphous-like sub-surface with a distorted lattice (Figure 3.5), which means the crystallinity of these regions are substantially compromised, resulting in the weakening of the Raman-active vibrations and the Raman signals (Figure 3.4).

3.3.1.6 EPR of N-P25 materials

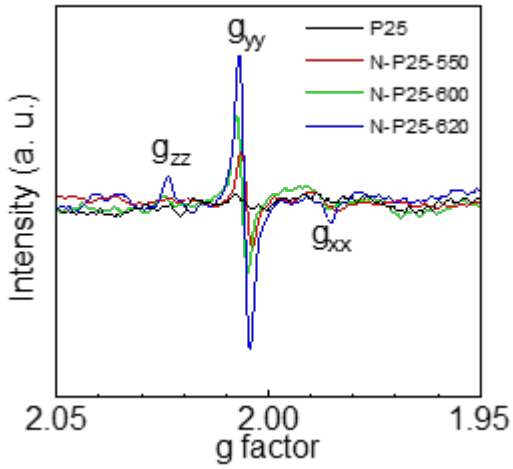

Figure 3.6 EPR patterns of N-P25 prepared by NH_3 treatment at different temperatures.

As mentioned before, it has been reported that the inclusion of substitutional N into TiO_2 will lead to the creation of V_Os. This is because the N^{3-} ion carries three negative charges, while O^{2-} carries two negative charges. And to balance the charges within the whole material to make it stay neutral, three O atoms will be substituted by only two N atoms, leaving an V_O unoccupied. On the other hand, the V_Os are generally considered as trapping sites for electrons and active sites of

many chemical reactions. Moreover, those electrons trapped in the surface V_Os can subsequently interact with O_2 molecules in the air to form paramagnetic O_2^- species which are detectable by EPR.[38,39] For a photocatalyst, the excited electron-hole pairs that can reach to the surface of the photocatalyst for the subsequent reactions are more important than those pairs recombine in the bulk. Consequently, EPR measurements were performed on the N-P25 samples, as shown in Figure 3.6. It is evident that pure P25 is silent on EPR and shows no signal at room temperature; while for N-P25-550, N-P25-600 and N-P25-620, an orthorhombic EPR signal with the g values of g_{zz}=2.023, g_{yy}=2.006 and g_{xx}=1.987 were observed. Also, the EPR signals increase with the N-doping concentrations, implying that N-doping is always accompanied by the formation of V_Os, as discussed above. The above observations are consistent with the fact that doping electronegative N species into anatase TiO_2 can create defects like Ti^{3+} and V_Os at different energy levels.[31,33] The photo-excitation of these colour centres and doped N providing extra intra-band levels is thought to account for our observed strong UV-Vis absorption over a broad range from the UV to the infrared.

Despite the creation of V_Os, their stability on the particle surface is still uncertain and has been rarely discussed in literature. Thus, in order to evaluate the stability of the surface V_Os and investigate the probable degeneration of these surface defects when exposed to air, EPR measurements were carried out after N-P25-550 was freshly prepared and exposed to air for different time ranges. Interestingly, after the sample was exposed to air at ambient conditions for 1.5 hours, 40% of the EPR signal gradually disappeared and after 24 hours, only 23% of the original signal remained, suggesting that the surface V_Os are not stable in air at room temperature (Figure 3.7a). This is attributed to the fact that the oxygen sources in

air (*i.e.*, O_2 and H_2O), when in contact with the particle surface, will gradually replenish the surface V_Os and redistribute the electrons. Such observation could also explain the fact that N-doped TiO_2 or hydrogenated TiO_2 do not necessarily show good photocatalytic overall water splitting activity under visible light illumination in air, because the surface defects are readily recovered by the oxygen sources in air. Even though the remaining oxygen defects in bulk can still exert strong visible light absorption, they hardly contribute to the photocatalytic performances, since they are not accessible for the chemical species. It should be clarified that defects are not always good in photocatalysts: defects deeply inside the band gap, also known as deep-level defects, are not desirable and can lead to more severe recombination issues. Only the shallow defects are desirable in photocatalysts, which can prolong the lifetime of the photo-generated charge carriers.[40] Subsequently, I noticed that after re-calcining the N-doped TiO_2 in a N_2 atmosphere at elevated temperatures, the EPR signals of these materials re-emerged and became even larger, implying that more surface V_Os were regenerated at elevated temperatures (Figure 3.7b). Control experiments were performed in an Ar atmosphere at elevated temperatures as well, which gave similar results as those in the N_2 atmosphere, confirming that N_2 could not dope the TiO_2 samples with extra N under the given experimental conditions. The surface V_Os formed in N-doped TiO_2 are vulnerable to oxygen sources at room temperature, but at elevated temperatures, the faster subsequent reactions can regenerate them to sustain the surface photocatalytic processes. DFT calculations have also demonstrated that N-doping leads to a large reduction in the formation energy of V_Os, indicating that V_Os are more easily generated after N-doping,[30] in accordance with the EPR results shown in Figure 3.7b. Similarly, thermal

treatments were also carried out in liquid water at different temperatures, considering the use of N-TiO_2 in water splitting reaction. Samples were dispersed in deionised water and loaded in a batch reactor, and after the thermal treatment for one hour, the reaction was quenched and the post-treatment samples were filtered, dried in vacuum and measured by EPR. As shown in Figure 3.7c, the increase of EPR signals with the treatment temperatures can be also observed. Similarly, samples were also treated in 10 bar of water vapour, which exhibits the same trend of EPR signal increase (Figure 3.7d). The above observation clearly suggests that the V_Os can be also regenerated at elevated temperatures under the photocatalytic water splitting conditions, even the N-TiO_2 particles are surrounded by water or water vapour.

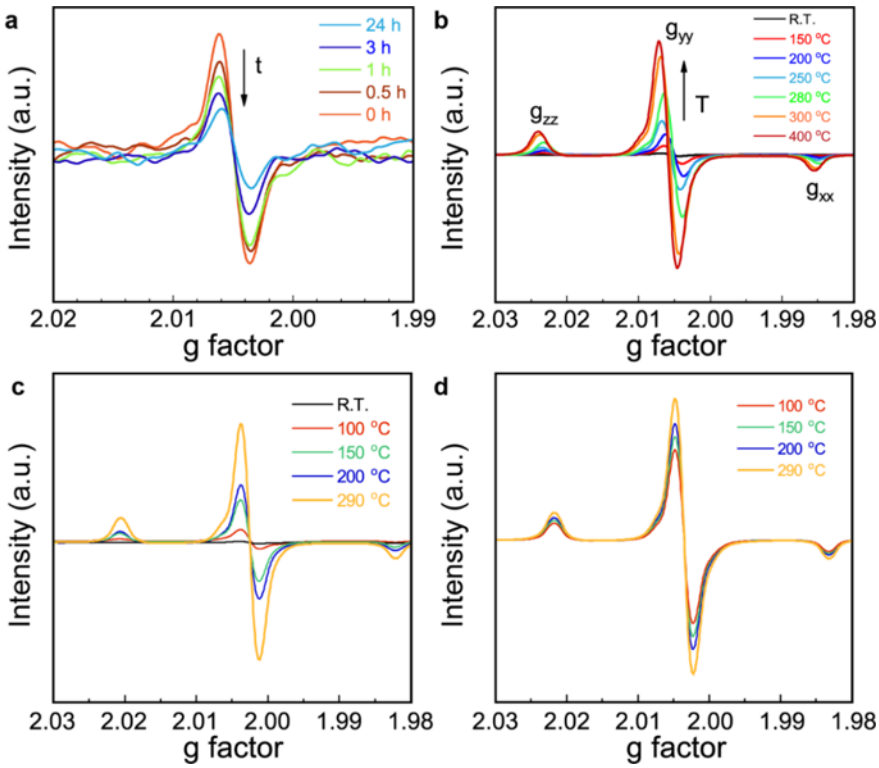

Figure 3.7 (a) EPR spectra of N-P25-550 after freshly made and exposed to air for different times; **(b)** EPR spectra of the deactivated N-P25-550 after re-calcination in N_2 at different temperatures; **(c)** EPR spectra of the deactivated N-P25-550 after treatment in liquid water at different temperatures; (**d)** EPR spectra of the deactivated N-P25-550 after treatment in water vapour at different temperatures.

3.3.2 Temperature effect on the POWS reaction

The POWS activity was then evaluated in pure water under visible light illumination in a batch reactor equipped with silica windows. The detailed temperature effect on the POWS activity was initially investigated on the N-P25-620 photocatalyst that possesses the highest N-doping level and most surface vacancies as the catalytic active sites, as shown in Figure 3.8. It is interesting to note that the photocatalytic activity of N-doped TiO_2 in water is highly dependent on the applied temperatures. However, the activity does not increase linearly, despite the kinetic and entropic contributions upon using higher temperatures where more surface V_Os are also formed. Apparently, the activity reaches a maximum value of H_2 production when the temperature rises to near 270°C but declines rapidly on further increasing the temperature.

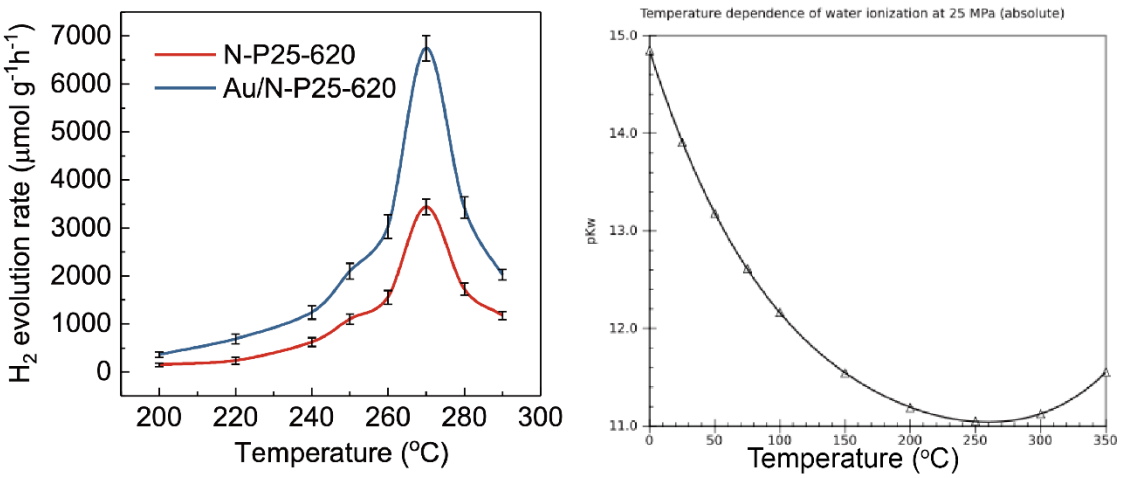

Figure 3.8 Left: Photocatalytic water splitting reaction activity tests of N-P25-620 and Au/N-P25-620 at different temperatures. **Right:** Temperature dependence of pK_w at the saturated vapour pressure. Reproduced from ref. 41.

Such behaviour in response to the temperature increase cannot be explained by the promoted kinetics at elevated temperatures, which should be in a positive correlation instead of a volcanic response. It has been reported that the ionic

dissociation of water to H^+ and OH^- is dependent on temperature, and the dissociation constant can be promoted to 25 times that at room temperature (1×10^{-14}) and peaks at around 260-270 °C before rapidly declining.[41] Our observed volcanic response of the photocatalytic activity against temperature appears to show a similar pattern as the reported temperature-dependent ionisation constant of water. We discounted the effect of associated saturated water pressure in the batch reactor as no promoting effect was observed in equivalent N_2 pressure without heating. In fact, pressure can influence the ionisation constants of water only at extremely high values.[41] As shown in Figure 3.8, the H_2 evolution rate of N-P25-620 reaches 3525 μmol g^{-1} h^{-1} at 270 °C.

Table 3.1 Photocatalytic activities (270 °C, under visible light irradiation), V_O concentrations, and N-doping concentrations of different N-P25 TiO_2 samples in this chapter and pristine P25 as a reference.

NH_3 treatment *T* (°C)	**Surface V_O (10^{16} counts mol^{-1})**	**N concentration (wt.%) (by XPS)**	**H_2 evolution rate (μmol g^{-1} h^{-1}) (270 °C)**
Not treated	Not detected	Not detected	Not detected
550	1.86	0.53	1980±95
600	8.74	1.41	2945±93
620	13.33	4.60	3525±122

Subsequently, the POWS activities of N-P25-550 and N-P25-600 were also evaluated with similar method at the optimised temperature of 270 °C, and both show exciting H_2 evolution rates of 1980 μmol g^{-1} h^{-1} and 2945 μmol g^{-1} h^{-1} respectively. It is also noteworthy that the trend of POWS activities of the N-P25 samples correlates well with the trend of V_O concentrations determined by EPR signals and surface N-doping concentrations determined by XPS (Table 3.1), indicating that the enhanced POWS activities can be attributed to the N-doping and the regenerable surface V_Os to a large extent. The surface V_O concentration

was obtained by double-integration of the EPR signal of the surface V_O at g=2.006.

Deposition of metal promoters as cocatalysts is a generally used strategy to enhance the photocatalytic activities so it was also investigated. Different metal depositions onto the N-P25-620 were attempted in this thesis, via the photo-deposition method, including gold, platinum, cobalt, palladium, silver and nickel, all of which are traditionally considered as good cocatalysts for the HER, and the results are shown in Figure 3.9. All of the as-prepared photocatalysts show enhanced water splitting activity compared with N-P25-620 to some extents.

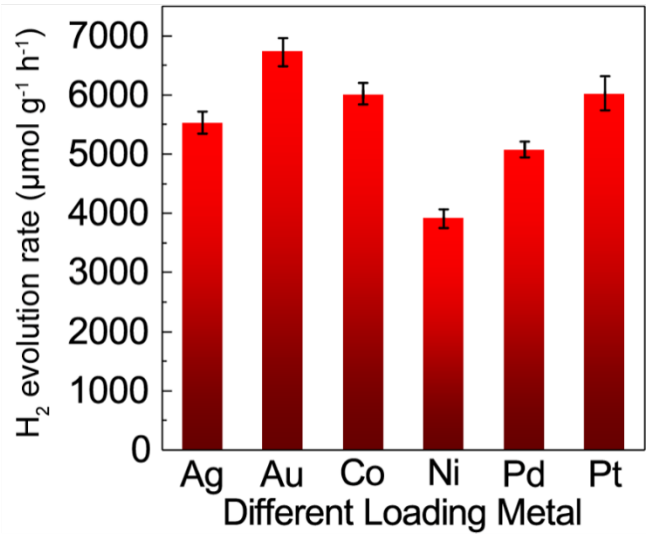

Figure 3.9 Photocatalytic activities of N-P25-620 decorated with different metals (1.0 wt.%) at 270 °C. Error bars indicate standard deviation.

However, it must be clarified that the photo-deposition method used here actually cannot result in Co or Ni nanoparticles due to the insufficiently negative conduction band minimum (CBM): the reduction potential of Co and Ni are -0.28 and -0.23 V vs. the standard hydrogen electrode (SHE), while the CBM of TiO_2 is *ca.* 0.3 V vs. SHE.[42] Therefore, Co or Ni nanoparticles cannot be obtained using this method. This may explain why the photocatalytic activity did not change obviously after "deposition of Ni" (Figure 3.9). On the contrary, in the case of Co, the photocatalytic activity was enhanced substantially even though Co nanoparticles could not form

(Figure 3.9). Oxide species, CoO_x, may be deposited on the TiO_2 surface, which may facilitate the OER half reaction, and finally result in the enhanced POWS activity. Among all the metal studied here, gold shows the highest enhancement effect, presumably due to the surface plasmon resonance (SPR) effect, giving a H_2 evolution rate of 6746 μmol g^{-1} h^{-1} at 270 °C. Unfortunately, I was not able to observe any SPR peak of Au in the UV-Vis spectra, because the N-P25-620 exhibited extremely high absorption across the whole UV-Vis-NIR region, but the Au nanoparticles could be observed using microscopic techniques. I did not look into the SPR effect carefully in this thesis, since it is kind of beyond the focus of this thesis, and the SPR effect of Au in photocatalytic systems has been extensively studied in literature.[43–45] It is noted that this optimal H_2 activity at 270 °C is substantially higher than the best photocatalytic systems claimed in the literature (which have mainly been evaluated at room temperature).

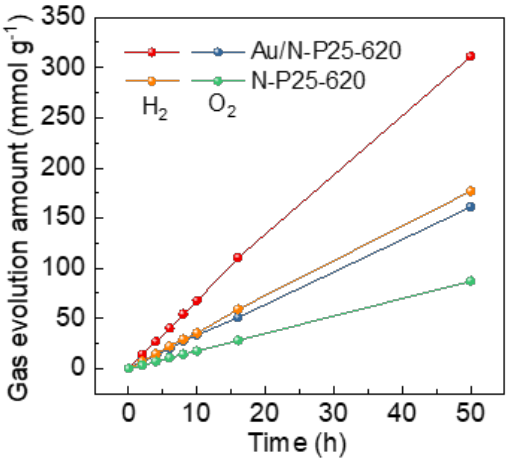

Figure 3.10 Stable splitting of water to 2:1 H_2/O_2 with no sacrificial reagent over N-P25-620 and Au/N-P25-620 at constant rates for 50 hours.

The stoichiometric and stable production of H_2 and O_2 in a 2:1 ratio is of tremendous importance when evaluating POWS systems. Therefore, a 50-hour reaction was then carried out at 270 °C to verify the stability of the 1.0 wt. % Au/N-

P25-620, as shown in Figure 3.10. Obviously, the Au/N-P25-620 photocatalyst gives a stable production of H_2 and O_2 in stoichiometric 2:1 molar ratio over 50 hours with no loss of N content according to our chemical analysis, showing an average H_2 evolution rate of around 6600 μmol g^{-1} h^{-1} at 270 °C. Unfortunately, pristine P25 TiO_2, with or without the high-temperature treatment in an inert atmosphere, showed no observable POWS activity under visible light irradiation, even at 270 °C, confirming that the N-doping is essential in this system.

Table 3.2 POWS performance of 1.0 wt% Au/ N-P25-620 at 270°C/60 bars (saturated equilibrium pressure of water) as compared to selected literature data.

Photocatalyst	**Light source**	**H_2 Evolution Rate (μmol h^{-1} g^{-1})**	**Ref.**
Au/N-TiO_2 (P25)	70 W W-lamp, ≥400 nm	6746±147	This work
CDots-C_3N_4	300 W Xe lamp, ≥420 nm	566	46
Pt/(Cring)-C_3N_4	300 W Xe lamp, ≥420 nm	150	47
Pt, Co modified g-C_3N_4	300 W Xe lamp, ≥420 nm	1.2	48
Cr-Rh oxide/($Ga_{1-x}Zn_x$)($N_{1-x}O_x$)	450 W high pressure mercury lamp, ≥436 nm	1543	49
Ni@NiO_x/$SrTiO_3$	AM 1.5 solar simulator	18	50
Pt, Co_3O_4/carbon nitride	300 W Xe lamp, ≥300 nm	155	51
Pt/$Bi_xY_{1-x}VO_4$	300 W Xe lamp, ≥300 nm	139	52

Table 3.3 QE for POWS of 1.0 wt% Au/ N-P25-620 at 270°C/60 bar (saturated equilibrium pressure of water) as compared with selected literature data.

Photocatalyst	Cocatalyst	Wavelength (nm)	QE*(%)	Ref.
N-doped P25	Au	437	76.7±2.1	This work
Vacuum-activated P25	Pt	420	1.17	[53]
Hydrogenated TiO_2	Pt	420	2.28	[54]
Unsupported Au NPs	/	300	2.7	[55]
W-doped TiO_2	Au	380	18.3	[56]
Hydrogenated N doped-TiO_2	Pt	420	9.0	[57]
Li-EDA treated P25	/	420	2.57	[58]

*Quantum efficiency results from literature were obtained in the presence of various amounts of sacrificial reagent such as methanol, while in this work it was measured in pure water (Milli. Q.).

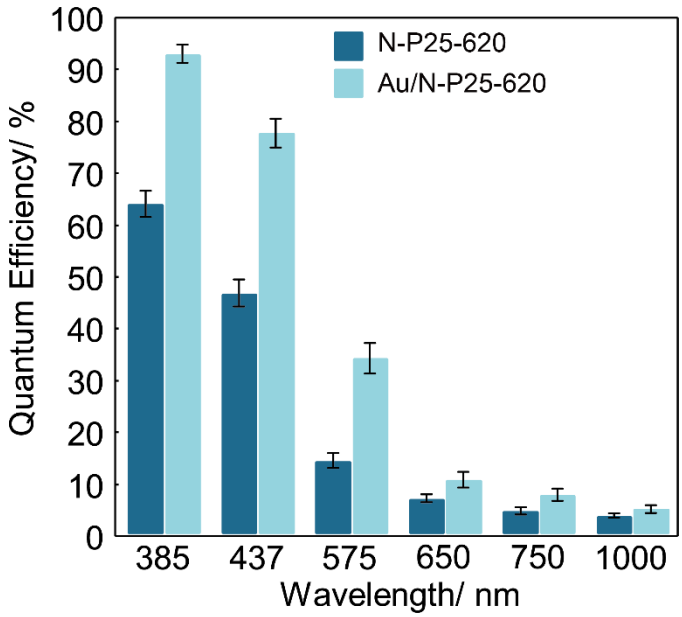

Figure 3.11 QE of the N-P25-620 and the Au/N-P25-620 at different wavelengths evaluated at 270 °C.

For a photocatalytic system, QE is one of the key parameters when evaluating the conversion efficiency of renewable solar energy to H_2 fuel systems.[33] Almost all the reported photocatalytic water splitting TiO_2 based systems suffer from extremely low QE in the visible light region (rarely exceeding 3 % at 420 nm),

which largely hinders any potential practical applications. For our photocatalytic system, the QE was evaluated at 270 °C at wavelengths of visible light and in the near infrared (NIR) using bandpass filters. The detailed method of the QE evaluation in this thesis has been described clearly in Chapter 2, and an example is given in Appendix Note A1. As illustrated in Figure 3.11, the QE becomes larger with decreasing wavelength and an impressive QE of 76.7% is obtained at 437 nm. Such high QE values in the visible light region have only been reported by chalcogenide systems with anticipated photo-corrosion issues and with the addition of a sacrificial reagent.[26] Clearly, the QE increased significantly after the deposition of Au nanoparticles, since Au nanoparticles could trap the photo-generated electrons and facilitate the H_2 evolution reaction. Also, the QE at 575 nm (which is very close to the SPR wavelength of Au nanoparticles, and the SPR wavelength varies with the particle size) increased more substantially, showing a 110 % enhancement, which could be attribute to the SPR effect of Au nanoparticles. Here, I demonstrate that this robust N-doped TiO_2 system can give equally high QE at elevated temperatures. Excitingly, this photocatalytic system can operate even at 1000 nm (1.24 eV), almost the minimum threshold energy required for water splitting with a QE of 2.7%. To the best of our knowledge, this system is the first example that the overall water splitting reaction can be accomplished under NIR irradiation with considerable Q.E. whilst exceptional photoactivity and QE in the visible region at 270 °C greatly exceeds values reported for TiO_2 systems (Table 3.3).

3.3.3 Separation of charge carriers

Time-resolved photoluminescence (TRPL) was used to investigate the recombination of photo-excited electron-hole pairs. PL spectra in Figure 3.12a

clearly show that the PL intensity decreases as the N-doping increasing – this is an indication that the lifetime of the photo-generated charge carriers also is more prolonged at a higher N-doping concentration. The main PL signal lies in the region of 400-600 nm, forming a very broad emission band (Figure 3.12a), while for N-P25-600 and N-P25-620, there is an additional emission signal emerging at *ca.* 900 nm, which can be attributed to the emission that involves the N-defect band.

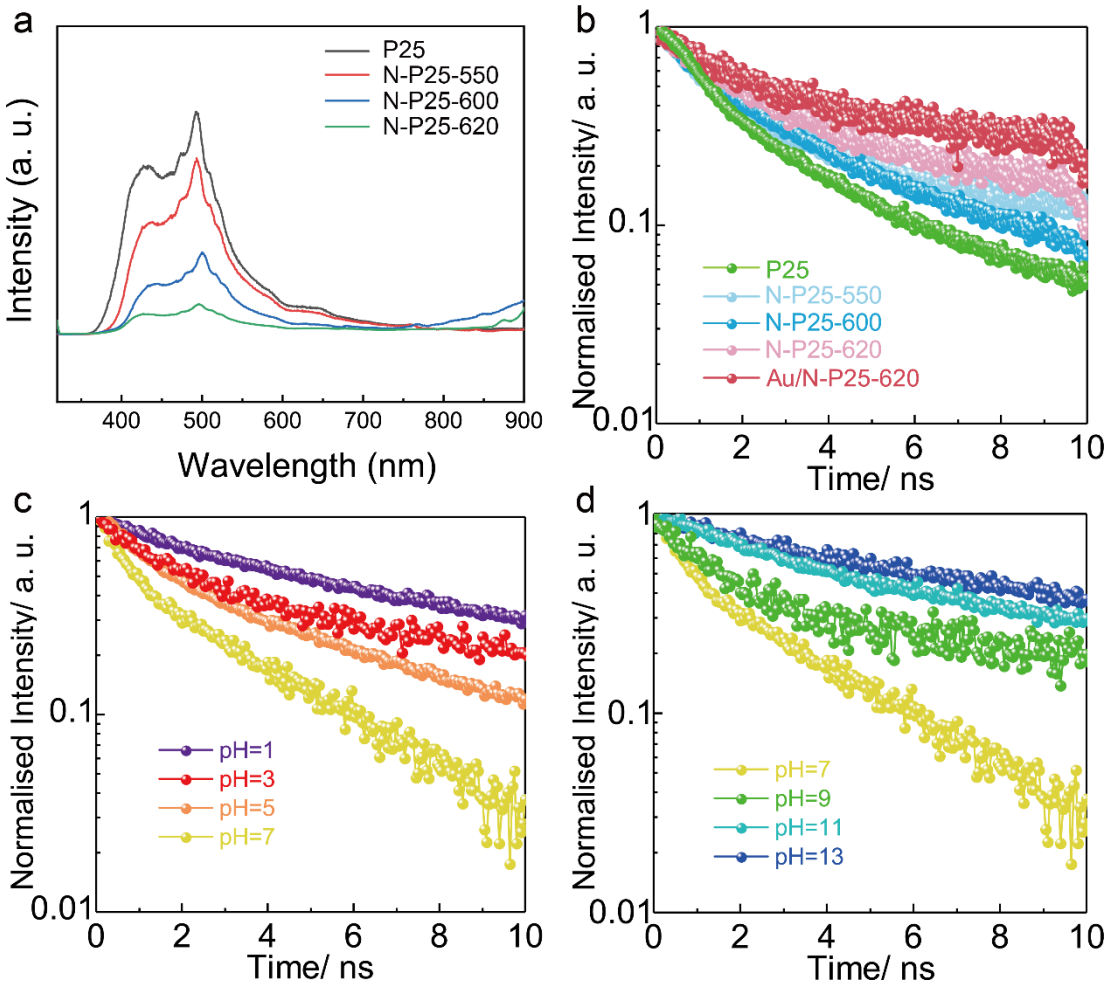

Figure 3.12 (a) PL spectra of P25 and N-P25 samples. TRPL spectra of **(b)** N-P25 treated by NH_3 at different temperatures and promoted by Au; **(c)** N-P25-620 after being soaked in acidic solutions with different pH and **(d)** N-P25-620 after being soaked in alkaline solutions with different pH. Conditions: the excitation wavelength is 266 nm and the probe wavelength for the TRPL is 500 nm.

As shown in Figure 3.12b, introduction of V_Os via N doping and subsequent Au deposition are both able to prolong the charge carrier lifetime, leading to an

increase to 2.56 ns from the 1.12 ns of pristine P25. It is widely agreed that the separation of photo-excited charge carriers plays an important role in the photocatalysis; therefore, TRPL can also be a powerful technique to understand the effect of using elevated temperature. As a result, the TRPL experiments were first conducted in air without water at different elevated temperatures to see if the increase in temperature could make any difference to the charge carrier lifetime. It is interesting to find that the measurements showed no apparent change with solely the temperature increase (as shown in Figure 3.13). Bear in mind that the photocatalytic water splitting activity is dramatically increased at elevated temperature and peaks at 270 °C, which coincides with the maximal water dissociation constant. It is therefore obvious that the significant temperature effect observed in the presence of water is due to the increased concentration of both H^+ and OH^- from the water dissociation. This can largely contribute to the enhanced photocatalytic performance at elevated temperatures.

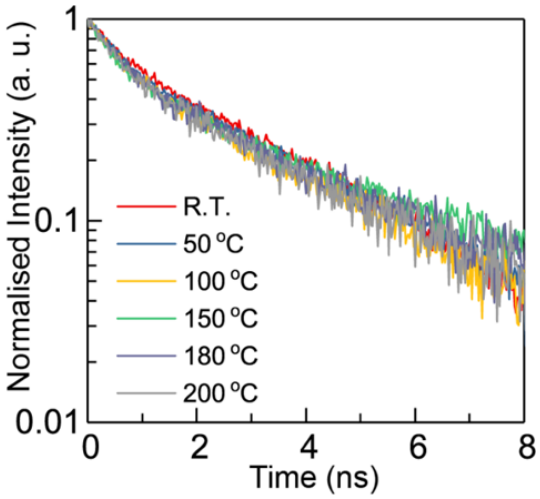

Figure 3.13 TRPL spectra of N-P25-620 measured in air at increasing temperature. Each TRPL spectrum was normalised to its highest intensity (*i.e.*, right after the laser pulse, t=0) for a more straightforward and clearer comparison. The actual intensity/amplitude of all the TRPL spectra in this figure is similar to each other. Therefore, temperature does not obviously influence either the PL spectra or the TRPL spectra.

The TRPL measurements were subsequently carried out in different H^+ and OH^- concentrations by soaking the N-P25-620 sample in acidic or alkaline solutions with various pH at ambient temperature to mimic the high temperature conditions and to correlate to the charge carrier lifetime. As expected, the charge carrier lifetime increased dramatically, as shown in Figures 3.12c and 3.12d, the fastest recombination rate was obtained at pH=7 where there were the lowest concentrations of H^+ and OH^-, and the charge carrier lifetime apparently increased with higher concentration of H^+ or OH^-, and H^+ and OH^- showed similar effect on the charge separation, and the charge carrier lifetimes were prolonged to the same degree. Clearly, the adsorption of H^+ or/and OH^- near the surface of the semiconductor could create a local electric field (LEF) which can attract the counter charged electron or hole species hence suppressing their recombination rate and enhancing the overall photocatalytic activity. As stated before, dissociation of H^+ and OH^- from water becomes more favourable at higher temperatures and peaks at around 270 ^oC. Consequently, the charge carrier lifetime is prolonged at elevated temperatures, compared to that at room temperature due to the simultaneously enhanced H^+ and OH^- concentrations, which allows chemical reactions to take place. It is noted that the correlation of pH with photocatalytic activity at a fixed temperature could have a more complex relationship since the increase in H^+ concentration in using lower pH will simultaneously decrease the concentration of OH^- due to water dissociation constant and will affect the overall kinetics. Thus, the addition of acid or alkali to the catalytic system may prolong the charge carrier lifetime, but it concomitantly decreases the concentration of counter ions (OH^- or H^+) due to ionisation equilibrium at room temperature, which is unfavourable kinetically, whereas the

use of high temperatures can increase both H^+ and OH^- at the same time by the promoted water ionisation, which is a promising and efficient way to promote the photocatalytic water splitting performances.

3.3.4 Practical application of the temperature-promoted POWS system

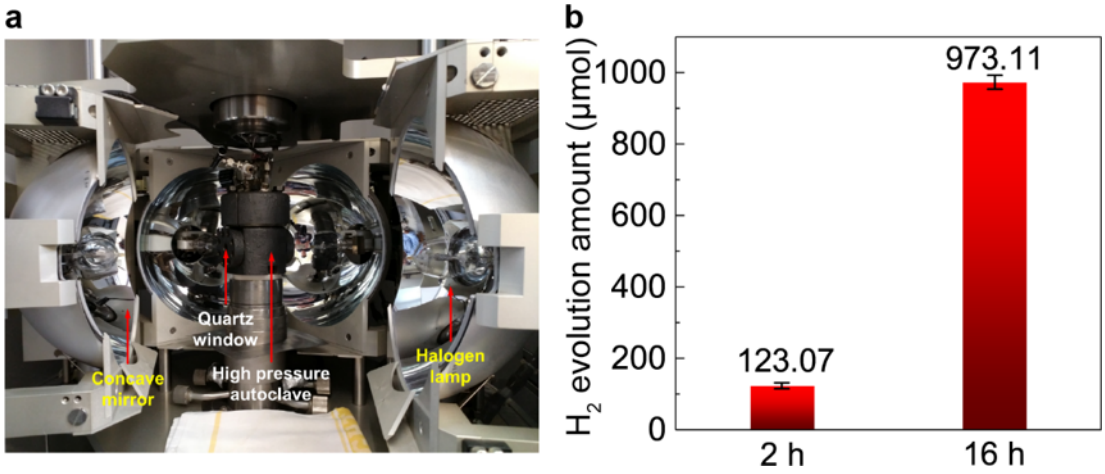

Figure 3.14 (a) photographic image of the light furnace used to mimic a solar concentrator; **(b)** The POWS activity tests of Au/N-P25-620 in the light furnace. This figure shows the total amount of the evolved H_2 gas (in μmol) after the reaction time of 2 h and 16 h. Conditions: 5 mg of Au/N-P25-620 was added to 10 mL of deionised H_2O in a 25-mL batch reactor under vigorous magnetic stirring, and Ar gas was used as the inert gas. Then the reactor was heated up to 270 °C and maintained for different reaction times. Both the heating and light irradiation are provided solely by the light furnace shown in **(a)**. The light furnace was operated by Dr. Dharmalingam Prabhakaran in the Department of Physics, University of Oxford.

Large-scale application of particulate photocatalytic systems has attracted increasing attention recently, due to its low cost compared with photovoltaic-powered electrolysis (PV-E) and photoelectrochemical (PEC) processes, and complicated reactor structures are not required.[59–61] Therefore, to demonstrate the technical feasibility of using solely the renewable light energy to supply the required thermal heat and visible photons for photocatalytic splitting of water in this new process, a light furnace was used to mimic the solar light concentrator without any direct thermal energy input from an electrical device. The reactor

temperature of 270 ^oC is maintained by this light source with the black body radiation, and a constant H_2 evolution rate of about 12 mmol $g^{-1}h^{-1}$ is achieved using Au/N-P25-620 for up to 16 hours of testing time (as shown in Figure 3.14). Different kinds of configurations and prototypes of solar concentrators were discussed recently[38] which are presumably helpful for scale-up H_2 production, such as parabolic cylinder reflectors that can provide enhanced light irradiation and temperature for solar energy applications.

Alternatively, the heat required for such a highly efficient photocatalytic water splitting system to produce H_2 may be provided by coupling with other exothermic processes for the subsequent H_2 utilisation at a comparable temperature range. For example, the formed H_2 if combined with N_2 (from air separation) can be used to produce ammonia which is a highly exothermic reaction. In addition, the H_2 evolution rate in our LEF enhanced water splitting system appears to match well with the ammonia evolution rate.[62,63] Based on our evaluation, the heat produced during ammonia synthesis could compensate the energy required for our LEF enhanced water splitting system, which gives an exciting possibility to turn the current natural gas dependent Haber-Bosch process to carbon-free photocatalytic practice for the ammonia synthesis. A similar scenario could be expected to couple with the strongly exothermic hydrogenation of CO_2 to methane, which may spark a new carbon-recycle technology for energy and environment. Some potential practical applications could be considered, which include the injection of separated H_2 from the photocatalytic splitting process at elevated temperatures for decentralised domestic devices into natural gas pipeline in UK and some parts of Europe, etc for caloric use of this renewable fuel. The calculations of the heat balance to prove the possibility of coupling the POWS system with other

exothermic systems are shown in Appendix Note A2.

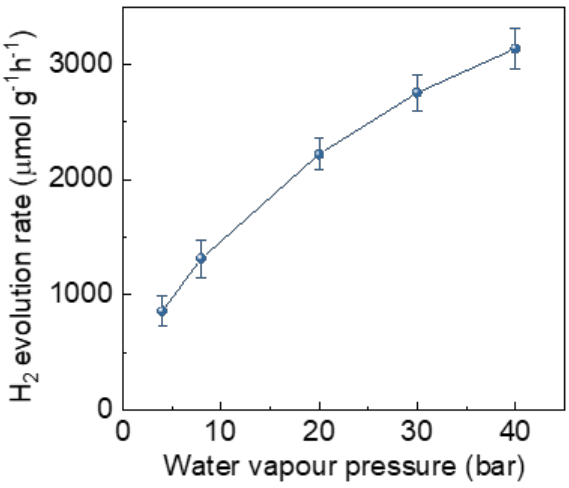

Figure 3.15 POWS performances over Au/N-P25-620 at different water vapour pressures at 270 °C. Error bars are defined as standard deviation.

Besides, further study in using water vapour at different pressures instead of liquid water is initiated, which is more controllable, easier to operate, possesses lower heat capacity and can be operated at lower pressure for the same temperature. As seen from Figure 3.15, the visible-light-driven water splitting system works well even using lower pressures of water vapour. A H_2 evolution rate of about 1500 μmol g^{-1} h^{-1} is achieved at a pressure of less than 10 bar.

3.4 Conclusion

In conclusion, a novel POWS system at elevated temperatures over N-TiO_2 based materials using visible light has been demonstrated in this chapter. A series of N-TiO_2 photocatalysts have been fabricated by a simple NH_3 treatment. XPS results show that the N species have been incorporated into the TiO_2 lattice as substitutional and interstitial N, respectively. The facilitated formation of surface V_Os in the presence of these N inclusions is also confirmed by EPR. It is evident that the visible-light-driven POWS reaction depends critically on the N and the

surface V_O content of N-TiO_2. I have also found that these surface defects as catalytically active centres are easily replenished in contact with oxygen sources at room temperature, leading to poor photocatalytic activity despite the existed bulk defects that can still take up visible light. However, the V_Os can be regenerated when heated to elevated temperatures. TRPL measurements show that the introduction of V_Os and deposition of a metal cocatalyst are both essential in prolonging the charge carrier lifetime to enable superior water splitting activity under visible light illumination. More importantly, lifetime of the photo-generated charge carriers can also be prolonged via local electric fields formed by high concentrations of adsorbed H^+ and OH^- resulting from enhanced water ionisation at elevated temperatures. Under these conditions, both H_2 evolution and regeneration of the electron depleted V_Os (photo-generated holes) to produce O_2 are greatly facilitated. Obviously, temperature shows remarkable effects on the POWS performances of N-TiO_2 nano-catalysts and extraordinary H_2 evolution rates and QEs have been achieved in this POWS system. Feasibility of potential practical application has also been considered by using a light furnace, by which heat and photons are both provided without engaging external electric heating device, and the sustainable H_2 evolution is maintained. Such POWS system may contribute to the future capture and utilisation of solar energy for H_2 production.

3.5 References

1. Li, Y., Peng, Y.-K., Hu, L., Zheng, J., Prabhakaran, D., Wu, S., Puchtler, T. J., Li, M., Wong, K.-Y., Taylor, R. A. & Tsang, S. C. E. Photocatalytic water splitting by N-TiO2 on MgO (111) with exceptional quantum efficiencies at elevated temperatures. *Nat. Commun.* **10**, 4421 (2019).
2. Wolff, C. M., Frischmann, P. D., Schulze, M., Bohn, B. J., Wein, R., Livadas, P., Carlson, M. T., Jäckel, F., Feldmann, J., Würthner, F. & Stolarczyk, J. K. All-in-one visible-light-driven water splitting by combining nanoparticulate and molecular co-catalysts on CdS nanorods. *Nat. Energy* **3**, 862–869 (2018).
3. Landman, A., Dotan, H., Shter, G. E., Wullenkord, M., Houaijia, A., Maljusch, A.,

Grader, G. S. & Rothschild, A. Photoelectrochemical water splitting in separate oxygen and hydrogen cells. *Nat. Mater.* **16**, 646–651 (2017).

4. Zhou, G., Shan, Y., Wang, L., Hu, Y., Guo, J., Hu, F., Shen, J., Gu, Y., Cui, J., Liu, L. & Wu, X. Photoinduced semiconductor-metal transition in ultrathin troilite FeS nanosheets to trigger efficient hydrogen evolution. *Nat. Commun.* **10**, 399 (2019).
5. Chen, X., Shen, S., Guo, L. & Mao, S. S. Semiconductor-based photocatalytic hydrogen generation. *Chem. Rev.* **110**, 6503–6570 (2010).
6. Li, Q., Guo, B., Yu, J., Ran, J., Zhang, B., Yan, H. & Gong, J. R. Highly efficient visible-light-driven photocatalytic hydrogen production of CdS-cluster-decorated graphene nanosheets. *J. Am. Chem. Soc.* **133**, 10878–10884 (2011).
7. Berry, G. D., Pasternak, A. D., Rambach, G. D., Smith, J. R. & Schock, R. N. Hydrogen as a future transportation fuel. *Energy* **21**, 289–303 (1996).
8. Boddy, P. J. Oxygen Evolution on Semiconducting TiO2. *J. Electrochem. Soc.* **115**, 199 (1968).
9. Fujishima, A. & Honda, K. Electrochemical Photolysis of Water at a Semiconductor Electrode. *Nature* **238**, 37–38 (1972).
10. Tabata, S., Nishida, H., Masaki, Y. & Tabata, K. Stoichiometric photocatalytic decomposition of pure water in Pt/TiO2 aqueous suspension system. *Catal. Letters* **34**, 245–249 (1995).
11. Sayama, K. & Arakawa, H. Effect of carbonate salt addition on the photocatalytic decomposition of liquid water over Pt-TiO2 catalyst. *J. Chem. Soc. - Faraday Trans.* **93**, 1647–1654 (1997).
12. Wang, Q. & Domen, K. Particulate Photocatalysts for Light-Driven Water Splitting: Mechanisms, Challenges, and Design Strategies. *Chem. Rev.* **120**, 919–985 (2020).
13. Liu, N., Häublein, V., Zhou, X., Venkatesan, U., Hartmann, M., MačKović, M., Nakajima, T., Spiecker, E., Osvet, A., Frey, L. & Schmuki, P. 'Black' TiO2 Nanotubes Formed by High-Energy Proton Implantation Show Noble-Metal-co-Catalyst Free Photocatalytic H2-Evolution. *Nano Lett.* **15**, 6815–6820 (2015).
14. Asahi, R., Morikawa, T., Ohwaki, T., Aoki, K. & Taga, Y. Visible-light photocatalysis in nitrogen-doped titanium oxides. *Science* **293**, 269–271 (2001).
15. Chen, X., Liu, L., Yu, P. Y. & Mao, S. S. Increasing solar absorption for photocatalysis with black hydrogenated titanium dioxide nanocrystals. *Science* **331**, 746–750 (2011).
16. Asahi, R., Morikawa, T., Irie, H. & Ohwaki, T. Nitrogen-doped titanium dioxide as visible-light-sensitive photocatalyst: Designs, developments, and prospects. *Chem. Rev.* **114**, 9824–9852 (2014).
17. Imanishi, A., Okamura, T., Ohashi, N., Nakamura, R. & Nakato, Y. Mechanism of water photooxidation reaction at atomically flat TiO 2 (rutile) (110) and (100) surfaces: Dependence on solution pH. *J. Am. Chem. Soc.* **129**, 11569–11578 (2007).
18. Padilha, A. C. M., Raebiger, H., Rocha, A. R. & Dalpian, G. M. Charge storage in oxygen deficient phases of TiO2: Defect Physics without defects. *Sci. Rep.* **6**, 2–8 (2016).
19. Wang, Z., Li, C. & Domen, K. Recent developments in heterogeneous photocatalysts for solar-driven overall water splitting. *Chem. Soc. Rev.* **48**, 2109–2125 (2019).

20. Maeda, K., Teramura, K., Lu, D., Saito, N., Inoue, Y. & Domen, K. Noble-Metal/Cr2O3 Core/Shell Nanoparticles as a Cocatalyst for Photocatalytic Overall Water Splitting. *Angew. Chemie* **118**, 7970–7973 (2006).

21. Polo, A. S., Itokazu, M. K. & Murakami Iha, N. Y. Metal complex sensitizers in dye-sensitized solar cells. *Coord. Chem. Rev.* **248**, 1343–1361 (2004).

22. Etacheri, V., Di Valentin, C., Schneider, J., Bahnemann, D. & Pillai, S. C. Visible-light activation of TiO2 photocatalysts: Advances in theory and experiments. *J. Photochem. Photobiol. C Photochem. Rev.* **25**, 1–29 (2015).

23. Wang, Q., Hisatomi, T., Jia, Q., Tokudome, H., Zhong, M., Wang, C., Pan, Z., Takata, T., Nakabayashi, M., Shibata, N., Li, Y., Sharp, I. D., Kudo, A., Yamada, T. & Domen, K. Scalable water splitting on particulate photocatalyst sheets with a solar-to-hydrogen energy conversion efficiency exceeding 1%. *Nat. Mater.* **15**, 611–615 (2016).

24. Han, B. & Hu, Y. H. Highly Efficient Temperature-Induced Visible Light Photocatalytic Hydrogen Production from Water. *J. Phys. Chem. C* **119**, 18927–18934 (2015).

25. Tian, B., Tian, B., Smith, B., Scott, M. C., Hua, R., Lei, Q. & Tian, Y. Supported black phosphorus nanosheets as hydrogen-evolving photocatalyst achieving 5.4% energy conversion efficiency at 353 K. *Nat. Commun.* **9**, 1397 (2018).

26. Han, Z., Qiu, F., Eisenberg, R., Holland, P. L. & Krauss, T. D. Robust photogeneration of H2in water using semiconductor nanocrystals and a nickel catalyst. *Science* **338**, 1321–1324 (2012).

27. Zhou, W., Li, W., Wang, J. Q., Qu, Y., Yang, Y., Xie, Y., Zhang, K., Wang, L., Fu, H. & Zhao, D. Ordered mesoporous black TiO2 as highly efficient hydrogen evolution photocatalyst. *J. Am. Chem. Soc.* **136**, 9280–9283 (2014).

28. Park, K. H., An, Y., Jung, S., Park, H. & Yang, C. The use of an n-type macromolecular additive as a simple yet effective tool for improving and stabilizing the performance of organic solar cells. *Energy Environ. Sci.* **9**, 3464–3471 (2016).

29. Foo, C., Li, Y., Lebedev, K., Chen, T. T., Day, S., Tang, C. & Tsang, S. C. E. Characterisation of oxygen defects and nitrogen impurities in TiO2 photocatalysts using variable-temperature X-ray powder diffraction. *Nat. Commun.* **12**, 661 (2021).

30. Di Valentin, C., Pacchioni, G., Selloni, A., Livraghi, S. & Giamello, E. Characterization of paramagnetic species in N-doped TiO 2 powders by EPR spectroscopy and DFT calculations. *J. Phys. Chem. B* **109**, 11414–11419 (2005).

31. Livraghi, S., Paganini, M. C., Giamello, E., Selloni, A., Di Valentin, C. & Pacchioni, G. Origin of photoactivity of nitrogen-doped titanium dioxide under visible light. *J. Am. Chem. Soc.* **128**, 15666–15671 (2006).

32. Makuła, P., Pacia, M. & Macyk, W. How To Correctly Determine the Band Gap Energy of Modified Semiconductor Photocatalysts Based on UV-Vis Spectra. *J. Phys. Chem. Lett.* **9**, 6814–6817 (2018).

33. Wang, J., Tafen, D. N., Lewis, J. P., Hong, Z., Manivannan, A., Zhi, M., Li, M. & Wu, N. Origin of photocatalytic activity of Nitrogen-doped TiO2 nanobelts. *J. Am. Chem. Soc.* **131**, 12290–12297 (2009).

34. Savio, A. K. P. D., Fletcher, J., Smith, K., Iyer, R., Bao, J. M. & Robles Hernández, F. C. Environmentally effective photocatalyst CoO-TiO2 synthesized by thermal precipitation of Co in amorphous TiO2. *Appl. Catal. B Environ.* **182**, 449–455 (2016).

35. Ren, Z., Chen, C., Fu, X., Wang, J., Fan, C., Qian, G. & Wang, Z. TiO2/C composites nanorods synthesized by internal-reflux method for lithium-ion battery

anode materials. *Mater. Lett.* **117**, 124–127 (2014).

36. Liu, X., Xing, Z., Zhang, Y., Li, Z., Wu, X., Tan, S., Yu, X., Zhu, Q. & Zhou, W. Fabrication of 3D flower-like black N-TiO2-x@MoS2 for unprecedented-high visible-light-driven photocatalytic performance. *Appl. Catal. B Environ.* **201**, 119–127 (2017).

37. Zhang, K., Zhou, W., Zhang, X., Sun, B., Wang, L., Pan, K., Jiang, B., Tian, G. & Fu, H. Self-floating amphiphilic black TiO2 foams with 3D macro-mesoporous architectures as efficient solar-driven photocatalysts. *Appl. Catal. B Environ.* **206**, 336–343 (2017).

38. D'Arienzo, M., Carbajo, J., Bahamonde, A., Crippa, M., Polizzi, S., Scotti, R., Wahba, L. & Morazzoni, F. Photogenerated defects in shape-controlled TiO 2 anatase nanocrystals: A probe to evaluate the role of crystal facets in photocatalytic processes. *J. Am. Chem. Soc.* **133**, 17652–17661 (2011).

39. Zhang, C., Zhou, Y., Bao, J., Sheng, X., Fang, J., Zhao, S., Zhang, Y. & Chen, W. Hierarchical Honeycomb Br-, N-Codoped TiO2 with Enhanced Visible-Light Photocatalytic H2 Production. *ACS Appl. Mater. Interfaces* **10**, 18796–18804 (2018).

40. Moss, B., Wang, Q., Butler, K. T., Grau-Crespo, R., Selim, S., Regoutz, A., Hisatomi, T., Godin, R., Payne, D. J., Kafizas, A., Domen, K., Steier, L. & Durrant, J. R. Linking in situ charge accumulation to electronic structure in doped SrTiO3 reveals design principles for hydrogen-evolving photocatalysts. *Nat. Mater.* **20**, 511–517 (2021).

41. Bandura, A. V. & Lvov, S. N. The ionization constant of water over wide ranges of temperature and density. *J. Phys. Chem. Ref. Data* **35**, 15–30 (2006).

42. Litter, M. I. Heterogeneous photocatalysis: Transition metal ions in photocatalytic systems. *Appl. Catal. B Environ.* **23**, 89–114 (1999).

43. Hou, W. & Cronin, S. B. A review of surface plasmon resonance-enhanced photocatalysis. *Adv. Funct. Mater.* **23**, 1612–1619 (2013).

44. Liu, Z., Hou, W., Pavaskar, P., Aykol, M. & Cronin, S. B. Plasmon resonant enhancement of photocatalytic water splitting under visible illumination. *Nano Lett.* **11**, 1111–1116 (2011).

45. Furube, A., Du, L., Hara, K., Katoh, R. & Tachiya, M. Ultrafast plasmon-induced electron transfer from gold nanodots into TiO2 nanoparticles. *J. Am. Chem. Soc.* **129**, 14852–14853 (2007).

46. Liu, J., Liu, Y., Liu, N., Han, Y., Zhang, X., Huang, H., Lifshitz, Y., Lee, S. T., Zhong, J. & Kang, Z. Metal-free efficient photocatalyst for stable visible water splitting via a two-electron pathway. *Science* **347**, 970–974 (2015).

47. Che, W., Cheng, W., Yao, T., Tang, F., Liu, W., Su, H., Huang, Y., Liu, Q., Liu, J., Hu, F., Pan, Z., Sun, Z. & Wei, S. Fast Photoelectron Transfer in (Cring)-C3N4 Plane Heterostructural Nanosheets for Overall Water Splitting. *J. Am. Chem. Soc.* **139**, 3021–3026 (2017).

48. Zhang, G., Lan, Z. A., Lin, L., Lin, S. & Wang, X. Overall water splitting by Pt/g-C3N4 photocatalysts without using sacrificial agents. *Chem. Sci.* **7**, 3062–3066 (2016).

49. Maeda, K., Teramura, K., Lu, D., Takata, T., Saito, N., Inoue, Y. & Domen, K. Photocatalyst releasing hydrogen from water. *Nature* **440**, 295 (2006).

50. Han, K., Kreuger, T., Mei, B. & Mul, G. Transient Behavior of Ni@NiOx Functionalized SrTiO3 in Overall Water Splitting. *ACS Catal.* **7**, 1610–1614 (2017).

51. Zheng, D., Cao, X. N. & Wang, X. Precise Formation of a Hollow Carbon Nitride Structure with a Janus Surface To Promote Water Splitting by Photoredox Catalysis. *Angew. Chem. Int. Ed.* **55**, 11512–11516 (2016).

52. Fang, W., Liu, J., Yang, D., Wei, Z., Jiang, Z. & Shangguan, W. Effect of Surface Self-Heterojunction Existed in BixY1-xVO4 on Photocatalytic Overall Water Splitting. *ACS Sustain. Chem. Eng.* **5**, 6578–6584 (2017).

53. Xing, M., Zhang, J., Chen, F. & Tian, B. An economic method to prepare vacuum activated photocatalysts with high photo-activities and photosensitivities. *Chem. Commun.* **47**, 4947–4949 (2011).

54. Zuo, F., Bozhilov, K., Dillon, R. J., Wang, L., Smith, P., Zhao, X., Bardeen, C. & Feng, P. Active facets on titanium(III)-doped TiO 2: An effective strategy to improve the visible-light photocatalytic activity. *Angew. Chem. Int. Ed.* **51**, 6223–6226 (2012).

55. Tian, B., Lei, Q., Zhang, W., Cui, Y., Tian, Y. & Tian, B. UV-driven overall water splitting using unsupported gold nanoparticles as photocatalysts. *Chem. Commun.* **54**, 1845–1848 (2018).

56. Liu, B., Su, S., Zhou, W., Wang, Y., Wei, D., Yao, L., Ni, Y., Cao, M. & Hu, C. Photo-reduction assisted synthesis of W-doped TiO2 coupled with Au nanoparticles for highly efficient photocatalytic hydrogen evolution. *CrystEngComm* **19**, 675–683 (2017).

57. Zhang, K., Zhou, W., Chi, L., Zhang, X., Hu, W., Jiang, B., Pan, K., Tian, G. & Jiang, Z. Black N/H-TiO2 nanoplates with a flower-like hierarchical architecture for photocatalytic hydrogen evolution. *ChemSusChem* **9**, 2841–2848 (2016).

58. Zhang, K., Wang, L., Kim, J. K., Ma, M., Veerappan, G., Lee, C. L., Kong, K. J., Lee, H. & Park, J. H. An order/disorder/water junction system for highly efficient co-catalyst-free photocatalytic hydrogen generation. *Energy Environ. Sci.* **9**, 499–503 (2016).

59. Hisatomi, T. & Domen, K. Reaction systems for solar hydrogen production via water splitting with particulate semiconductor photocatalysts. *Nat. Catal.* **2**, 387–399 (2019).

60. Takata, T. & Domen, K. Particulate Photocatalysts for Water Splitting: Recent Advances and Future Prospects. *ACS Energy Lett.* **4**, 542–549 (2019).

61. Pinaud, B. A., Benck, J. D., Seitz, L. C., Forman, A. J., Chen, Z., Deutsch, T. G., James, B. D., Baum, K. N., Baum, G. N., Ardo, S., Wang, H., Miller, E. & Jaramillo, T. F. Technical and economic feasibility of centralized facilities for solar hydrogen production via photocatalysis and photoelectrochemistry. *Energy Environ. Sci.* **6**, 1983–2002 (2013).

62. Inoue, Y., Kitano, M., Kim, S. W., Yokoyama, T., Hara, M. & Hosono, H. Highly dispersed ru on electride [Ca24Al28O 64]4+(e-)4 as a catalyst for ammonia synthesis. *ACS Catal.* **4**, 674–680 (2014).

63. Lin, B., Heng, L., Fang, B., Yin, H., Ni, J., Wang, X., Lin, J. & Jiang, L. Ammonia Synthesis Activity of Alumina-Supported Ruthenium Catalyst Enhanced by Alumina Phase Transformation. *ACS Catal.* **9**, 1635–1644 (2019).

Chapter 4 Effects of the local electric field on photocatalytic overall water splitting reaction

This chapter is adapted from the work by Yiyang Li, Simson Wu, Jianwei Zheng, Yung-Kang Peng, Dharmalingam Prabhakaran, Robert A. Taylor, Shik Chi Edman Tsang, published in Materials Today in 2020. The figures are reproduced with permission. Copyright 2020 Elsevier.[1]

4.1 Introduction

As demonstrated before, a typical photocatalytic reaction involves three fundamental steps, namely, excitation, charge separation, and surface chemical reactions. Much progress has been achieved to broaden the absorption spectra by band gap engineering and facilitate the surface reactions by loading cocatalysts, however, the separation of charge carriers remains untamed and in most cases the charge recombination readily takes place, leading to poor quantum efficiency (QE) and photocatalytic activities. Apparently, the photo-generated electron-hole pairs must possess a sufficient lifetime to capture both H^+ and OH^- species derived from the water molecules to allow efficient photocatalysis to take place. Therefore, strategies for suppressing the charge recombination are required.

Recent reports have shown that polarisation plays an important role in the separation of these photo-generated electrons and holes, which prolongs the lifetime of charge carriers, therefore leading to enhanced photocatalytic performance.[2–4] The introduction of an electric field to enhance the polarisation has recently been demonstrated to be an efficient approach for improving the charge separation both in bulk and on surface of the photocatalysts. Zhang's group reported a new strategy to introduce an internal electric field to Bi_3O_4Cl by carbon

incorporation.[3] The resulting C-doped Bi_3O_4Cl achieved a bulk charge separation efficiency of 80 %, therefore the charge carrier lifetime was prolonged from less than 500 ps to around 4000 ps, which is attributed to the strong internal electric field. This catalyst enabled photocatalytic water oxidation under visible light in the absence of sacrificial reagents; however, H_2 was scarcely detected because the CB is more positive than the H_2-evolving potential. Likewise, the same research group also reported a Janus Cl_2-$Bi_{12}O_{17}$-MoS_2 bilayer junction photocatalyst with strong internal electric field for H_2 evolution, in which the carrier lifetime was claimed to be 3446 ns and a H_2 evolution rate of 33 mmol g^{-1} h^{-1} was obtained with ascorbic acid as the hole scavenger.[4] However, the above strategies require fine control during the synthesis and only apply to a few circumstances, hindering it from wider applications.

As demonstrated in Chapter 3, a novel POWS system has been developed which is operated at elevated temperatures, where the water ionic dissociation is greatly enhanced and the surface adsorbed ion species create a local polarisation, which subsequently prolong the charge carrier lifetimes. Enlightened by such phenomenon, it came to my mind that I can use solid-state materials to create a stronger local electric field. In fact, polar-faceted materials have long been studied in catalysis since late 20th century, and the studies covered semiconductor surfaces, oxide surfaces, ultra-thin oxide films, and oxide interfaces.[5–7] For polar surfaces, the orientation is such that each repeat unit grows in the direction perpendicular to the surface, resulting in a non-zero dipole moment on the surfaces. Thus, electric fields and electrostatic forces are generated on polar surfaces[5], making such materials good candidates for the study of local polarisation effect.

In addition, two-dimensional (2D) materials such as graphene, transition metal dichalcogenides (TMDs), etc. have been proved to show great potential toward catalysis, energy conversion and many other fields in recent decades, among which single-layer MoS_2 (SL-MoS_2) has attracted considerable attention for photocatalytic and electrochemical H_2 evolution reaction (HER) due to its suitable band structure and low overpotential.[8–12] It has also been reported that with the reduction of the thickness of MoS_2, the optical, electronic and magnetic properties change dramatically.[13–15] The absorption properties and band structures have been therefore well studied,[14] which proved that as MoS_2 is exfoliated to monolayer, its band gap is broadened, making its conduction band and valance band possess sufficient thermodynamic driving forces to drive the H_2 and O_2 evolution reactions ($E_{VB} = +1.69\,V\ vs.SHE;\ E_{CB} = -0.11\,V\ vs.SHE$), respectively.[16,17] These make the SL-MoS_2 promising for solar-light-driven photocatalytic water splitting systems. However, so far, the SL-MoS_2 are still commonly used as a substitute of noble metal like Pt in photocatalytic or electrocatalytic H_2 evolution systems, and very few studies reported MoS_2 alone as the photocatalyst. Plus, sacrificial reagents are frequently engaged in such photocatalytic water splitting systems to capture the photo-generated holes due to the fast intrinsic charge recombination process, leading to unwanted by-products and extra costs.[11,12,18]

4.2 Objectives

Here in this chapter, I aim to explore the local polarisation effect on the POWS reaction system. As stated before, the local polarisation effect can provide local electric fields (LEFs) which will facilitate the charge carrier separation process, leading to enhanced POWS performances. Fortunately, the LEF can be provided

by polar-faceted materials. Therefore, the N-doped TiO_2 is firstly assembled with polar-faceted MgO (111) and its non-polar counterparts, MgO (110) and MgO (100), respectively. The influence of the local polarisation on the lifetime and POWS performance is therefore investigated.

Following the same idea, the 2D SL-MoS_2 is studied by assembling with the polar-faceted materials. The monolayer nature makes it more sensitive to the local electric field, considering the polarisation is quite localised within a small range; and the structural flexibility of the monolayer material allows it to form stronger interactions with the supports. Except for the previously mentioned MgO, CeO_2 and ZnO are also studied, and layered double hydroxides (LDHs) are engaged as well. POWS performances are subsequently investigated and with the help of time-resolved technique, the influence on the charge separation can also be studied. By involving two widely studied photocatalysts, TiO_2 and MoS_2, and different kinds of polar-faceted materials, the objective of this chapter is to show that the local polarisation can be a versatile strategy in photocatalysis. And also, the relationships between polarity, lifetime of the charge carriers, and POWS activity are carefully investigated and discussed.

4.3 Results and discussion

4.3.1 Electric field effects on TiO_2 based materials

4.3.1.1 LEF introduced by the polar-faceted MgO(111)

Enlightened by the results presented in Chapter 3, I realised that the local polarisation plays an important role in the POWS system. Therefore, the polar-faceted metal oxides were synthesised as supports to introduce local electric field due to the strong surface polarities. MgO(111) was firstly explored, and the non-

polar counterparts, MgO(110) and MgO(100), were also included for comparison. As is well known, the polar MgO(111) nanocrystals give surfaces of both negative (O^{2-}) or positive (Mg^{2+}) terminations,[19,20] giving a strong LEF to the catalyst particles (Figure 4.1A). TEM images shown in Figure 4.1B confirm the lattice fringes of 0.244 nm, 0.148 nm and 0.214 nm for MgO(111), MgO(110) and MgO(100) respectively, indicating the successful synthesis of the MgO samples with different exposed facets.

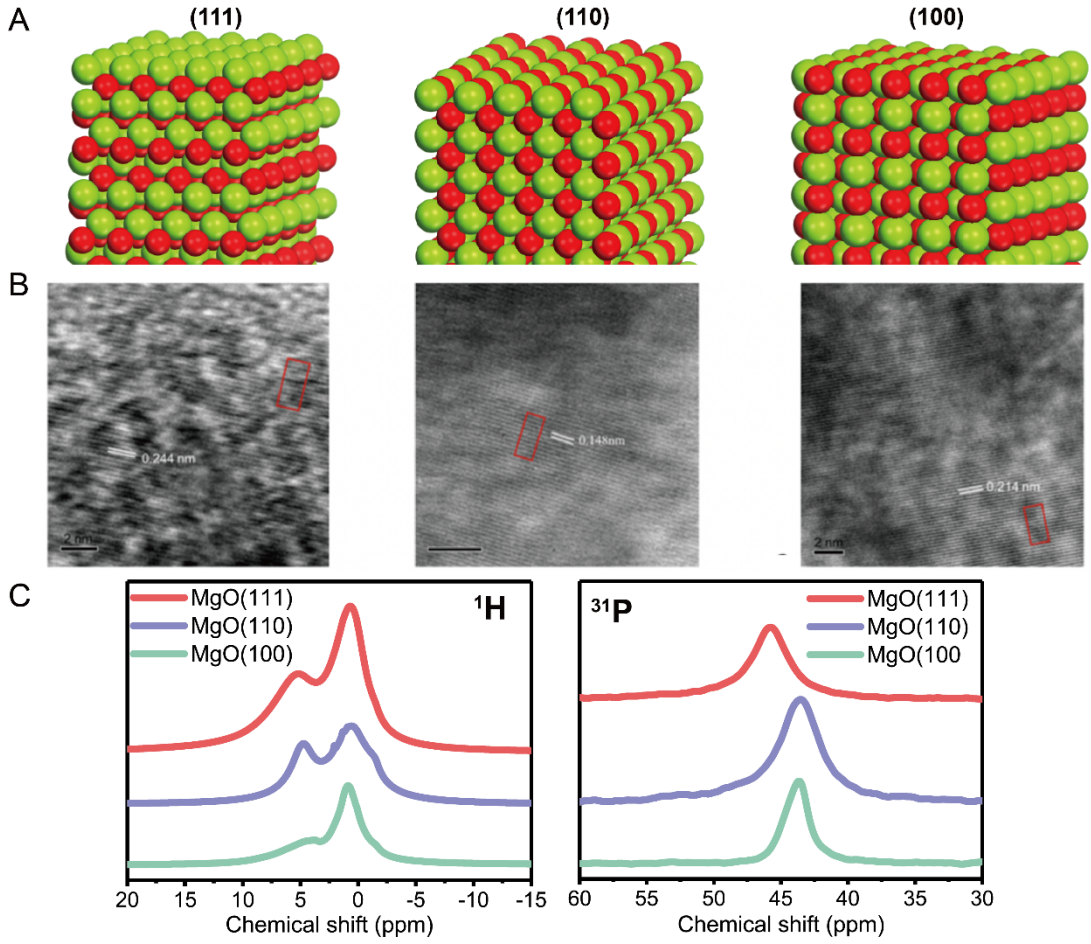

Figure 4.1 (A) Schematic illustrations of different MgO facets (O: red; Mg: green); **(B)** HRTEM images of MgO(111), (110) and (100) nanostructures; **(C)** ^{1}H NMR and TMPO-assisted ^{31}P MAS NMR measurements of MgO (111), (110), (100), respectively, which show the surface polarity of MgO (111) creates substantial chemical shifts to ^{1}H and ^{31}P. HRTEM images were acquired by Dr. Simson Wu, and NMR experiments were performed by Dr. Guangchao Li.

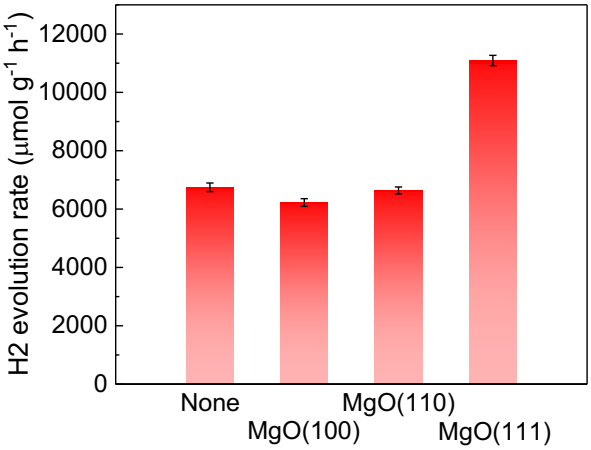

Figure 4.2 POWS activity tests of the 1 wt.% Au/N-P25-620 photocatalyst combined with different MgO supporting materials, including non-polar MgO(100) and MgO(110), and also the polar-faceted MgO(111). POWS reaction is performed at 270 °C with visible light irradiation.

^{1}H MAS NMR was carried out to evaluate the interaction of H^{+} with oxygen anions in bulk phase of MgO(111), (110) and (100) respectively. As shown in Figure 4.1C, a chemical shift at around 0.7 ppm can be observed in all MgO supports, which is attributed to the protons from isolated hydroxyl groups (*i.e.*, Mg-OH) and physical-adsorbed water molecules;[21] while the other peak observed at lower field, which can be assigned to the protons attached to the bridging oxygen (*i.e.*, Mg-O(H)-Mg), shifted to 5.43 ppm for MgO(111) compared with 4.78 ppm for MgO(110) and 4.74 ppm for MgO(100). Such a significant difference between polar MgO(111) surface and non-polar MgO(110) and (100) surface is due to the preferential proton adsorption on polar surface. Trimethylphosphine oxide (TMPO, chemical formula: $OP(CH_3)_3$) probe assisted ^{31}P MAS NMR was subsequently engaged to further confirm the surface polarity of MgO(111).[21,22] TMPO has lone pairs at the O atom, so it is a Lewis base and able to interact with the surface Lewis acid species, such as Mg^{2+} or H^{+}, which forms Lewis acid-base adducts. Such Lewis acid-base interactions can be observed through the change of chemical states by the

difference of chemical shifts in ^{31}P NMR. As shown in Figure 4.1C, a shift to 45.8 ppm for MgO(111) from 43 ppm for MgO(110) and (100) can be observed (chemical shift of physically adsorbed TMPO in ^{31}P NMR is at around 41 ppm), which also confirmed the surface polarity of the MgO(111) support.

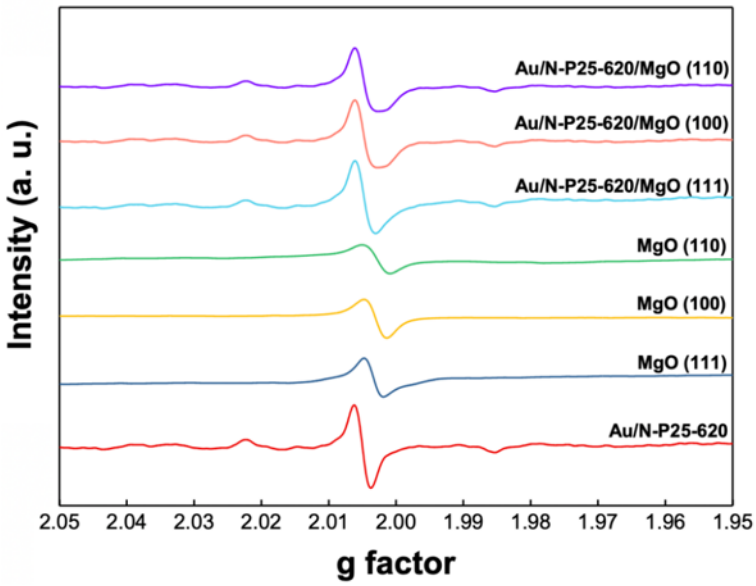

Figure 4.3 EPR spectra of Au/N-P25-620 with and without mixing with polar MgO(111), and non-polar MgO(100) and MgO(110), respectively.

Subsequently, the MgO materials were combined with the 1 wt.% Au/N-P25-620 that shows extraordinary POWS performance as comprehensively studied in Chapter 3. The POWS activity of the resulted Au/N-P25-620/MgO(111) photocatalyst was then tested using the same method, which gives a much enhanced and stable H_2 evolution rate of 11092 μmol g^{-1} h^{-1} with O_2 to H_2 at 1:2 ratio at 270 ^{o}C, while non-polar Au/N-P25-620/MgO (100) or (110) shows no rate promotion compared to that without the MgO support (Figure 4.2). To rule out the influence of other factors like oxygen vacancies (V_Os), EPR measurements were then carried out for the Au/N-P25-620 combined with polar and non-polar MgO supports. As can be seen from Figure 4.3, all the MgO supports showed small and similar signal at g=2.003, which can be assigned to the surface defects such as

V_Os of the MgO.[23,24] After mixing with the Au/N-P25-620 the mixtures showed similar patterns as the Au/N-P25-620 alone. In another word, the enhancement of the photocatalytic performance could not be due to the change of V_O concentrations, considering the different behaviours between polar MgO(111) and its non-polar counterparts.

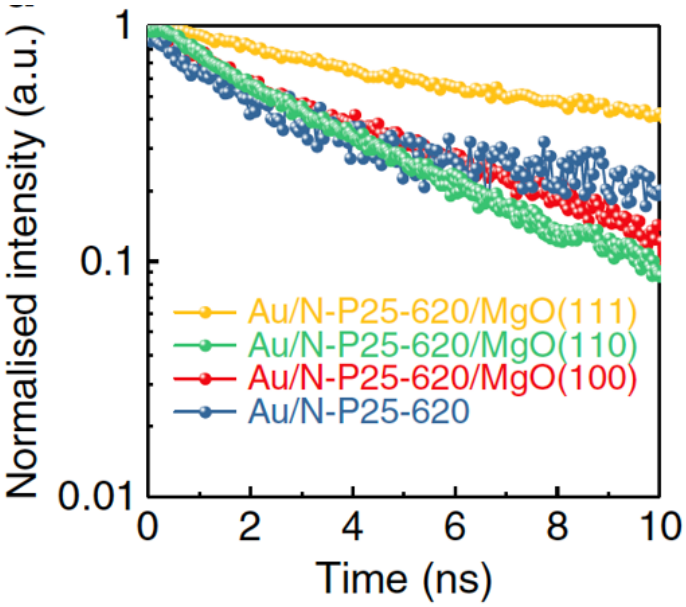

Figure 4.4 TRPL spectra of Au/N-P25-620 with and without MgO supports.

As mentioned before, the polarisation effect of the LEF is able to influence the separation of the photo-generated electron-hole pairs, therefore, TRPL was engaged to investigate the changes of the charge carrier lifetimes of the TiO_2-based photocatalysts combined with different MgO supports. As shown in Figure 4.4, MgO(111) shows strong effect on prolonging the charge carrier lifetime of the Au/N-P25-620 from 2.56 ns to 5.76 ns, whereas non-polar MgO(100) or (110) shows no apparent influence. Thus, it is indicated that the use of polar-faceted MgO(111) can introduce a strong LEF, which prolongs the charge carrier lifetimes and therefore enhances the photocatalytic water splitting activities. QE was also measured, which was further promoted to 81.8 % at 437 nm and 3.2 % at 1000

nm with the inclusion of MgO(111) (Figure 4.5). Activities of the MgO supports were also tested separately to confirm the MgO alone shows no contribution to POWS activity. A 10-cycle stability test was carried out for the Au/N-P25-620/MgO(111) which showed a stable photocatalytic activity (Figure 4.6).

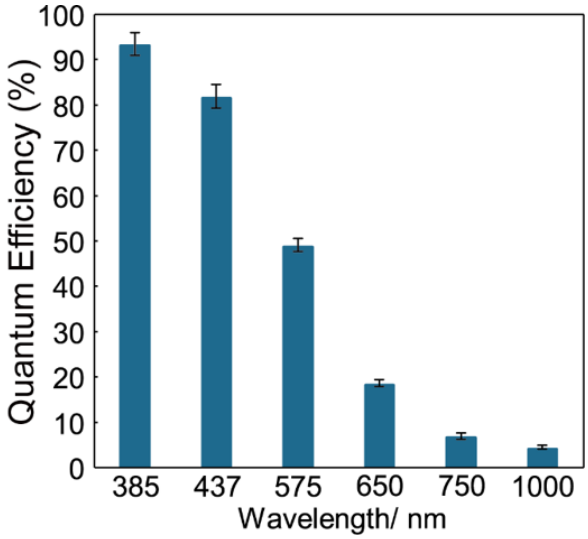

Figure 4.5 QEs of Au/N-P25-620/MgO(111) photocatalyst at different wavelengths.

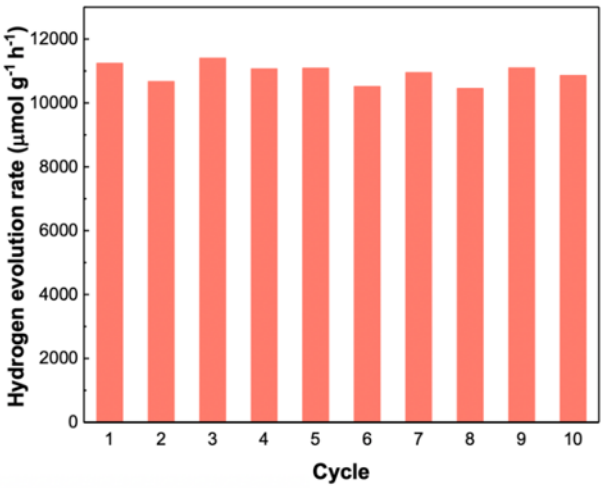

Figure 4.6 Stability test of Au/N-P25-620/MgO(111): 10 mg of Au/N-P25-620/MgO(111) was used in the POWS activity test (detailed method of activity testing has been demonstrated in Chapter 2). After reaction, the photocatalyst was separated by centrifuge and dried at 60 °C under vacuum overnight. This recycled photocatalyst was then used for the POWS activity test again, following exactly the same procedures. The photocatalyst was used and recycled for 10 cycles in total, and the activity of each cycle is shown in this figure.

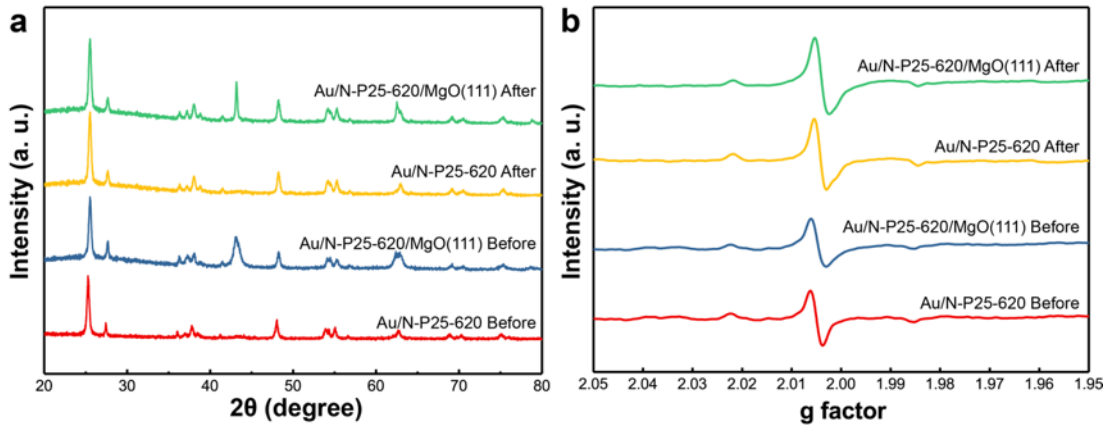

Figure 4.7 Post-reaction characterisations of the photocatalyst. XRD **(a)** and EPR **(b)** spectra of Au/N-P25-620 and Au/N-P25-620/MgO(111) before and after the 10-cycle photocatalytic water splitting test.

The used catalyst was characterised using XRD and EPR (Figure 4.7), which again suggested the good stability of the Au/N-P25-620/MgO (111) photocatalyst. For the Au/N-P25-620/MgO(111) photocatalyst, the XRD peaks of MgO became sharper after the reaction, indicating that there could be aggregation of the MgO(111) nanostructures during the POWS reaction at 270 °C. Also, the EPR signal increases after the reaction for both the Au/N-P25-620 and Au/N-P25-620/MgO(111), which agrees with the observations demonstrated in Chapter 3: the surface V_Os can be regenerated at elevated temperatures, no matter in an inert atmosphere or in liquid water, thus giving an increased EPR signal after the POWS reaction at 270 °C.

4.3.1.2 Investigation of the LEF

Further efforts were made to confirm the enhancement is due to the LEF effect. Since there might be artefacts introduced by different sizes and morphologies of the MgO supports, leading to different interfaces and catalytic behaviours, then N-TiO_2 with different particle sized were made and mixed with MgO(111). It has been considered that the LEF is a localised effect which makes only short-range influence.[2] Theoretically, more obvious LEF effect can be obtained on the N-TiO_2

with smaller particle size. Commercial ST-01 TiO_2 and sol-gel synthesised TiO_2 were treated with NH_3 flow and mixed with polar-faceted MgO (111), of which the size characterisation by TEM was shown in Figure 4.8. Visible-light-driven POWS performance was then evaluated over these photocatalysts, and indeed as we expected, smaller particle sizes led to more obvious enhancement of activities caused by LEF. It is noted that by changing the particle size of the N-TiO2 nanoparticles, the surface area also changes, which may influence the photocatalytic activity as well. Therefore, the LEF effect was quantified by an enhancement factor to rule out the influence of different surface areas, which was determined as the ratio of the H_2 evolution rates between N-TiO_2/MgO (111) and N-TiO_2, instead of comparing the absolute value of the H_2 evolution rate. Clearly, the enhancement factors increased as the particle sizes decreased, as shown in Table 4.1, the H_2 evolution rate of sol-gel prepared N-TiO_2 (9.7±0.3 nm) increased by a factor of 2.07 after mixed with MgO (111), while that of the N-P25-620 (35.3±4.7 nm) increased by only 1.64 times when mixed with the same polar oxide support.

Table 4.1 The N-TiO_2 inverse size-dependent enhancement with the LEF introduced by the polar MgO(111) support.

Cat. *	**Mean size (nm)**	**H_2 evolution rate (μmol h^{-1} g^{-1})**		**Enhancement**
		With MgO	**Without MgO**	
N-P25-620	35.3±4.7	11092	6746	1.64
N-ST-01-640	23.8±2.1	12078	6825	1.77
Sol-gel N-TiO_2	9.7±0.3	14538	7024	2.07

*1 wt.% Au was deposited onto each photocatalyst by photo-reduction method before the activity test.

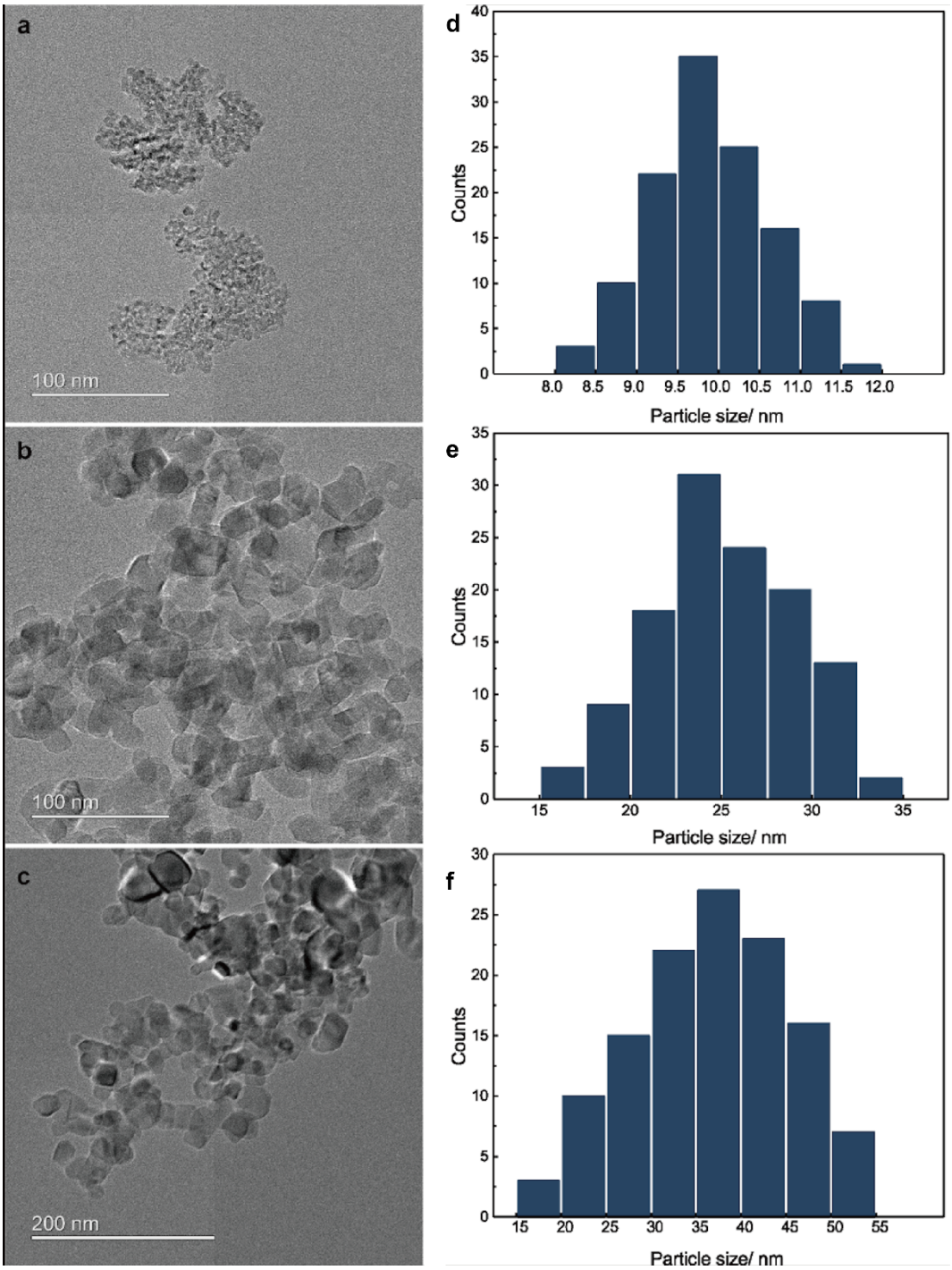

Figure 4.8 TEM images of the N-doped TiO_2 photocatalysts. **a:** different sizes of N-TiO_2 prepared by a sol-gel method; **b:** N-ST-01 and **c:** N-P25-620, together with the corresponding average particle size dispersions **(d-f)**. TEM images were acquired by Dr. Tianyi Chen.

4.3.2 Electric field effects on 2D MoS_2 based materials

4.3.2.1 Characterisations of MoS_2 based materials

The above results show that the local polarisation effect becomes more substantial

as the photocatalyst particles getting smaller, therefore, I realised that 2D materials such as SL-MoS_2 would presumably be promising for a better investigation of this effect. SL-MoS_2 monolayers were then prepared via a chemical exfoliation method, and decorated with atomically dispersed metal atoms by hydrothermal process[1,15]. The morphologies of the SL-MoS_2 were initially characterised by TEM, as shown in Figure 4.9. Compared with the large particle of extensive layered-structure morphology of the bulk form, it is exciting to observe the exfoliated SL-MoS_2 as thin monolayers. Atomic force microscopy (AFM) subsequently confirmed that the thickness of individual layers is about 0.6-0.7 nm, which is in good accordance with the layer thickness of *ca.* 0.65 nm of the S-Mo-S building block (Figure 4.10).

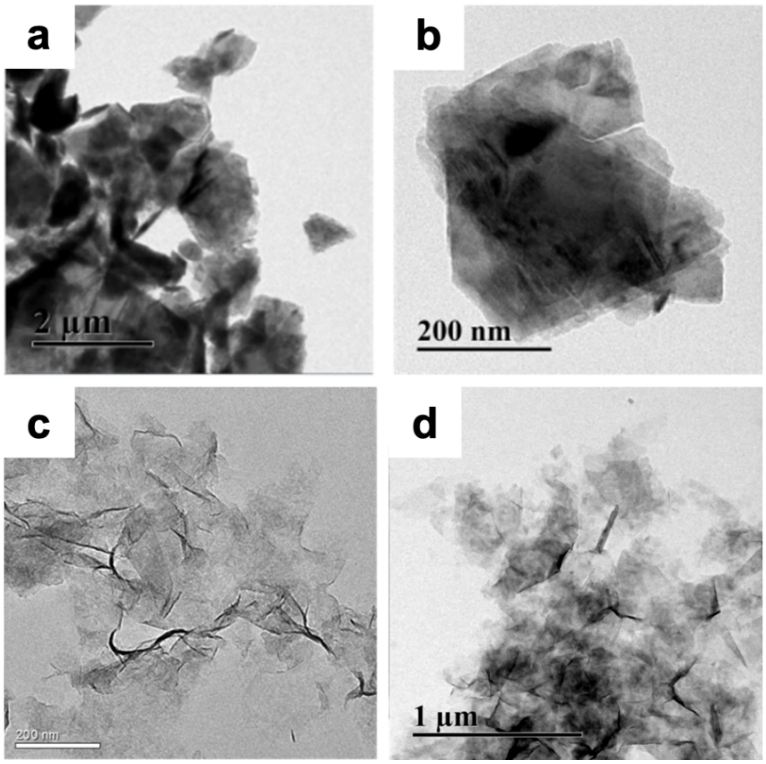

Figure 4.9 Conventional TEM image analyses of **(a, b)** bulk MoS_2, showing layered structure of crystal MoS_2, with lateral size varying from 0.5 to 2µm; **(c)** SL-MoS_2 and **(d)** Co:SL-MoS_2. After the incorporation of Co atoms, the morphology of SL-MoS_2 remains a sheet-like structure. Reproduced from ref. [1,15].

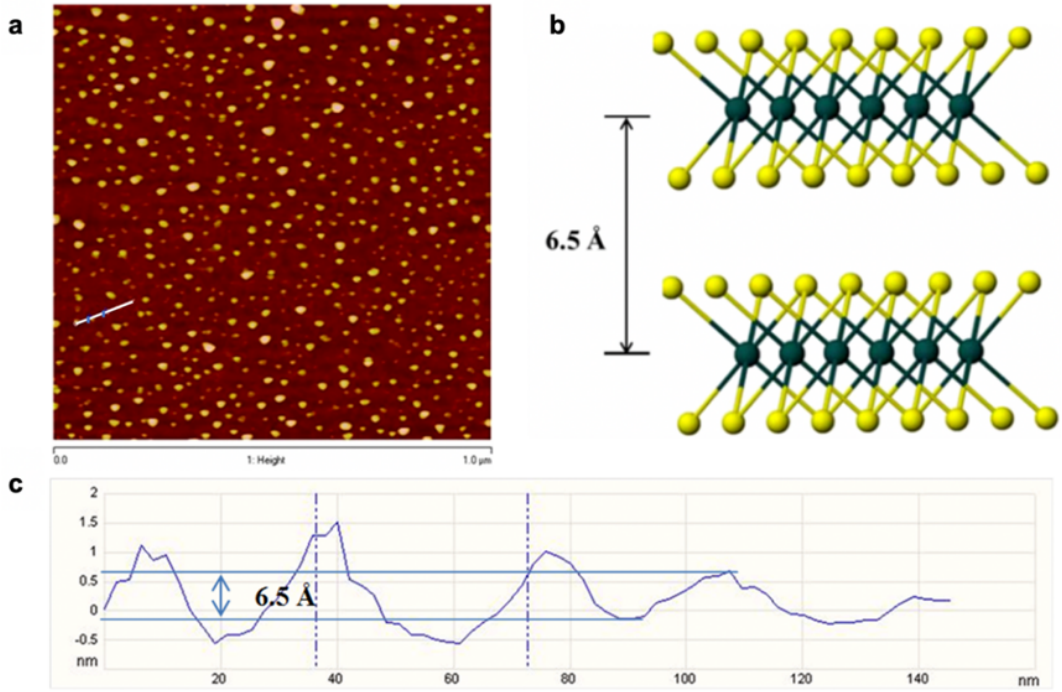

Figure 4.10 (a) AFM image of SL-MoS_2 spin-coated on a Si substrate; **(b)** a model of MoS_2 structure perpendicular to c axis. **(c)** height profile of the AFM image. Reproduced with permission from ref. 1,15. 100 flakes in **(a)** were scanned, with the majority of heights between 0.6-0.7nm. The lateral dimension of the MoS_2 monolayers is approximately 20-40 nm. It can be seen that the step heights of individual layers of 0.6-0.7 nm. This value is comparable to *ca.* 0.65 nm of a single layer of the S-Mo-S building block. Statistical analysis of 100 flakes revealed that 56% of the flakes to be monolayer, 28% of two layers and 13% of three layers and so on. The average topographic height is around 1.04 nm.

The metal doped SL-MoS_2 materials were then investigated with microscopic techniques as well, as can be seen in Figure 4.9d, after the incorporation of Co atoms, the morphologies of SL-MoS_2 still remained sheet-like structure. Then the Co:SL-MoS_2 was looked into in more details (Figure 4.11). HAADF-STEM together with electron energy loss spectroscopy (EELS), confirmed the existence of the Co single atoms on the Mo atop sites. The HAADF-STEM images of Fe:SL-MoS_2 and Ru:SL-MoS_2 are also shown in Figure 4.11, which again imply that single atoms are attached onto the single layer nanosheets and overlap the Mo and S positions. XRD measurements were also carried out before and after the chemical exfoliation process, not surprisingly, the XRD peaks were barely present after the exfoliation,

implying the successful preparation of the single layer nanosheets (Figure 4.12). Moreover, no apparent re-stacking happened after metal loading via hydrothermal treatment, given that the XRD patterns of the metal doped SL-MoS_2 are almost flat lines (Figure 4.12b).

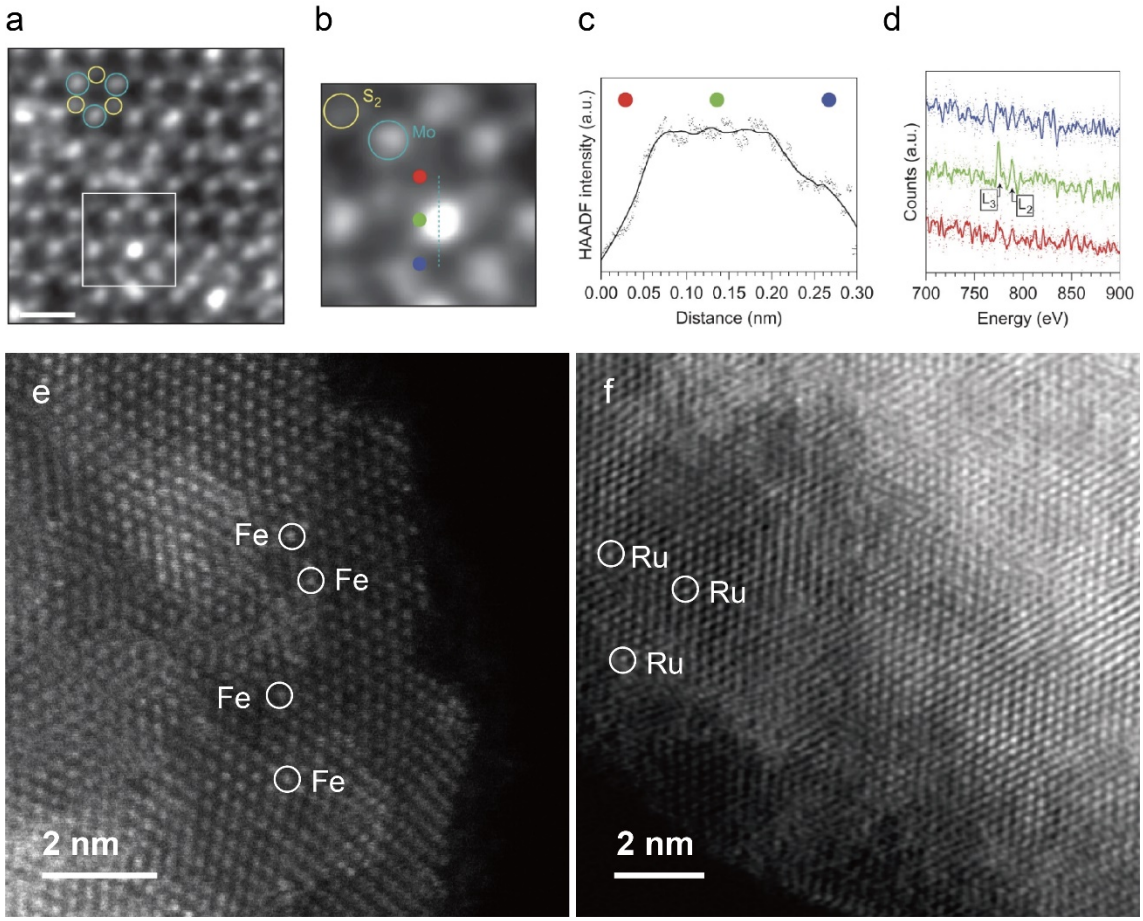

Figure 4.11 (a) HAADF-STEM image of Co–$SMoS_2$. Scale bar, 0.5 nm. **(b)** A magnified view of the boxed area of **a**. Simultaneous acquisition HAADF **(c)** and EELS **(d)** acquired along the line in **b**, with EELS extracted from above (red), on (green), and below (blue) the Co atom on the Mo atop site. The L_3 and L_2 edges for Co are indicated, confirming the scanned atomic column contains a Co atom. **(e, f)** HAADF-STEM images of **(e)** Fe:SL-MoS_2 and **(f)** Ru:SL-MoS_2

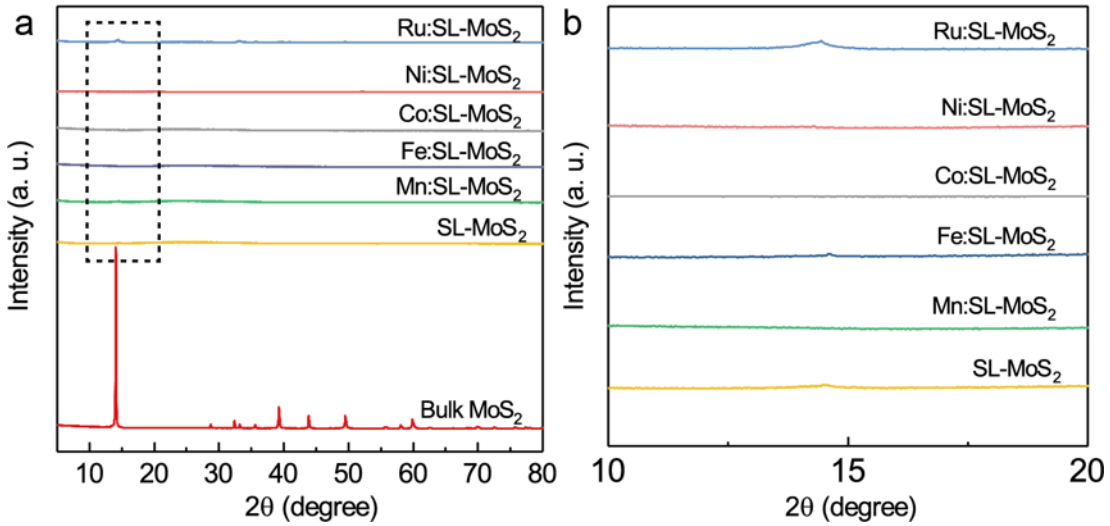

Figure 4.12 (a) XRD patterns of bulk MoS_2, SL-MoS_2 and the metal-doped SL-MoS_2; **(b)** Enlarged XRD patterns of SL-MoS_2 and the metal-doped SL-MoS_2 in the range of 10-20°, as indicated in **(a)**.

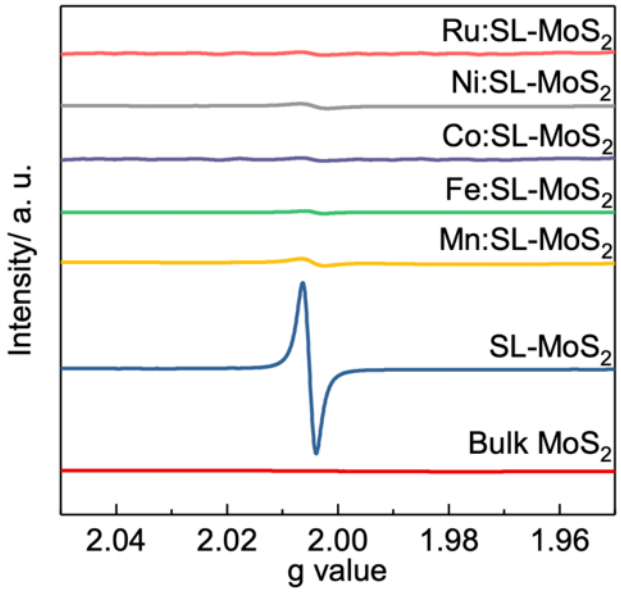

Figure 4.13 EPR spectra of bulk MoS_2, SL-MoS_2 and the metal-doped SL-MoS_2.

EPR experiments were carried out to investigate the surface defects, as shown in Figure 4.13. SL-MoS_2 showed an increased EPR signal at around g=2.005, which originated from the sulphur vacancies, while bulk MoS_2 remained silent on EPR. It is also shown that after the metal doping, the signal sharply decreased compared with pure SL-MoS_2, implying the metal species were favourably anchored on the sulphur vacancy sites. A control experiment was carried out by treating the SL-

MoS_2 with the hydrothermal process, but without adding any metal precursors. The result showed that EPR signal remained after the hydrothermal treatment in the absence of the metal precursors.

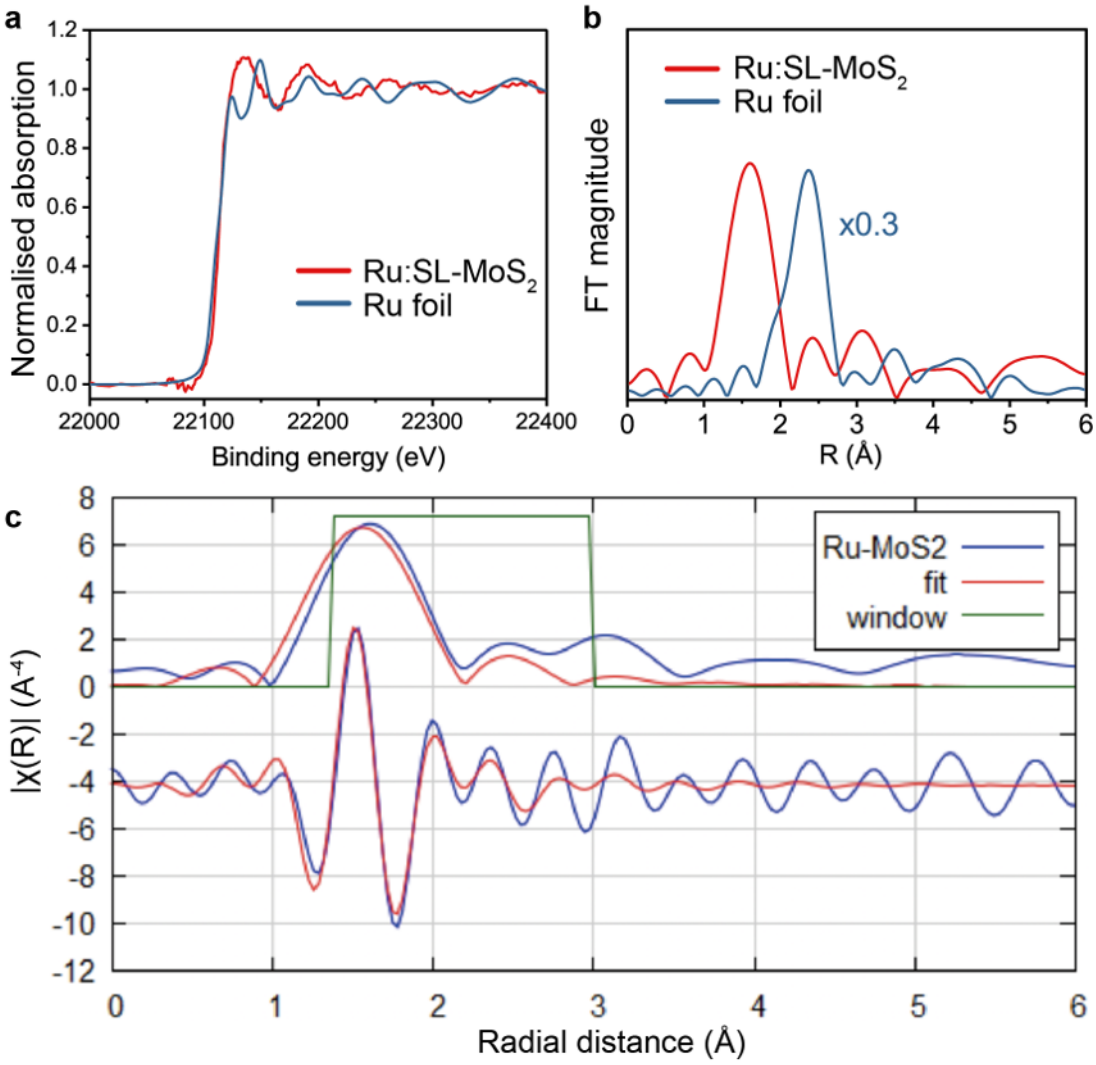

Figure 4.14 (a) Ru K-edge XANES spectra of the Ru:SL-MoS_2 and the Ru (0) foil reference. **(b)** FT-EXAFS spectra of the Ru:SL-MoS_2 and the Ru (0) foil reference for Ru K-edge. **(c)** Fourier transforms of k^3-weighted Ru K-edge of the EXAFS spectrum of the Ru:SL-MoS_2. These XANES and EXAFS were performed and analysed by Dr. Simson Wu of Prof. Edman Tsang' s group.

To investigate the local structures of the decorated metal species more precisely, X-ray absorption near edge structure (XANES) and extended X-ray absorption fine structure (EXAFS) measurements were conducted. Figure 4.14a shows the XANES curves of the Ru:SL-MoS_2 sample and the Ru (0) foil reference at Ru K-

edge. It is found that the Ru:SL-MoS_2 shares nearly the same absorption edge as Ru foil, suggesting the presence of Ru (0) species in the sample. Fourier transformed (FT) EXAFS spectra of Ru K-edge showed no peak related to Ru-Ru scattering at 2.42 Å (before phase shift), indicating the absence of Ru-Ru bond in the Ru:SL-MoS_2. Instead, the peak at 1.68±0.03 Å was observed, which is attributed to the contribution of Ru-S scattering. Subsequent least-squares fitting of the EXAFS spectrum (Figure 4.14c) revealed a three-sulphur coordination to the Ru at 1.68±0.03 Å (coordination number: 2.8±0.3; R-range: 1.3-3.0; Debye Waller's factor: 0.006±0.001; R-factor: 3.5%), which concomitantly matches with our expectation that the doped Ru atoms are anchored in the S sites with each Ru surrounded by 3 nearest sulphur atoms.

4.3.2.2 POWS performance of MoS_2-based materials

The POWS performance was then evaluated at 270 ^oC under visible light irradiation. The bulk MoS_2 showed no activity for this reaction, while SL-MoS_2 exhibited a H_2 evolution rate of 157 μmol $g^{-1}h^{-1}$. Control experiments that carried out in dark or in the absence of catalysts showed no activity, confirming the stoichiometric H_2 and O_2 evolution (as will be shown later in this chapter) is due to the photocatalytic water splitting over the MoS_2-based photocatalysts. UV-Vis diffuse reflectance spectroscopy (DRS) was performed for the SL-MoS_2, which indicates that the SL-MoS_2 exhibits good visible light absorption in the range of 400-700 nm (Figure 4.15a), and the Tauc plot gives a band gap energy of 1.93 eV (Figure 4.15b). The POWS activity can be largely enhanced after the metal doping, among which the Ru-doped SL-MoS_2 (Ru:SL-MoS_2) shows the best H_2 evolution rate of 821 μmol $g^{-1}h^{-1}$ (Figure 4.15c). Therefore, the following study was focused on the Ru:SL-MoS_2.

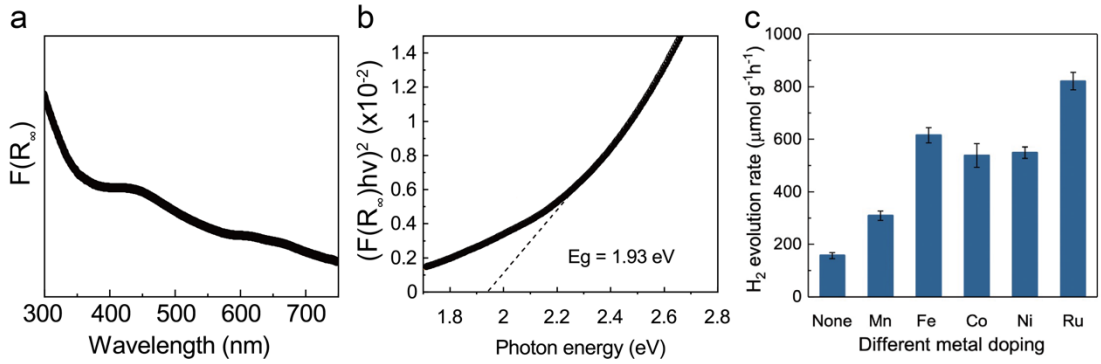

Figure 4.15 (a) UV-Vis absorption spectra of the SL-MoS_2 converted from the UV-Vis DRS using the Kubelka-Munk function. **(b)** Tauc plot of the SL-MoS_2 derived from **(a)**. **(c)** Photocatalytic water splitting performance over different metal-doped MoS_2 single layer. Error bars indicate the standard deviations.

4.3.2.3 Characterisations of the polar-faceted metal oxides

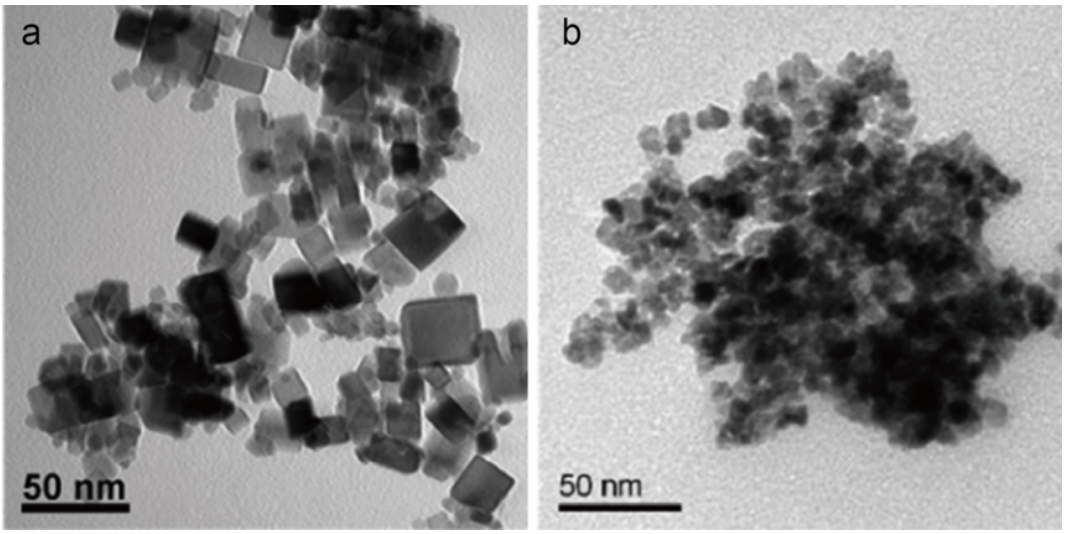

Figure 4.16 TEM images of **(a)** polar-faceted CeO_2 nanocubes with predominant (100) surfaces and **(b)** non-polar CeO_2 nanospheres.

Subsequently, the study of local polarisation effect was carried out by assembling the Ru:SL-MoS_2 with various polar-faceted metal oxide supports. Besides the MgO(111), MgO(110), and MgO(100) which have been discussed before, polar CeO_2(100) nanocubes (NCs), polar ZnO(0001) nanoplates (NPs), non-polar CeO_2 nanospheres (NSs), and non-polar ZnO nanorods (NRs) were also included for the study of local polarisation effect. These polar surfaces display alternative anion and cation layers hence the top surfaces possess non-zero polarity.

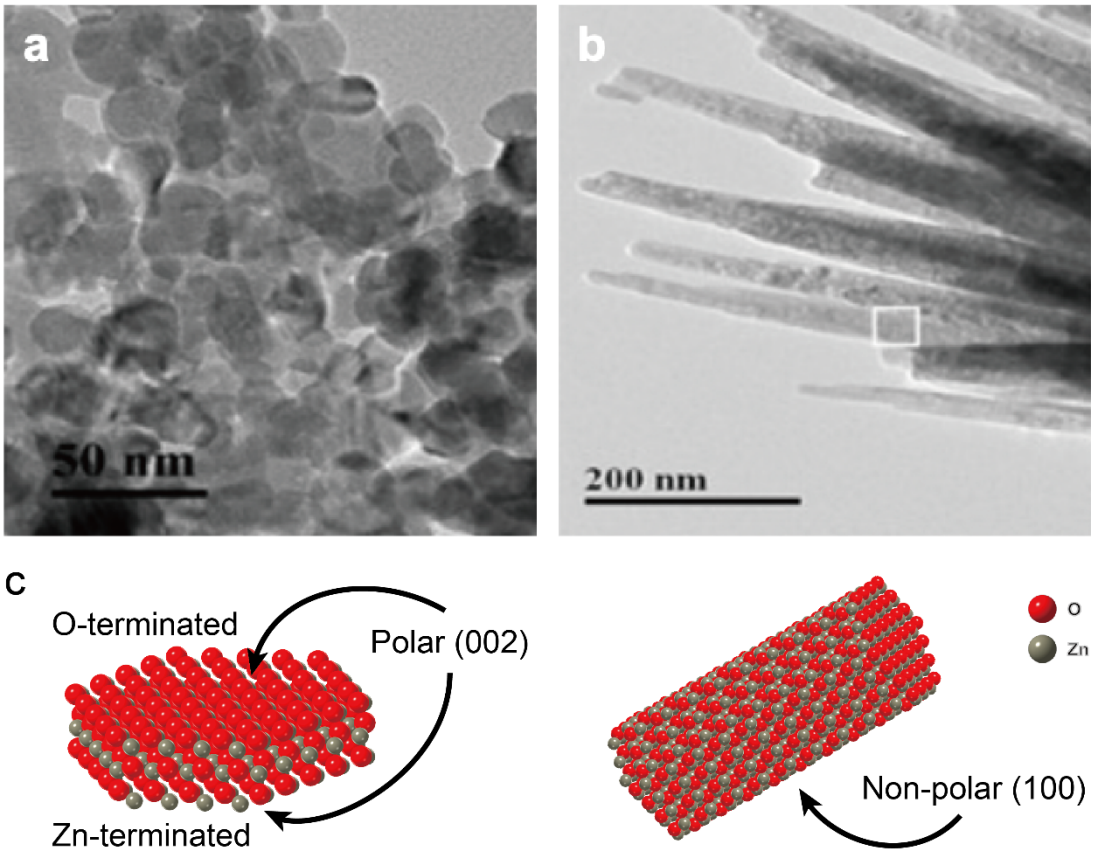

Figure 4.17 TEM images of **(a)** polar-faceted ZnO (0001) nanoplates and **(b)** non-polar ZnO nanorods. **(c)** Schematic illustration of the polar and non-polar facets of the ZnO nanoplates and nanorods.

Microscopic images of the polar and non-polar metal oxide support are displayed in Figures 4.16 and 4.17. For example, distinctive layers of Ce^{4+} and O^{2-} in (100) terminal facets can be directly visualised in Figure 4.16. Morphologies of ZnO nanoplates and nanorods are shown in Figure 4.17. The unique surface polarity of the polar oxides was further confirmed by the solid-state nuclear magnetic resonance (NMR) (Figure 4.18). The probe-assisted ^{31}P NMR results clearly showed the different ^{31}P chemical shift of the polar-faceted metal oxides compared with their non-polar counterparts. More characterisations were then carried out to exclude the influence of the structural differences. XRD patterns barely change with different dominant facet exposure. Taking CeO_2 as an example, the NCs and

NSs share similar XRD patterns as can be seen in Figure 4.19, with the NCs exhibiting slightly stronger signals than the NSs. Such similarities can also be observed for the MgO and ZnO samples. EPR analysis was then performed on the polar-faceted and non-polar oxides, which indicates that MgO(111) and ZnO NPs show no obviously difference compared with their non-polar counterparts, while CeO_2 NCs shows higher signal intensity which can be attributed to the formation of Ce^{3+} at the surface,[22,25] as shown in Figure 4.20.

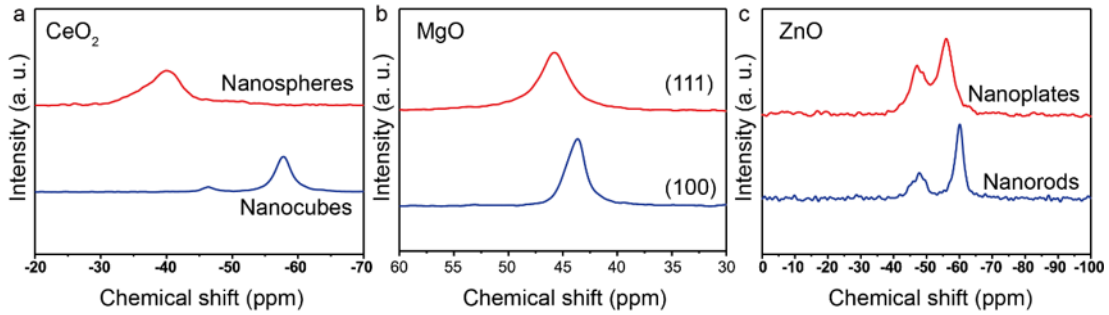

Figure 4.18 TMP-probed ^{31}P NMR of polar-faceted and non-polar **a:** CeO_2, **b:** MgO and **c:** ZnO.

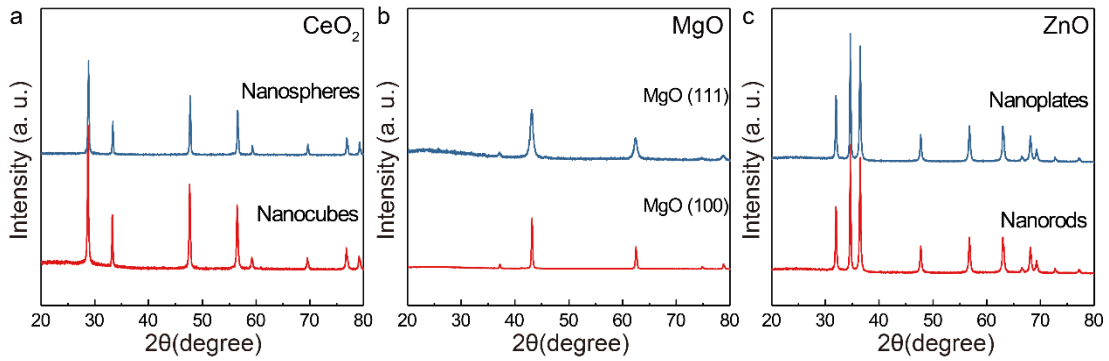

Figure 4.19 XRD patterns of polar and non-polar faceted **a:** CeO_2, **b:** MgO and **c:** ZnO.

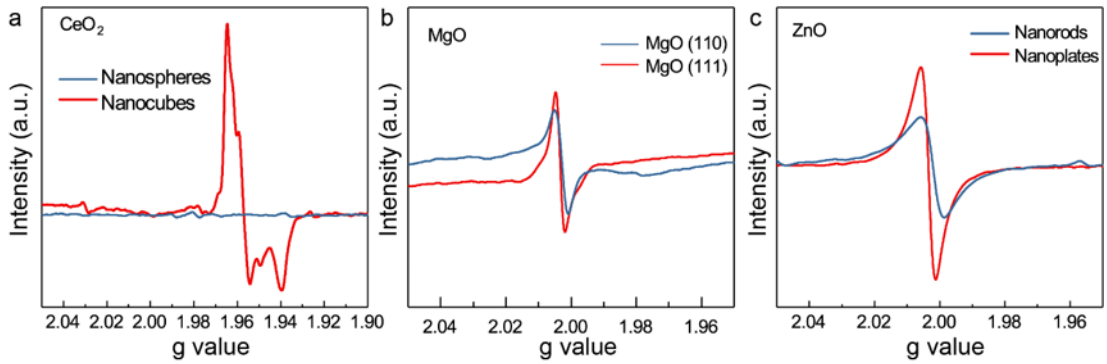

Figure 4.20 EPR spectra of polar and non-polar faceted **a:** CeO_2, **b:** MgO and **c:** ZnO.

4.3.2.4 Assembly of Ru:SL-MoS_2 and polar-faceted metal oxides

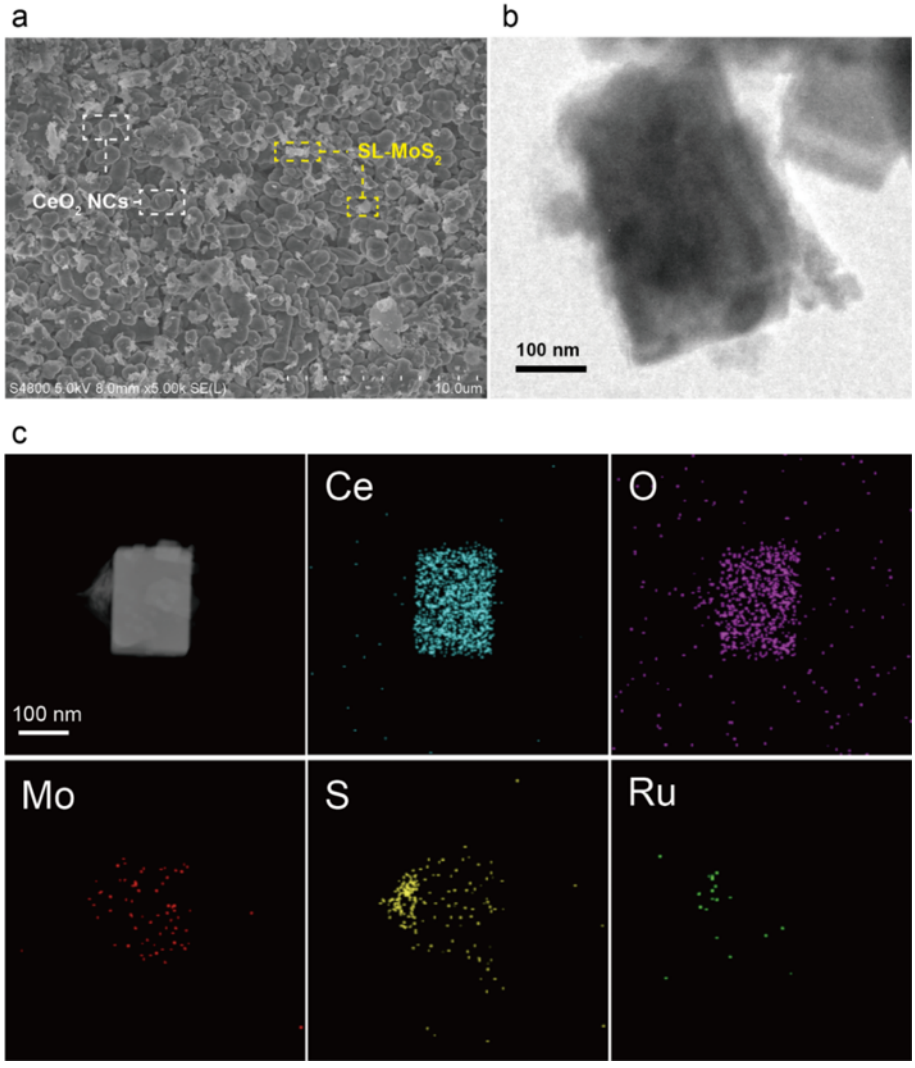

Figure 4.21 (a) SEM images of Ru:SL-MoS_2/CeO_2 NCs; **(b)** TEM and **(c)** EDS elemental mapping of selected Ru:SL-MoS_2 on a cubic CeO_2 particle.

TEM images of a typical assembled photocatalyst, Ru:SL-MoS_2/CeO_2 NCs, is shown in Figure 4.21. Clearly, the SL-MoS_2 monolayers are well dispersed on the surface of the CeO_2 nanocubes, which is further confirmed by the energy-dispersive spectroscopy (EDS) mapping (Figure 4.21c).

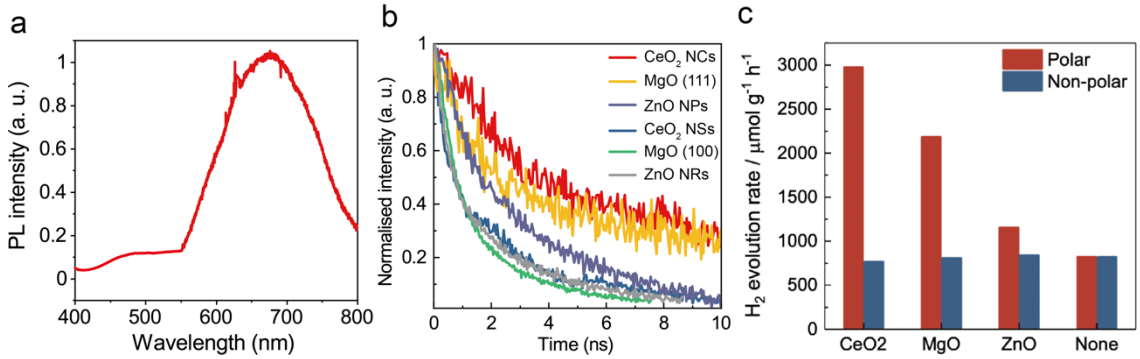

Figure 4.22 (a) PL spectrum of the SL-MoS_2 (excitation wavelength: 400 nm). **(b)** TRPL spectra and **(c)** the POWS activity of the Ru:SL-MoS_2 assembled with the polar and non-polar oxide supports. The TRPL spectra were recorded at a probe wavelength of 680 nm.

The charge separation process of the assembled materials was investigated by photoluminescence (PL) spectroscopy. The PL spectrum of the SL-MoS_2 shows a broad emission band ranging from 600 nm to 800 nm (Figure 4.22a). The charge carrier lifetimes of the Ru:SL-MoS_2 were much prolonged after assembled with the polar faceted oxide materials, showing a more than four-fold improvement from 1.02 ns to 4.53 ns after mixed with CeO_2 NCs, and for the assembly with the MgO(111) and ZnO NPs, the lifetimes were increased to 3.10 ns and 1.32 ns, respectively. However, those that combined with the non-polar metal oxides showed no such obvious change (Figure 4.22b). Subsequently, the photocatalytic water splitting performance of these assembled materials were evaluated. Excitingly, the photocatalytic activity of Ru:SL-MoS_2 was greatly enhanced after assembled to the polar-faceted oxides. As seen in Figure 4.22c, the Ru:SL-MoS_2/CeO_2 NCs shows a high H_2 evolution rate of 2977 μmol $g^{-1}h^{-1}$ under visible

light irradiation, while those of Ru:SL-MoS_2/MgO(111) and Ru:SL-MoS_2/ZnO NPs are 2184 μmol $g^{-1}h^{-1}$ and 1152 μmol $g^{-1}h^{-1}$, respectively. On the other hand, the combination with their non-polar counterparts were also tested which still showed no improvement of the photocatalytic activities of overall water splitting reaction (Figure 4.22c). It is noted that there has been nearly 4 times promotion of activity when blended with polar CeO_2 NCs support. It is noted that CeO_2 is also a good catalyst due to its high oxygen mobility, and it is used in the solid oxide fuel cells.[26] In addition, ZnO has been used in the Z-scheme photocatalytic systems to form heterojunctions for better charge separation.[27] Some may argue that the enhanced POWS activity is due to these favourable properties of the oxide supports. Obviously, the greatly prolonged lifetime of the photo-generated charge carriers finally results in the remarkable enhancement of photocatalytic activities.

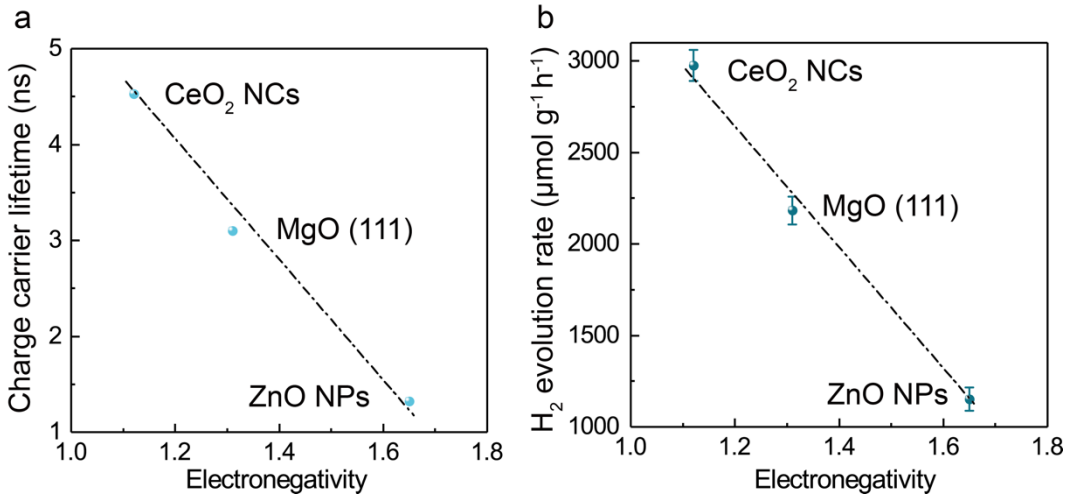

Figure 4.23 (a) The charge carrier lifetime and **(b)** the POWS performance of the Ru:SL-MoS_2 photocatalysts promoted by the polar-faceted oxide supports plotted against the electronegativities of the metal elements.

To strike more understanding of the controlling of the charge separation process via the polarisation effect by using polar-faceted oxides, we tried to find the relationship between the polarity and photocatalytic activities. Obviously, polarity is related to the electronegativity difference of the metal and oxygen in a polar-

faceted oxide, and the metal with lower electronegativity gives higher polarity near the surface of the polar-faceted oxide in this negative to positive layer configuration. Thus, the photocatalytic activities and the charge carrier lifetimes are plotted against the polarity, respectively (Figure 4.23). It is interesting to see that both the photocatalytic activities and the charge carrier lifetimes showed apparent linear relationships with the polarity within experimental errors, which confirmed that the charge carrier lifetime of a photocatalyst can be proportionally prolonged by the local electric field introduced by the polarisation effect of the polar-faceted oxide supports.

4.3.2.5 Assembly of Ru:SL-MoS_2 and LDHs

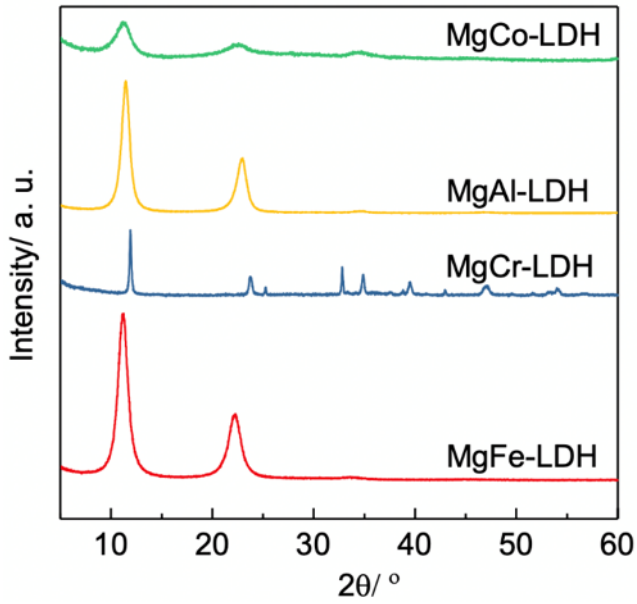

Figure 4.24 XRD patterns of different Mg-contained LDHs prepared by co-precipitation method.

Bearing in mind that the local polarisation effect observed so far should not be limited to the polar-faceted metal oxides, but can be extended to other material systems, thus, further exploration of the local polarisation effect was attempted on layered double hydroxides (LDHs). LDHs are also well-defined materials with layered structures, which consist of metal layers and hydroxide layers carrying

alternative negative and positive charge along their main crystallographic [100] direction. Thus, the LDHs can also introduce a local electric field via the surface polarity. Moreover, the surface polarity can be more flexibly controlled by changing the metal elements and ratios of the LDHs. Various LDHs were thus prepared by co-precipitation method, including MgAl-LDH, MgCr-LDH, MgFe-LDH and MgCo-LDH, and each of them was then assembled with the Ru:SL-MoS_2 by refluxing in water. As shown in Figure 4.24, the structure of each LDH was confirmed by XRD, the characteristic peaks were observed at $2\theta=11.4^o$ and 22.9^o, implying the existence of (003) and (006) facets of the layered structure of the LDHs.[28,29] There are also some additional peaks in the XRD spectrum of MgCr-LDH, which is attributed to $Mg(OH)_2$ and MgO,[30] thus, the synthesis of this LDH material needs further optimisations in the future research.

Obviously, the charge carrier separation was substantially facilitated when Ru:SL-MoS_2 was combined with LDHs, the charge carrier lifetime increases from 1.02 ns of Ru:SL-MoS_2 to 2.62 ns of Ru:SL-MoS_2/MgAl-LDH. Photocatalytic activity of water splitting reaction was then evaluated likewise. As expected, the photocatalytic performance was also apparently enhanced compared with Ru:SL-MoS_2. It is exciting to see that the most common MgAl-LDH showed the highest enhancement factor among the four selected LDHs, leading to a H_2 evolution rate of 1811 μmol $g^{-1}h^{-1}$ (as can be seen from Figure 4.25), which is among the best of the visible-light-driven overall water splitting systems. The layered structure of LDHs allows the formation of the oriented polarisation inside the LDHs, which leads to the presence of the local electric field near the surface, therefore prolongs the lifetime of the photo-generated charge carriers in the Ru:SL-MoS_2, resulting in the enhanced photocatalytic activities (Figure 4.25).

4.3.2.6 Correlation of polarisation and POWS performance

Now that the promotion of polarisation effect introduced by polar-faceted metal oxides and LDHs as supports have been studied separately, then for better understanding of this effect and further rational design of photocatalysts with prolonged the charge carrier lifetimes, the unification of the two systems must be achieved. It should be taken into account that the binary metal oxides and LDHs have different compositions and structures. Thus, the contribution of Mg and the corresponding trivalent metal should both be taken into account, and the metal ratios should be considered. So, a total polarity is developed as shown in the following equations:

For polar-faceted metal oxides:

$$\text{Total polarity } \chi_T = \chi_{oxygen} - \chi_{metal} \qquad \textbf{Equation 4.1}$$

For LDHs:

$$\text{Total polarity } \chi_T = \chi_{oxygen} - (\chi_{Mg} \times \omega_{Mg} + \chi_2 \times \omega_2) \qquad \textbf{Equation 4.2}$$

where χ_{oxygen}, χ_{metal}, χ_{Mg}, χ_2 are the electronegativity of oxygen, metal ions in metal oxides, magnesium and the trivalent metal ions in the LDHs; and ω_{Mg}, ω_2 are the molar percentage of magnesium and the trivalent metal in the LDHs.

In Equation 4.1, the χ_T of polar-faceted oxides is defined by the difference between the electronegativity of oxygen and metal; while for those of LDHs, both trivalent metal and bivalent metal (Mg) are considered, and the contribution of each is normalised depending on the molar ratio, as demonstrated in Equation 4.2. Then all the photocatalytic activities and the charge carrier lifetimes of the Ru:SL-MoS_2 based materials are plotted against the χ_T. Interestingly, linear relationships are clearly observed, as a result, the charge carrier lifetimes are found proportional

to the χ_T (Figure 4.25a), which confirms that the charge separation process can be controlled by tuning the local polarity through different polar-faceted supports. Such facilitated charge separation therefore contributes to the enhanced photocatalytic performance, making the photocatalytic water splitting activities also proportional to the total polarities χ_T (Figure 4.25b). Strong LEF is exerted to the catalyst by the surface of the polar-faceted materials, and such polarisation effect prolong the lifetime of the charge carriers at the interfaces, which largely enhances the photocatalytic activities. So far, the CeO_2 NCs shows the highest enhancement because of its strongest polarity of Ce-O bond (which is perpendicular to the exposed (100) surfaces of the CeO_2 nanocubes) according to the difference in electronegativity between Ce and O.

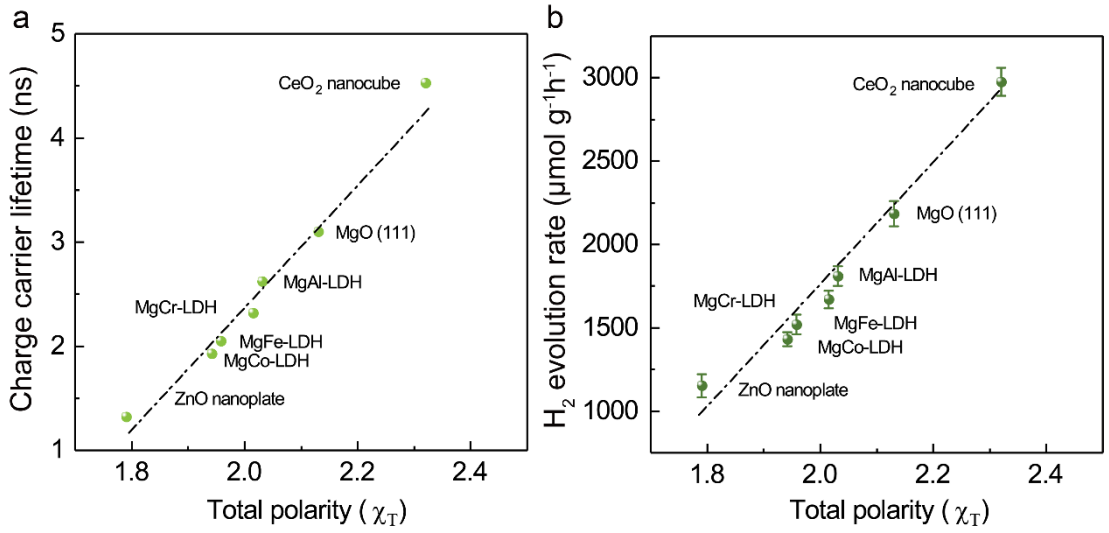

Figure 4.25 The semi-quantitative relationships of total polarity χ_T of the Ru:SL-MoS_2 photocatalyst enhanced by polar-faceted metal oxides and LDHs supports **(a)** the relationship between total polarity χ_T and the charge carrier lifetime. **(b)** the relationship between total polarity χ_T and the photocatalytic H_2 evolution rates.

Ru:SL-MoS_2 and Ru:SL-MoS_2/CeO_2 NCs were then tested for 10 hours, both of which showed good stability without obvious change of the H_2 evolution rates. As shown in Figure 4.26a. Both catalysts showed a stable and stoichiometric production of H_2 and O_2. It is widely agreed that for a photocatalytic system, the

QE, which evaluates the conversion efficiency of the photons at a certain wavelength to H_2, is one of the most important parameters when evaluating the performance of renewable solar energy to H_2 fuel systems.[31]

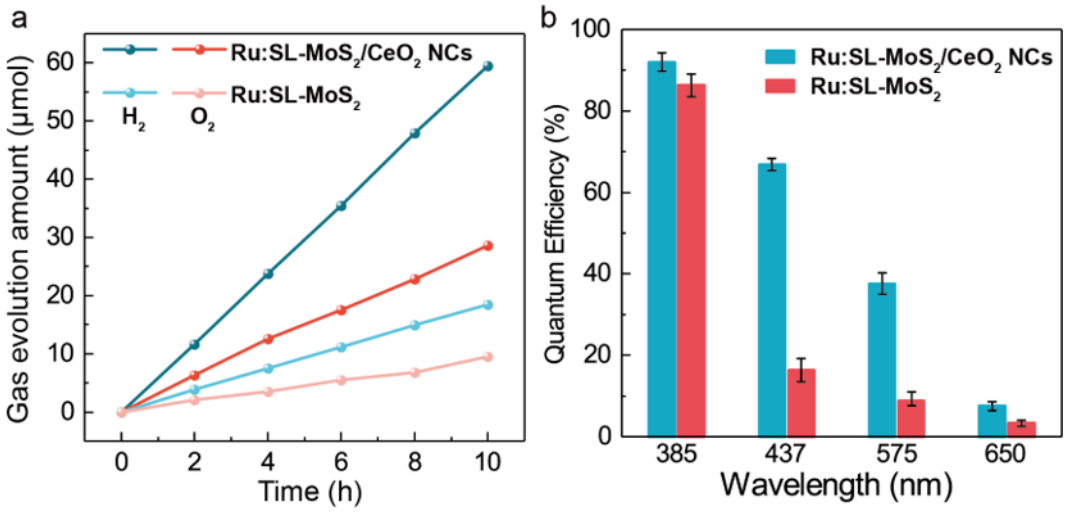

Figure 4.26 (a) POWS activity tests over Ru:SL-MoS_2 with and without polar CeO_2 NCs support at constant rate for 10 hours. This figure shows the amount of the evolved H_2 gas (in μmol) against the reaction time. Conditions: the amount of catalyst that contains 5 mg of the Ru:SL-MoS_2 was added to 10 mL of deionised H_2O in a 25-mL batch reactor under vigorous magnetic stirring, and Ar gas was used as the inert gas. Then the batch reactor was heated up to 270 °C and maintained for different reaction time before cooling down to room temperature. **(b)** QEs of Ru:SL-MoS_2 with and without the polar CeO_2 NCs at different wavelengths.

Different from the overall solar-to-hydrogen conversion efficiency or H_2 evolution rate, the QE provides more detailed and fundamental information about the photocatalytic systems, bearing in mind that a photocatalyst performs differently when harnessing the photons at different wavelengths. Remarkable QE has been frequently reported in the presence of sacrificial reagents, unfortunately, for the overall water splitting system, almost all the reported QEs were extremely low under the visible light irradiation (rarely exceeding 5% at 420 nm), which cannot reach the requirement of any practical applications. In our photocatalytic system, the QE was evaluated at 270 ℃ with the highest water ionisation at wavelengths

ranging from ultraviolet to visible light using different band pass filters. As illustrated in Figure 4.26b, high QE of about 90% were obtained for each photocatalyst at 385 nm due to high absorption, and it is exciting that when the light irradiation is changed to visible light, an extraordinary QE of 66.8 % for Ru:SL-MoS_2/CeO_2 NCs can still be maintained at 437 nm, which is more than 10 times higher than most results reported so far. QE sharply drops with further increasing the wavelength due to the rapid decrease of photon absorption at longer wavelengths. However, the MoS_2-based photocatalysts show considerable QE of 7.5 % at even 650 nm at elevated temperature. Similarly, the POWS reaction was also performed in the light furnace to mimic the solar light concentrator without any direct thermal energy input from an electrical device. The reactor temperature of 270 ^oC is maintained by this light source, and a constant H_2 evolution rate of about 3 mmol g^{-1} h^{-1} and 10 mmol g^{-1} h^{-1} are achieved over Ru:SL-MoS_2 without and with a polar CeO_2 support, respectively, indicating the great potential of further application of this photocatalytic water splitting system over nano-catalysts

4.4 Conclusion

In conclusion, the electric field effects on N-TiO_2 and SL-MoS_2 based photocatalysts were systematically demonstrated in this chapter. All the photocatalysts exhibited greatly enhanced activity for the POWS reaction at elevated temperature with a LEF introduced by polar-faceted supports. It was demonstrated that the photo-generated charge carrier separation can be substantially facilitated by assembling with polar-faceted materials, which can exert strong LEF in proximity of the interfaces. The resulted prolonged the charge carrier lifetimes allow the charge carriers travel to the surface of the photocatalysts and make the subsequent chemical reactions take place. Deeper understandings

of the relationships between the strength of LEF, photocatalytic activity and charge carrier lifetime were obtained by studying the Ru:SL-MoS_2 supported on different polar-faceted supports, with the help of TRPL. The results have shown that both the photocatalytic activity and the charge carrier lifetime exhibit an obvious linear relationship with the strength of the LEF. Therefore, the local polarisation effect is confirmed to show strong enhancement to photocatalysis by promoting the separation of the photoexcited electron-hole pairs. This observation provides a simple but versatile approach to control the recombination process and rationally design the photocatalysts using polar support materials, for not only the water splitting system, but also other valuable photocatalytic processes, which may also contribute to the future utilisation of solar energy.

4.5 References

1. Li, Y., Wu, S., Zheng, J., Peng, Y.-K., Prabhakaran, D., Taylor, R. A., Chi, S. & Tsang, S. C. E. 2D photocatalysts with tuneable supports for enhanced photocatalytic water splitting. *Mater. Today* **41**, 34–43 (2020).
2. Chen, F., Huang, H., Guo, L., Zhang, Y. & Ma, T. The Role of Polarization in Photocatalysis. *Angew. Chem. Int. Ed.* **58**, 10061–10073 (2019).
3. Li, J., Cai, L., Shang, J., Yu, Y. & Zhang, L. Giant Enhancement of Internal Electric Field Boosting Bulk Charge Separation for Photocatalysis. *Adv. Mater.* **28**, 4059–4064 (2016).
4. Li, J., Zhan, G., Yu, Y. & Zhang, L. Superior visible light hydrogen evolution of Janus bilayer junctions via atomic-level charge flow steering. *Nat. Commun.* **7**, 11480 (2016).
5. Noguera, C. Polar oxide surfaces. *J. Phys. Condens. Matter* **12**, R367–R410 (2000).
6. Goniakowski, J., Finocchi, F. & Noguera, C. Polarity of oxide surfaces and nanostructures. *Reports Prog. Phys.* **71**, 1 (2008).
7. Noguera, C. & Goniakowski, J. Polarity in oxide nano-objects. *Chem. Rev.* **113**, 4073–4105 (2013).
8. Pesci, F. M., Sokolikova, M. S., Grotta, C., Sherrell, P. C., Reale, F., Sharda, K., Ni, N., Palczynski, P. & Mattevi, C. MoS2/WS2 Heterojunction for Photoelectrochemical Water Oxidation. *ACS Catal.* **7**, 4990–4998 (2017).
9. Jia, T., Kolpin, A., Ma, C., Chau-Ting Chan, R., Kwok, W. M. & Tsang, S. C. E. A graphene dispersed CdS–MoS2 nanocrystal ensemble for cooperative photocatalytic hydrogen production from water. *Chem. Commun.* **50**, 1185–1188 (2014).

10. Yin, X. L., Li, L. L., Jiang, W. J., Zhang, Y., Zhang, X., Wan, L. J. & Hu, J. S. MoS2/CdS Nanosheets-on-Nanorod Heterostructure for Highly Efficient Photocatalytic H2 Generation under Visible Light Irradiation. *ACS Appl. Mater. Interfaces* **8**, 15258–15266 (2016).

11. Kumar, D. P., Hong, S., Reddy, D. A. & Kim, T. K. Noble metal-free ultrathin MoS2 nanosheet-decorated CdS nanorods as an efficient photocatalyst for spectacular hydrogen evolution under solar light irradiation. *J. Mater. Chem. A* **4**, 18551–18558 (2016).

12. Chang, K., Li, M., Wang, T., Ouyang, S., Li, P., Liu, L. & Ye, J. Drastic layer-number-dependent activity enhancement in photocatalytic H2 evolution over nMoS2/CdS (n ≥ 1) under visible light. *Adv. Energy Mater.* **5**, 1402279 (2015).

13. Chhowalla, M., Shin, H. S., Eda, G., Li, L. J., Loh, K. P. & Zhang, H. The chemistry of two-dimensional layered transition metal dichalcogenide nanosheets. *Nat. Chem.* **5**, 263–275 (2013).

14. Lau, T. H. M., Lu, X., Kulhavý, J., Wu, S., Lu, L., Wu, T. S., Kato, R., Foord, J. S., Soo, Y. L., Suenaga, K. & Tsang, S. C. E. Transition metal atom doping of the basal plane of MoS2 monolayer nanosheets for electrochemical hydrogen evolution. *Chem. Sci.* **9**, 4769–4776 (2018).

15. Liu, G., Robertson, A. W., Li, M. M. J., Kuo, W. C. H., Darby, M. T., Muhieddine, M. H., Lin, Y. C., Suenaga, K., Stamatakis, M., Warner, J. H. & Tsang, S. C. E. MoS2 monolayer catalyst doped with isolated Co atoms for the hydrodeoxygenation reaction. *Nat. Chem.* **9**, 810–816 (2017).

16. Mak, K. F., Lee, C., Hone, J., Shan, J. & Heinz, T. F. Atomically thin MoS2: A new direct-gap semiconductor. *Phys. Rev. Lett.* **105**, 2–5 (2010).

17. Rasmussen, F. A. & Thygesen, K. S. Computational 2D Materials Database: Electronic Structure of Transition-Metal Dichalcogenides and Oxides. *J. Phys. Chem. C* **119**, 13169–13183 (2015).

18. Zong, X., Yan, H., Wu, G., Ma, G., Wen, F., Wang, L. & Li, C. Enhancement of photocatalytic H2 evolution on CdS by loading MoS2 as cocatalyst under visible light irradiation. *J. Am. Chem. Soc.* **130**, 7176–7177 (2008).

19. Zhu, K., Hu, J., Kübel, C. & Richards, R. Efficient preparation and catalytic activity of MgO(111) nanosheets. *Angew. Chem. Int. Ed.* **45**, 7277–7281 (2006).

20. Hu, J., Zhu, K., Chen, L., Kübel, C. & Richards, R. MgO(111) Nanosheets with unusual surface activity. *J. Phys. Chem. C* **111**, 12038–12044 (2007).

21. Peng, Y. K., Ye, L., Qu, J., Zhang, L., Fu, Y., Teixeira, I. F., McPherson, I. J., He, H. & Tsang, S. C. E. Trimethylphosphine-Assisted Surface Fingerprinting of Metal Oxide Nanoparticle by 31P Solid-State NMR: A Zinc Oxide Case Study. *J. Am. Chem. Soc.* **138**, 2225–2234 (2016).

22. Peng, Y. K., Fu, Y., Zhang, L., Teixeira, I. F., Ye, L., He, H. & Tsang, S. C. E. Probe-Molecule-Assisted NMR Spectroscopy: A Comparison with Photoluminescence and Electron Paramagnetic Resonance Spectroscopy as a Characterization Tool in Facet-Specific Photocatalysis. *ChemCatChem* **9**, 155–160 (2017).

23. Search, H., Journals, C., Contact, A., Iopscience, M., Phys, S. S. & Address, I. P. ESR hyperfine investigation of the Vo centre in MgO. *J. Phys. C Solid State Phys.* **7**, 3981 (1974).

24. Henderson, B. & Wertz, J. E. Defects in the alkaline earth oxides. *Adv. Phys.* **17**, 749–855 (1968).

25. Peng, Y.-K., Hu, Y., Chou, H. L., Fu, Y., Teixeira, I. F., Zhang, L., He, H. & Tsang,

S. C. E. Mapping surface-modified titania nanoparticles with implications for activity and facet control. *Nat. Commun.* **8**, 675 (2017).

26. Thieu, C. A., Yang, S., Ji, H. Il, Kim, H., Yoon, K. J., Lee, J. H. & Son, J. W. Achieving performance and longevity with butane-operated low-temperature solid oxide fuel cells using low-cost Cu and CeO2 catalysts. *J. Mater. Chem. A* **10**, 2460–2473 (2022).

27. Maeda, K., Takata, T., Hara, M., Saito, N., Inoue, Y., Kobayashi, H. & Domen, K. GaN:ZnO solid solution as a photocatalyst for visible-light-driven overall water splitting. *J. Am. Chem. Soc.* **127**, 8286–8287 (2005).

28. Zhang, J., Xie, X., Li, C., Wang, H. & Wang, L. The role of soft colloidal templates in the shape evolution of flower-like MgAl-LDH hierarchical microstructures. *RSC Adv.* **5**, 29757–29765 (2015).

29. Silva, C. G., Bouizi, Y., Fornés, V. & García, H. Layered double hydroxides as highly efficient photocatalysts for visible light oxygen generation from water. *J. Am. Chem. Soc.* **131**, 13833–13839 (2009).

30. Wang, H., Sun, X., Liu, Z. & Lei, Z. Creation of nanopores on graphene planes with MgO template for preparing high-performance supercapacitor electrodes. *Nanoscale* **6**, 6577–6584 (2014).

31. Wang, J., Tafen, D. N., Lewis, J. P., Hong, Z., Manivannan, A., Zhi, M., Li, M. & Wu, N. Origin of photocatalytic activity of Nitrogen-doped TiO2 nanobelts. *J. Am. Chem. Soc.* **131**, 12290–12297 (2009).

Chapter 5 Magnetic Field Effects on Photocatalytic Water Splitting Performance

This chapter is adapted from the work by Yiyang Li, Zihan Wang, Yiqi Wang, András Kovács, Christopher Foo, Rafal E. Dunin-Borkowski, Yunhao Lu, Robert A. Taylor, Chen Wu and Shik Chi Edman Tsang, published in Energy & Environmental Science in 2022. The figures are reproduced with permission. Copyright 2022 Royal Society of Chemistry.[1]

5.1 Introduction

It is quite obvious that most photocatalytic overall water splitting (POWS) systems reported so far are greatly hindered by the intrinsic slow generation but fast recombination of the photo-generated charge carriers.[2] In the previous chapters, it was demonstrated that the separation of the photo-generated charge carriers and the regeneration of oxygen vacancies (V_Os) can be promoted by using elevated temperatures, which leads to enhanced water dissociation and favourable reaction kinetics (Chapter 3).[3–6] Such observation enabled further investigation of the impacts of local fields: for example, it is illustrated that the charge carrier lifetime and the POWS activity are both enhanced linearly by the local electric field introduced by polar-faceted materials at 270 ^{o}C (Chapter 4).[3,5] Building upon these previous observations, more efforts have been made to find a more facile and efficient method to facilitate the separation of the charge carriers. Although the effects of magnetic field in chemical reaction have been studied in some early organic research since 1920s,[7–9] their application in the POWS reaction using solid-state photocatalysts has rarely been investigated, because it is generally believed that the Zeeman energy produced by a magnetic field is

negligible compared to the Gibbs free energy of the POWS reaction (*ca.* 273 kJ mol^{-1}).[10,11] Here in this chapter, I systematically explored the magnetic field effects (MFEs) on POWS performance as a novel non-contact technique at elevated temperatures over N-doped TiO_2 (N-TiO_2) photocatalysts.

5.2 Objectives

The MFEs on particulate POWS system has scarcely been reported before, but studies on MFEs for other photocatalytic systems are emerging recently, including nitrogen fixation,[12] denitrification of contaminated water,[13] CO_2 conversion,[14] and dye degradation,[10,11,15] where an external magnetic field is applied during material preparation or reaction. Such effects have been attributed to the enhanced adsorption of charged species,[13] regulation of internal field,[12] facilitated migration of charge carriers,[19,20] etc. Obviously, even though the Zeeman energy is small, MFEs can contribute to photocatalysis through other pathways. However, it should be noted that conventional semiconductor photocatalysts such as TiO_2 exhibits very low magnetic flux even under strong magnetic fields,[10–13] hence giving insignificant effect on the photocatalytic performance. Moreover, the mechanism of the MFEs has not been systematically studied in the reported works, thus deep understandings of such effects are still absent. Lorentz force can be produced on charge carriers, the strength of which is dependent on charge, relative velocity and magnetic induction intensity. The Lorentz force is always vertical to the moving direction, which changes the movement of the charge carriers according to the left-hand rule. In general, excited electrons and holes are generated upon irradiation, where positive and negative charges are staying very close and moving together. Under the

influence of a local magnetic field, the positive and negative charges experience the Lorentz forces to the opposite directions, which will facilitate the separation especially at elevated temperature, therefore prolonging the lifetime.

Here in this chapter, I have demonstrated that by placing the N-doped TiO_2 (N-TiO_2) photocatalyst in proximity to the superparamagnetic Fe_3O_4 nanoparticles (NPs) under an external magnetic field, a very strong local magnetic flux can be induced, which leads to an efficient H_2 and O_2 evolution in a stoichiometric 2:1 ratio from pure water under visible light irradiation at 270 ^oC. An extraordinary H_2 evolution rate (21.2 mmol g^{-1} h^{-1}), QE (e. g. 88.7 % at 437 nm) and an unprecedented STH efficiency of 11.9$\pm$0.5% can be achieved, exceeding the practical STH target of 10 %. An overall energy efficiency of 1.16$\pm$0.05% has been demonstrated as well. Investigations of the charge and spin properties of electrons suggest that this remarkable enhancement originates from the magnetically induced Lorentz force facilitating the charge separation, as well as the dramatic suppression of charge carrier recombination in a strong spin-polarised energy band in N-TiO_2 during illumination. This facilitates alternative reaction routes to charge relaxation by water splitting at a high rate at elevated temperature. Mechanism of the MFEs was explored with the help of time-resolved photoluminescence (TRPL) technique and first-principles density-functional theory (DFT) calculations, and the contribution of each effect was studied quantitatively at different magnetic field strengths.

5.3 Results and discussion

5.3.1 Characterisations of the magnetic photocatalysts

5.3.1.1 Structural and morphological characterisations

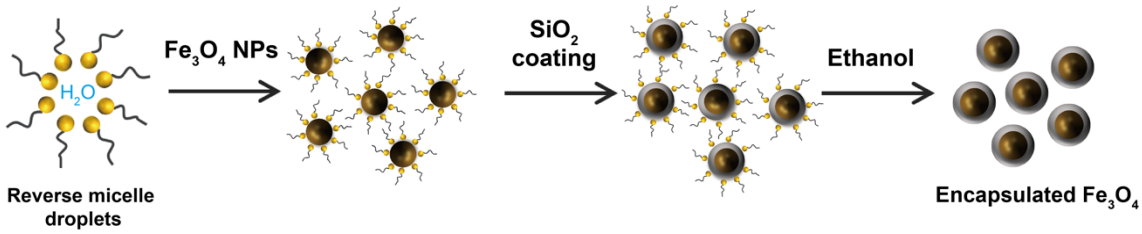

Figure 5.1 Schematic illustration of the encapsulation of Fe_3O_4 NPs by the reverse micelle method.

Superparamagnetic Fe_3O_4 NPs encapsulated in silica were initially synthesised using a method adopted from our previous study in order to obtain an enhanced local magnetic flux under an external magnetic field (Figure 5.1).[16] High-resolution transmission electron microscopy (HRTEM) was then engaged to characterise the morphology of the as-prepared materials. As shown in Figure 5.2, the length of ten lattice fringes of a Fe_3O_4 nanoparticle was measured to be 2.979 nm, of which the lattice spacing is 0.298 nm, corresponding to the (220) plane of Fe_3O_4 structure.

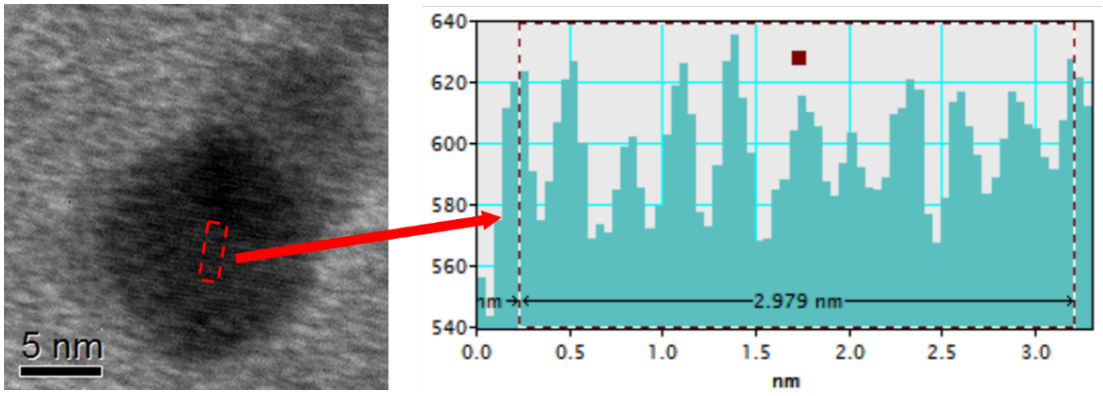

Figure 5.2 Left: HRTEM image of an Fe_3O_4 NP. **Right:** 10 d-spacings between 11 consecutive lattice fringes are selected and shown in this figure, of which the total distance is 2.979 nm, thus, an average d-spacing can be calculated as *ca.* 0.298 nm, corresponding to the (220) plane of Fe_3O_4 structure.

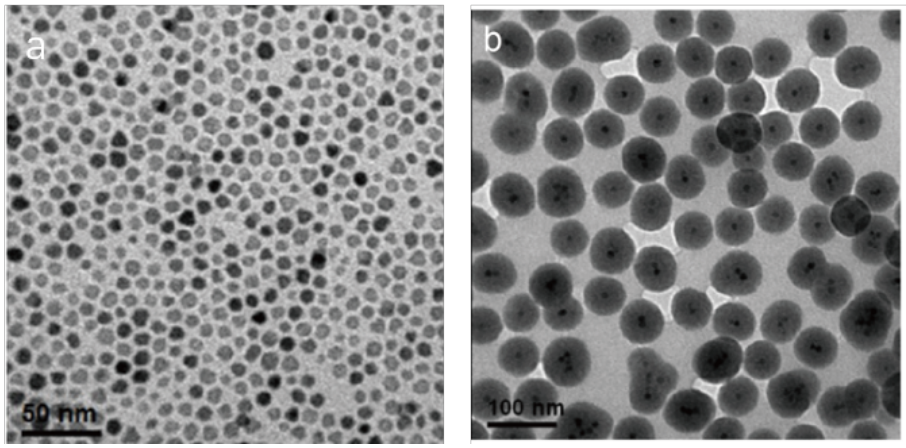

Figure 5.3 (a) TEM images of Fe_3O_4 NPs (8 nm). **(b)** TEM image of Fe_3O_4@SiO_2. These images were acquired by Dr. Tianyi Chen.

TEM clearly shows the well-dispersed Fe_3O_4 NPs have been synthesised with a high crystallinity, giving a mean particle size of *ca.* 8 nm, as shown in Figure 5.3a. Subsequently, using a reverse micelle method, the Fe_3O_4 NPs are successfully encapsulated in silica, forming a core/shell nano-structure (denoted as Fe_3O_4@SiO_2) with an average shell thickness of *ca.* 26 nm, as shown in Figure 5.3b.

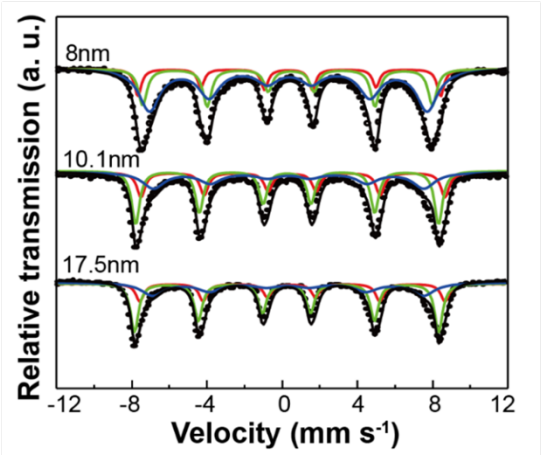

Mean particle size (nm)	Fe_3O_4 (%)	Fe_2O_3 (%)
8	78	22
10.1	64	36
17.5	53	47

Figure 5.4 Left: Mössbauer spectra of the Fe_3O_4 NPs with different mean particle sizes (black: collected overall response curves; blue and red (superparamagnetic): Fe_3O_4 phase; green: Fe_2O_3 phase). **Right:** Quantitative analysis of the Mössbauer spectra shown on the left, indicating the composition of Fe_3O_4 and Fe_2O_3 in each sample.

The synthesis of Fe_3O_4 NPs with different mean sizes was also attempted by

controlling the amount of the surfactant, which leads to the coexistence of Fe_2O_3 and Fe_3O_4 phases.[16] The two phases were differentiated quantitatively by Mössbauer spectroscopy (Figure 5.4). It was noticed that larger particle size gives rise to a larger proportion of the Fe_2O_3 phase due to the partial oxidation. Therefore, the Fe_3O_4 NPs with a mean size of 8 nm is further studied in order to explore the effects of the local magnetic flux.

Characterisations were carried out on X-ray diffraction (XRD), as shown in Figure 5.5. The XRD pattern of pure magnetic Fe_3O_4 NPs gives the characteristic peaks at 2θ values of 30.40°, 35.58°, 53.72°, 56.58°, and 62.74°, representing well the single phase crystalline *fcc* structure of Fe_3O_4.[17]

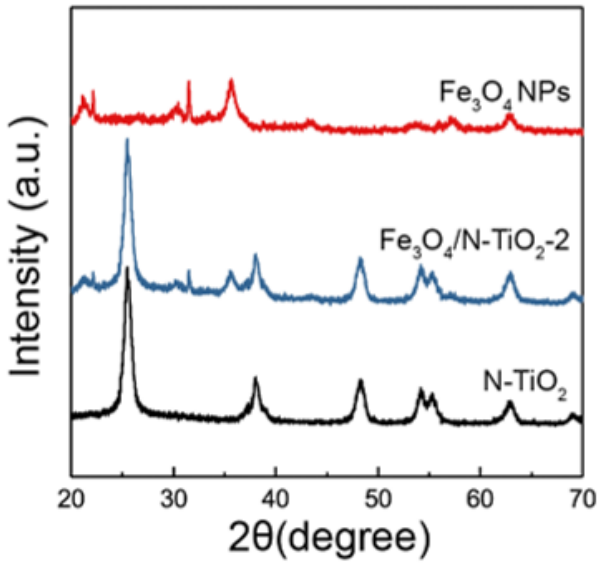

Figure 5.5 XRD patterns of Fe_3O_4 NPs, Fe_3O_4/N-TiO_2-2, and N-TiO_2, obtained on the Bruker D8 Advance diffractometer in the Department of Chemistry.

Unfortunately, the Fe_3O_4@SiO_2 did not show any photocatalytic activity toward the POWS reaction under visible light irradiation, because of the large band gap of SiO_2 as the shell, while Fe3O4 in the core can hardly absorb the light irradiation or reach the chemical species in the solution. Subsequently, the Fe_3O_4 NPs were then combined with TiO_2 via a sol-gel method, followed by a high-temperature NH_3

treatment for N-doping, with a Fe_3O_4 content of 20 wt.% (denoted as Fe_3O_4/N-TiO_2-2). The XRD pattern shows peaks at 2θ = 25.48°, 38.06°, 48.21°, 54.19°, 55.28° and 62.91°, indicating the existence of anatase phase TiO_2, and no phase transformation to rutile phase can be observed (Figure 5.5).

5.3.1.2 XPS of Fe_3O_4/N-TiO_2 materials

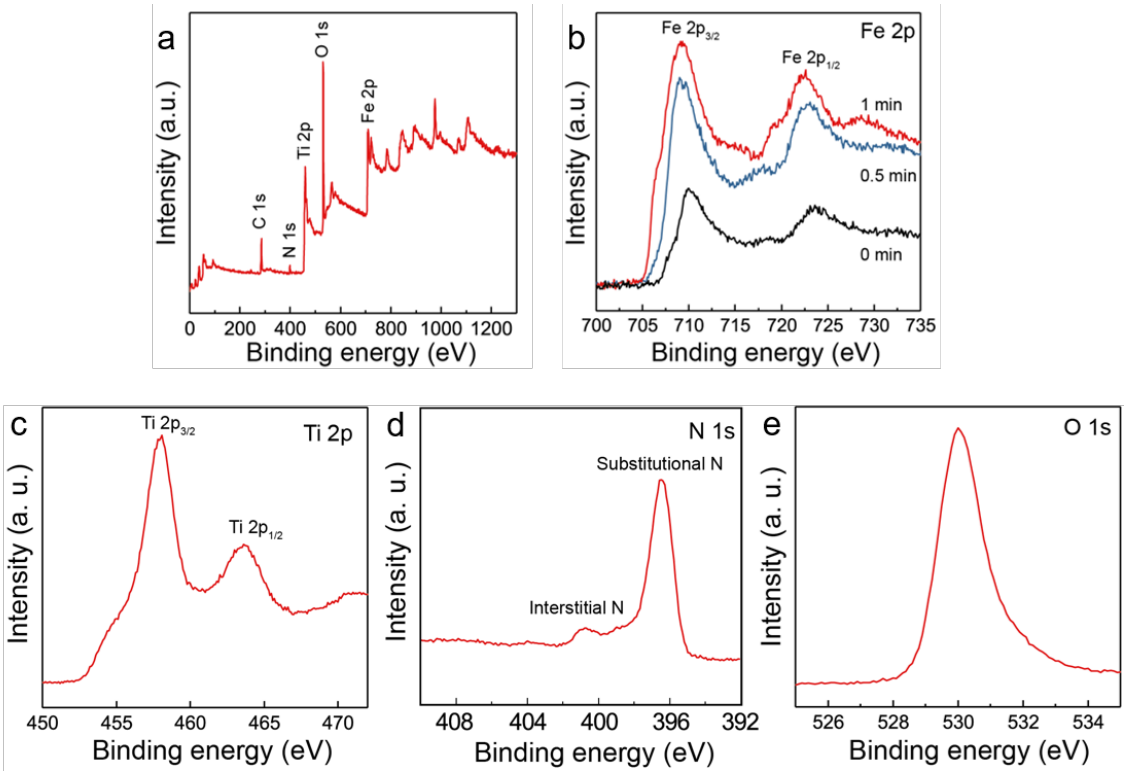

Figure 5.6 (a) XPS survey spectra of Fe_3O_4/N-TiO_2-2. **(b)** Fe 2p XPS spectra of Fe_3O_4/N-TiO_2-2 obtained at different ion-sputtering times. Etching was achieved by an Ar^+ sputtering gun with a etching rate of 1 nm min^{-1}. High resolution **(c)** Ti 2p, **(d)** N 1s and **(e)** O 1s XPS spectra of Fe_3O_4/N-TiO_2-2 without ion-sputtering.

Depth-profiling X-ray photoelectron spectroscopy (XPS) was performed to investigate the chemical species of Fe_3O_4/N-TiO_2-2. The sample was etched by an ion-beam for different time periods so as to obtain the chemical information from the surface/subsurface to the inner region. A typical XPS survey spectrum shows peaks of N 1s, O 1s, Ti 2p and Fe 2p (Figure 5.6a). Moreover, the Fe 2p peaks show an increasing trend when the sample is sputtered, indicating the

Fe_3O_4 NPs are mostly encapsulated in the N-TiO_2 (Figure 5.6b and Table 5.1). High resolution XPS spectra of Ti 2p, N 1s and O 1s are also shown in Figures 5.6c-5.6e, indicating that the doped N atoms mainly take up the substitutional positions, with a small portion occupying the interstitial sites, which is similar to what has been demonstrated in more details in Chapter 3.

Table 5.1 The concentration of Fe species in the Fe_3O_4/N-TiO_2-2 at different etching times derived from the XPS spectra in Figure 5.6b.

Etching time (min)	Fe concentration (wt. %)
0	3.23
0.5	16.28
1	26.37

5.3.1.3 EPR of Fe_3O_4/N-TiO_2 materials

Continuous wave electron paramagnetic resonance (CW-EPR) was performed at room temperature using an X-band (9.39 GHz) microwave to observe the V_Os in the photocatalysts (Figure 5.7). The Fe_3O_4 NPs gives a very broad and strong resonance signal at a field of around 3150 Gauss, due to the unpair electrons of the paramagnetic Fe(II) and Fe(III) species and the dipolar interaction between the NPs[18]. The EPR experiments were also carried out on the Fe_3O_4/N-TiO_2-2 photocatalyst before and after the N doping, both of which showed much smaller EPR signal compared with that of the Fe_3O_4 NPs due to the magnetic dilution of TiO_2. Also, the strong and broad signal of Fe_3O_4 NPs makes the signal changes of the TiO_2 species not distinguishable. Therefore, measurements were performed on pure anatase TiO_2 and N-TiO_2 which was synthesised following the same procedure and N doping. Apparently, pure TiO_2 is observed silent on the EPR, while after N doping, a peak at a g-value of 2.003 can be observed as shown in

Figure 5.7d, which is attributed to surface V_Os.[19] The V_Os were created during the ammonia treatment in accordance to our previous study showing that more V_Os can better harness the visible light and facilitate the O_2 evolution reaction[3,19]. Moreover, further EPR measurements were carried out by calcining the N-TiO_2 in an Ar flow at different temperatures for 1h and allowed to naturally cool down to room temperature. Then the sample was exposed to air for 10 min before EPR measurements. As can be seen in Figure 5.7a, it showed an anisotropic g tensor (g_{zz}=2.026, g_{yy}=2.006, g_{xx}=1.998), which is originated from the $O_2^{\cdot-}$ radicals (resulted from the O_2 molecules stabilised on the surface V_Os);[20] another signal of g=2.012 was observed which can be attributed to the doped interstitial N species. Clearly, the signal of $O_2^{\cdot-}$ radicals indicative to the surface V_Os increases with the calcination temperature; while the signal of doped N remains the same.

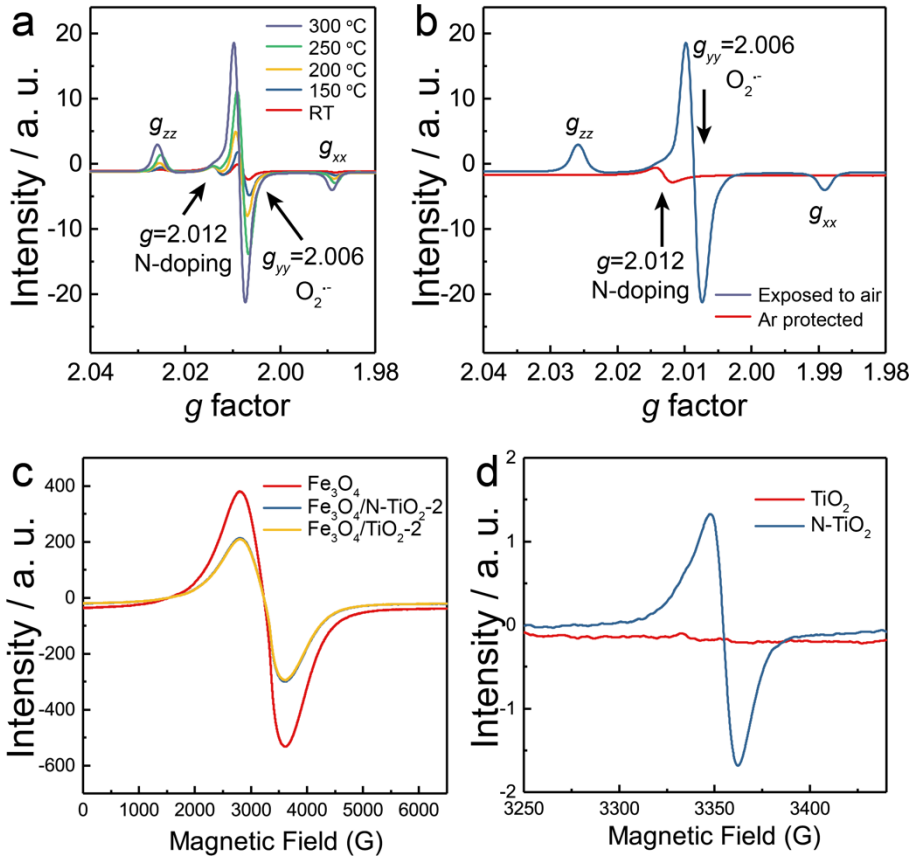

Figure 5.7 EPR study of the magnetic photocatalysts. **(a, b)** EPR spectra of N-TiO_2 calcined in Ar at different temperatures. **(c)** EPR spectra of Fe_3O_4 NPs,

Fe_3O_4/N-TiO_2-2 and Fe_3O_4/TiO_2-2. **(d)** EPR spectra of N-TiO_2 and TiO_2.

5.3.1.4 UV-Vis absorption of Fe_3O_4/N-TiO_2 materials

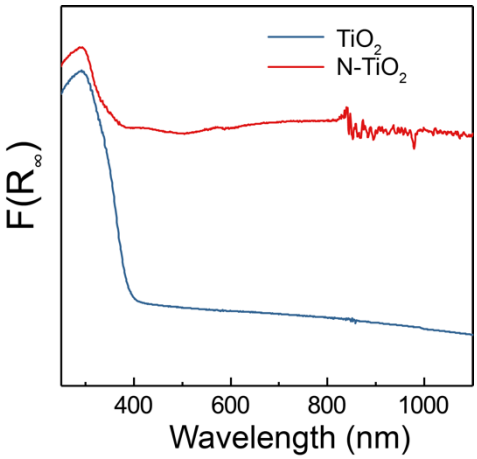

Figure 5.8 UV-Vis diffuse reflectance spectra of N-TiO_2 and TiO_2. Spectra were recorded within the wavelength range of 250-1100 nm at room temperature and converted using the Kubelka-Munk function.

The visible light absorption of the material was also substantially enhanced after N doping, which was investigated by UV-Vis DRS (Figure 5.8). Apparently, the original absorption edge of the pristine TiO_2 at around 400 nm was greatly extended, and the N-doped TiO_2 showed strong absorption at even 1000 nm, which covers the whole visible light spectrum and some near infrared regime.

5.3.1.5 Magnetic properties of Fe_3O_4/N-TiO_2 materials

The magnetic properties of the Fe_3O_4 NPs, Fe_3O_4/N-TiO_2-2, and N-TiO_2 were investigated with a superconducting quantum interference device (SQUID) magnetometer, and the magnetisation curves of the materials are shown in Figure 5.9. The saturation magnetisation (M_s) values of Fe_3O_4 and Fe_3O_4/N-TiO_2-2 are 1.82×10^5 and 6.85×10^4 A m^{-1} (43.01 and 16.19 emu g^{-1} in CGS unit system). The saturated magnetisation value of the Fe_3O_4/N-TiO_2-2 is smaller than the Fe_3O_4 NPs because of the inclusion of the N-TiO_2. The as-prepared samples exhibit

superparamagnetic feature as seen in Figure 5.9 since the Fe_3O_4 around 8 nm is smaller than the critical size of 20 nm. Due to the lack of magnetic coupling, the materials can be magnetised under an external magnetic field but will not retain a substantial residual magnetism upon removal of the external field.

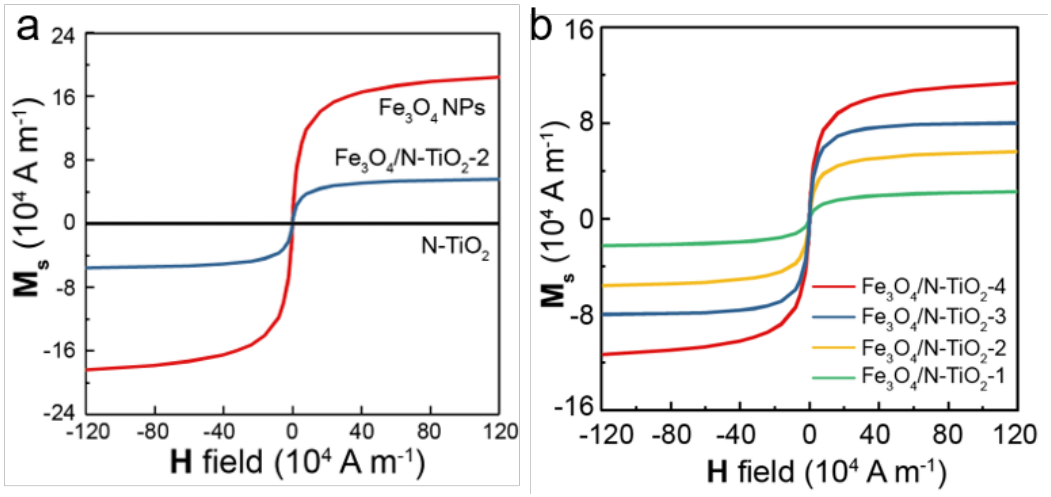

Figure 5.9 (a) Magnetisation curves of Fe_3O_4 NPs, Fe_3O_4/N-TiO_2-2 and N-TiO_2. **(b)** Magnetisation curves of Fe_3O_4/N-TiO_2 photocatalysts with different contents of Fe_3O_4 NPs.

5.3.2 POWS performance and optimisations

5.3.2.1 Effects of local magnetic flux density

The photocatalytic performances of the as-prepared photocatalysts were then evaluated for the POWS reaction at 270 °C under a visible light irradiation, which is the optimal temperature in this POWS system as discussed in the previous chapters. Different metal NPs were deposited on the Fe_3O_4/N-TiO_2-2 photocatalyst via a photo-reduction method, since previous studies have shown that deposition of noble metal such as Au and Pt can greatly improve the H_2 evolution performance.[3,21–23] According to the volcanic curve for the electrocatalytic H_2 evolution reaction, Pt has the optimal adsorption energy with H_2, followed by Pd and Ru.[24,25] Basically, the POWS activity of the metal-deposited photocatalysts

follows this volcano curve, however, the Au-decorated Fe_3O_4/N-TiO_2-2 showed the highest POWS activity in this case (Figure 5.10a), which is not in accordance with the volcano curve. Therefore, as mentioned previously in Chapter 3, I believe that the localised plasmon resonance effect of the Au NPs could play a role in this POWS system, which has been extensively studied in the Au/TiO_2 system in literature,[26,27] but is not studied in detail in this thesis.

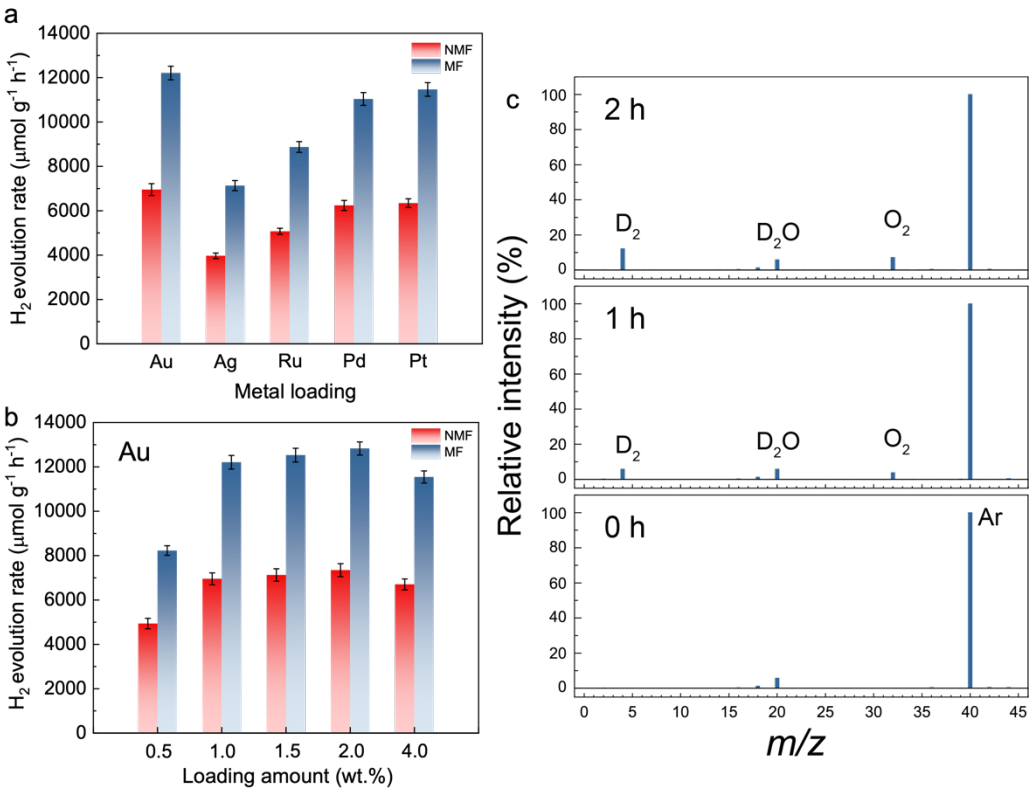

Figure 5.10 (a) POWS performance of the Fe_3O_4/N-TiO_2-2 photocatalyst decorated with 1 wt.% of different metal NPs via a photo-deposition method. **(b)** POWS performance of the Au-decorated Fe_3O_4/N-TiO_2-2 photocatalyst with different Au loading amounts. NMF: no magnetic field; MF: with magnetic field. **(c)** Isotopic study of the POWS reaction on Fe_3O_4/N-TiO_2-2 photocatalyst decorated with 1 wt.% of Au NPs. The products were measured by mass spectrometer (Hiden Analytical) after the reaction time labelled in each figure, as indicated in the figure. All signals are re-scaled by the signal of the inert component Ar (The relative intensity of Ar is 100 %).

Then the loading amount of Au NPs was optimised, as shown in Figure 5.10b. Clearly, the POWS activity levels off when the loading amount is increased beyond

1 wt.%; Moreover, the activity shows a small drop when the loading reaches 4 wt.%, which is presumably due to the shielding effect of the NPs, resulting in less photons reaching the N-TiO_2.[28] Consequently, 1 wt.% Au NPs were used for all the photocatalysts as a H_2 evolution cocatalyst. Initial experiments were performed over N-TiO_2 and Fe_3O_4/N-TiO_2-2 photocatalysts without external magnetic field, both of which showed good performance toward POWS, giving similar H_2 evolution rates of around 7000 μmol g^{-1} h^{-1}. Control experiments were also performed, which confirmed that Fe_3O_4 NPs, SiO_2 and Fe_3O_4@SiO_2 all showed no detectable H_2 evolution, indicating that N-TiO_2 is the only photocatalytically active component in the catalysts under these conditions. Moreover, no activity could be observed at elevated temperatures if either the light illumination or a photocatalyst is absent. The stoichiometry of products (H_2 and O_2) was investigated quantitatively by gas chromatograph, which indicates a H_2:O_2 ratio of 2.01±0.04 throughout this work. N_2 was not detected in the gaseous products, which excludes the influence of mixed air in the system. The isotopic studies were then carried out by using D_2O rather than H_2O to confirm that H_2 is generated from the POWS reaction instead of the photocatalyst itself or any other possible organic contaminants (Figure 5.10c). Also, the influence of electron transfer between N-TiO_2 and Fe_3O_4 NPs was excluded by introducing an insulated silica layer in between (Fe_3O_4@SiO_2/N-TiO_2-2), which showed similar POWS activity as that of Fe_3O_4/N-TiO_2-2 without the silica layer. The amounts of Fe_3O_4 and N-TiO_2 were maintained the same in each catalyst and neither SiO_2 nor Fe_3O_4@SiO_2 showed any activity toward the POWS reaction. Thus, the following studies were carried out with the Fe_3O_4/N-TiO_2 materials without the silica layer.

Subsequently, to study the MFE on the POWS system, an external static magnetic

field of 180 mT was applied by two paralleled permanent magnets near the reactor. The applied external magnetic flux density $\mathbf{B_{external}}$ in the centre of the two magnets was measured by a Gauss metre. Excitingly, the POWS activity of Fe_3O_4/N-TiO_2-2 increases to 12210 μmol g^{-1} h^{-1}, showing an enhancement of 76%. The photocatalytic activity of the N-TiO_2, however, almost keeps the same. The lack of a detectable change on N-TiO_2 with and without an external magnetic field indicates its weak field flux density whereas superparamagnetic Fe_3O_4 nanoparticles can generate much stronger local field flux upon magnetisation. The M-H curves of the samples in Figure 5.9 exhibit that the Fe_3O_4 NPs are crucial for providing sufficient local magnetic field induced by the external field.

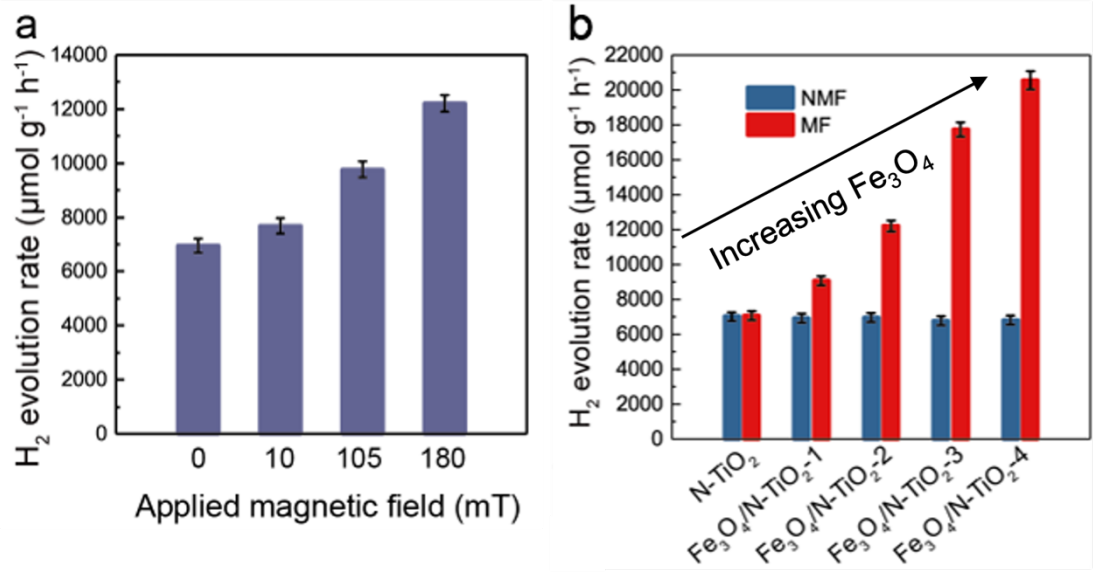

Figure 5.11 (a) POWS activity tests of Fe_3O_4/N-TiO_2-2 under external magnetic field of different strengths; **(b)** POWS activity tests of N-TiO_2 and Fe_3O_4/N-TiO_2 photocatalysts with and without external magnetic field (180 mT) (NMF=no magnetic field, MF=magnetic field). 1 wt.% Au was deposited onto the photocatalysts via the photo-reduction method before use.

More explorations were attempted to further confirm the influence of the magnetic field on the POWS system. For a magnetic-field-promoted catalytic system, the enhancement of the photocatalytic performance should show dependency on the

intensity of the external magnetic field. Therefore, the POWS performance was then evaluated in magnetic fields of different intensities by changing the distances between the permanent magnet to the centre of the batch reactor. The permanent magnet was placed at different distances which results in the field strengths of 105 mT and 10 mT, respectively. The photocatalytic performance was then evaluated, showing a decreasing trend as the field strength is reduced (Figure 5.11a). Apparently, the POWS activity over Fe_3O_4/N-TiO_2-2 is clearly dependent on the strength of the external magnetic field, while the pure N-TiO_2 hardly shows any responses to the external magnetic field change.

To further understand the local MFEs on the POWS system over N-TiO_2 based photocatalysts, a series of Fe_3O_4/N-TiO_2 photocatalysts with increasing Fe_3O_4 NPs contents were fabricated (the amounts of the Fe_3O_4 NPs in Fe_3O_4/N-TiO_2-1, Fe_3O_4/N-TiO_2-2, Fe_3O_4/N-TiO_2-3 and Fe_3O_4/N-TiO_2-4 are 10 wt.%, 20 wt.%, 30 wt.% and 40 wt.%, respectively). Then the magnetisation curves of the samples were measured by SQUID, as shown in Figure 5.9b. Apparently, the saturated magnetisation values vary with the Fe_3O_4 NPs content. The POWS activities were then tested at 270 ^oC as well under visible light irradiation with an external magnetic field of 180 mT. The results are shown in Figure 5.11b, which clearly indicates that the magnetic photocatalysts become more sensitive to the external magnetic field as the content of the Fe_3O_4 NPs increasing. This can be attributed to the stronger local magnetic flux induced by the external static magnetic field, as indicated by the magnetisation curves: the photocatalysts which contain more Fe_3O_4 show stronger magnetism, which means a stronger induced local magnetic field flux will be generated in close proximity to the photocatalysts. The above observation further confirms that the POWS activities strongly depend on the

intensity of the local magnetic flux induced by the external magnetic field, implying the dramatic MFEs in the POWS systems.

Similar work has also been undertaken on the commercially available P25 TiO_2 to simplify the catalyst design. It was doped with N and then combined with the Fe_3O_4 NPs. The resulted photocatalyst contains 40 wt.% of Fe_3O_4 NPs, the same as that in the Fe_3O_4/N-TiO_2-4. Excitingly, the simple mixture of N-doped P25 and Fe_3O_4 NPs results in a significantly enhanced POWS performance in the external magnetic field (180 mT), making such magnetic field promoted system more practical for further application. It is noteworthy that in this case, the Fe_3O_4 NPs have not experienced any high-temperature ammonia treatment. Although this catalyst exhibited slightly lower enhancement under external magnetic field due to geometric longer distance between the magnetic phase from catalytic sites, the high-temperature ammonia treatment causing insurmountable issue on the Fe_3O_4 nanoparticles is not evidenced. Similar work has also been attempted on commercial ST-01, which exhibits a similar conclusion.

5.3.2.2 Effects on separation of charge carriers

Time-resolved photoluminescence (TRPL) was engaged in this study to investigate the changes of charge separation process with or without an external magnetic field, therefore to understand the MFEs more comprehensively. N-TiO_2 and Fe_3O_4/N-TiO_2-2 photocatalysts were firstly measured. Obviously, both materials show similar charge carrier lifetimes when an external magnetic field is absent; while the charge carrier lifetime of Fe_3O_4/N-TiO_2-2 was substantially prolonged when the magnetic field of 180 mT was applied, and that of the pure N-TiO_2 remain unchanged. Such difference of the response to the external magnetic field coincides well with what was observed in the POWS activity tests. Therefore,

the enhanced POWS activities are attributed to the facilitated charge carrier separation.

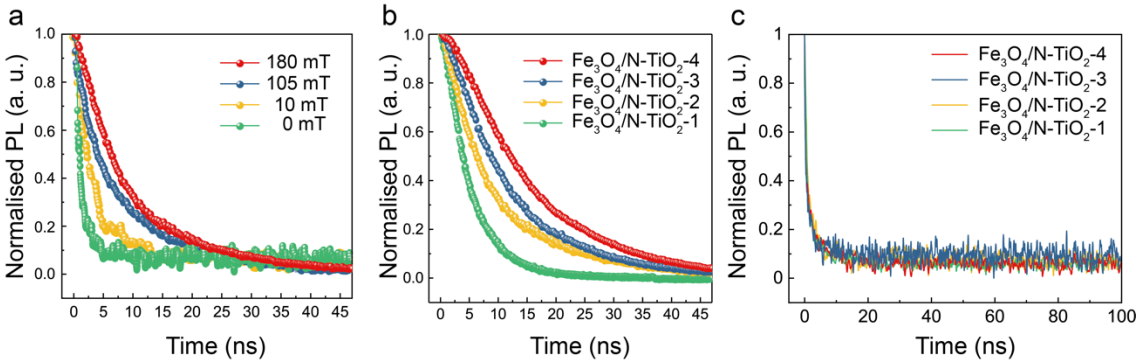

Figure 5.12 (a) TRPL spectra of Fe_3O_4@N-TiO_2-2 with an external magnetic field of different strengths. **(b)** TRPL spectra of Fe_3O_4/N-TiO_2 photocatalysts with an external magnetic field of 180 mT. **(c)** TRPL spectra of Fe_3O_4/N-TiO_2 photocatalysts without the external magnetic field. The Fe_3O_4NPs content was set to be 10%, 20%, 30% and 40 wt% for Fe_3O_4/N-TiO_2-1, Fe_3O_4/N-TiO_2-2, Fe_3O_4/N-TiO_2-3 and Fe_3O_4/N-TiO_2-4, respectively.

As mentioned earlier in this chapter, charge carriers can be influenced by the Lorentz force when moving in a magnetic field, and the electrons and holes experience the Lorentz forces to different directions when they are moving together, according to the left-hand rule. Additionally, magnetisation curves showed that the Fe_3O_4/N-TiO_2-2 photocatalyst can be readily magnetised which means a strong local magnetic flux can be induced near the Fe_3O_4 NPs. Apparently, the Lorentz force from the strong local magnetic flux density can greatly facilitate the separation of charge carriers, which results in the prolonged charge carrier lifetime, as indicated by the TRPL results (Figure 5.12). Subsequently, further TRPL experiments were carried out on Fe_3O_4/N-TiO_2-2 photocatalyst under magnetic fields with different field strengths. Not surprisingly, the charge carrier lifetime increased with the magnetic field strength, confirming that the changes of the charge carrier lifetime are due to the applied magnetic field, and also suggesting that the charge recombination process is supressed more significantly

under a stronger induced magnetic field (Figure 5.12a).

Photocatalysts with different Fe_3O_4 NPs contents were then tested, and all the samples show similar TRPL spectra without external magnetic field (Figure 5.12c). When measured with an external magnetic field of 180 mT, TRPL results show that the charge carrier lifetime was prolonged more substantially as the content of Fe_3O_4 increasing (Figure 5.12b), which is in accordance with the previous magnetisation experiments and the POWS activity tests. Our previous reports showed that elevated temperatures solely would not obviously influence the charge carrier lifetime in our system.[3,5] The above observations indicate that the charge separation in the Fe_3O_4/N-TiO_2 photocatalysts is dominated by the local magnetic flux induced by the external magnetic field, therefore the N-TiO_2 showed no significant response to the magnetic field because of the weak local magnetic flux it could generate. In addition, the MFEs become more efficient when the external magnetic field is stronger, since stronger external field will induce stronger local magnetic flux according to the magnetisation curves (Figure 5.9). This could also explain the reason why the samples contain more Fe_3O_4 NPs show higher response to the external field even under a fixed external field.

5.3.2.3 Electron holography of Fe_3O_4/N-TiO_2 materials

Combined correlative off-axis electron holography in TEM and energy dispersive X-ray spectroscopy spectrum imaging in STEM has been studied. It has been known that the off-axis electron holography allows to recover the electron optical phase shift of electrons that interact with the in-plane components of the electromagnetic field present within and around the sample.[29] The EDX chemical measurements were to map the Fe_3O_4 within the agglomerates and correlate to the phase measurements of the N-TiO_2. Agglomerated areas of the Fe_3O_4/N-TiO_2-

2 and Fe_3O_4/N-TiO_2-4 samples were briefly examined using both off-axis electron holography and EDX imaging, as shown in Figure 5.13.

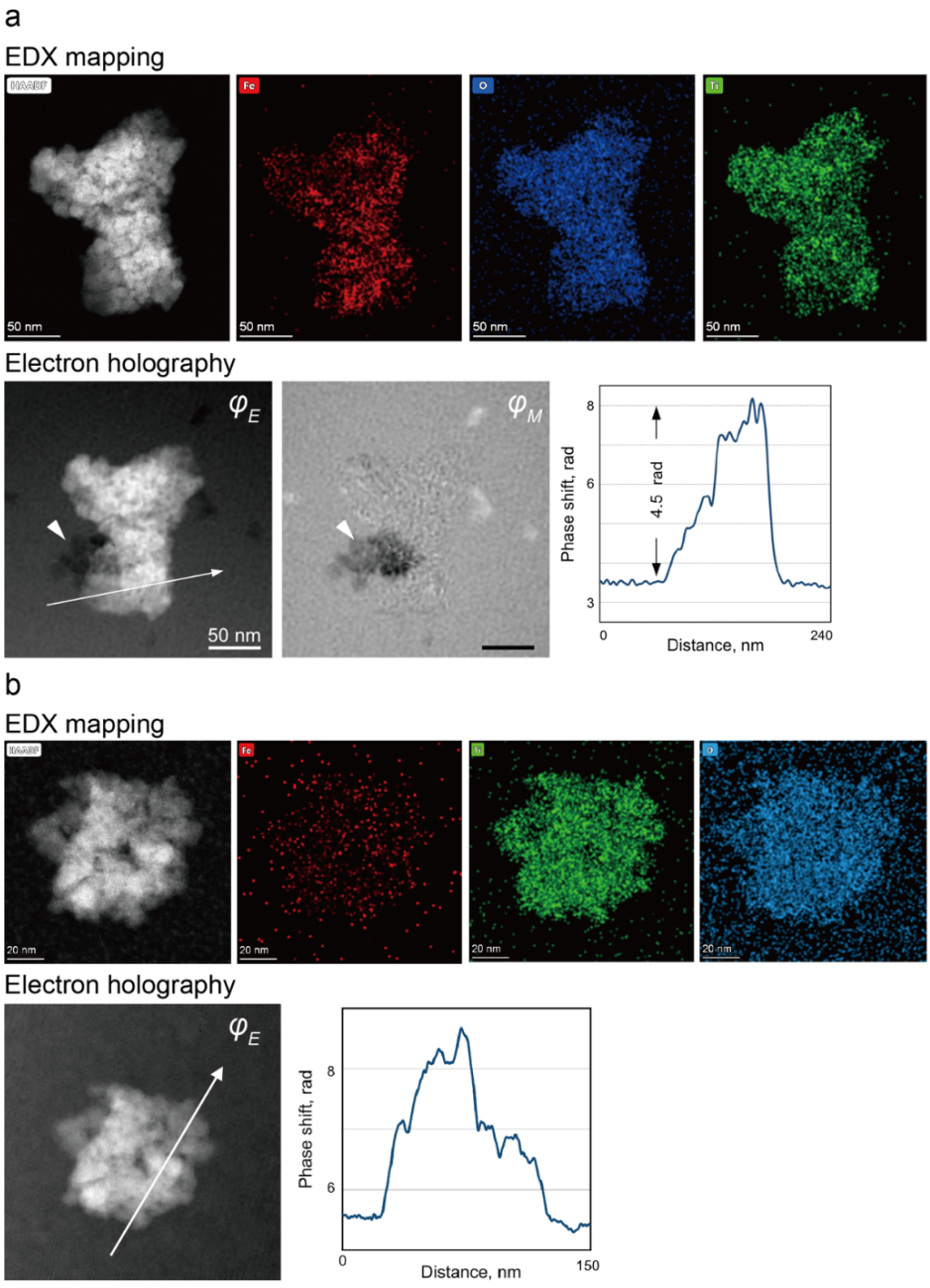

Figure 5.13 Energy dispersive X-ray spectroscopy (EDS) and the correlative off-axis electron holography studies of the **(a)** Fe_3O_4/N-TiO_2-4 and **(b)** Fe_3O_4/N-TiO_2-2 photocatalysts. The Fe_3O_4NPs content was 20% and 40 wt.% for Fe_3O_4/N-TiO_2 and Fe_3O_4/N-TiO_2-4, respectively.

The electrostatic (φ_E) and magnetic phase shifts (φ_M) was carefully separated by turning the sample over inside the electron microscope and taking the difference

of two experiments.[29] These preliminary electron holography studies indicated the superparamagnetic nature of the photocatalysts (Figure 5.13). It is noteworthy that in both POWS activity tests and TRPL measurements, the photocatalysts have shown similar responses to the external magnetic field, therefore it is not hard to realise that the magnetic field influences the photocatalytic process by inducing a strong local magnetic field near the Fe_3O_4 NPs, which facilitates the charge separation and prolongs the charge carrier lifetime, resulting in a greatly enhanced POWS performance.

5.3.2.4 Correlation of MFEs and POWS performance

As mentioned before, it is known that charged bodies in motion can be affected by the Lorentz force produced by a magnetic field, and the photo-generated electrons and holes in the Fe_3O_4/N-TiO_2 experience Lorentz forces to opposite directions according to the left-hand rule when they are moving together, accounting for the prolonged charge carrier lifetime. Therefore, the correlation between the enhancement of POWS performance and the local induced magnetic flux density $\mathbf{B_{local}}$ was further investigated to study the Lorentz force effect (Figure 5.14). The $\mathbf{B_{local}}$ of the Fe_3O_4/N-TiO_2 samples can be derived from the M-H curves. The Lorentz force is given by $\mathbf{F} = q(\mathbf{v} \times \mathbf{B})$, where the **F** changes linearly with **B**. For the N-TiO_2 sample, the external magnetic field alone shows no obvious effect on the POWS performance, when the induced local magnetic field is absent. Therefore, only the local magnetic flux generated by the Fe_3O_4 NPs is considered in the correlation. The photocatalytic activity was plotted against the local magnetic flux density ($\mathbf{B_{local}}$) of the Fe_3O_4 NPs. Surprisingly, the H_2 evolution rate, although showing positive correlation with the local magnetic induction $\mathbf{B_{local}}$, did not change linearly. Also, Fe_3O_4/N-TiO_2 with a higher Fe_3O_4 content always gives higher

POWS performance even the local magnetic flux density is similar (Figure 5.14a). It is noticed that the average distance (**r**) from the core of Fe_3O_4 NPs to the catalyst surface (where the chemical reactions take place) decreases as the concentration of Fe_3O_4 NPs increases and the corresponding magnetic field strength is inversely proportional to $\mathbf{r^2}$. The distances were measured from the TEM images and then the POWS performance was plotted against $\mathbf{B_{local}/r^2}$ (Bearing in mind that the local magnetic flux density decays rapidly with the change of distance, only those Fe_3O_4 NPs near the surface were considered. See Figure 5.14d). Interestingly, upon calibration of the local magnetic flux density using these distances, all the samples appeared to show a similar response to $\mathbf{B_{local}/r^2}$, exhibiting an overall positive correlation. Further scrutiny indicates that the POWS performance increases linearly until $\mathbf{B_{local}/r^2}$= ~0.7, after which point it increases much more sharply, deviating from a linear relationship (Figure 5.14b). The linear influence originated from the Lorentz force effect could be described as follows:

$$\mathrm{H_2\ evolution\ rate} = 7042.22\frac{\mathbf{B_{local}}}{\mathbf{r^2}} + 6988.42 \qquad \textbf{Equation 5.1}$$

$$(\mathbf{R^2} = 0.9818)$$

where $\mathbf{B_{local}}$ is the local induced magnetic flux density and $\mathbf{r}$ is the average distance from the core of Fe_3O_4 NPs to the catalyst surface.

Additionally, 40 wt.% Fe_3O_4/N-TiO_2 with different N-doping concentrations were also prepared by controlling the temperature of the NH_3 treatment during N-doping,[3] and the POWS performance was then tested with and without the external magnetic field (180 mT). The POWS reaction was carried out at 270 °C with the irradiation of a 300-W Xe lamp which included UV and visible light, considering the extremely low absorption of pure TiO_2 in the visible light regime. The magnetic field

effect (MFE) enhancement of each catalyst was defined as:

$$MFE\ enhancement = \frac{Activity_{with\ MF} - Activity_{NMF}}{Activity_{NMF}} \qquad \textbf{Equation 5.2}$$

Clearly, the enhancement introduced by the MFE also shows a linear relationship with the N concentration at low doping level but increases sharply when the N concentration is higher (Figure 5.14c). Consequently, the above results imply that the MFE does not originate solely from the Lorentz force effect, especially when the local magnetic field is higher than the critical point of $\mathbf{B_{local}/r^2}$= ~0.7 and the N-doping content is increased. Such observations lead us to further investigation of the materials using DFT calculations to identify other factors contributing to the MFE.

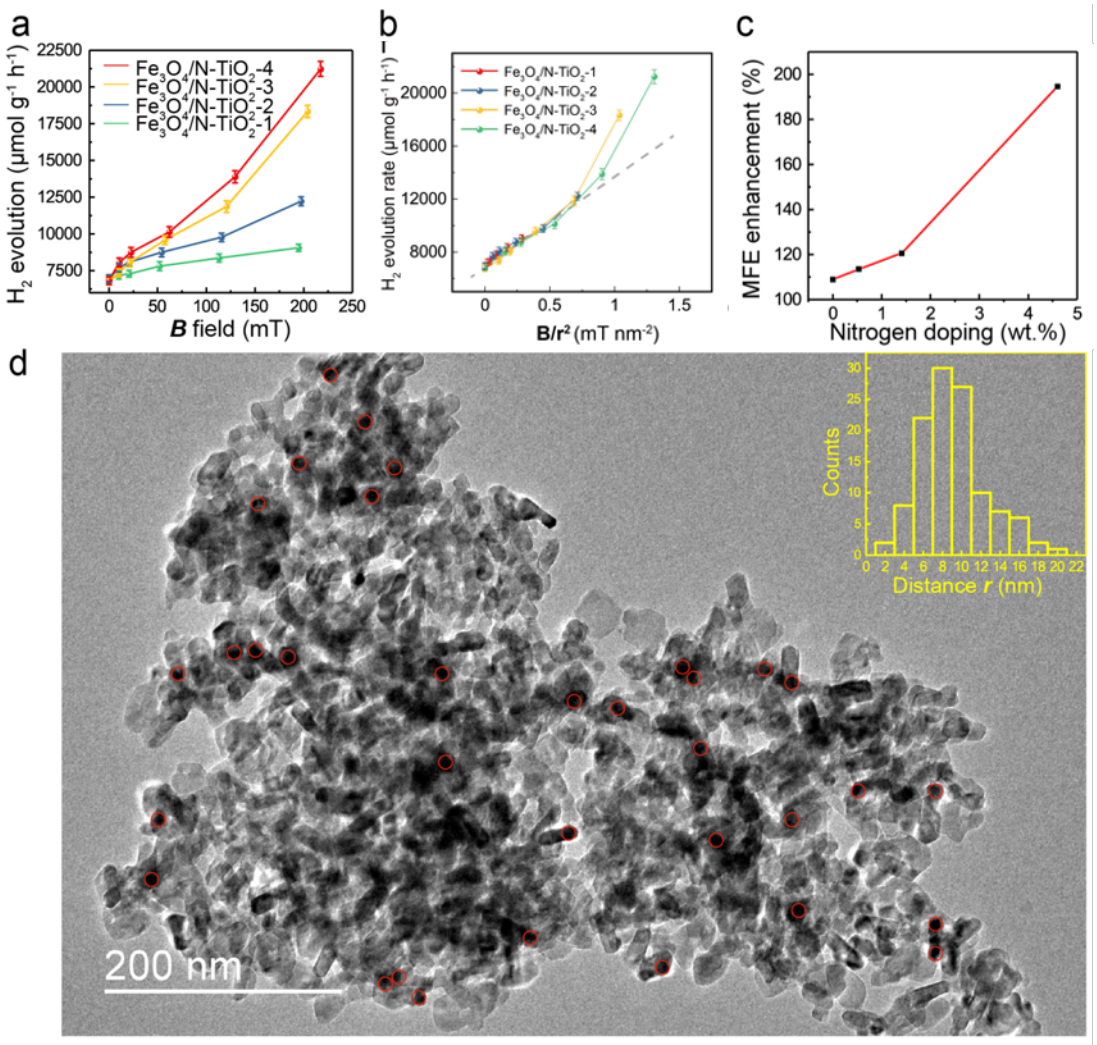

e

Sample	Mean distance ***r*** (nm)
Fe_3O_4/N-TiO_2-1	25.9 ± 3.2
Fe_3O_4/N-TiO_2-2	17.4 ± 2.4
Fe_3O_4/N-TiO_2-3	15.3 ± 1.8
Fe_3O_4/N-TiO_2-4	11.2 ± 1.3

Figure 5.14 (a) the relationship between the POWS performance of Fe_3O_4/N-TiO_2 photocatalysts with different Fe_3O_4 concentration and the local magnetic induction $\mathbf{B_{local}}$. **(b)** The relationship between the POWS performance and $\mathbf{B_{local}/r^2}$. All error bars indicate the standard deviation. **(c)** The POWS performances of the Fe_3O_4/N-TiO_2 photocatalysts with different N-doping levels in the N-TiO_2, of which the Fe_3O_4 concentrations were all maintained as 40 wt.%, tested with an external magnetic field of 180 mT. **(d)** A typical HRTEM image of Fe_3O_4/N-TiO_2-4, from which the average distance from Fe_3O_4 core to the catalyst surface (***r***) was estimated. The distance distribution is shown as inserted. **(e)** Summary of the average distance ***r*** (with errors) of each sample. The error bar indicates the standard deviation.

5.3.3 Evaluation of the spin-polarisation effect by DFT

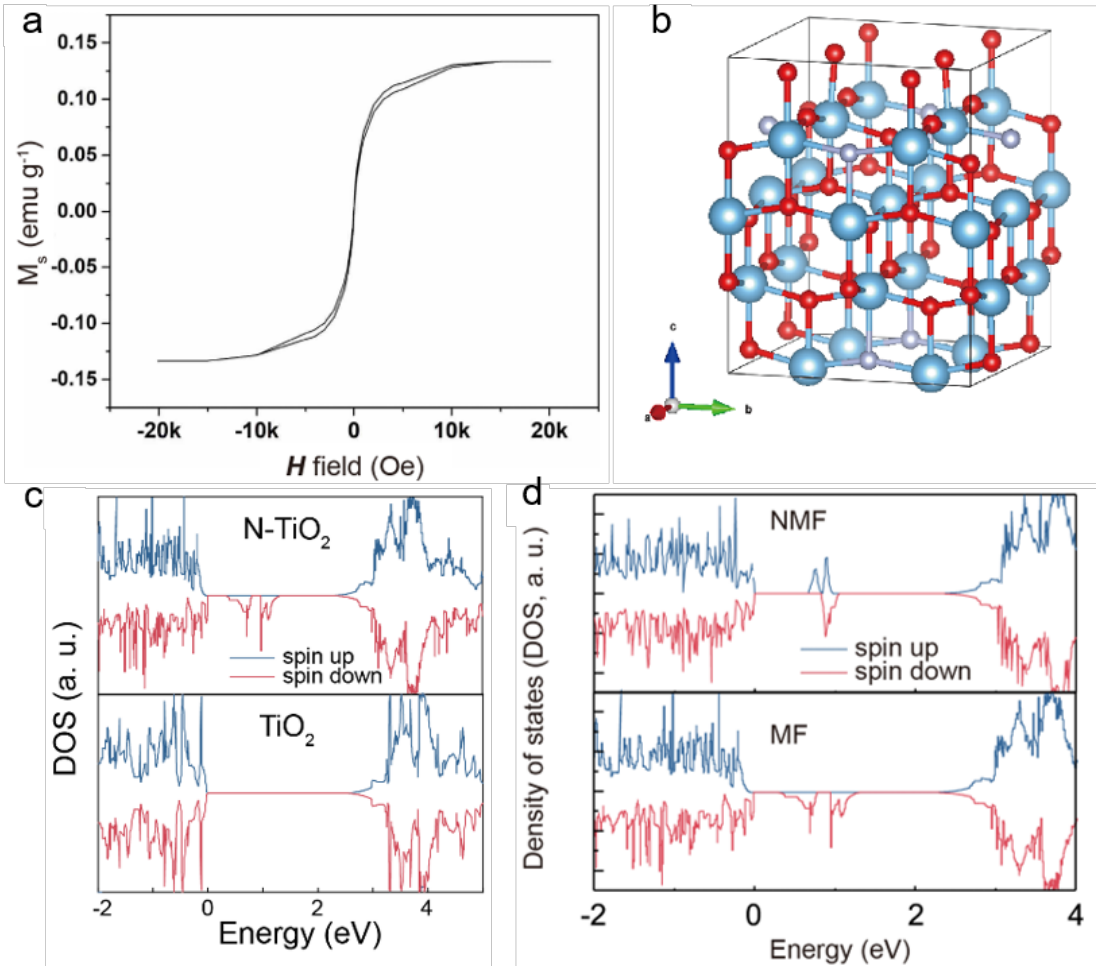

Figure 5.15 (a) ***M-H*** curve of N-TiO_2 photocatalyst after subtraction of the diamagnetic signal; **(b)** The constructed $Ti_{16}O_{28}N_4$ supercell for DFT calculation (O: red; Ti: blue; N: purple). **(c)** Calculated total DOS of $Ti_{16}O_{28}N_4$ supercell (N-TiO_2) and $Ti_{16}O_{32}$ supercell (pure TiO_2) with the local magnetic field alignment. **(d)** Calculated total DOS of the $Ti_{16}O_{28}N_4$ supercell without and with the external magnetic field (NMF=no magnetic field; MF=magnetic field).

Apart from the electromagnetic properties, the quantum mechanical properties of the electron, such as angular momentum (spin) has long been neglected in photocatalytic studies. It is noted that magnetic moments exist in the N-TiO_2 (Figure 5.15a), implying that the cooperative alignment of such moments under a magnetic field may influence the POWS performance together with the above-discussed Lorentz force effect. It has been reported

that N-substitution of O atoms in N-TiO_2 of low N content could generate defective holes, and the hole-mediated double exchange through the strong p-p interaction between N and O can give spins correlation to this material[30]. Considering the XPS spectra showed the doped N were dominantly in the substitutional sites, a $Ti_{16}O_{28}N_4$ supercell based on the structure of anatase TiO_2 with *ca.* 4.4 wt.% substitutional N-doping derived from our recent study (ref. [31]) was constructed and studied by the first-principles DFT calculations, as shown in Figure 5.15b.

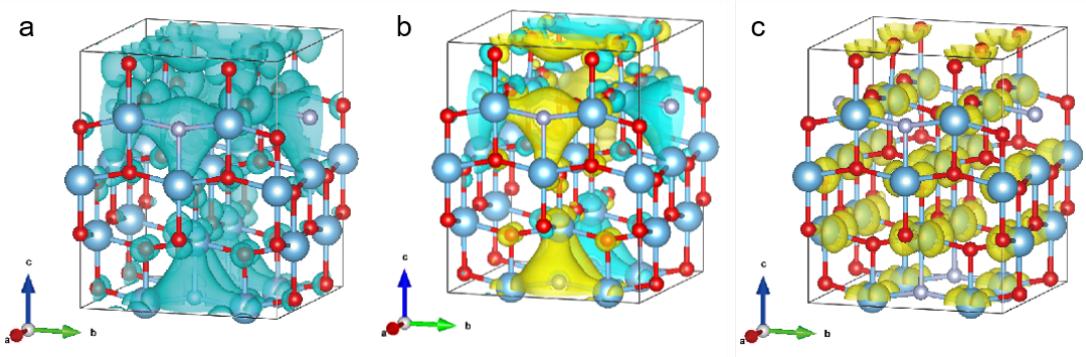

Figure 5.16 (a) 3D spatial distributions of spin polarisation of N-doped $Ti_{16}O_{28}N_4$ model in defect band with the local magnetic field and **(b)** that without any external magnetic field. Yellow surfaces represent the charge density of spin-up electrons and blue surfaces represent the charge density of spin-down electrons. The value of the iso-surface is set to be 0.001eV/Å. **(c)** Calculated partial charge density of CBM with the magnetic field. The value of iso-surface is set to be 0.001eV/Å. The yellow surfaces represent the distribution of the total electron densities in the CBM near each atom.

The calculated total density of states (DOS) of N-TiO_2 clearly showed that the defect states were created within the band gap near the Fermi level, which originated from the N-doping, while such an additional band was absent in the pure TiO_2 model (Figure 5.15c). These defect states are not localised in contrast to the previous literature of the low N content, but form a wide band extended to the valence band (VB) instead, due to the strong interaction between the N atoms at our high N-doping concentration, which

also accounts for the enhanced visible light absorption[32]. The defect states can be distributed on two spin channels (spin-up and spin-down), but only one spin channel occurs in the band gap region of N-TiO_2 under a magnetic field (Figure 5.15d), indicative that the magnetic moments can be well-aligned in the material.

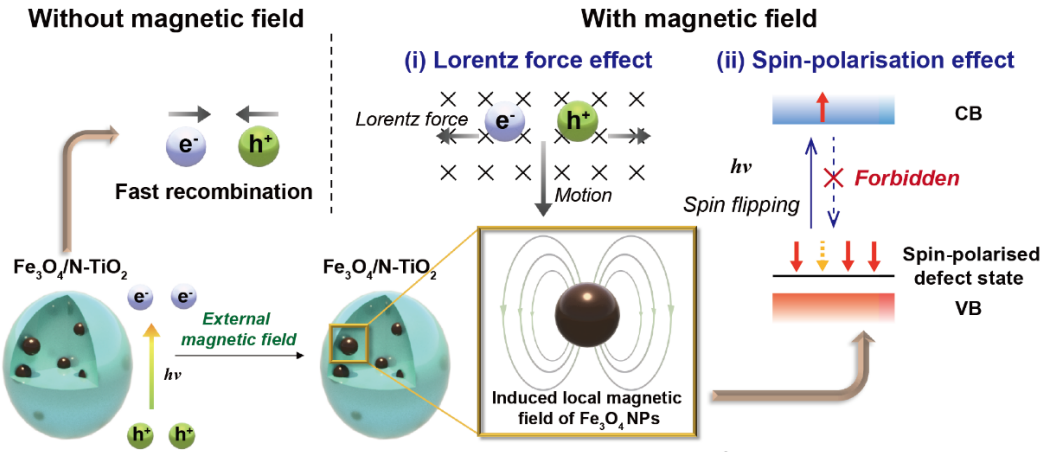

Figure 5.17 Schematic illustration of the magnetic field promoted POWS system, where the charge separation is facilitated by the local magnetic induction.

The calculated spatial spin distribution also indicated a strong spatial spin polarisation: only the blue surface that represented the spin-down channel was observed, whist the spin-up channel was absent (Figure 5.16a). On the other hand, as shown in Figure 5.15d, the total DOS clearly indicates that the defect band is not polarised, and the magnetic moments are distributed on the two spin channels when a magnetic field is absent. The presence of both yellow and blue surfaces in Figure 5.16b also suggests the existence of both spin channels in the defect band without the influence of a magnetic field. Meanwhile, the magnetic field has little effect on the conduction band (CB): the calculated partial charge density of the CBM is almost the same no matter whether a magnetic field is present or not (Figure 5.16c). Clearly,

in the presence of an induced local magnetic field from Fe_3O_4 NPs, the cooperative magnetic moments in N-TiO_2 align in parallel in the high spatial spin polarised environment. When an electron is excited to the CB, it is likely to undergo spin relaxation during the transfer, losing its original spin characteristics and changing to the other state (spin-up), due to spin-orbit coupling, etc.[33] The spin-orbit coupling is a relativistic interaction of an electron's spin with its motion inside a potential. It can be thought of as a Zeeman effect product of two relativistic effects: the apparent magnetic field seen from the electron's perspective and the magnetic moment of the electron associated with its intrinsic spin. Therefore, electrons can change their spin due to this spin-orbit interaction. Subsequently, upon recombination, the lack of a spin-up channel makes it more difficult for the spin-up electrons to come back to the VB. Overall, both the slow spin flips and the opposing Lorentz forces result in a prolonged charge carrier lifetime, as observed from TRPL measurements. The above proposed mechanism is illustrated in Figure 5.17. Considering the photocatalyst particles are highly dispersed in the suspension during the reaction, the interaction of local magnetic fields between different particles would be negligible. The prolonged lifetimes of the photo-generated charge carriers greatly reduce the chance of recombination, therefore enhance the diffusion to the surface to facilitate the H^+ reduction and OH^- oxidation reactions from water. Such observation can also explain the relationship seen in Figure 5.14c: as the N concentration increases, the magnetic moments in the defect band (which consists of N orbitals) also increase, forming an extended energy band, which accounts for the dramatic spin-polarisation effect. While at low doping

levels, the defect band is too narrow and localised to show any spin-polarisation effect in an external magnetic field. Therefore, the spin-polarisation effect dominates at high N-doping concentration under high magnetic flux. Since the Lorentz force effect can be described by Equation 5.1, the contribution of the spin-polarisation effect can be evaluated quantitatively. Analyses of the results shows that at $\mathbf{B_{local}/r^2}$=0.71, the spin-polarisation accounted for only 8.9% of the MFEs, while the contribution increased to 22.6% at a stronger local magnetic flux ($\mathbf{B_{local}/r^2}$=1.31). These observations imply the opportunity of rational design of photocatalysts by modifying different aspects of the MFEs (*i.e.*, charge and spin features) in order to control the charge separation and charge carrier lifetime, which presumably have profound meanings to both academic study and practical application of photocatalytic technologies.

5.3.4 Evaluation of practicality

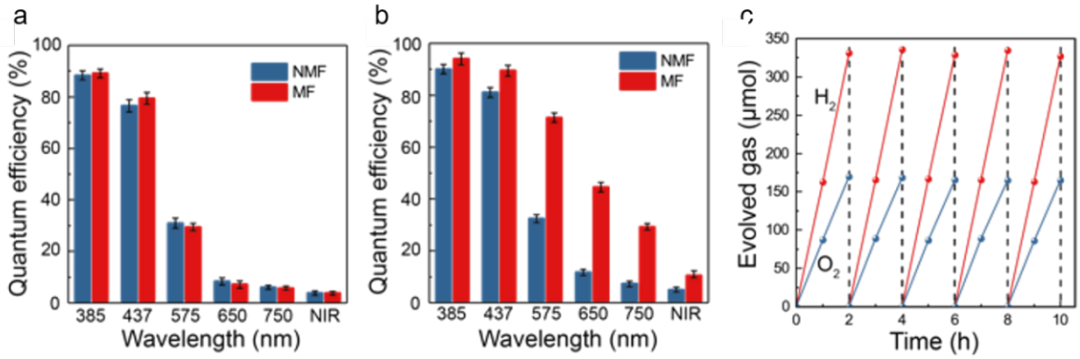

Figure 5.18 QE of N-TiO_2 **(a)** and Fe_3O_4/N-TiO_2-4 **(b)** photocatalysts with and without external magnetic field (NMF=no magnetic field; MF=magnetic field of 180 mT). Error bars indicate the standard deviations; **(c)** Repeatable tests of Fe_3O_4/N-TiO_2-4 photocatalyst at 270 °C and 180 mT followed by cooling to room temperature in each cycle, respectively.

The application potential of this POWS system was further evaluated by QE and STH conversion efficiency, both of which are widely recognised as key

parameters for solar conversion systems.[34]

Figure 5.18a clearly shows that the internal QEs of N-TiO_2 were not influenced by an external magnetic field, while Figure 5.18b shows that Fe_3O_4/N-TiO_2-4 displays a sensitive response to the magnetic field, giving impressive QEs of 96.2 % at 385 nm and 88.7 % at 437 nm. The measurement of the internal QE in the near infrared (NIR) regime has also been attempted by using a bandpass filter which allows a wavelength range of 800-1200 nm to pass through. Excitingly, it gives an enhanced internal QE of 10.8 % even in this NIR regime on the Fe_3O_4/N-TiO_2-4 photocatalyst under a magnetic field of 180 mT. The theoretical efficiency limit of a solar conversion system was carefully analysed by Shockley and Queisser (known as Shockley-Queisser limit or detailed-balance limit).[35] Such limit was then further considered for photochemical systems by Ross and Hsiao.[36] It has been demonstrated that there is always a part of the photon energy that cannot do useful work, thus, for a given reaction, the threshold energy that is capable of driving the reaction must exceed the minimum thermodynamic requirement (free energy) of the reaction by 0.2-0.3 eV.[35–38] Such energy difference could be minimised by different approaches, such as engaging light trapping techniques, concentrated light irradiation, high-purity light absorbers, etc.[56] Detailed evaluation and discussions of this threshold wavelength are given in Appendix Note A1. Moreover, the STH conversion efficiency has been evaluated for our POWS system. As demonstrated by Domen *et al.* recently, it is quite common that the POWS reaction is carried out under various non-standard conditions including reduced pressure, cooling, or heating, etc., thus the changes of the free

energy must be considered by default.[39] Also should be noted is that in our batch process, the partial pressures of the evolved H_2 and O_2 change as the reaction proceeding. Additionally, in our system, the reaction is performed at a constant volume, thus, the Helmholtz free energy is used instead of the Gibbs free energy. Therefore, the free energy has been corrected for the operating temperature and the partial pressures in the system (Appendix Note A3). As a result, a time-averaged STH efficiency of 11.9±0.5% has been achieved from this local magnetic field promoted POWS system under a magnetic field of 180 mT (Appendix Note A3). Recyclability of the Fe_3O_4/N-TiO_2-4 photocatalyst was evaluated by recycling the catalysts for 5 times, showing no obvious change in photocatalytic activity (Figure 5.18c), and it is presumably that Fe_3O_4 NPs are protected by the N-TiO_2 coating from oxidation. It is also noteworthy that our POWS reaction could still proceed even in the presence of considerable pressures of H_2 and O_2 that make the reaction less favourable thermodynamically, and drive the reverse reaction more considerably. Subsequently, an overall energy conversion efficiency of 1.16±0.05% has been demonstrated when the energy input for heating is considered (details can be found in Appendix Note A3). Although this overall energy efficiency of 1.16% appears to be low, it should be emphasised this is not the situation that is anticipated in the future design. It is apparent that solar light could also provide heat by irradiation, photothermal effect, etc. Thus, in an ideal future design, the energy for heating is not provided by external source but from concentrated solar light, therefore, the energy consumption for heating the water and reactor could be excluded in that scenario, and a higher overall energy efficiency could be expected. In

addition, the superheated water carries quite large thermal energy, which may subsequently be used for additional energy generation, *i.e.*, H_2 by steam turbine-electrolyser. Thus, by considering the availability of solar heating and additional H_2 generation, the actual overall energy efficiency could be much higher upon further optimisation. Nevertheless, the current value is still superior to the recently reported values in literature in the related fields.[40,41]

5.4 Conclusion

In conclusion, superparamagnetic Fe_3O_4 NPs and a series of Fe_3O_4/N-TiO_2 photocatalysts have been successfully synthesised, showing exceptional POWS performance under visible light irradiation with an external magnetic field. The structural, absorption and magnetic properties of the materials have been carefully investigated. A remarkable H_2 evolution rate of 21,230 μmol g^{-1} h^{-1} and QE of 88.7 % at 437 nm are obtained at 270 °C over 40 wt.% Fe_3O_4/N-TiO_2 under an external magnetic field of 180 mT due to the greatly prolonged charge carrier lifetimes over this photocatalyst. An outstanding STH efficiency of 11.9±0.5% can be demonstrated by our simple set-up particulate POWS system with anticipated low capex cost. In addition to the Lorentz force effect, spin-polarisation is for the first time demonstrated systematically in this N-doped TiO_2 structure under an external magnetic field: the Lorentz effect contributes dominantly when the field strength is weak, but when the field strength is strong enough ($\mathbf{B_{local}/r^2}$>0.7), the spin-polarisation effect can be triggered to further improve the photocatalytic activity, accounting for 22.6% contribution at $\mathbf{B_{local}/r^2}$=1.31. Both effects lead to prolonged charge carrier lifetime and facilitate photocatalysis over the N-

TiO_2 based material. As such this work provides insights on the use of the two fundamental features of electrons including charge and spin in the magnetic field promoted photocatalysis. To unlock the full potential of MFEs, not only can various photocatalytic systems be designed with tuned charge and/or spin characteristics, but also the strength of the local magnetic field can be tuned by engineering related photocatalysts in the proximity of stronger superparamagnetic alloy shells or under a stronger external field, further contributing to novel responsive solar energy conversion technologies and the rational design of various photocatalytic systems with high efficiency.

5.5 References

1. Li, Y., Wang, Z., Wang, Y., Kovács, A., Foo, C., Dunin-Borkowski, R. E., Lu, Y., Taylor, R. A., Wu, C. & Tsang, S. C. E. Local magnetic spin mismatch promoting photocatalytic overall water splitting with exceptional solar-to-hydrogen efficiency. *Energy Environ. Sci.* **15**, 265–277 (2022).
2. Wolff, C. M., Frischmann, P. D., Schulze, M., Bohn, B. J., Wein, R., Livadas, P., Carlson, M. T., Jäckel, F., Feldmann, J., Würthner, F. & Stolarczyk, J. K. All-in-one visible-light-driven water splitting by combining nanoparticulate and molecular co-catalysts on CdS nanorods. *Nat. Energy* **3**, 862–869 (2018).
3. Li, Y., Peng, Y.-K., Hu, L., Zheng, J., Prabhakaran, D., Wu, S., Puchtler, T. J., Li, M., Wong, K.-Y., Taylor, R. A. & Tsang, S. C. E. Photocatalytic water splitting by N-TiO2 on MgO (111) with exceptional quantum efficiencies at elevated temperatures. *Nat. Commun.* **10**, 4421 (2019).
4. Li, Y. & Tsang, S. C. E. Unusual Catalytic Properties of High-Energetic-Facet Polar Metal Oxides. *Acc. Chem. Res.* **54**, 366–378 (2021).
5. Li, Y., Wu, S., Zheng, J., Peng, Y.-K., Prabhakaran, D., Taylor, R. A., Chi, S. & Tsang, S. C. E. 2D photocatalysts with tuneable supports for enhanced photocatalytic water splitting. *Mater. Today* **41**, 34–43 (2020).
6. Li, Y. & Tsang, S. C. E. Recent Progress and Strategies for Enhancing Photocatalytic Water Splitting. *Mater. Today Sustain.* **9**, 100032 (2020).
7. Selwood, P. W. Magnetism and catalysis. *Chem. Rev.* **38**, 41–82 (1946).
8. Steiner, U. E. & Ulrich, T. Magnetic Field Effects in Chemical Kinetics and Related Phenomena. *Chem. Rev.* **89**, 51–147 (1989).
9. Okumura, H., Endo, S., Joonwichien, S., Yamasue, E. & Ishihara, K. N. Magnetic field effect on heterogeneous photocatalysis. *Catal. Today* **258**, 634–647 (2015).
10. Li, J., Pei, Q., Wang, R., Zhou, Y., Zhang, Z., Cao, Q., Wang, D., Mi, W. & Du, Y. Enhanced Photocatalytic Performance through Magnetic Field Boosting Carrier

Transport. *ACS Nano* **12**, 3351–3359 (2018).

11. Gao, W., Lu, J., Zhang, S., Zhang, X., Wang, Z., Qin, W., Wang, J., Zhou, W., Liu, H. & Sang, Y. Suppressing Photoinduced Charge Recombination via the Lorentz Force in a Photocatalytic System. *Adv. Sci.* **6**, 1901244 (2019).
12. Zhao, Z., Wang, D., Gao, R., Wen, G., Feng, M., Song, G., Zhu, J., Luo, D., Tan, H., Ge, X., Zhang, W., Zhang, Y., Zheng, L., Li, H. & Chen, Z. Magnetic‐Field‐Stimulated Efficient Photocatalytic N 2 Fixation over Defective BaTiO 3 Perovskites . *Angew. Chemie* **133**, 12017–12025 (2021).
13. Zhao, J., Li, N., Yu, R., Zhao, Z. & Nan, J. Magnetic field enhanced denitrification in nitrate and ammonia contaminated water under 3D/2D Mn2O3/g-C3N4 photocatalysis. *Chem. Eng. J.* **349**, 530–538 (2018).
14. Jiang, M. P., Huang, K. K., Liu, J. H., Wang, D., Wang, Y., Wang, X., Li, Z. Da, Wang, X. Y., Geng, Z. Bin, Hou, X. Y. & Feng, S. H. Magnetic-Field-Regulated TiO2 {100} Facets: A Strategy for C-C Coupling in CO2 Photocatalytic Conversion. *Chem* **6**, 2335–2346 (2020).
15. Zhao, C., Zhou, L., Zhang, Z., Gao, Z., Weng, H., Zhang, W., Li, L. & Song, Y. Y. Insight of the Influence of Magnetic-Field Direction on Magneto-Plasmonic Interfaces for Tuning Photocatalytical Performance of Semiconductors. *J. Phys. Chem. Lett.* **11**, 9931–9937 (2020).
16. Peng, Y. K., Lui, C. N. P., Chen, Y. W., Chou, S. W., Raine, E., Chou, P. T., Yung, K. K. L. & Tsang, S. C. E. Engineering of Single Magnetic Particle Carrier for Living Brain Cell Imaging: A Tunable T1-/T2-/Dual-Modal Contrast Agent for Magnetic Resonance Imaging Application. *Chem. Mater.* **29**, 4411–4417 (2017).
17. Mishra, P., Patnaik, S. & Parida, K. An overview of recent progress on noble metal modified magnetic Fe3O4 for photocatalytic pollutant degradation and H2 evolution. *Catal. Sci. Technol.* **9**, 916–941 (2019).
18. Köseoğlu, Y. Effect of surfactant coating on magnetic properties of Fe3O4 nanoparticles: ESR study. *J. Magn. Magn. Mater.* **300**, e327–e330 (2006).
19. Di Valentin, C., Pacchioni, G., Selloni, A., Livraghi, S. & Giamello, E. Characterization of paramagnetic species in N-doped TiO 2 powders by EPR spectroscopy and DFT calculations. *J. Phys. Chem. B* **109**, 11414–11419 (2005).
20. Feng, N., Lin, H., Song, H., Yang, L., Tang, D., Deng, F. & Ye, J. Efficient and selective photocatalytic CH4 conversion to CH3OH with O2 by controlling overoxidation on TiO2. *Nat. Commun.* **12**, (2021).
21. Mubeen, S., Hernandez-Sosa, G., Moses, D., Lee, J. & Moskovits, M. Plasmonic photosensitization of a wide band gap semiconductor: Converting plasmons to charge carriers. *Nano Lett.* **11**, 5548–5552 (2011).
22. Hou, W. & Cronin, S. B. A review of surface plasmon resonance-enhanced photocatalysis. *Adv. Funct. Mater.* **23**, 1612–1619 (2013).
23. Zhan, C., Wang, Z. Y., Zhang, X. G., Chen, X. J., Huang, Y. F., Hu, S., Li, J. F., Wu, D. Y., Moskovits, M. & Tian, Z. Q. Interfacial Construction of Plasmonic Nanostructures for the Utilization of the Plasmon-Excited Electrons and Holes. *J. Am. Chem. Soc.* **141**, 8053–8057 (2020).
24. Zeradjanin, A. R., Vimalanandan, A., Polymeros, G., Topalov, A. A., Mayrhofer, K. J. J. & Rohwerder, M. Balanced work function as a driver for facile hydrogen evolution reaction - Comprehension and experimental assessment of interfacial catalytic descriptor. *Phys. Chem. Chem. Phys.* **19**, 17019–17027 (2017).
25. Seh, Z. W., Kibsgaard, J., Dickens, C. F., Chorkendorff, I., Nørskov, J. K. &

Jaramillo, T. F. Combining theory and experiment in electrocatalysis: Insights into materials design. *Science* **355**, 146 (2017).

26. Ingram, D. B. & Linic, S. Water splitting on composite plasmonic-metal/semiconductor photoelectrodes: Evidence for selective plasmon-induced formation of charge carriers near the semiconductor surface. *J. Am. Chem. Soc.* **133**, 5202–5205 (2011).

27. Furube, A., Du, L., Hara, K., Katoh, R. & Tachiya, M. Ultrafast plasmon-induced electron transfer from gold nanodots into TiO2 nanoparticles. *J. Am. Chem. Soc.* **129**, 14852–14853 (2007).

28. Zhu, S. & Wang, D. Photocatalysis: Basic principles, diverse forms of implementations and emerging scientific opportunities. *Adv. Energy Mater.* **7**, 1700841 (2017).

29. Kovács, A. & Dunin-Borkowski, R. E. Magnetic Imaging of Nanostructures Using Off-Axis Electron Holography. *Handb. Magn. Mater.* **27**, 59–153 (2018).

30. Tao, J. G., Guan, L. X., Pan, J. S., Huan, C. H. A., Wang, L., Kuo, J. L., Zhang, Z., Chai, J. W. & Wang, S. J. Density functional study on ferromagnetism in nitrogen-doped anatase TiO2. *Appl. Phys. Lett.* **95**, 93–96 (2009).

31. Foo, C., Li, Y., Lebedev, K., Chen, T. T., Day, S., Tang, C. & Tsang, S. C. E. Characterisation of oxygen defects and nitrogen impurities in TiO2 photocatalysts using variable-temperature X-ray powder diffraction. *Nat. Commun.* **12**, 661 (2021).

32. Wang, W., Tadé, M. O. & Shao, Z. Nitrogen-doped simple and complex oxides for photocatalysis: A review. *Prog. Mater. Sci.* **92**, 33–63 (2018).

33. Pan, L., Ai, M., Huang, C., Yin, L., Liu, X., Zhang, R., Wang, S., Jiang, Z., Zhang, X., Zou, J. J. & Mi, W. Manipulating spin polarization of titanium dioxide for efficient photocatalysis. *Nat. Commun.* **11**, 418 (2020).

34. Wang, Z., Li, C. & Domen, K. Recent developments in heterogeneous photocatalysts for solar-driven overall water splitting. *Chem. Soc. Rev.* **48**, 2109–2125 (2019).

35. Shockley, W. & Queisser, H. J. Detailed balance limit of efficiency of p-n junction solar cells. *J. Appl. Phys.* **32**, 510–519 (1961).

36. Ross, R. T. & Hsiao, T. L. Limits on the yield of photochemical solar energy conversion. *J. Appl. Phys.* **48**, 4783–4785 (1977).

37. Bolton, J. R., Stricklert, S. J. & Connolly, J. S. Limiting and realizable efficiencies of Solar Photolysis of Water. *Nature* **316**, 495–500 (1985).

38. Bolton, J. R. Solar fuels. *Science* **202**, 705–711 (1978).

39. Wang, Z., Hisatomi, T., Li, R., Sayama, K., Liu, G., Domen, K., Li, C. & Wang, L. Efficiency Accreditation and Testing Protocols for Particulate Photocatalysts toward Solar Fuel Production. *Joule* **5**, 344–359 (2021).

40. Takata, T., Jiang, J., Sakata, Y., Nakabayashi, M., Shibata, N., Nandal, V., Seki, K., Hisatomi, T. & Domen, K. Photocatalytic water splitting with a quantum efficiency of almost unity. *Nature* **581**, 411–414 (2020).

41. Nishiyama, H., Yamada, T., Nakabayashi, M., Maehara, Y., Yamaguchi, M., Kuromiya, Y., Tokudome, H., Akiyama, S., Watanabe, T., Narushima, R., Okunaka, S., Shibata, N., Takata, T., Hisatomi, T. & Domen, K. Photocatalytic solar hydrogen production from water on a 100 m2-scale. *Nature* **598**, 304–307 (2021).

Chapter 6 Photocatalytic Seawater Splitting System

6.1 Introduction

It has been demonstrated in Chapters 3-5 that the local polarisation plays a tremendously important role in improving the POWS performance at elevated temperatures, which facilitates the separation of the photo-generated charge carriers. Many recent studies have also reported similar conclusions.[1–5] Different strategies have been developed and demonstrated in Chapters 3-5, such as using polar-faceted materials to provide local electric field (LEF), or using the magnetic field effects (MFEs), etc., which has encouraged me to think deeper about this high-temperature POWS system and inspired me of further improvement to push this system closer to the practical applications. Although extensive efforts are dedicated to the POWS studies in pure water, actually, more than 90% of the water resource on the earth surface is stored in seas and oceans, which are salty;[6–11] not to mention that the desalination and purification (*e.g.*, reverse osmosis, distillation, ion exchange, etc.) largely adds up to the overall capital costs of this technology.[12–14] Obviously, H_2 evolution via splitting of the seawater or brackish water is more desirable for large-scale applications and able to mitigate the fresh water resource shortage, however, systematic study and in-depth understanding of the photocatalytic seawater splitting are still limited. Contradictory views regarding the effect of seawater on the POWS performance emerge in recent literature, for example, Tian *et al.* presented that a supported black phosphor nanosheets catalyst could split seawater with a much lower H_2 evolution rate than that in pure water;[8] while it was reported that photocatalytic H_2 evolution could be enhanced for WO_3 nano-arrays and GaN-based catalysts in seawater because of higher charge mobility.[7,15] Meanwhile, the cations in seawater were reported able

to polarise the carboxyl groups on the surface of a carbon dots (CDs) photocatalyst, leading to stronger electron-trapping and resulting in an enhanced H_2O_2 photoproduction.[9] Opinions contradict in the field of seawater electrolysis as well.[10,16–18] Clearly, unlike pure water, the ionic species in seawater exert various effects on catalytic reactions; and a common concern is that the anions like Cl^- can be photocatalytically oxidised, forming Cl_2 or ClO^- (see Equations 6.1 and 6.2), which are corrosive to many materials.[15] Thus, it is challenging to develop an efficient and stable catalytic system for such a salty environment. Also noteworthy is that the ionic species in seawater carry charges that generate LEF in their vicinity, and such LEF could facilitate the separation of the photo-generated charge carriers, as demonstrated in the previous chapters.

Oxidation: $2Cl^- + 2h^+ == Cl_2$

Reduction: $2H_2O + 2e^- == H_2 + 2OH^-$ **Equation 6.1**

Oxidation: $2OH^- + Cl^- + 2h^+ == ClO^- + H_2O$

Reduction: $2H_2O + 2e^- == H_2 + 2OH^-$ **Equation 6.2**

6.2 Objectives

As mentioned before, the POWS reaction using particulate suspension has been recognised as a promising approach for harnessing solar energy. Thus, if such system could be operated using natural seawater, it could be more desirable. However, the majority of the POWS studies have been focusing on pure water, while more than 90% of water resource on the earth surface is in seas and oceans, which are salty water. In this chapter, the facet-engineered N-doped TiO_2 (denoted as N-TiO_2) is taken as an example. I systematically studied the POWS reaction in the salty environments, where H_2 and O_2 were stoichiometrically and stably

produced at 270 °C. Artificial seawaters are prepared to simulate the water resources at different areas in the world, and a natural seawater sample was collected from Bournemouth in the UK. I will focus on the effects of the ionic species in this chapter and attempt to explore the mechanism of this system at 270 °C. Besides, the underlying principles will be investigated with the help of various techniques. High angle annular dark field scanning transmission electron microscopy (HAADF-STEM) will be used to understand the facet-dependent trapping of the charge carriers. Ambient pressure X-ray photoelectron spectroscopy (AP-XPS) study is carried out using the trimethylphosphine (TMP) as a surface probe to further understand the polarisation effect. With the help of density functional theory (DFT) calculations, the surface trappings of the photo-generated electrons and holes upon photoexcitation will be illustrated. I believe all these investigations about the local polarisation will help to understand the effects of the ionic species in the seawater. This versatile system will also be applied to other important semiconductor photocatalysts, such as perovskite oxynitride materials.

6.3 Results and discussion

6.3.1 Characterisations of the facet-engineered TiO_2 nanocrystals

Facet-controlled TiO_2 nanostructures were prepared using hydrofluoric acid as a structure-directing agent (SDA) based on our previous report, followed by NH_3 treatment at high temperature to obtain the N-doped TiO_2 (denoted as N-TiO_2) and remove the surface F-group at the same time.[2,19] The as-prepared N-TiO_2 material has then been comprehensively characterised by various experimental techniques, such as transmission electron microscopy (TEM), X-ray powder diffraction (XRD), Raman spectroscopy, electron paramagnetic resonance (EPR) spectroscopy, X-

ray photoelectron spectroscopy (XPS), UV-visible diffuse reflectance spectroscopy (UV-Vis DRS), etc., which are discussed in details in the following sub-sections.

6.3.1.1 XRD patterns of TiO_2 and N-TiO_2

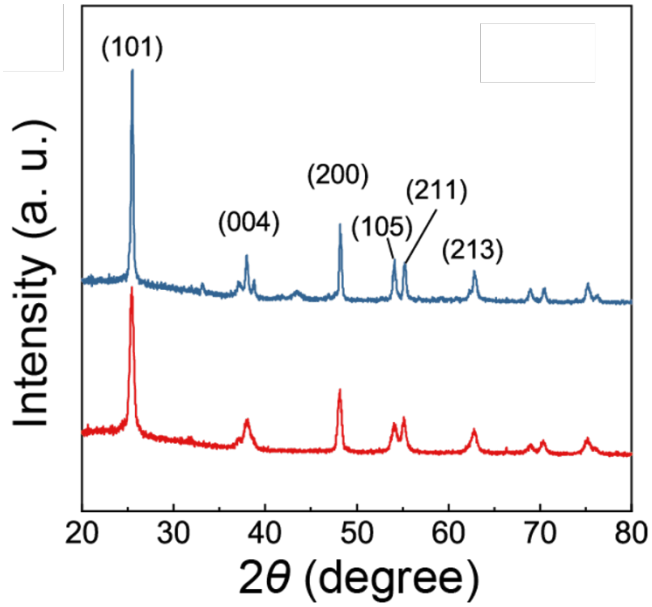

Figure 6.1 XRD patterns of the as-prepared facet-engineered TiO_2 (red) and N-TiO_2 (blue). The N-TiO_2 presented here was obtained by treating the facet-engineered TiO_2 with NH_3 flow at 600 ^oC for 8 h. The characteristic peaks of anatase TiO_2 phase have been labelled.

XRD measurements were performed to investigate the structural information of the as prepared facet-engineered TiO_2 and N-TiO_2, and the XRD patterns are shown in Figure 6.1. As can be seen, both the pristine TiO_2 and N-TiO_2 exhibit the anatase TiO_2 phase. The characteristic peaks at 2θ of 25.3^o, 37.8^o and 48.1^o can be observed in Figure 6.1 for both materials, which are corresponding to the (101), (004) and (200) crystal facets of anatase TiO_2, respectively. No rutile peak emerges after the ammonia treatment as shown in Figure 6.1, indicating the high-temperature ammonia treatment does not lead to a substantial phase transformation from anatase to the more stable rutile phase. However, it should be noted that there is a small peak at 2θ of 43.3^o emerging after the NH_3 treatment, which could be attributed to the local oxynitride phase (TiO_xN_y) that has been

discussed in Chapter 3.

6.3.1.2 Microscopic studies of N-TiO_2

HAADF-STEM was engaged to investigate the morphologies of the TiO_2-based materials. The HAADF-STEM images show that the N-TiO_2 exhibits lattice fringes with d-spacings of 0.237 and 0.352 nm, in accordance with the [004] and [101] crystallographic planar directions of anatase TiO_2, respectively (Figure 6.2), which indicates the exposure of the polar (001) and non-polar (101) facets for the N-TiO_2 nanocrystals. The interfacial angle of 68.3° can also be observed in the HAADF-STEM images shown in Figure 6.2, which further confirms the exposed facets.

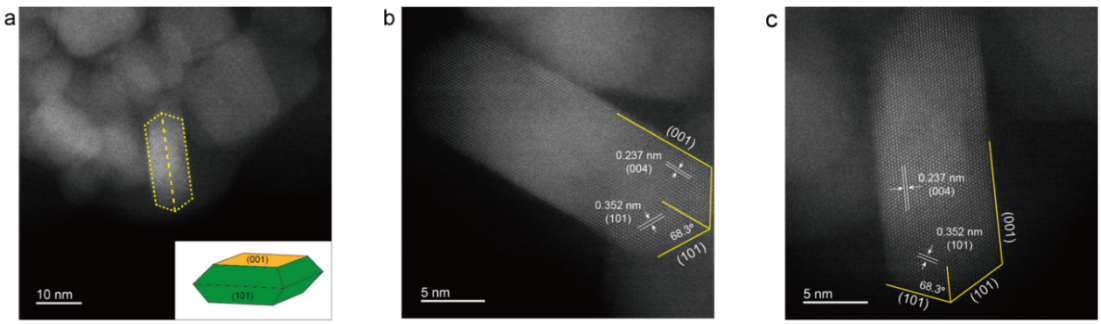

Figure 6.2 STEM images of the as prepared facet-engineered N-TiO_2. **a** low-magnification HAADF-STEM image showing the morphology of N-TiO_2; **b, c** high-magnification HAADF-STEM images showing the lattice spacings and exposed crystal facets.

Then, according to the Wulff construction, the ratio of the exposed (101) and (001) facets can be calculated (Figure 6.3). The percentages of exposed (101) and (001) facets estimated to be 38 % and 62 %, respectively.

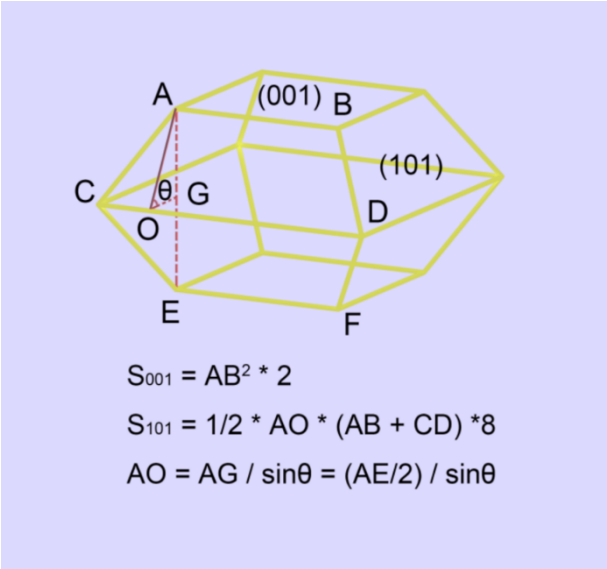

Figure 6.3 Simulated shape of the TiO_2 anatase single crystal and the calculation process for percentage of (001) facets (θ of 68.3° is the interfacial angle between (001) and (101)).[20]

6.3.1.3 XPS of N-TiO_2 materials

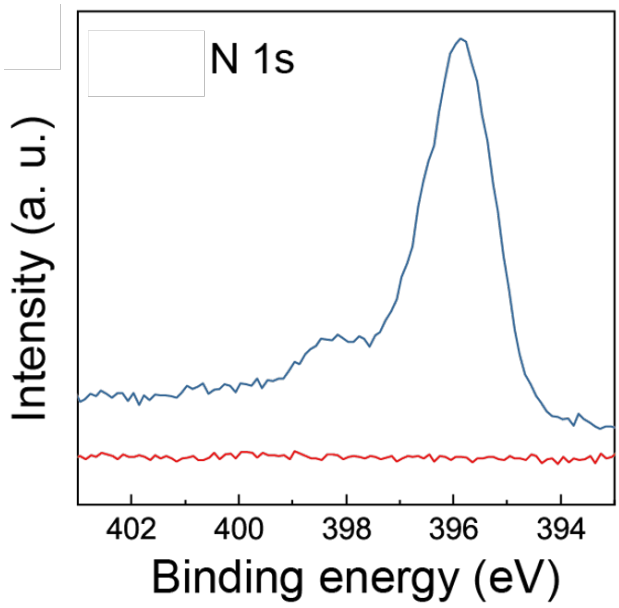

Figure 6.4 High resolution N 1s XPS spectra of the as prepared facet-engineered TiO_2 (red) and N-TiO_2 (blue).

The *ex situ* XPS was used to obtain the elemental information of the as-prepared materials, which indicates that the N atoms were successfully doped into the TiO_2 nanocrystals and the surface F-groups were removed (Figure 6.4). A peak can be

observed at a binding energy (BE) of 396 eV for the N-TiO_2, which originates from the N atoms substituting the original O atoms according to literature;[21,22] while there is obviously no such signal detected for the pristine TiO_2. It has been demonstrated in the previous chapters that the N-doping would lead to greatly enhanced absorption of visible and infrared light. Also, the surface oxygen vacancies (V_Os) are introduced by the N-doping. More details have been discussed in Chapter 3.

6.3.1.4 EPR of facet-engineered TiO_2 based materials

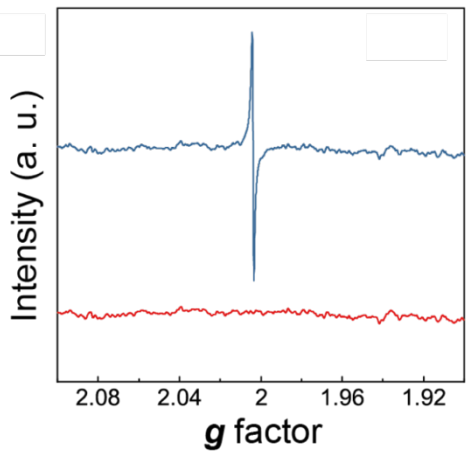

Figure 6.5 EPR spectra of the as-prepared facet-engineered TiO_2 (red) and N-TiO_2 (blue).

EPR spectroscopy was engaged to investigate the unpaired electron species in the TiO_2-based materials. As demonstrated before, the surface V_Os can trap the unpaired electrons from the semi-conductive oxide, and then form the radicals with the O_2 from air, which is detectable by EPR. As shown in Figure 6.5, an obvious EPR signal is recorded at g=2.003 for the N-TiO_2, while the pristine TiO_2 is silent on EPR measurement.

6.3.1.5 UV-Vis DRS of facet-engineered TiO_2 based materials

UV-Vis DRS was used to investigate the absorption properties of the materials,

and the measured reflectance spectra were transformed to the corresponding absorption spectra by applying the Kubelka-Munk function. As shown in Figure 6.6, the pristine facet-engineered TiO_2 exhibits an absorption edge at about 390 nm, while after NH_3 treatment at 600 ^oC for N-doping, the N-TiO_2 shows a greatly enhanced absorption in both the visible light and near infrared regimes. Such observation is in accordance with what was demonstrated for the P25 TiO_2 materials in Chapter 3. This large enhancement in the absorption property also results in an obvious colour change from white to navy blue.

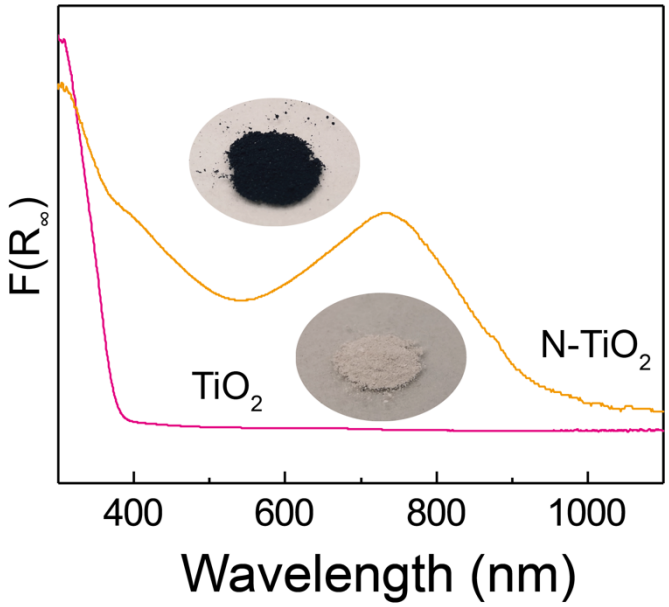

Figure 6.6 UV-Vis absorption spectra transformed from UV-Vis DRS by the Kubelka-Munk function.

6.3.1.6 Raman spectroscopy of the TiO_2-based materials

Raman spectroscopy was engaged to obtain more structural information of the TiO_2-based materials. As shown in Figure 6.7, four major peaks that represent the E_g, B_{1g}, A_{1g} and E_g Raman-active vibrational modes, are located at 142, 394, 516 and 636 cm^{-1}, respectively. These results indicate the predominant phase of anatase.[23,24] Obviously, the peaks of the N-doped sample exhibit a certain degree of weakening and broadening, implying the TiO_2 lattice is disrupted by the N-

doping and the formation of V_Os after the NH_3 treatment.[25,26] However, the diffraction peaks are still similar to that of pristine P25, which indicates that the major anatase structure has not been changed during NH_3 treatment, in consistence with XRD results.

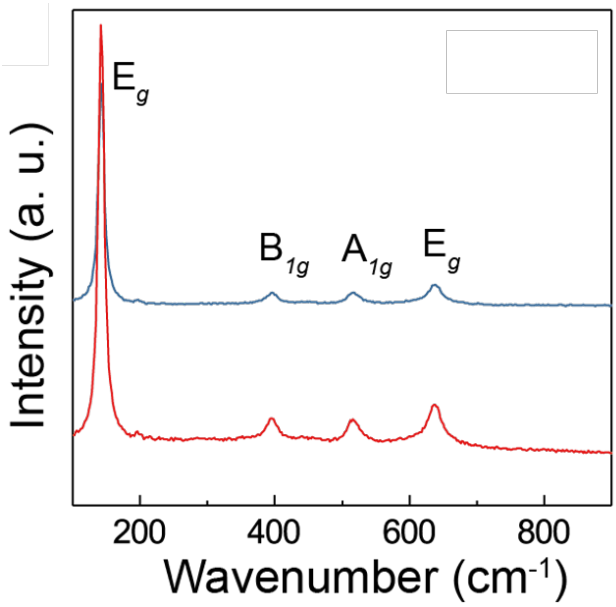

Figure 6.7 Raman spectra of the as-prepared facet-engineered TiO_2 (red) and N-TiO_2 (blue).

6.3.2 Effect of ionic species on the POWS system

6.3.2.1 Effect of electrolytes on POWS performance

As demonstrated before, the sluggish surface and sub-surface V_O regeneration process, which is widely considered as the rate determining step for the POWS reaction on TiO_2-based materials at ambient conditions, could be greatly accelerated at elevated temperatures.[2,27] Therefore, other effects such as polarisation effect can be better investigated at elevated temperatures.[2] Consequently, in this chapter, the POWS activity tests are carried out at 270 °C which has been shown to be the optimal temperature in such POWS system (Chapter 3).[2]

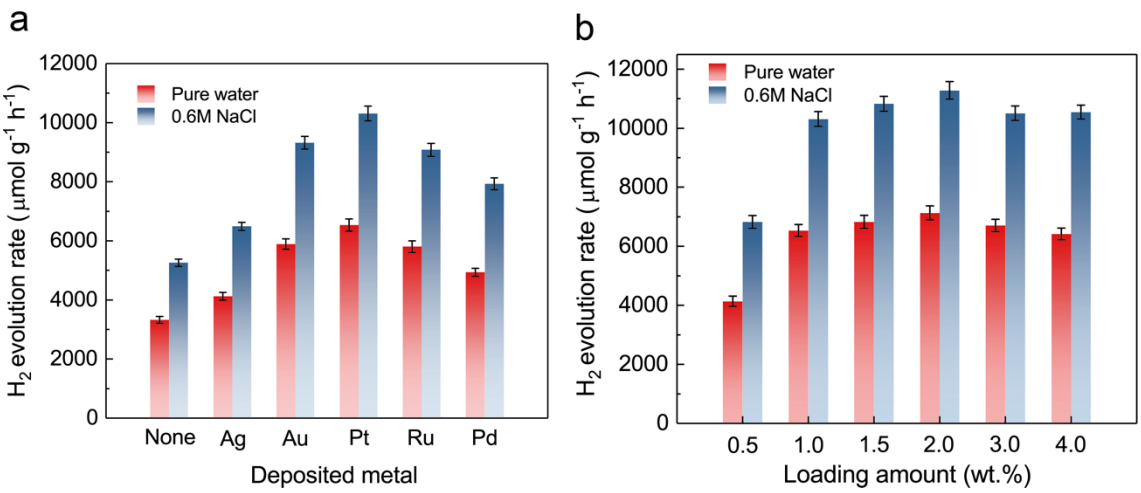

Figure 6.8 Optimisation of cocatalyst loading and loading amount. **(a)** POWS activity of the facet-controlled N-TiO_2 loaded with 1 wt.% of different metal nanoparticles (NPs) as the cocatalyst via a photo-deposition method. **(b)** POWS activity of the facet-controlled N-TiO_2 loaded with Pt NPs of different loading amounts. The POWS activity was evaluated in a batch reactor at 270 °C with simulated solar irradiation (AM 1.5G).

Typically, 1 wt.% of Pt nanoparticles (NPs) were deposited on the N-TiO_2 nanocrystals via a photo-deposition method before catalytic test as a H_2 evolution cocatalyst. Different metals have also been studied likewise, which shows that Pt exhibits the highest enhancement on the photocatalytic performance, followed by Au that has been widely studied for the surface plasmon resonance effect.[28,29] This follows a similar trend as what was discussed in more details in Chapter 5, where the promoting effect of the metal NPs was compared against the volcano curve for the electrocatalytic H_2 evolution reaction. The loading amount is then optimised as well, as shown in Figure 6.8. Clearly, the POWS activity levels off when the loading amount is increased beyond 1 wt.%; moreover, the activity shows a small drop when the loading amount exceeds 3 wt.%, which is presumably due to the shielding effect of the NPs, resulting in less photons reaching the N-TiO_2 photocatalyst particles.[30]

In order to understand the effects of ionic species in seawater on the photocatalytic

performance in this system, I first used the NaCl aqueous solutions with different concentrations instead of seawater to avoid the complexity. Bearing in mind that the salt concentration of seawater is a function of the location, which varies greatly among different areas of the world, I therefore investigated a wide range of NaCl concentrations up to 6.0 mol L^{-1} (Figure 6.9). The POWS performances increase proportionally with the concentration of the NaCl solution up to 3.0 mol L^{-1}, showing an enhancement from 6428 to 24750 μmol g^{-1} h^{-1}, while the enhancement becomes less significant when the concentration is higher than 3 mol L^{-1}.

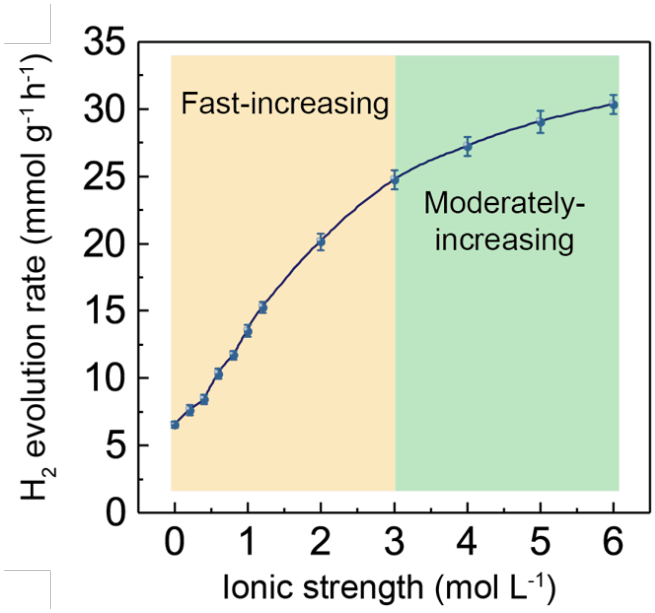

Figure 6.9 POWS performance measured in the NaCl aqueous solutions with different concentrations at 270 °C. Error bars indicate the standard deviations of GC analysis.

A common concern of the photocatalysis in seawater (or solutions containing Cl^- ions) is that the Cl^- oxidation may take place during the photocatalytic splitting of seawater, resulting in the production of corrosive Cl_2 or ClO^-. According to Equations 6.1 and 6.2, the Cl^- oxidation reaction will inevitably lead to a pH increase of the solution. Thus, pH was measured before and after the reaction, which showed no obvious change, indicating there was no Cl^- oxidation observed

in this system, probably due to the high oxidation potential of Cl^- ions (= +1.36 V vs. NHE compared with = +1.23 V vs. NHE at pH = 0).[15] Gas chromatograph (GC) analysis of the gaseous product also showed no signal of Cl_2 gas.

Subsequently, other neutral electrolytes were also studied likewise: the POWS activities were measured in different electrolyte solutions that share the same concentration of 0.2 mol L^{-1}, all of which showed enhanced POWS performance at 270 ^oC compared with that measured in pure water (Figure 6.10). But the enhancement varies among different electrolytes, presumably due to the different radii and charges of the ions, which will be discussed in detail later. An organic compound, sodium dodecyl sulphate, which is the main component of many hygiene products and may also exist in seawater due to water pollution, was also studied. Even though the H_2 evolution rate was enhanced by 55 %, no O_2 was detected in the gas phase after reaction. Instead, CO_2 and CO were observed by GC analysis, which suggested that the organic compound could act as a sacrificial reagent in this system, leading to the undesired carbon emission. Also noteworthy is that the acidic or alkaline compounds, such as HCl or Na_2CO_3, which largely change the pH of the solution, showed no enhancement to the POWS performance, but even decelerated the reaction. This is presumably because that the acidic/alkaline compounds substantially suppress the water dissociation, resulting in much lowered concentration of OH^-/H^+ ions, which is kinetically unfavourable for the corresponding O_2/H_2 evolution reactions.

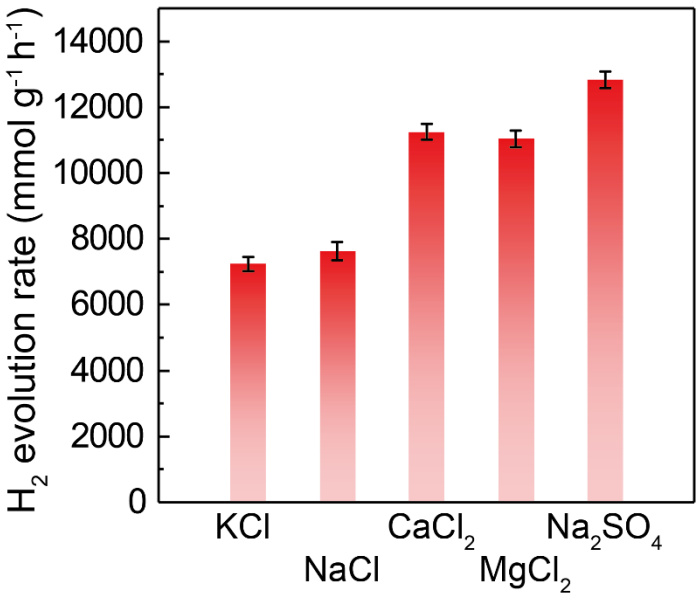

Figure 6.10 POWS activity of Pt/N-TiO_2 tested in different aqueous solutions (the concentration is kept at 0.2 mol L^{-1} for all measurements) at 270 °C. Error bars show the standard deviation. Typically, 1 wt.% of Pt NPs were loaded to the N-TiO_2 as the cocatalyst via a photo-deposition method before use.

6.3.2.2 TRPL of N-TiO_2 in the presence of electrolyte solution

TRPL spectroscopy was used to investigate the separation of the photo-generated charge carriers in the photocatalyst. The TRPL spectra of N-TiO_2 photocatalyst were obtained with the sample being soaked in different aqueous electrolyte solutions (Figure 6.11). Obviously, as the ionic strength of the NaCl solution increases, the decay of the TRPL spectrum becomes slower (Figure 6.11a), which is presumably due to the local electric field generated by the ionic species adsorbed on the surface of the photocatalyst particles. Moreover, when measured in different electrolyte solutions with the same ionic strength, the TRPL decay curves appear almost the same (Figure 6.11b). Then, the obtained spectra were fitted using a biexponential function and the fitting parameters are given in Table 6.1.

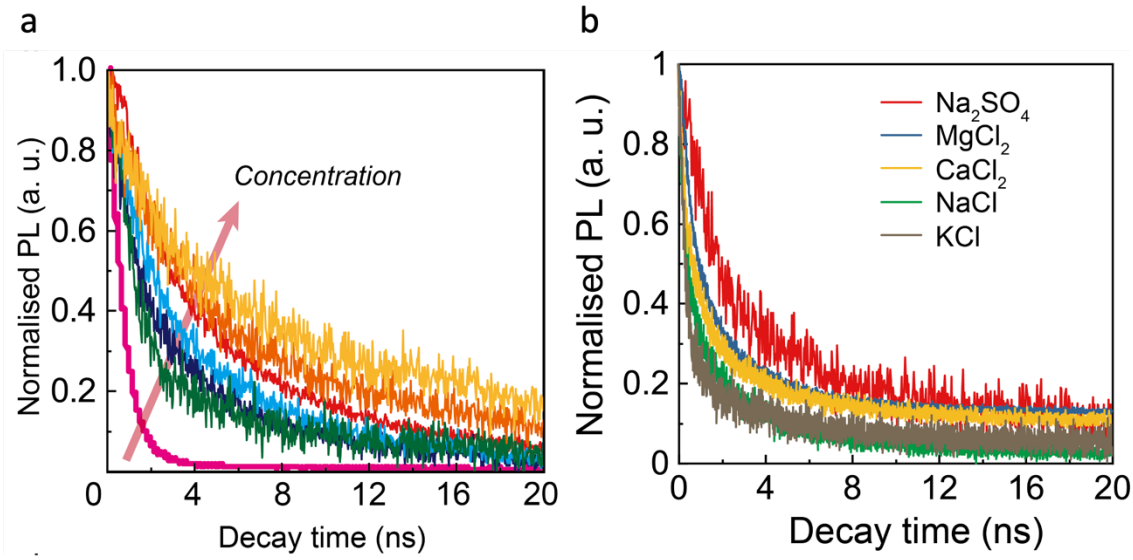

Figure 6.11 (a) TRPL spectra of N-TiO_2 nanocrystals measured in NaCl aqueous solutions. The concentration of the NaCl solution increases along the arrow and the values are 0, 1, 2, 3, 4, 5 and 6 mol L^{-1}, respectively. **(b)** TRPL spectra of N-TiO_2 nanocrystals measured in different electrolyte aqueous solutions, respectively. The concentration is 0.2 mol L^{-1} for all the three solutions.

Clearly, there are two decay components, of which the fast component can be attributed to the intrinsic recombination process of TiO_2 in the bulk region, which is hardly influenced by the ionic species in the solution. However, a slow component was also differentiated which showed a positive correlation with the ionic strength of the solution, therefore, it is attributed to the suppressed recombination due to the LEF introduced by the ionic species near the surface: the photo-generated charge carriers near the surface are obviously more prone to the LEF of the ionic species adsorbed on the catalyst surface, compared with those in the bulk. In addition, it should be clarified that this LEF only influences the dynamics of the charge carriers, without changing the PL spectra, which means the LEF could not change the energy levels or the band structure of the photocatalysts, at least this was not observed in this thesis. Consequently, the average lifetime of the photo-generated charge carriers was greatly prolonged in the aqueous solutions. Also, it is found that acidic and alkaline electrolytes, HCl

and Na_2CO_3, substantially prolong the charge carrier lifetime, however, they show negative effects on the POWS performance due to the unfavourable kinetics as demonstrated in the previous section.

Table 6.1 Fitting parameters of the TRPL spectra of the N-TiO_2 photocatalyst in different solutions.[a]

Solution	f_1 (%)	τ_1 (ns)	f_2 (%)	τ_2 (ns)	$\tau_{average}$
Pure water	26.4	0.75	73.6	2.34	1.92±0.02
1.0 M NaCl (aq.)	9.1	0.70	90.9	4.38	4.05±0.03
2.0 M NaCl (aq.)	6.0	0.76	94.0	6.13	5.81±0.03
3.0 M NaCl (aq.)	5.0	0.72	95.0	7.83	7.47±0.04
4.0 M NaCl (aq.)	5.5	0.69	94.5	8.73	8.29±0.05
5.0 M NaCl (aq.)	4.5	0.73	95.5	9.53	9.13±0.06
6.0 M NaCl (aq.)	4.1	0.74	95.9	10.12	9.75±0.06
0.2 M KCl (aq.)	16.5	0.67	83.5	2.78	2.44±0.03
0.2 M NaCl (aq.)	18.1	0.69	81.9	2.91	2.51±0.03
0.2 M $CaCl_2$ (aq.)	11.0	0.71	89.0	3.61	3.29±0.03
0.2 M $MgCl_2$ (aq.)	13.6	0.70	86.4	3.52	3.14±0.04
0.2 M Na_2SO_4 (aq.)	11.9	0.71	88.1	3.98	3.59±0.04

[a] The charge carrier lifetime is obtained by fitting the TRPL spectra using a biexponential decay function. TRPL measurements are performed on the sample powders soaked in different solutions at room temperature. τ_1 and τ_2 are the lifetimes of the fast and the slow decay components; $\tau_{average}$ is the average lifetime of the charge carriers; f_1 and f_2 are the contribution of the fast and the slow decay components to the average lifetime of the charge carriers, respectively.

6.3.2.3 Effect of artificial and natural seawater

So far, it can be clearly seen that the POWS performance of the Pt/N-TiO_2 photocatalyst can be greatly enhanced in aqueous solutions of electrolytes, and the charge carrier lifetime can be substantially prolonged presumably due to the facilitated local electric field. I then looked into the more complicated cases: seawater. Although the global average salt concentration of seawater is 3.5 wt.%

(*ca.* 0.6 mol L^{-1}), extreme case like the Dead Sea has a high salt concentration of around 31.5 wt.%.[7,31] Obviously, collecting the natural seawater samples all over the world in person is unrealistic and unnecessary in this work. Therefore, seawater of different water areas of the world were selected and simulated in our lab, based on the analysis data reported in literature (Table 6.2).[32–35]

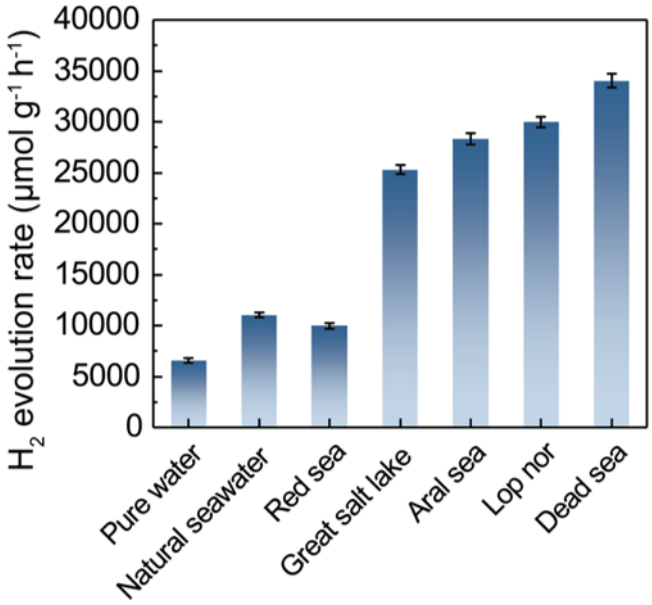

Figure 6.12 POWS activity of Pt/N-TiO_2 tested in different artificial seawater samples at 270 °C. Error bars show the standard deviation.

Table 6.2 Compositions of the simulated seawaters using the data from Ref. [32–35]

	NaCl	KCl	$CaCl_2$	$MgCl_2$	Na_2SO_4	Ionic strength (mol L^{-1})
Dead sea	3.5	0.3	0.2	0.7	/	6.50
Lop Nor	3.54	0.2	/	0.56	/	5.42
Aral Sea	1	0.06	/	0.5	0.7	4.66
Great Salt Lake	2.4	0.15	/	0.3	0.15	3.90
Red sea	0.62	/	/	0.03	/	0.71

Impressively, enhancement of the POWS performance was observed in the artificial seawaters to different extents (Figure 6.12). The pH of the solutions was

measured before and after the reactions as well, which showed no observable change, indicating the stoichiometric splitting of water and no other side reactions taking place. The Dead Sea water that has the highest salt content shows the best H_2 evolution rate of 34,035 μmol g^{-1} h^{-1}, followed by the Lop Nor which exhibits a rate of 29,968 μmol g^{-1} h^{-1}. The Red Sea, which has a salt concentration of the global average (3.5 wt.%, 0.6 mol L^{-1}), gives a lower H_2 evolution rate of 9,972 μmol g^{-1} h^{-1}. Natural seawater was also collected from Bournemouth, UK, and tested for POWS activity after filtration, which excitingly also showed an enhanced activity of 11,048 μmol g^{-1} h^{-1} compared with that in pure water (Figure 6.12). It should be noted that the activity obtained from natural seawater is very similar to that from the artificial Red Sea water, because they share a similar salt concentration of the global average (3.5 wt.%, 0.6 mol L^{-1}), confirming that the difference of the POWS activity is mainly originated from the different salt concentrations of the artificial seawaters.

6.3.2.4 TRPL study in the presence of artificial seawater

TRPL studies were carried out similarly, and the TRPL spectra obtained in different artificial seawaters are shown in Figure 6.13. Generally, the TRPL signal decays more slowly when the total ionic strength of the artificial seawater increases, which is in accordance with the previous observations for NaCl solutions. Then these spectra were also fitted using a biexponential decay function and the results are given in Table 6.3. Similarly, both the fast and slow decay components can be observed in each TRPL spectrum measured in the artificial seawater samples, and the results indicate that the average lifetime of the electron/hole pairs is greatly prolonged to different extents in the artificial seawaters. Not surprisingly, the longest average lifetime of 10.28 ns was observed for Pt/N-TiO_2 soaked in the

Dead Sea water that has the highest ionic strength (Figure 6.13 and Table 6.2).

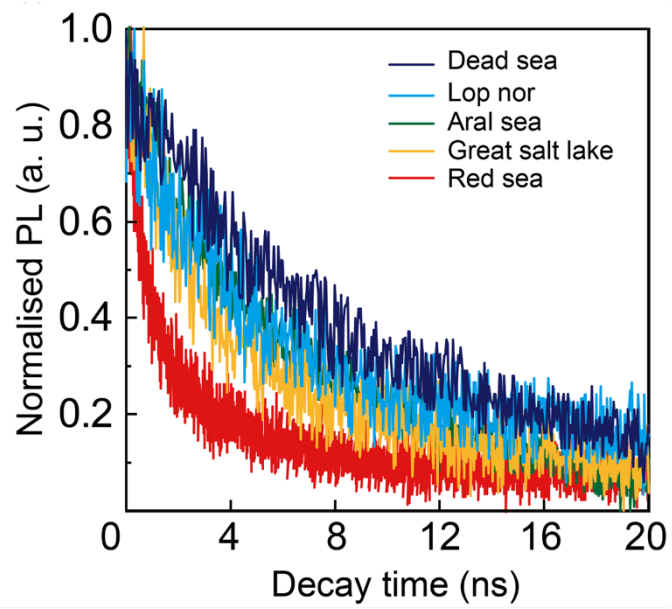

Figure 6.13 TRPL spectra of N-TiO_2 nanocrystals measured in different artificial seawaters. The composition of the artificial seawater samples is shown in Table 6.2.

Table 6.3 Fitting parameters of the TRPL spectra of the N-TiO_2 photocatalyst in different artificial seawaters.[a]

Solution	f_1 (%)	τ_1 (ns)	f_2 (%)	τ_2 (ns)	$\tau_{average}$
Dead sea	3.7	0.73	96.3	10.65	10.28±0.06
Lop Nor	4.8	0.73	95.2	9.71	9.28±0.06
Aral Sea	4.5	0.69	95.5	9.21	8.83±0.05
Great Salt Lake	5.2	0.70	94.8	8.32	7.92±0.04
Red sea	12.5	0.67	87.5	3.64	3.27±0.03

[a] The charge carrier lifetime is obtained by fitting the TRPL spectra using a biexponential decay function. TRPL measurements are performed on the sample powders soaked in different solutions at room temperature. τ_1 and τ_2 are the lifetimes of the fast and the slow decay components; $\tau_{average}$ is the average charge carrier lifetime; f_1 and f_2 are the contribution of the fast and the slow decay components to the average charge carrier lifetime, respectively.

6.3.3 Mechanism investigation of the ionic effect

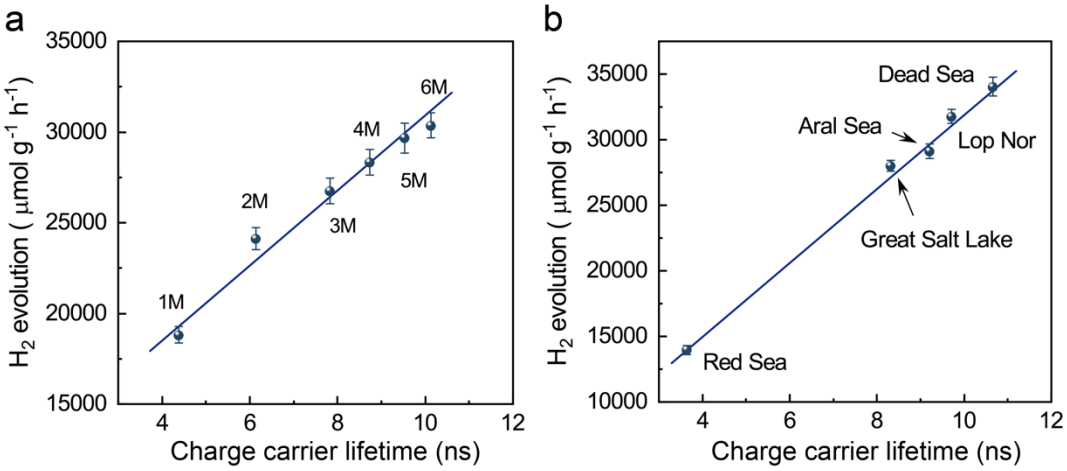

Figure 6.14 Linear relationships between the charge carrier lifetime and the POWS activity.

As can be seen from the section 6.3.2, obviously, the POWS activity shows a positive correlation with the ionic strength of the electrolyte solutions and artificial seawaters, and so does the lifetime of the photo-generated charge carriers. Therefore, the POWS activity (represented by the H_2 evolution rate) was then plotted against the charge carrier lifetime, as shown in Figure 6.14. Clearly, the POWS performance exhibits a linear relationship with the charge carrier lifetime, indicating that the ionic species in the aqueous solutions largely prolong the charge carrier lifetime in the Pt/N-TiO_2 photocatalyst and lead to the substantially enhanced photocatalytic performance. In another word, the ionic species influence the photocatalytic activity by facilitating the separation of the charge carriers and suppressing their recombination. Therefore, the charge carrier separation process has been studied more deeply to illustrate the mechanism of the ionic effect, as detailed in the following sub-sections.

6.3.3.1 Facet-selective photo-deposition

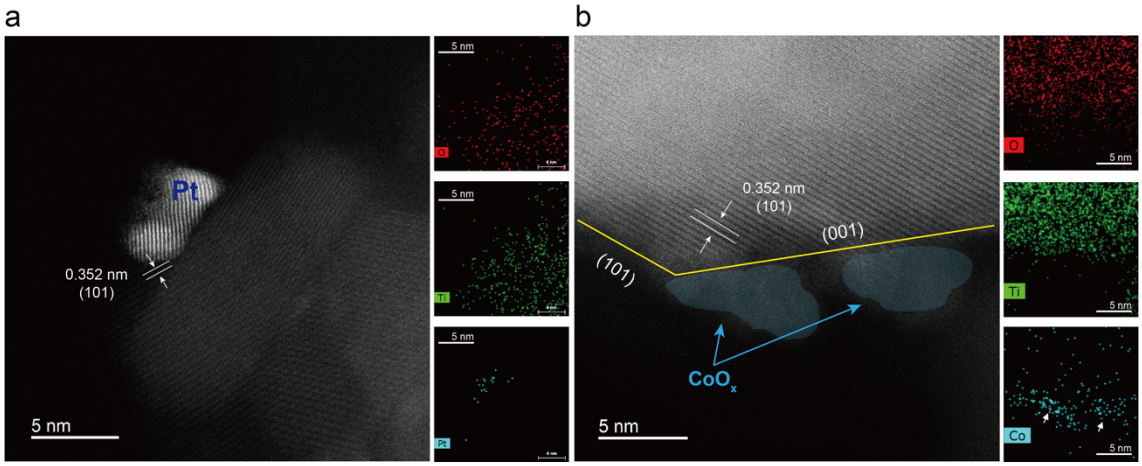

Figure 6.15 HAADF-STEM images and EDS mappings of the facet-controlled N-TiO_2 nanocrystals loaded with **(a)** Pt NPs and **(b)** CoO_x NPs via the facet-selective photo-deposition method, which clearly show that Pt NPs are favourably deposited on (101) facets and CoO_x are dominantly deposited on (001) facets.

The mechanism of the charge separation process was then investigated by HAADF-STEM. Different NPs were separately loaded onto the facet-controlled N-TiO_2 via a facet-selective photo-deposition method.[36,37] It has been demonstrated that upon light irradiation, the photo-excited electrons/holes migrate to the surfaces of semiconductor particles and then reduce/oxidise the chemical species in the solution, respectively, forming deposited NPs if the chemical potential is appropriate.[1] Therefore, these deposited NPs can be considered as indicators of the photo-generated electrons and holes on the surface of the catalyst particles. In this chapter, Pt NPs and CoO_x NPs were fabricated through the photo-reduction and photo-oxidation of the Pt(II) and Co(II) precursors, respectively. As previously mentioned in Chapter 3, Pt(II) can be readily reduced to Pt(0) by the photo-generated electrons in the conduction band during the photo-deposition process. On the contrary, Co(II) cannot be reduced in such conditions, because the electrons in the conduction band do not have a sufficiently negative potential, but it can be oxidised by the photo-generated holes in the valence band in the

presence of $NaIO_3$ as an electron-scavenger, forming Co(III) oxide (CoO_x) NPs. As shown in Figure 6.15, Pt NPs were deposited preferentially on the (101) facets, while the CoO_x NPs were favourably deposited on the (001) facets. These observed anisotropic photo-depositions of different NPs indicated a charge polarisation effect inside the photocatalyst particle, driven by an internal electric field originated from the work function difference between the facets.[1] The above evidences indicate that the photo-generated electrons favourably migrate to the (101) facets of the N-TiO_2 upon illumination, leaving the holes on the (001) facets. In a chemical sense, this could mean that the Ti-O bonds on the (001) surfaces are weaker than those on the (101) surfaces, thus, V_Os (holes) are readily generated on the (001) surfaces upon illumination, which then act as the active centres for O_2 evolution, while the electrons migrate to the (101) surfaces (accumulate at Ti or metal NPs) for H_2 evolution. According to the above observations, it can be expected that the cations (*e.g.*, Na^+) and the anions (*e.g.*, Cl^-) ions in the solution would preferentially be adsorbed on the respective facet, depending on the charge that the facet carries (similar to the behaviours observed for the Pt(II) and Co(II) precursors). This facet-selective adsorption, in turn, suppresses the charge carriers' recombination by introducing a local electric field on the surface.

6.3.3.2 *In situ* AP-XPS study of the facet-controlled N-TiO_2

AP-XPS was then engaged to investigate the surface electronic features of N-TiO_2 using TMP as a surface probe. As demonstrated in our previous studies, the nucleophilic TMP molecule can form stable adducts with the exposed Lewis acid (LA) sites (*e.g.*, five-coordinated Ti^{4+}) on the surface.[19,38] Such interaction between TMP and the surface LA sites is very sensitive to any change of the surface

chemical environment and the local electron density, which can be observed as the shift of binding energy (BE) on P 2p XPS spectra. Therefore, the surface charge separations among different facets are allowed to be differentiated and analysed. Facet-controlled N-TiO_2 photocatalyst was investigated by this probe-assisted AP-XPS technique and 0.2 mbar of TMP was directed into the experimental chamber during the measurements. XPS spectra were collected with and without light irradiation. Generally, when TMP is added to the sample, the Ti 2p signal shifts to a lower BE since TMP is a Lewis base that can make the surface Ti^{4+} more electron-rich by forming adducts; while the O 1s signal remains the same (Figure 6.16a. Upon irradiation, the signal of Ti 2p shifts to further lower BE and that of O 1s shifts to higher BE, mainly because the electrons are excited from the valence band (VB, consists of O 2p) to the conduction band (CB, consists of Ti 3d). Also, the shifts of the signals are recovered when light is off, showing that the BE shifts are due to the photo-excitation instead of any sample damage. It should be noted that the Ti 2p and O 1s spectra do not only show the surface electronic features in this case, since it is widely agreed that the XPS sampling depth is up to several nanometres into the bulk region. On the other hand, the surface features can be better investigated from the P 2p spectra since the TMP molecules can only adsorb on the surface of the photocatalyst particle. As shown in the P 2p spectra in Figure 6.16a, doublet signals can be identified in P 2p spectra, which are attributed to the P $2p_{3/2}$ and P $2p_{1/2}$ of the surface adsorbed TMP molecules, respectively, when illumination is absent. But upon illumination, two sets of doublet peaks can be observed by deconvolution of the spectrum. Clearly, one set of peaks shift to a higher BE, while the other to a lower BE (Table 6.4).

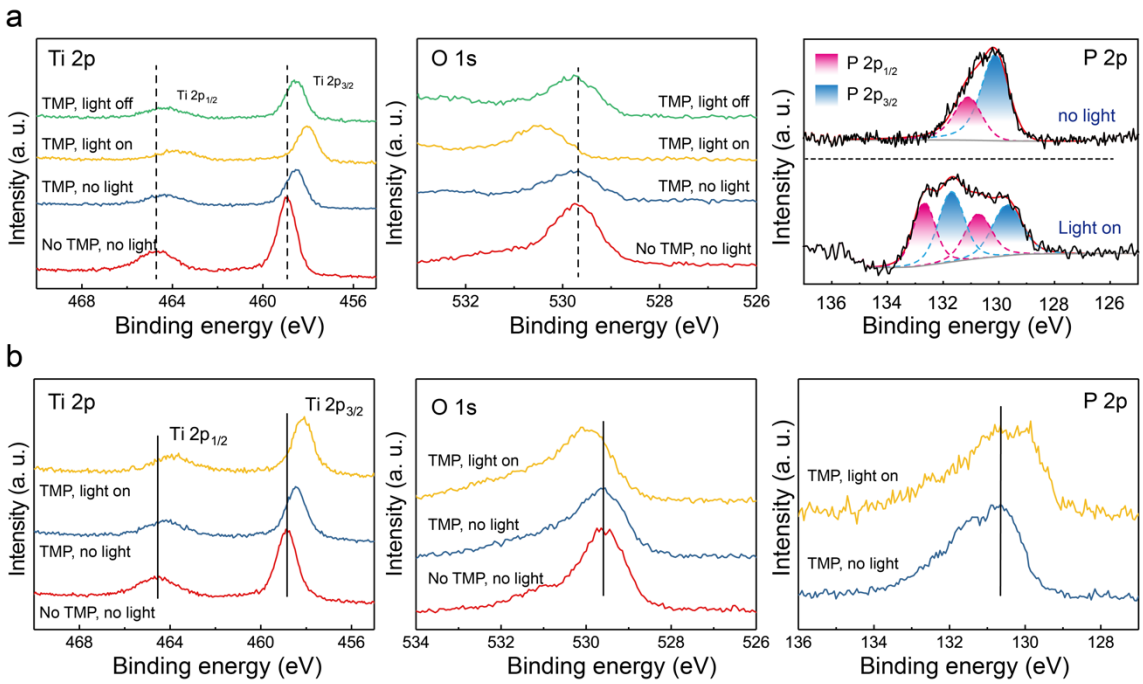

Figure 6.16 (a) High resolution Ti 2p, O 1s and P 2p AP-XPS spectra of the facet-engineered N-TiO_2 nanocrystals. (b) High resolution Ti 2p, O 1s and P 2p AP-XPS spectra of the N-TiO_2 powders without facet-engineering.

Such a peak splitting could not be observed on the Ti 2p or O 1s spectra, because, as mentioned before, XPS is not strictly a surface analysis technique, but has a sampling depth of a few nanometres. Therefore, some subtle surface information is averaged by the signals from the sub-surface region. On the contrary, TMP molecules can only adsorb on the outmost surface, which makes the P 2p spectra extremely sensitive to any change of the surface chemical environments. As indicated by the STEM studies, the (001) facets favourably host the photo-generated holes while the electrons favour the (101) facets, rendering them electropositive and electronegative, respectively. Obviously, this conclusion is reinforced by the AP-XPS results: (001) become electropositive upon illumination due to trapping the holes, thus the P 2p of TMP molecules adsorbed on the electron-deficient (001) facets shifts to a higher BE; on the contrary, those adsorbed on the electron-rich (101) facets shift to a lower BE. Quantitative analysis

suggests that the ratio of the peak areas is around 40:60, which is in accordance with the ratio of (101) and (001) facets, confirming the attribution of the signals. Control experiments have been performed on the N-TiO_2 powders that exhibit more than 95% exposure of the (101) facet: the AP-XPS results do not indicate any surface polarisation effect (Figure 6.16b).

Table 6.4 BE of the fitted components of the AP-XPS P 2p spectra in Figure 6.16.

	P $2p_{3/2}$		**P $2p_{1/2}$**	
Light off	130.28 eV		131.23 eV	
	P $2p_{3/2}$ up	**P $2p_{3/2}$ down**	**P $2p_{1/2}$ up**	**P $2p_{1/2}$ down**
Light on	131.78 eV	129.68 eV	132.68 eV	130.73 eV

6.3.3.3 DFT studies on the ionic effects

DFT calculations were then carried out to understand the effect of the ionic species in seawater. A N-doped TiO_2 supercell was constructed, then the (101) and (001) facets were studied separately (Figures 6.17a and 6.17b). According to the STEM and AP-XPS studies demonstrated above, the polarisation takes place among different surfaces of the particle upon photo-excitation, making the (001) surface electropositive and the (101) surface electronegative. Therefore, in the DFT studies, anions and cations are placed onto the (001) and (101) surfaces, respectively, in order to investigate their adsorption behaviours.

The adsorption energy (E_{ads}) can be calculated in each case (Table 6.5). Holes/electrons are then added to the surface models deliberately to simulate the charge polarisation upon excitation. Taking the Cl^- ion as an example, when the (001) surface is neutral (*i.e.*, before excitation), the E_{ads} is calculated to be -0.55 eV. When a hole is placed on this surface (*i.e.*, polarisation takes place between

different surface after excitation), the E_{ads} is substantially reduced to -0.82 eV. The reduction of the E_{ads} indicates the enhanced chemisorption of the ionic species on the surface due to the stronger charge interactions. Clearly, the above results indicate that the polarisation effect among surfaces enables stronger interaction between the ionic species and the surface. Obviously, the intensity of such surface polarisation effect can be indicated by the difference between the E_{ads} before and after excitation. Likewise, similar calculations have been attempted for other cations and anions, as shown in Table 6.5. It can be expected that this effect will vary among different ions, depending on the ionic radius and charge, since the nature of this effect is the electrostatic interaction between charge carriers.

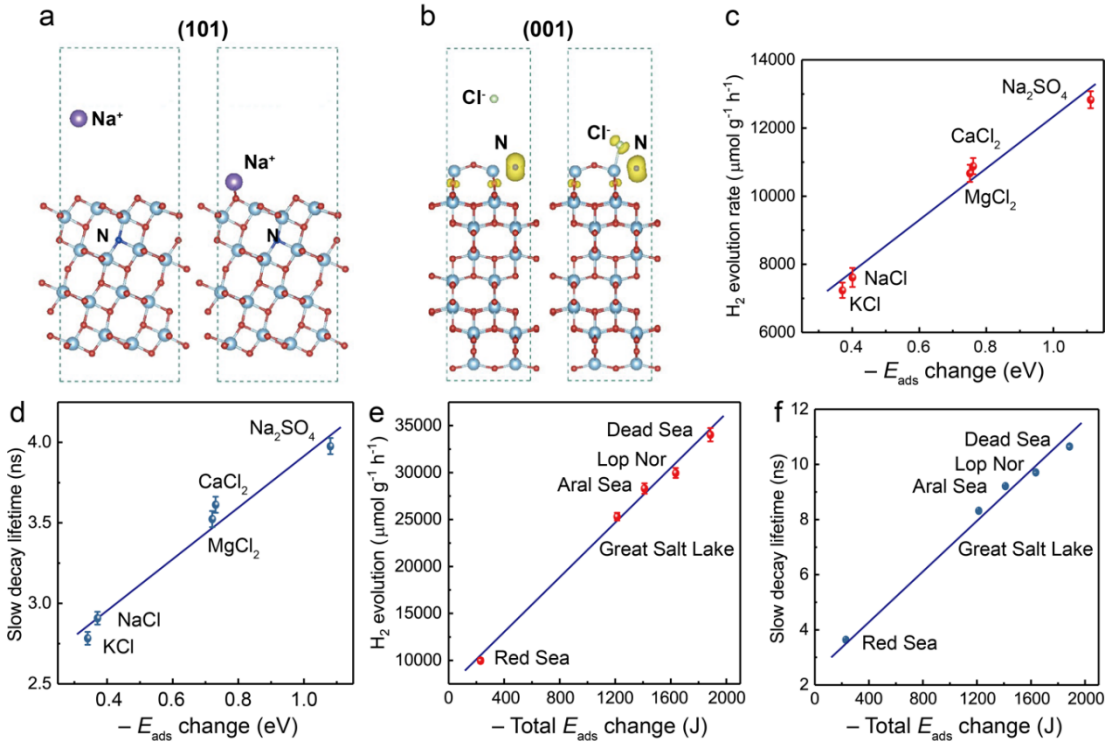

Figure 6.17 Correlations of the DFT computational results with the POWS performance and the charge carrier lifetime. **(a)** Na^+ ion adsorbed on (101) facet and **(b)** Cl^- adsorbed on (001) facet. respectively. Correlations between **(c)** POWS activity and **(d)** lifetime of the slow decay component with the E_{ads} change for different electrolyte. Correlations between **(e)** POWS activity and **(f)** lifetime of the slow decay component with the total E_{ads} change for different artificial seawater. Error bars indicate the standard deviations.

Table 6.5 The DFT calculation of the adsorption energy of different ions and electrolytes. †

	Chemical species	**E_{ads} (neutral surface) (eV)**	**E_{ads} (charged surface) (eV)**	**Energy difference (eV)**
Ions on (101) surface	K^+	0.05	0	-0.05
	Na^+	0.13	0.05	-0.08
	Mg^{2+}	1.05	0.89	-0.16
	Ca^{2+}	0.4	0.23	-0.17
Ions on (001) surface	Cl^-	-0.55	-0.82	-0.27
	SO_4^{2-}	-1.16	-2.06	-0.9
Electrolytes	KCl	-0.5	-0.82	-0.32
	NaCl	-0.42	-0.77	-0.35
	$CaCl_2$	-0.7	-1.41	-0.71
	$MgCl_2$	-0.05	-0.75	-0.7
	Na_2SO_4	-0.9	-1.96	-1.06

† The E_{ads} change is the difference between the E_{ads} of ion adsorbed on the neutral surface and the charged surface, which simulates the interaction between the adsorbed ion and the charge carrier that is trapped on the surface after photoexcitation. The positive E_{ads} values of the cations in this table (*e.g.*, especially 1.05 eV for Mg^{2+}) indicate that the adsorption of the cations on the TiO_2 surfaces is not favourable, but the adsorption can be facilitated to different extents after photo-excitation. For the electrolytes, the E_{ads} values could be derived from the E_{ads} of each individual ion using the corresponding chemical formula of the electrolyte compound. Likewise, the total E_{ads} change for different artificial seawaters can be calculated, taking the concentrations of different electrolytes into account.

Therefore, to obtain deeper understandings, the relationship between the POWS activity, lifetime of the charge carriers, and E_{ads} have been explored. It is noted that in the computational models, only one cation or anion is placed on the surface in each case, while in practical situations, we cannot solely study the cation or anion, since the whole system has to be charge-neutral. Therefore, given that different electrolytes are studied in this work (Figure 6.10), the E_{ads} of each electrolyte has

been calculated based on the respective chemical formula, and in such cases, the concentration can be considered the same for each electrolyte in the DFT calculations. Consequently, the POWS performance and the lifetime of the slow decay component are evaluated in different electrolyte solutions with the same concentration (0.2 mol L^{-1}) and the results are plotted against the E_{ads} (Figures 6.17c and 6.17d). Clearly, as the polarisation effect becoming stronger (more negative E_{ads} change), the charge carrier lifetime is greatly prolonged, resulting in enhanced POWS activity, and linear correlations can be observed. Further investigations are attempted for the artificial seawaters. As demonstrated before, artificial seawaters are made by mixing different electrolytes according to the data in literature. So, the total E_{ads} change can be calculated by considering the concentration of each electrolyte in the seawater sample (Table 6.5). Excitingly, both the POWS activity and the charge carrier lifetime, again, show linear correlations with the total E_{ads} change in the artificial seawaters (Figures 6.17e and 6.17f). Obviously, the strong interaction between the ionic species and the polarised surfaces plays an important role in this photocatalytic system, which can facilitate the surface trapping of the photo-generated charge carriers, resulting in a prolonged lifetime of the photo-generated electron/hole pairs, which is also supported by the TRPL results. In our POWS system at elevated temperatures, the separation and surface trapping of the photo-generated charge carriers is the key step: as shown in Figure 6.14, the POWS activity is positively correlated with the charge carrier lifetime. The prolonged lifetime will allow higher chance for the charge carriers to encounter the H^+ and OH^- ions in the solution to facilitate the H_2 and O_2 evolution reactions, hence giving higher POWS activity.

Clearly, the above HAADF-STEM, AP-XPS and DFT results together confirm that

the surface polarisation takes place upon photoexcitation, due to the electric field introduced by the different surface energies of (001) and (101) facets: photo-generated electrons are favourably migrating to the (101) surfaces which possess lower surface energy, leaving the photo-generated holes on the (001) surfaces, which facilitates the adsorption of cations and anions on the respective facet. Such facilitated surface adsorption of the ionic species, in turn, attracts the electrons and holes by Coulomb force, suppressing the charge recombination and prolonging the charge carrier lifetime. In our seawater splitting system, the photocatalyst particles are surrounded by plenty of ionic species and the surface adsorption can readily take place, thus, the separation of photo-generated charge carriers is greatly promoted, resulting in enhanced POWS performance. Besides, the N-doping also makes it easier to regenerate the surface V_Os by the sub-surface O atoms at elevated temperatures, due to enhanced oxygen mobility,[27] which also facilitates the surface charge polarisation.

6.3.4 Evaluation of QE and STH efficiency

QE of Pt/N-TiO_2 in different environments was then evaluated, which clearly shows the remarkable enhancements due to the polarisation effect (Figure 6.18a). High QE of 97.3 % and 85.8 % are obtained at 385 and 440 nm, respectively, in the artificial Dead Sea water. While in pure water, the QE drops sharply at longer wavelengths, giving a QE less than 10 % at long wavelengths (650 to 850 nm), which is in accordance with previous reports.[2,39,40]

Such a decrease in QE, especially the sudden drop at 650 nm, can be attributed to the wavelength-dependent electron-hole pair generation: as recently reported, the absorbed photons with longer wavelengths may not efficiently generate excited electron-hole pairs, but excite the local transitions instead, which finally dissipates

as heat and does not contribute to photocatalytic reactions.[41,42] Besides, it has been demonstrated that high excess excitation energy (*i.e.*, short-wavelength excitation) leads to better charge separation and stronger electron-phonon coupling, which means that these charge carriers are more likely to migrate to the surface trapping sites instead of taking the radiative recombination pathway.[43–45] On the contrary, long wavelength excitation results in enhanced local polaron formation, which decreases the mobility of the photo-generated charge carriers and increases their recombination, resulting in less carriers reaching the catalyst surface to participate in chemical reactions.[46,47]

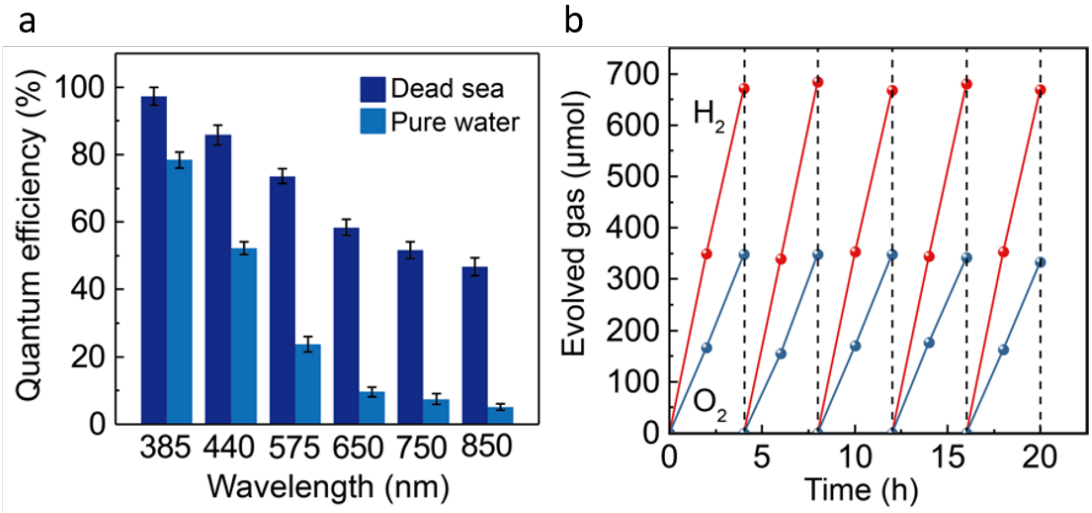

Figure 6.18 a QE evaluations of 1 wt.% Pt/N-TiO_2 in pure water and artificial Dead Sea water by using incident wavelengths of 385, 437, 575, 620, 750 and 850 nm, respectively, at 270 °C. QE measurements were carried out with a similar procedure as that stated before. Error bars indicate the standard deviation. **b** 5-cycle stability test of 1 wt.% Pt/N-TiO_2 in artificial Dead Sea water. This figure shows the total amount of the evolved H_2 and O_2 after different reaction time. 5 mg of the catalyst was used and the reaction was carried out at 270 °C under the simulated solar irradiation.

When the artificial seawater is used, it is noted that the QE at short wavelengths is hardly influenced by the surrounding environment since the charge carriers have high excess energy; while the polarisation effect is more pronounced for the carriers with lower excess excitation energy, because the moving directions of the

charge carriers are easier to be changed by the LEF when the charge carriers have a low kinetic energy/velocity, resulting in a substantial QE enhancement in the longer-wavelength regime (575 to 850 nm), and consequently, a high QE of *ca.* 50 % is recorded at 850 nm (Figure 6.18a).

Table 6.6 Device-to-device comparison of the overall water splitting performance in this work with the related systems reported in literature.

System type	**Catalyst**	**H_2 evolution (mL h^{-1}) / cell voltage ‡**	**STH (%) †**	**Ref.**
Particulate POWS	**Pt/N-TiO_2**	**4.1 (1 Sun)** **9.7 (Concentrated)**	**20.3**	**This work**
Electrolyser	Porous MoO_2(+)//Porous MoO_2(-)	4.5 / 1.53V	14.5	49
Electrolyser	IrO_2-Al_2O_3(+)//Pt/C(-)	7.5 / 3V	7.4	50
Electrolyser	NiFe LDH-NS@DG(+)//NiFe LDH-NS@DG(-)	8.7 / 1.5V	14.3	51
Electrolyser	NiFe LDH(+)//NiO/Ni-CNT(-)	8.9 / 1.5V	14.8	52
Electrolyser	NiFeOOH(+)//$MoNi_4$(-)	61.9 / 1.464V	15.1	53
PV-E	$CH_3NH_3PbI_3$-NiFe LDH	4.5	12.3	54
PV-E	Si PV-Fe:$Co_2Mo_3O_8$	86	15.1	55
PV-E	InGaP/GaAs/GaInNAsSb-PEM electrolyser	13.5	30	56
PEC	GaInP-GaInAs	7.5	14	57
PEC	InGaP/GaAs	2.2	9	58
PEC	Ba-Ta_3N_5	0.75	1.5	59

‡ The H_2 evolution rate of various lab-scale devices is compared in in mL h^{-1} at the reported optimal operating conditions. The electrolysers presented in this table are all single-cell devices.

† STH efficiency was evaluated under AM 1.5G simulated solar irradiation. For the electrolyser systems, the electrical-to-chemical energy conversion efficiency was calculated from the cited papers, and then the STH efficiency was calculated assuming the electrolyser was integrated with a silicon-based PV device with a solar-to-electrical energy efficiency of 18 %. For PV-E and PEC systems, the STH efficiency was obtained from the respective paper directly, without any assumption or further mathematic treatments.

The STH conversion efficiency of this seawater splitting system is also carefully investigated. A STH conversion efficiency of 20.3±0.5% is achieved from this particulate POWS system in the artificial Dead Sea water at 270 ^{o}C, which even exceeds those reported for many PEC and PV-E systems (Table 6.6). Notably, the Pt/N-TiO_2 photocatalyst shows a stable and stoichiometric evolution of H_2 and O_2 without any obvious activity drop over 5 cycles (Figure 6.18b). Besides, it has been reported that a proper solar furnace which concentrates natural solar light can reach a high temperature of even 1000 ^{o}C.[48] Thus, a lab-scale light concentrated furnace was used to mimic such solar furnace, which shows that the stable and efficient POWS activity at 270 ^{o}C can be maintained solely by the concentrated light without any other electrical heating. An even more exceptional photocatalytic activity of 40,237 μmol g^{-1} h^{-1} (equivalent to a H_2 evolution rate of *ca.* 10 mL h^{-1} at standard temperature and pressure) is observed over 20 hours, due to the high intensity of the concentrated light. This H_2 evolution rate is comparable in the order of magnitude with those reported for alkaline electrolysers (Table 6.6), but this particulate POWS system is a direct single-step light harnessing process with all thermal and photon energy inputs from the solar concentrator.

6.4 Conclusion

In conclusion, we have systematically studied the effects of ionic species on the POWS performances over a Pt-supported facet-controlled N-doped TiO_2 photocatalyst. It was found that the activities increased with the ionic strength of the aqueous solutions. With the help of TRPL technique, such enhancement of photocatalytic activities was correlated with the charge carrier lifetime of the photocatalyst under different conditions, which were greatly prolonged by the ionic species. Acidic and alkaline electrolytes were also briefly studied, showing

negative effects on this system, while the organic ionic species acted as sacrificial reagent and led to unwanted CO and CO_2 production. A high H_2 evolution rate of 34,035±711 μmol g^{-1} h^{-1} was observed in an artificial Dead Sea water, with a QE of 85.8±2.6 % at 440 nm. Excitingly, a STH conversion efficiency of 20.3±0.5 % is obtained, which even outperformed the PV-E and PEC systems. The mechanism was deeply investigated by STEM and AP-XPS and it was demonstrated that the selective adsorption of the ionic species on different facets could facilitate the local polarisation of the photo-generated electrons and holes, thus resulting in the prolonged lifetime of charge carriers and enhanced POWS performance. We have also showed such system has good potential for other semiconductor photocatalysts, such as perovskite oxynitride. The obtained steady H_2 evolution of 10 mL h^{-1} in the lab-scale solar furnace is comparable with the evolution rate of electrolysers. A recent life cycle assessment indicates some environmental concerns about the water electrolysis for large-scale H_2 production.[60] This direct single-step light harnessing POWS system may provide an alternative option. It is also believed this study can provide a novel but pragmatic strategy for harvesting solar energy by splitting more abundant water resource in seas and oceans.

6.5 References

1. Takata, T., Jiang, J., Sakata, Y., Nakabayashi, M., Shibata, N., Nandal, V., Seki, K., Hisatomi, T. & Domen, K. Photocatalytic water splitting with a quantum efficiency of almost unity. *Nature* **581**, 411–414 (2020).
2. Li, Y., Peng, Y.-K., Hu, L., Zheng, J., Prabhakaran, D., Wu, S., Puchtler, T. J., Li, M., Wong, K.-Y., Taylor, R. A. & Tsang, S. C. E. Photocatalytic water splitting by N-TiO2 on MgO (111) with exceptional quantum efficiencies at elevated temperatures. *Nat. Commun.* **10**, 4421 (2019).
3. Li, Y. & Tsang, S. C. E. Recent Progress and Strategies for Enhancing Photocatalytic Water Splitting. *Mater. Today Sustain.* **9**, 100032 (2020).
4. Chen, F., Huang, H., Guo, L., Zhang, Y. & Ma, T. The Role of Polarization in Photocatalysis. *Angew. Chem. Int. Ed.* **58**, 10061–10073 (2019).
5. Wolff, C. M., Frischmann, P. D., Schulze, M., Bohn, B. J., Wein, R., Livadas, P., Carlson, M. T., Jäckel, F., Feldmann, J., Würthner, F. & Stolarczyk, J. K. All-in-one

visible-light-driven water splitting by combining nanoparticulate and molecular co-catalysts on CdS nanorods. *Nat. Energy* **3**, 862–869 (2018).

6. Jin, H., Wang, X., Tang, C., Vasileff, A., Li, L., Slattery, A. & Qiao, S. Z. Stable and Highly Efficient Hydrogen Evolution from Seawater Enabled by an Unsaturated Nickel Surface Nitride. *Adv. Mater.* **33**, 2007508 (2021).

7. Liu, J., Xu, S. M., Li, Y., Zhang, R. & Shao, M. Facet engineering of WO3 arrays toward highly efficient and stable photoelectrochemical hydrogen generation from natural seawater. *Appl. Catal. B Environ.* **264**, 118540 (2020).

8. Tian, B., Tian, B., Smith, B., Scott, M. C., Hua, R., Lei, Q. & Tian, Y. Supported black phosphorus nanosheets as hydrogen-evolving photocatalyst achieving 5.4% energy conversion efficiency at 353 K. *Nat. Commun.* **9**, 1397 (2018).

9. Wu, Q., Cao, J., Wang, X., Liu, Y., Zhao, Y., Wang, H., Liu, Y., Huang, H., Liao, F., Shao, M. & Kang, Z. A metal-free photocatalyst for highly efficient hydrogen peroxide photoproduction in real seawater. *Nat. Commun.* **12**, 483 (2021).

10. Lu, X., Pan, J., Lovell, E., Tan, T. H., Ng, Y. H. & Amal, R. A sea-change: Manganese doped nickel/nickel oxide electrocatalysts for hydrogen generation from seawater. *Energy Environ. Sci.* **11**, 1898–1910 (2018).

11. Mase, K., Yoneda, M., Yamada, Y. & Fukuzumi, S. Seawater usable for production and consumption of hydrogen peroxide as a solar fuel. *Nat. Commun.* **7**, 11470 (2016).

12. Culp, T. E., Khara, B., Brickey, K. P., Geitner, M., Zimudzi, T. J., Wilbur, J. D., Jons, S. D., Roy, A., Paul, M., Ganapathysubramanian, B., Zydney, A. L., Kumar, M. & Gomez, E. D. Nanoscale control of internal inhomogeneity enhances water transport in desalination membranes. *Science* **371**, 72–75 (2021).

13. Di Vincenzo, M., Tiraferri, A., Musteata, V. E., Chisca, S., Sougrat, R., Huang, L. B., Nunes, S. P. & Barboiu, M. Biomimetic artificial water channel membranes for enhanced desalination. *Nat. Nanotechnol.* **16**, 190–196 (2021).

14. Yao, Y., Zhang, P., Jiang, C., DuChanois, R. M., Zhang, X. & Elimelech, M. High performance polyester reverse osmosis desalination membrane with chlorine resistance. *Nat. Sustain.* **4**, 138–146 (2021).

15. Guan, X., Chowdhury, F. A., Pant, N., Guo, L., Vayssieres, L. & Mi, Z. Efficient Unassisted Overall Photocatalytic Seawater Splitting on GaN-Based Nanowire Arrays. *J. Phys. Chem. C* **122**, 13797–13802 (2018).

16. Hausmann, J. N., Schlögl, R., Menezes, P. W. & Driess, M. Is direct seawater splitting economically meaningful? *Energy Environ. Sci.* **14**, 3679–3685 (2021).

17. Kibria, M., Khan, M. A., Al-Attas, T. A., Roy, S., Rahman, M. M., Ghaffour, N., Thangadurai, V., Larter, S., Hu, J. & Ajayan, P. Seawater Electrolysis for Hydrogen Production: A Solution Looking for a Problem? *Energy Environ. Sci.* **14**, 4831–4839 (2021).

18. Ma, Y. Y., Wu, C. X., Feng, X. J., Tan, H. Q., Yan, L. K., Liu, Y., Kang, Z. H., Wang, E. B. & Li, Y. G. Highly efficient hydrogen evolution from seawater by a low-cost and stable CoMoP@C electrocatalyst superior to Pt/C. *Energy Environ. Sci.* **10**, 788–798 (2017).

19. Peng, Y.-K., Hu, Y., Chou, H. L., Fu, Y., Teixeira, I. F., Zhang, L., He, H. & Tsang, S. C. E. Mapping surface-modified titania nanoparticles with implications for activity and facet control. *Nat. Commun.* **8**, 675 (2017).

20. Hu, Y., Guo, B., Fu, Y., Ren, Y., Tang, G., Chen, X., Yue, B. & He, H. Facet-dependent acidic and catalytic properties of sulfated titania solid superacids. *Chem.*

Commun. **51**, 14219–14222 (2015).

21. Di Valentin, C., Pacchioni, G., Selloni, A., Livraghi, S. & Giamello, E. Characterization of paramagnetic species in N-doped TiO 2 powders by EPR spectroscopy and DFT calculations. *J. Phys. Chem. B* **109**, 11414–11419 (2005).
22. Livraghi, S., Paganini, M. C., Giamello, E., Selloni, A., Di Valentin, C. & Pacchioni, G. Origin of photoactivity of nitrogen-doped titanium dioxide under visible light. *J. Am. Chem. Soc.* **128**, 15666–15671 (2006).
23. Savio, A. K. P. D., Fletcher, J., Smith, K., Iyer, R., Bao, J. M. & Robles Hernández, F. C. Environmentally effective photocatalyst CoO-TiO2 synthesized by thermal precipitation of Co in amorphous TiO2. *Appl. Catal. B Environ.* **182**, 449–455 (2016).
24. Ren, Z., Chen, C., Fu, X., Wang, J., Fan, C., Qian, G. & Wang, Z. TiO2/C composites nanorods synthesized by internal-reflux method for lithium-ion battery anode materials. *Mater. Lett.* **117**, 124–127 (2014).
25. Liu, X., Xing, Z., Zhang, Y., Li, Z., Wu, X., Tan, S., Yu, X., Zhu, Q. & Zhou, W. Fabrication of 3D flower-like black N-TiO2-x@MoS2 for unprecedented-high visible-light-driven photocatalytic performance. *Appl. Catal. B Environ.* **201**, 119–127 (2017).
26. Zhang, K., Zhou, W., Zhang, X., Sun, B., Wang, L., Pan, K., Jiang, B., Tian, G. & Fu, H. Self-floating amphiphilic black TiO2 foams with 3D macro-mesoporous architectures as efficient solar-driven photocatalysts. *Appl. Catal. B Environ.* **206**, 336–343 (2017).
27. Foo, C., Li, Y., Lebedev, K., Chen, T. T., Day, S., Tang, C. & Tsang, S. C. E. Characterisation of oxygen defects and nitrogen impurities in TiO2 photocatalysts using variable-temperature X-ray powder diffraction. *Nat. Commun.* **12**, 661 (2021).
28. Ingram, D. B. & Linic, S. Water splitting on composite plasmonic-metal/semiconductor photoelectrodes: Evidence for selective plasmon-induced formation of charge carriers near the semiconductor surface. *J. Am. Chem. Soc.* **133**, 5202–5205 (2011).
29. Furube, A., Du, L., Hara, K., Katoh, R. & Tachiya, M. Ultrafast plasmon-induced electron transfer from gold nanodots into TiO2 nanoparticles. *J. Am. Chem. Soc.* **129**, 14852–14853 (2007).
30. Zhu, S. & Wang, D. Photocatalysis: Basic principles, diverse forms of implementations and emerging scientific opportunities. *Adv. Energy Mater.* **7**, 1700841 (2017).
31. Neev, D. & Emery, K. O. The Dead Sea: Depositional Processes and Environments of Evaporites. *Isr. Geol. Surv. Bull.* **41**, 147 (1967).
32. Gertman, I., Kress, N., Katsenelson, B. & Zavialov, P. Equations of state for the Dead Sea and Aral Sea : Searching for common approaches. *IOLR Rep.* 7–12 (2010).
33. Nissenbaum, A. The microbiology and biogeochemistry of the Dead Sea. *Microb. Ecol.* **2**, 139–161 (1975).
34. Whelan, J. A. Great Salt Lake, Utah: Chemical and Physical Variations of the Brine. *Water-Resources Bull.* **17**, 11–15 (1973).
35. Sun, M. G. & Ma, L. C. Potassium-rich brine deposit in Lop Nor basin, Xinjiang, China. *Sci. Rep.* **8**, 1–9 (2018).
36. Meng, A., Zhang, J., Xu, D., Cheng, B. & Yu, J. Enhanced photocatalytic H2-production activity of anatase TiO2 nanosheet by selectively depositing dual-

cocatalysts on (101) and (001) facets. *Appl. Catal. B Environ.* **198**, 286–294 (2016).

37. Zhang, H., Wang, W., Zhao, H., Zhao, L., Gan, L. Y. & Guo, L. H. Facet-Dependent Interfacial Charge Transfer in Fe(III)-Grafted TiO2 Nanostructures Activated by Visible Light. *ACS Catal.* **8**, 9399–9407 (2018).

38. Peng, Y.-K., Keeling, B., Li, Y., Zheng, J., Chen, T., Chou, H. L., Puchtler, T. J., Taylor, R. A. & Tsang, S. C. E. Unravelling the key role of surface features behind facet-dependent photocatalysis of anatase TiO2. *Chem. Commun.* **55**, 4415–4418 (2019).

39. Li, Y., Wu, S., Zheng, J., Peng, Y.-K., Prabhakaran, D., Taylor, R. A., Chi, S. & Tsang, S. C. E. 2D photocatalysts with tuneable supports for enhanced photocatalytic water splitting. *Mater. Today* **41**, 34–43 (2020).

40. Li, Y., Wang, Z., Wang, Y., Kovács, A., Foo, C., Dunin-Borkowski, R. E., Lu, Y., Taylor, R. A., Wu, C. & Tsang, S. C. E. Local magnetic spin mismatch promoting photocatalytic overall water splitting with exceptional solar-to-hydrogen efficiency. *Energy Environ. Sci.* **15**, 265–277 (2022).

41. Piekner, Y., Ellis, D. S., Grave, D. A., Tsyganok, A. & Rothschild, A. Wasted photons: photogeneration yield and charge carrier collection efficiency of hematite photoanodes for photoelectrochemical water splitting. *Energy Environ. Sci.* **14**, 4584–4598 (2021).

42. Grave, D. A., Ellis, D. S., Piekner, Y., Kölbach, M., Dotan, H., Kay, A., Schnell, P., van de Krol, R., Abdi, F. F., Friedrich, D. & Rothschild, A. Extraction of mobile charge carrier photogeneration yield spectrum of ultrathin-film metal oxide photoanodes for solar water splitting. *Nat. Mater.* **20**, 833–840 (2021).

43. Ellingson, R. J., Blackburn, J. L., Yu, P., Rumbles, G., Mićić, O. I. & Nozik, A. J. Excitation energy dependent efficiency of charge carrier relaxation and photoluminescence in colloidal InP quantum dots. *J. Phys. Chem. B* **106**, 7758–7765 (2002).

44. Ye, Z., Lin, X., Wang, N., Zhou, J., Zhu, M., Qin, H. & Peng, X. Phonon-assisted up-conversion photoluminescence of quantum dots. *Nat. Commun.* **12**, 4283 (2021).

45. Tautz, R., Da Como, E., Wiebeler, C., Soavi, G., Dumsch, I., Fröhlich, N., Grancini, G., Allard, S., Scherf, U., Cerullo, G., Schumacher, S. & Feldmann, J. Charge photogeneration in donor-acceptor conjugated materials: Influence of excess excitation energy and Chain length. *J. Am. Chem. Soc.* **135**, 4282–4290 (2013).

46. Carneiro, L. M., Cushing, S. K., Liu, C., Su, Y., Yang, P., Alivisatos, A. P. & Leone, S. R. Excitation-wavelength-dependent small polaron trapping of photoexcited carriers in α-Fe2O3. *Nat. Mater.* **16**, 819–825 (2017).

47. Lane, P. A., Cunningham, P. D., Melinger, J. S., Esenturk, O. & Heilweil, E. J. Hot photocarrier dynamics in organic solar cells. *Nat. Commun.* **6**, 7558 (2015).

48. Garcia, D., Liang, D., Tibúrcio, B. D., Almeida, J. & Vistas, C. R. A three-dimensional ring-array concentrator solar furnace. *Sol. Energy* **193**, 915–928 (2019).

49. Jin, Y., Wang, H., Li, J., Yue, X., Han, Y., Shen, P. K. & Cui, Y. Porous MoO2 Nanosheets as Non-noble Bifunctional Electrocatalysts for Overall Water Splitting. *Adv. Mater.* **28**, 3785–3790 (2016).

50. Hamidah, N. L., Shintani, M., Ahmad Fauzi, A. S., Putri, G. K., Kitamura, S., Hatakeyama, K., Sasaki, M., Quitain, A. T. & Kida, T. Graphene Oxide Membranes with Cerium-Enhanced Proton Conductivity for Water Vapor Electrolysis. *ACS Appl.*

Nano Mater. **3**, 4292–4304 (2020).

51. Jia, Y., Zhang, L., Gao, G., Chen, H., Wang, B., Zhou, J., Soo, M. T., Hong, M., Yan, X., Qian, G., Zou, J., Du, A. & Yao, X. A Heterostructure Coupling of Exfoliated Ni–Fe Hydroxide Nanosheet and Defective Graphene as a Bifunctional Electrocatalyst for Overall Water Splitting. *Adv. Mater.* **29**, 1700017 (2017).

52. Gong, M., Zhou, W., Tsai, M. C., Zhou, J., Guan, M., Lin, M. C., Zhang, B., Hu, Y., Wang, D. Y., Yang, J., Pennycook, S. J., Hwang, B. J. & Dai, H. Nanoscale nickel oxide/nickel heterostructures for active hydrogen evolution electrocatalysis. *Nat. Commun.* **5**, 4695 (2014).

53. Zhou, H., Yu, F., Zhu, Q., Sun, J., Qin, F., Yu, L., Bao, J., Yu, Y., Chen, S. & Ren, Z. Water splitting by electrolysis at high current densities under 1.6 volts. *Energy Environ. Sci.* **11**, 2858–2864 (2018).

54. Luo, J., Im, J. H., Mayer, M. T., Schreier, M., Nazeeruddin, M. K., Park, N. G., Tilley, S. D., Fan, H. J. & Grätzel, M. Water photolysis at 12.3% efficiency via perovskite photovoltaics and Earth-abundant catalysts. *Science* **345**, 1593–1596 (2014).

55. Yi, X., Song, L., Ouyang, S., Wang, N., Chen, H., Wang, J., Lv, J. & Ye, J. Cost-Efficient Photovoltaic-Water Electrolysis over Ultrathin Nanosheets of Cobalt/Iron–Molybdenum Oxides for Potential Large-Scale Hydrogen Production. *Small* **17**, 2102222 (2021).

56. Jia, J., Seitz, L. C., Benck, J. D., Huo, Y., Chen, Y., Ng, J. W. D., Bilir, T., Harris, J. S. & Jaramillo, T. F. Solar water splitting by photovoltaic-electrolysis with a solar-to-hydrogen efficiency over 30%. *Nat. Commun.* **7**, 13237 (2016).

57. May, M. M., Lewerenz, H. J., Lackner, D., Dimroth, F. & Hannappel, T. Efficient direct solar-to-hydrogen conversion by in situ interface transformation of a tandem structure. *Nat. Commun.* **6**, 8286 (2015).

58. Varadhan, P., Fu, H. C., Kao, Y. C., Horng, R. H. & He, J. H. An efficient and stable photoelectrochemical system with 9% solar-to-hydrogen conversion efficiency via InGaP/GaAs double junction. *Nat. Commun.* **10**, 5282 (2019).

59. Li, Y., Zhang, L., Torres-Pardo, A., González-Calbet, J. M., Ma, Y., Oleynikov, P., Terasaki, O., Asahina, S., Shima, M., Cha, D., Zhao, L., Takanabe, K., Kubota, J. & Domen, K. Cobalt phosphate-modified barium-doped tantalum nitride nanorod photoanode with 1.5% solar energy conversion efficiency. *Nat. Commun.* **4**, 2566 (2013).

60. Osman, A. I., Mehta, N., Elgarahy, A. M., Hefny, M., Al-Hinai, A., Al-Muhtaseb, A. H. & Rooney, D. W. Hydrogen production, storage, utilisation and environmental impacts: a review. *Environ. Chem. Lett.* **20**, 153–188 (2022).

Chapter 7 Conclusions and outlook

7.1 Conclusions

This thesis has systematically demonstrated different strategies for improving the efficiency of POWS systems for the production of H_2 fuel at elevated temperatures. It is agreed in this field that the efficiency of the POWS system is mainly determined by three fundamental processes, namely, (i) photon absorption, (ii) charge carrier separation and migration and (iii) surface chemical reactions.[1,2] Since the first demonstration of photoelectrochemical water splitting on TiO_2 by Honda and Fujishima in 1972,[3] great progress has been achieved to facilitate the above-mentioned step (i) and step (iii); however, the efficient charge carrier separation remains difficult to obtain and deeper understanding of this process is still required. Therefore, starting from the most widely studied photocatalyst, TiO_2, this thesis has unravelled some fundamental principles behind the POWS reaction, and developed more efficient approaches for enhancing the efficiency of this reaction. By involving the elevated reaction temperatures, it is demonstrated that the POWS performance can be substantially improved due to the facilitated local electric field (LEF).[4] Enlightened by this observation, other strategies including the use of polar-faceted supports and local magnetic field have been explored to further promote the separation of the photo-generated electron/hole pairs and suppress their recombination. Building upon all these works, it is shown that seawater can be decomposed to H_2 and O_2 with very promising efficiency, which takes this POWS system closer to the practical applications.

After introducing the research background and describing the experimental methods in Chapter 1 and Chapter 2 respectively, Chapter 3 starts to examine the use of elevated temperatures in the POWS system over TiO_2-based catalysts for

efficient H_2 evolution.[5] Commercial P25 TiO_2 is doped with N at different concentrations to broaden the visible light absorption range. Unlike most works in this field that involve the use of sacrificial reagents, only pure water is used as the reactant in this thesis, which avoids the additional capital costs and unwanted carbon emission. Detailed investigations of the temperature effect reveal that the POWS performance reaches the maximum at 260-270 ^oC, which coincides with the temperature-dependent ionic dissociation of water. Meanwhile, time-resolved photoluminescence (TRPL) studies confirm that the increased concentration of H^+ or OH^- ions in water leads to the prolonged lifetime of the photo-generated electron/hole pairs. Therefore, at elevated temperatures, the water dissociation is greatly promoted, increasing the concentrations of H^+ and OH^- ions in water and on the surface of the catalyst. The adsorbed ions form strong LEF near the surface, leading to suppressed charge carrier recombination and the enhanced POWS activity. Electron paramagnetic resonance studies show that the surface active sites - surface oxygen vacancies - are easily replenished by water and oxygen in air; however, they can be regenerated at elevated temperatures, which is further confirmed by another work in our group, where systematic synchrotron X-ray diffraction studies have been carried out.[6] Such facilitated regeneration of the surface oxygen vacancies can also contribute to the POWS reaction activity, since it is an important step in the O_2 evolution reaction.[7] Consequently, the use of elevated temperatures is proved to be highly effective to improve the POWS performance by facilitating the LEF and the regeneration of the oxygen vacancies.

Chapter 4 moves on to further enhancing the LEF through engaging the polar-faceted supports.[8] Polar surfaces, different from the non-polar counterparts, have a diverging electrostatic surface energy due to the presence of a non-zero dipole

moment, which makes the polar surfaces quite unique.[9] However, such high-energy surfaces tend to cancel out the surface polarity feature to lower their energy, which will be thermodynamically more favourable, and such relaxation processes lead to various surface features such as surface defects, making the polar surfaces highly active in many chemical reactions.[10,11] In Chapter 4, polar-faceted MgO(111), ZnO(0001), and CeO_2(001) have been fabricated, all of which show enhancements to the POWS activity. TRPL studies indicate that after combining with the polar-faceted metal oxides, the charge carrier lifetime of the N-doped TiO_2 photocatalyst becomes much longer which means that the recombination of the electron/hole pairs is greatly suppressed. On the other hand, the non-polar MgO, ZnO and CeO_2 do not show such effects, and both the POWS activity and the charge carrier lifetime remain the same. Obviously, the strong polarisation of the polar-faceted metal oxides leaves a local electric field on the surface,[12] which can influence the migration of the photo-generated charge carriers and suppress their recombination, resulting in enhanced POWS performance.[8] It is shown that such effects become more remarkable when the average particle size of the photocatalyst reduces. Consequently, a two-dimensional (2D) material, MoS_2 monolayer, is studied in this chapter as well, to further explore this LEF effect originating from the surface polarisation. The 2D MoS_2 shows more significant effects after assembling with the polar-faceted metal oxide supports because of the flexibility of the monolayer and the resulting improved better interaction between the monolayer and the supports. I further extended the study of the LEF effects to layered double hydroxide (LDH) materials, which are also polar-faceted and shows similar surface polarisation. Subsequently, the LEF strength is defined by considering the structure, composition and the electronegativities of all

elements in the polar-faceted supports. It is then shown that both the POWS activity and the lifetime show linear correlation with the LEF strength. It is very clearly shown in Chapter 3 and Chapter 4 that the separation of the photo-generated charge carriers plays a really important role in improving the performance of the POWS system at elevated temperatures and the LEF could influence the migration of the charge carriers through the Coulomb force.

Chapter 5 then moves on to the magnetic field effects (MFEs) on the POWS system,[13] given that the charge carriers experience the Lorentz force when they are moving in a magnetic field, which may also facilitate the charge carrier separation processes. Superparamagnetic Fe_3O_4 nanoparticles are fabricated and combined with the N-doped TiO_2 photocatalysts, which clearly exhibit substantially improved POWS activity in the presence of an external magnetic field. Such enhancement shows obvious linear positive correlation with the strength of the magnetic field and the concentration of the Fe_3O_4 NPs in the composite, while the use of an external magnetic field to bare N-TiO_2 does not lead to any change in the photocatalytic activity. With the help of the superconducting quantum interference device (SQUID), it is illustrated that a very strong local magnetic flux could be induced near the superparamagnetic Fe_3O_4 NPs when an external magnetic field is present. It is then shown that the POWS activity exhibits a linear correlation with the local magnetic flux density when the local magnetic flux is relatively weak. However, when the local magnetic flux density is higher or the N-doping concentration is increased, the MFEs become more significant, deviating from the original linear correlation. Therefore, further density functional theory calculations have been attempted, which suggest a more spin-polarised environment in the N-TiO_2 photocatalysts at a higher doping level. The spin-

polarised energy band only allows the electrons with one spin state to occupy, hence suppressing the recombination of the electrons with the forbidden spin state, which further prolongs the lifetime of the charge carriers.[14]

Building upon the results demonstrated in Chapters 3-5, Chapter 6 investigates a more practical case - the photocatalytic splitting of seawater. It has been illustrated that the local field effects are more significant for the POWS system at elevated temperatures since the sluggish regeneration of oxygen vacancies is greatly promoted at such conditions. It is also noted that there is a large number of ionic species in seawater, which can presumably provide a LEF near the catalyst surface, similar to what has been discussed in Chapter 3. Different electrolytes are investigated in this chapter, and it is shown that the neutral electrolyte solutions could greatly enhance the POWS performance, while the acidic or alkaline solutions show negative effects, presumably due to the unfavourable kinetics. Systematic catalytic studies and DFT calculations demonstrate that such enhancement is highly dependent on the polarisation effect among different facets. Likewise, the TRPL confirms the suppression of the charge carrier recombination processes in the solutions. Different artificial seawater samples are prepared in lab based on the data from literature, all of which exhibit remarkable effects on both activity and lifetime. Natural seawater was collected from Bournemouth, UK, which is also proved to enhance the POWS activity at elevated temperatures.

Overall, the thesis has provided some versatile and facile strategies for improving the efficiency of the POWS system for solar energy conversion and H_2 evolution, especially through tuning the separation of the photo-generated charge carriers at elevated temperatures. Stable and efficient photocatalysts have been developed and fabricated, and the fundamental principles are deeply explored by various

characterisation techniques and computational studies, which is believed to contribute to the rational design of photocatalysts for the related systems. Additionally, it offers a novel non-contact approach which involves the use of magnetic fields. The successful demonstration of the photocatalytic seawater splitting also brings the POWS system closer to the practical application and will presumably provide new research directions in this field.

7.2 Outlook

In order to improve the efficiency of the POWS system for H_2 evolution at elevated temperatures, the recombination of the photo-generated charge carriers must be greatly suppressed. This thesis has provided novel approaches for achieving this goal, such as using LEF or local magnetic field. Studies have been mainly carried out on the most widely investigated photocatalyst, TiO_2-based materials. Therefore, the next step could be to explore other material systems. For example, perovskite materials (cubic structure with a general chemical formula of ABX_3) have received much attention for solar conversion technologies because of their tuneable structural and physicochemical properties.[15–17] Some perovskites exhibit distorted structures that relate to the ratio of the radii of cation A and B.[15] Such structural distortion may lead to changes of the physical, electrical, and photocatalytic properties. Moreover, new perovskite derivatives have been developed in recent years, such as double perovskites[15] and layered perovskites[16], which all show interesting properties. Some perovskite materials have been reported to possess a strong internal electric field within the materials, which could also facilitate the separation of the electron/hole pairs.[18] Moreover, regarding the development of the magnetic field effects, other magnetic NPs should be constructed, such as FeCo or FePt alloys, which show a higher response to the external magnetic field

and generate stronger local magnetic flux.[19,20]

Further efforts could also be made to improve the practical aspects of this system. It should be noted that simply illuminating the reactor with the natural sunlight would not be able to heat up the system to the operating temperature of 270 °C. Thus, in this thesis, it has been demonstrated that the reaction temperature of 270 °C could be maintained by a light-concentrated furnace, and the ultimate goal is to use the concentrated solar light. Some prototypes of such solar furnaces have been demonstrated in literature, which could reach very high temperatures up to thousands of Kelvins using the concentrated solar light.[21–23] Further optimisation will be needed to match the furnace design with the requirements of the POWS system in this thesis, and the reactor should be painted with black coating to maximise the light absorption. Furthermore, it is also noted that in a POWS reaction, a large portion of the photon energy is actually converted to thermal energy by the photocatalyst particles, instead of being effectively stored in the chemical fuel. Such heat is transferred to the surrounding environment. Therefore, further utilisation of such thermal energy generated during the POWS reaction should be attempted. In the conventional POWS systems at room temperature, the low-quality heat is very difficult to be collected and used; however, in the high-temperature POWS system demonstrated in this thesis, the high-quality heat is stored in the superheated water and steam; then the steam can be fed into a turbine generator, followed by water electrolysis for additional H_2 evolution. It is strongly believed that further development and optimisation of such integrated systems can be accomplished by researchers with engineering expertise. Therefore, with the strong international incentives to decarbonise our energy sources, the POWS system at elevated temperatures is a very promising

technique which will greatly contribute to the solar conversion technologies in the foreseeable future.

7.3 References

1. Wang, Q. & Domen, K. Particulate Photocatalysts for Light-Driven Water Splitting: Mechanisms, Challenges, and Design Strategies. *Chem. Rev.* **120**, 919–985 (2020).
2. Peng, Y. K. & Tsang, S. C. E. Facet-dependent photocatalysis of nanosize semiconductive metal oxides and progress of their characterization. *Nano Today* **18**, 15–34 (2018).
3. Fujishima, A. & Honda, K. Electrochemical Photolysis of Water at a Semiconductor Electrode. *Nature* **238**, 37–38 (1972).
4. Li, Y. & Tsang, S. C. E. Recent Progress and Strategies for Enhancing Photocatalytic Water Splitting. *Mater. Today Sustain.* **9**, 100032 (2020).
5. Li, Y., Peng, Y.-K., Hu, L., Zheng, J., Prabhakaran, D., Wu, S., Puchtler, T. J., Li, M., Wong, K.-Y., Taylor, R. A. & Tsang, S. C. E. Photocatalytic water splitting by N-TiO2 on MgO (111) with exceptional quantum efficiencies at elevated temperatures. *Nat. Commun.* **10**, 4421 (2019).
6. Foo, C., Li, Y., Lebedev, K., Chen, T. T., Day, S., Tang, C. & Tsang, S. C. E. Characterisation of oxygen defects and nitrogen impurities in TiO2 photocatalysts using variable-temperature X-ray powder diffraction. *Nat. Commun.* **12**, 661 (2021).
7. Di Valentin, C., Pacchioni, G., Selloni, A., Livraghi, S. & Giamello, E. Characterization of paramagnetic species in N-doped TiO 2 powders by EPR spectroscopy and DFT calculations. *J. Phys. Chem. B* **109**, 11414–11419 (2005).
8. Li, Y., Wu, S., Zheng, J., Peng, Y.-K., Prabhakaran, D., Taylor, R. A., Chi, S. & Tsang, S. C. E. 2D photocatalysts with tuneable supports for enhanced photocatalytic water splitting. *Mater. Today* **41**, 34–43 (2020).
9. Nosker, R. W., Mark, P. & Levine, J. D. Polar surfaces of wurtzite and zincblende lattices. *Surf. Sci.* **19**, 291–317 (1970).
10. Diebold, U., Koplitz, L. V. & Dulub, O. Atomic-scale properties of low-index ZnO surfaces. *Appl. Surf. Sci.* **237**, 336–342 (2004).
11. Li, Y. & Tsang, S. C. E. Unusual Catalytic Properties of High-Energetic-Facet Polar Metal Oxides. *Acc. Chem. Res.* **54**, 366–378 (2021).
12. Pojani, A., Finocchi, F., Goniakowski, J. & Noguera, C. A theoretical study of the stability and electronic structure of the polar {111} face of mgo. *Surf. Sci.* **387**, 354–370 (1997).
13. Li, Y., Wang, Z., Wang, Y., Kovács, A., Foo, C., Dunin-Borkowski, R. E., Lu, Y., Taylor, R. A., Wu, C. & Tsang, S. C. E. Local magnetic spin mismatch promoting photocatalytic overall water splitting with exceptional solar-to-hydrogen efficiency. *Energy Environ. Sci.* **15**, 265–277 (2022).
14. Pan, L., Ai, M., Huang, C., Yin, L., Liu, X., Zhang, R., Wang, S., Jiang, Z., Zhang, X., Zou, J. J. & Mi, W. Manipulating spin polarization of titanium dioxide for efficient photocatalysis. *Nat. Commun.* **11**, 418 (2020).
15. Peña, M. A. & Fierro, J. L. G. Chemical structures and performance of perovskite oxides. *Chem. Rev.* **101**, 1981–2017 (2001).

16. Zhang, G., Liu, G., Wang, L. & Irvine, J. T. S. Inorganic perovskite photocatalysts for solar energy utilization. *Chem. Soc. Rev.* **45**, 5951–5984 (2016).

17. Wang, W., Tadé, M. O. & Shao, Z. Research progress of perovskite materials in photocatalysis- and photovoltaics-related energy conversion and environmental treatment. *Chem. Soc. Rev.* **44**, 5371–5408 (2015).

18. Takata, T., Jiang, J., Sakata, Y., Nakabayashi, M., Shibata, N., Nandal, V., Seki, K., Hisatomi, T. & Domen, K. Photocatalytic water splitting with a quantum efficiency of almost unity. *Nature* **581**, 411–414 (2020).

19. Sun, S. Recent Advances in Chemical Synthesis, Self-Assembly, and Applications of FePt Nanoparticles. *Adv. Mater.* **18**, 393–403 (2006).

20. Bai, G., Jin, J., Wu, C. & Yan, M. Ultrafine FeCo Nanoparticles Isolated by Ultrathin Dielectric Shells for Microwave Application. *ACS Appl. Nano Mater.* **2**, 3570–3576 (2019).

21. Cui, Z., Bai, F., Zhang, X., Zang, C., Zhu, H. & Wang, Z. A line-focused solar furnace for large area thermal experiment. *AIP Conf. Proc.* **2303**, 110001 (2020).

22. Rodriguez, J., Cañadas, I. & Zarza, E. New PSA high concentration solar furnace SF40. *AIP Conf. Proc.* **1734**, 070028 (2016).

23. Garcia, D., Liang, D., Tibúrcio, B. D., Almeida, J. & Vistas, C. R. A three-dimensional ring-array concentrator solar furnace. *Sol. Energy* **193**, 915–928 (2019).

Appendix

Appendix Note A1 Calculation of QE

A typical QE calculation is shown below, taking Fe_3O_4/N-TiO_2-4 as an example (demonstrated in Chapter 5):

For the measurement of the QE of the Fe_3O_4/N-TiO_2-4 photocatalyst at 437 nm, the H_2 amount analysed by GC is 5.25 μmol in the 2-hour experiment, corresponding to 3.159×10^{18} H_2 molecules ($N = n \times N_A$). During the period of 2 hours, the energy of the light irradiation: $W=P\times t$. With the bandpass filter of 437 nm, the light irradiation power was measured to be P = 0.45 mW at the centre of the batch reactor (the power of light was measured using a Thorlabs S121C standard photodiode power sensor, which had been calibrated by Thorlabs before it was delivered, and was used without further calibration), therefore, the energy W = 0.00045 × 7200 = 3.24 J, which contains the photon (437 nm) numbers of 7.123×10^{18} ($\varepsilon = h\nu$). Then, the QE can be calculated using Equation 2.15.

$$QE\ (\%) = (2\times3.159\times10^{18})/\ (7.123\times10^{18}) \times100\% = 88.7\ \%$$

As in the energy evaluation of solar conversion systems by Ross and Bolton, there is always an energy difference of 0.2-0.3 eV between the absorbed photon energy and the energy that can do useful work. Thus, the threshold wavelength which is just capable of driving the reaction can be calculated based on the equation (assuming an energy loss of 0.3 eV):

$$\lambda_t = \frac{hc}{\frac{\Delta G^\theta}{n} + U_{loss}}$$

The result is *ca.* 970 nm, which means only the photons with a wavelength shorter than 970 nm can drive the POWS reaction. Bolton et al. gave an example in their

work: for a reaction with a potential of 1.052 V, the threshold wavelength is 880 nm. In the case shown here, the reaction potential is 0.979 V for a 2-hour reaction, which is smaller than that in the example. Thus, the calculated threshold wavelength of 970 nm is reasonable.

Appendix Note A2 Calculations of heat balance

$2H_2O$ === $2H_2 + O_2$

$N_2 + 3H_2$ === $2NH_3$ ΔH_1 = -91.8 kJ mol^{-1}

$CO_2 + 4H_2$ === $CH_4 + 2H_2O$ ΔH_2 = -165.0 kJ mol^{-1}

For ammonia synthesis reaction, assuming 1 kg NH_3 is synthesised, then the molar number is:

n (NH_3) = $\frac{m(NH3)\ (g)}{M(NH3)\ (g/mol)}$ = $\frac{1000\ g}{17.031\ g/mol}$ = 58.72 mol

Required amount of H_2 to produce 1 kg NH_3 is:

n (H_2) = n (NH_3) (mol) × 1.5 = 58.72 mol × 1.5 = 88.08 mol

Required amount of water to provide 88.08 mol of H_2 is:

n (H_2O) = n (H_2) = 88.08 mol

m (H_2O) = n (H_2O) ×M (H_2O) = 88.08 mol × 18.015 g/mol = 1586.76 g

Heat produced during this ammonia synthesis process is:

Q_1= $\frac{1}{2}$ n (NH_3)× $(-\Delta H_1)$ = $\frac{1}{2}$ × 58.72 mol × 91.8 kJ/mol × 1000 J/kJ = 2.70 × 10^6 J

Heat required to heat up this amount of water from room temperature (25 °C) to 270 °C (the optimised temperature in our photocatalytic overall water splitting system) is:

Q_2= cm ΔT= 4.18 J·g^{-1}·K^{-1} × 1586.76 g × (270 - 25) K = 1.63 × 10^6 J

Apparently, $Q_1 > Q_2$

For CO_2 hydrogenation to methane, assuming 1 kg CH_4 is synthesised:

n (CH_4) = $\frac{m(\mathrm{CH4})\ (g)}{M(\mathrm{CH4})\ (g/mol)}$ = $\frac{1000\ g}{16.043\ g/mol}$ = 62.33 mol

Required amount of H_2 to produce 1 kg CH_4 is:

n (H_2) = n (CH_4) (mol) × 4 = 62.33 mol × 4 = 249.32 mol

Required amount of water to provide 249.32 mol of H_2 is:

n (H_2O) = n (H_2) = 249.32 mol

m (H_2O) = n (H_2O) (mol) × M (H_2O) (g/mol) = 249.32 mol × 18.015 g/mol = 4491.50 g

Heat produced during the CO_2 hydrogenation to methane process is:

Q_3 = n (CH_4) × $(-\Delta H_2)$ = 62.33 mol × 165 kJ/mol × 1000 J/kJ = 1.03×10^7 J

Heat required to heat up this amount of water from room temperature (25 ^oC) to 270 ^oC (the optimised temperature in our photocatalytic overall water splitting system):

Q_4 = cm ΔT = 4.18 $J \cdot g^{-1} \cdot K^{-1}$ × 4491.50 g × (270 - 25) K = 4.60×10^6 J

Apparently, $Q_3 > Q_4$

Appendix Note A3 Calculation of energy efficiencies

(Taking the Fe_3O_4/N-TiO_2-4 in Chapter 5 as an example; reaction is performed at 270 °C with an external magnetic field of 180 mT)

a. Calculation of the Gibbs free energy at 298 K and 101.325 kPa

For the reaction:

H_2O (l) ==H_2 (g) + 0.5O_2 (g)

The standard enthalpy of reaction is:

$$\Delta_r H_m^\ominus = 0 + 0.5 \times 0 - (-286) = 286\ \mathrm{kJ/mol}$$

The standard entropy change of reaction is:

$$\Delta_r S_m^\ominus = 130.684 + 0.5 \times 205.138 - 69.91 = 163.343\ \mathrm{J/(mol \cdot K)}$$

According to the equation of Gibbs free energy:

$$\Delta_r G_m^\ominus = \Delta_r H_m^\ominus - T\Delta_r S_m^\ominus$$

The standard Gibbs free energy at 298 K is:

$$\Delta_r G_m^\ominus = 286 - 298 \times 163.343 \times 10^{-3} = 237\ \mathrm{kJ/mol}$$

b. Calculation of the Gibbs free energy at 543 K and 101.325 kPa

According to the Van't Hoff equation:

$$\frac{d \ln K}{d T} = -\frac{\Delta H^\ominus}{RT^2}$$

Therefore,

$$\ln \frac{K_2}{K_1} = -\frac{\Delta H^\ominus}{R}\left(\frac{1}{T_2} - \frac{1}{T_1}\right)$$

Also,

$$\Delta_r G_m^\ominus = -RT \ln K$$

Then

$$-\frac{\Delta_r G_m^\ominus (T_2)}{RT_2} + \frac{\Delta_r G_m^\ominus (T_1)}{RT_1} = -\frac{\Delta H^\ominus}{R}\left(\frac{1}{T_2} - \frac{1}{T_1}\right)$$

Thus, the Gibbs free energy at 543 K and 101.325 kPa can be calculated:

$$\Delta_r G_m^\ominus (543K) = 196.73\ kJ/mol$$

The reactant at 270 °C in our system is still liquid water, which is under the saturated vapour pressure of *ca.* 60 bar at 270 °C. Thus, the phase change from liquid water to water vapour is not considered, since this process is not involved in the reaction. As the result shows, the Gibbs free energy at 270 °C (543 K) indeed decreases by about 40 kJ/mol, but it is still much higher than zero, which means the reaction is still not thermodynamically favourable at this temperature.

c. Correction of the Gibbs free energy for the reaction pressure

According to the Van't Hoff isotherm:

$$\Delta_r G_m = \Delta_r G_m^\ominus + RT\ \ln Q$$

where $\Delta_r G_m$ is the Gibbs free energy of reaction under non-standard states at temperature T; $\Delta_r G_m^\ominus$ is the Gibbs free energy of the reaction at T and 101.325 kPa; Q is the thermodynamic reaction quotient.

For the POWS reaction, Q can be defined as:

$$Q = \frac{p_{H_2}}{p^\ominus} \cdot \left(\frac{p_{O_2}}{p^\ominus}\right)^{0.5}$$

Also, assuming the gas phase in the batch reactor follows the ideal gas law:

$$p_{H_2} V = n_{H_2} RT$$

Based on the reaction stoichiometry,

$$p_{H_2} = 2p_{O_2}$$

It should be emphasised that this POWS system was conducted at constant temperature (T=543 K) and volume (V=20 mL), thus, the Helmholtz free energy, ΔA, was then used in the subsequent calculation of the efficiencies. Given that:

$$A = U - TS$$

$$G = A + PV$$

It is also noticed that in our system, the partial pressures of H_2 and O_2 change over the reaction progress, resulting in a changing free energy. Therefore, the free energy has been corrected for different partial pressures throughout the whole reaction process, and the STH efficiencies can be calculated accordingly. Consequently, the average free energy and average STH over the reaction progress are calculated:

$$Time - average\ \Delta A = 203.3 \pm 5.4\ \mathrm{kJ\ mol^{-1}}$$

$$Time - average\ \eta_{STH} = 11.9 \pm 0.5\ \%$$

d. Evaluation of the energy input required for heating

Additionally, I have estimated the energy required to heat your system to 270 °C. Considering a photocatalytic process operated under steady state at 270 °C, energy is required to heat the input liquid water from room temperature 25 °C to 270 °C. The energy for heating the reactor is not considered in this calculation since this is not an intrinsic property of the POWS reaction and highly dependent on the reactor design; also, when the system is operating under a steady state, energy is only required to compensate the heat loss, which can be minimised by

covering the reactor with adiabatic materials, then this part of energy could presumably be negligible. In our system, 5 mL of water was used as the reactant when the energy efficiencies were evaluated.

When water is heated to 270 °C, the saturated vapour pressure is established, which can be calculated according to the Clausius–Clapeyron relation:

$$\frac{\mathrm{d\,P}}{\mathrm{d\,T}} = \frac{\mathrm{PL}}{\mathrm{T^2R}}$$

where P is the pressure, R is the specific gas constant, L is the specific latent heat of the substance, and T is the temperature.

Assuming L is independent to the temperature, then the relation can be integrated, giving:

$$\ln\frac{\mathrm{P_2}}{\mathrm{P_1}} = -\frac{\mathrm{L}}{\mathrm{R}}\left(\frac{1}{\mathrm{T_2}} - \frac{1}{\mathrm{T_1}}\right)$$

For water, L=40.68 kJ/mol, thus, the saturated vapour pressure at 270 °C is:

$$\mathrm{P}(543\ \mathrm{K}) = 60.36\ \mathrm{bar}$$

Assuming it follows the ideal gas law, the amount of H_2O in the gas phase is:

$$\mathrm{n_{vapour}} = \frac{\mathrm{pV}}{\mathrm{RT}} = \frac{60.36 \times 101.325\ \mathrm{kPa} \times 0.015\ \mathrm{L}}{8.314 \times 543\ \mathrm{K}} = 0.02\ \mathrm{mol}$$

$$\mathrm{m_{vapour}} = 0.02\ \mathrm{mol} \times 18\frac{\mathrm{g}}{\mathrm{mol}} = 0.36\ \mathrm{g}$$

Clearly, only a small portion of water transfers to vapour. Thus, the energy for heating the 5 mL of H_2O from room temperature to 270 °C is calculated as follows, assuming the heat capacity does not significantly change with temperature:

From 25 °C to 100 °C:

$$Q_1 = m_{water} C_{p,water} \Delta T = 5\ g \times 4.184 \frac{J}{g \cdot K} \times 75\ K = 1569\ J$$

At 100 °C:

$$Q_2 = nL = 0.02\ mol \times 40680 \frac{J}{mol} = 813.6$$

From 100 °C to 270 °C:

$$Q_3 = m_{water} C_{p,water} \Delta T + m_{vapour} C_{p,vapour} \Delta T$$

$$= 4.64\ g \times 4.184 \frac{J}{g \cdot K} \times 170\ K + 0.36\ g \times 1.85 \frac{J}{g \cdot K} \times 170\ K$$

$$= 3413.56\ J$$

Therefore, the total energy required for heating is:

$$Q_{water} = Q_1 + Q_2 + Q_3 = 5796\ J$$

The above has shown the energy required to heat water up to 270 °C. Moreover, I also evaluated the actual overall energy conversion efficiency, $\eta_{overall}$, experimentally. I tried my best to cover the experimental set-up with a band heater and thermally insulating materials such as silica wool, thermal foil, etc., to reduce the heat loss, however, a 'perfect' insulation layer cannot be achieved and the heat loss is inevitable. The heating process was controlled by a Parr 4838 thermo-controller under the proportional integral derivative (PID) mode and monitored with a SpecView-3 software. When the temperature reached 270 °C, the heater started to operate at a low output level to compensate the heat loss. Thus, the actual energy input could be calculated by integrating the power-time curve and the actual overall energy conversion efficiency can be obtained.

The actually energy consumed for heating up the whole system (reactor + reactant + photocatalyst) from 20 to 270 °C and maintaining the temperature at 270 °C for

20 hours is:

$$Q_{actual} = 53174\ J$$

The energy input from the solar simulator is:

$$E_{solar} = P \cdot \pi \cdot r^2 \cdot t = 5652\ J$$

Subsequently, the actual overall energy conversion efficiency can be calculated:

$$\eta_{overall} = \frac{n_{hydrogen} \times \text{average free energy (543K)}}{E_{solar} + Q_{actual}} \times 100\% = 1.16 \pm 0.05\%$$

By comparing the Q_{water} and Q_{actual}, it is obvious that the majority of the energy input is consumed by heating the reactor instead of the reactant, and this part of energy could vary greatly between different reactor designs. Also, the system could be working for even longer period of time without the need of heating up the reactor again, but only a small amount of energy is required to compensate the heat loss (given that a perfect thermal insulation is hardly achievable).